Dissertation

Linear and Nonlinear Properties of Numerical Methods for the Rotating Shallow Water Equations

Submitted by

Chris Eldred

Department of Atmospheric Science

In partial fulfillment of the requirements

For the Degree of Doctor of Philosophy

Colorado State University

Fort Collins, Colorado

Summer 2015

Doctoral Committee:

Advisor: David Randall

Thomas Birner
Wayne Schubert
Don Estep
Peter Lauritzen
Rainer Bleck

Abstract

Linear and Nonlinear Properties of Numerical Methods for the Rotating Shallow Water Equations

The shallow water equations provide a useful analogue of the fully compressible Euler equations since they have similar conservation laws, many of the same types of waves and a similar (quasi-) balanced state. It is desirable that numerical models posses similar properties, and the prototypical example of such a scheme is the 1981 Arakawa and Lamb (AL81) staggered (C-grid) total energy and potential enstrophy conserving scheme, based on the vector invariant form of the continuous equations. However, this scheme is restricted to a subset of logically square, orthogonal grids. The current work extends the AL81 scheme to arbitrary non-orthogonal polygonal grids, by combining Hamiltonian methods (work done by Salmon, Gassmann, Dubos and others) and Discrete Exterior Calculus (Thuburn, Cotter, Dubos, Ringler, Skamarock, Klemp and others).

It is also possible to obtain these properties (along with arguably superior wave dispersion properties) through the use of a collocated (Z-grid) scheme based on the vorticity-divergence form of the continuous equations. Unfortunately, existing examples of these schemes in the literature for general, spherical grids either contain computational modes; or do not conserve total energy and potential enstrophy. This dissertation extends an existing scheme for planar grids to spherical grids, through the use of Nambu brackets (as pioneered by Rick Salmon).

To compare these two schemes, the linear modes (balanced states, stationary modes and propagating modes; with and without dissipation) are examined on both uniform planar grids (square, hexagonal) and quasi-uniform spherical grids (geodesic, cubed-sphere). In

addition to evaluating the linear modes, the results of the two schemes applied to a set of standard shallow water test cases and a recently developed forced-dissipative turbulence test case from John Thuburn (intended to evaluate the ability the suitability of schemes as the basis for a climate model) on both hexagonal-pentagonal icosahedral grids and cubed-sphere grids are presented. Finally, some remarks and thoughts about the suitability of these two schemes as the basis for atmospheric dynamical development are given.

Acknowledgements

I must start here by first thanking my advisor, Dr. David Randall for his many words of encouragement and patience; and for agreeing to take me on as a transfer graduate student. This work would not have been possible without his support and willingness to allow me to purse my own ideas. Thank you to my committee members (Dr. Thomas Birner, Dr. Wayne Schubert, Dr. Don Estep, Dr. Peter Lauritzen and Dr. Rainer Bleck) for the invaluable feedback they have provided me, and for the generous donation of their time. I would also like to thank the members of my research group (in particular, Celal Konor and Ross Heikes) for many lively conversations and debates that immeasurably improved this work. To my fellow graduate students and friends (Brandon Wolding, Doug Stolz, John Peters, Elizabeth Thompson and many others)- thanks for your advice and guidance on my journey. I owe my sanity to the many other friends (chief among them Brendan Fowler, James Miner, Mary Miner and Robert Janda) who have always been there for me. Finally, thanks to my family and Nikki for their unwavering support through this long process. This work was funded through the Department of Energy Computational Science Graduate Fellowship, for which I am grateful.

This dissertation is typset in LaTeX using a document class designed by Leif Anderson.

Table of Contents

Abstract ii

Acknowledgements iv

List of Tables ix

List of Figures x

Chapter 1. Introduction 1

1.1. Numerical Methods Should Reflect Reality 1

1.2. Physics and Parameterizations 6

1.3. Hamiltonian Structure of the Equations Governing Atmospheric Flow 8

1.4. Desirable Properties for Discretization Schemes of the Rotating Shallow Water Equations 9

1.5. The Current State of Affairs 17

1.6. What This Work Addresses 28

1.7. What This Work Does Not Address 31

1.8. Organization of Thesis 33

Chapter 2. Rotating Shallow Water Equations in Continuous Form 34

2.1. Continuous Shallow Water Equations 34

2.2. Potential Vorticity 49

2.3. Conserved Quantities 49

2.4. Subgrid Turbulence Operators 53

2.5. Chapter Summary 56

Chapter 3. Generalized C Grid Scheme 57

3.1. General Nonlinear Formulation (Discrete Exterior Calculus and Discrete Hamiltonian) 57
3.2. Linear Mimetic Properties 72
3.3. Discrete Conservation 75
3.4. Summary of Required Operator Properties 79
3.5. Specific Schemes 82
3.6. Doubly Conservative Version of $\mathbf{Q}$ 87
3.7. Results for Doubly Conservative $\mathbf{Q}$ 91
3.8. Other Desirable Properties 92
3.9. Chapter Summary 94

Chapter 4. Generalized Z Grid Scheme 96
4.1. General Nonlinear Formulation 96
4.2. Linear Mimetic Properties 108
4.3. Discrete Conservation 109
4.4. Schemes 111
4.5. Other Desirable Properties 113
4.6. Chapter Summary 115

Chapter 5. Linear Modes 116
5.1. Continuous Equations 116
5.2. Discrete Equations 125
5.3. Numerical Stationary Modes 130
5.4. Numerical Propagating Modes 138
5.5. Chapter Summary 163

Chapter 6. Evaluation and Comparison of the Generalized C and Z Grid Schemes 164
6.1. Details of Runs 164
6.2. Order of Accuracy 171
6.3. Williamson Test Case 2- Solid Body Rotation (TC2) 181
6.4. Williamson Test Case 5- Flow over a Mountain (TC5) 186
6.5. Rossby-Haurwitz Wave (TC6) 187
6.6. Barotropically Unstable Jet (Galewsky) 191
6.7. Shallow Water Held-Suarez Analogue (Held Suarez) 198
6.8. Chapter Summary 225

Chapter 7. Conclusions 227
7.1. Linear Modes Summary 227
7.2. Test Cases Summary 228
7.3. Selection of a scheme for developing a weather model 230
7.4. Selection of a scheme for developing a climate model 231
7.5. Future Work 232

Bibliography 234

Appendix A. Hamiltonian Methods 244
A.1. Infinite Dimensional Non-Canonical Hamiltonian Systems 244
A.2. Linearized Hamiltonian Dynamics 246
A.3. Conserved Quantities 247

Appendix B. Horizontal Grids and Discretization Methods 251
B.1. Design of a Numerical Method 251
B.2. Horizontal Mesh Overview 252

B.3. Specific Meshes 258
B.4. Field Function Representation 261
Appendix C. Discrete Exterior Calculus 264
C.1. Discrete Exterior Calculus in 2D 264
Appendix D. Dispersion Relations and Allowed Wavenumbers for Planar Grids 271
D.1. Dispersion Relations for Planar Grids 271
D.2. Allowed Wavenumbers for Planar Grids 273

List of Tables

3.1 List of discrete variables and their diagnostic equations 59

3.2 Summary of required operator properties 81

5.1 Grid Details 149

6.1 Simulation Details 164

6.2 Grid Properties for Tweaked Geodesic Grids 166

6.3 Grid Properties for SCVT Geodesic Grids 166

6.4 Grid Properties for Spring Dynamics $\beta = 0.8$ Geodesic Grids 167

6.5 Grid Properties for Spring Dynamics $\beta = 1.1$ Geodesic Grids 167

6.6 Grid Properties for Cubed Sphere Grids 168

B.1 Mesh element neighbor stencils 256

List of Figures

1.1 Diagram of the possible linear modes encountered in a numerical model of the shallow water equations. Green modes are physical, while red modes are numerical artifacts. 4

1.2 Diagram of the components of a modern atmospheric model. Note the overlap between tracer transport and dynamics. In practice, there should probably be overlap between all three components, but traditionally the dynamics/transport and the physics are developed largely independently. This thesis deals only with the dynamics component (shown in green). 7

1.3 Image showing the interplay between physics, dynamics and transport that characterizes an atmospheric dynamical core, and the role of truncation scale in determining what constitutes the necessary physics. 7

1.4 Diagram of (some of) the desirable properties of a model that influence its ability to achieve realistic simulations. The boxes on the far left represent two possible approaches to achieving some of these properties. 10

1.5 Various choices of grid staggering for the shallow water equations. 19

1.6 A general non-orthogonal polygonal grid with an associated dual grid. If m and n are parallel for every edge, then the grid is orthogonal. 26

3.1 Discrete variables and their staggering on the horizontal mesh 58

3.2 Diagram of the discrete exterior derivative D_2 on a triangular mesh. Obtained from http://brickisland.net/cs177/?p=274 60

3.3 Depiction of the action of the various Hodge star operators on a uniform triangular grid. Obtained from http://brickisland.net/cs177/?p=274 61

3.4 The discrete DeRham cohomology induced by the incidence matrices and Hodge stars 62

3.5 Actions of **R** and **W** for the C grid scheme 62

3.6 Diagram of doubly conservative **Q** operator. For a given edge (denoted by the green circle), the potential vorticity flux is a weighted sum of the mass flux at each red circled edge, where the weights are a linear combination of the potential vorticity at each blue circled vertex..... 88

4.1 Discrete variables and staggering for the generalized Z grid scheme 98

5.1 Fluid height for stationary mode with frequency equal to zero on icosahedral grid (C grid scheme)..... 136

5.2 Fluid height for stationary mode with frequency equal to zero on cubed-sphere grid (C grid scheme)..... 136

5.3 Relative vorticity for stationary mode with frequency equal to zero on icosahedral grid (C grid scheme)..... 137

5.4 Relative vorticity for stationary mode with frequency equal to zero on cubed-sphere grid (C grid scheme)..... 137

5.5 Fluid height for stationary mode with frequency $3.07873e^{-16}$ on icosahedral grid (C grid scheme)..... 137

5.6 Fluid height for stationary mode with frequency $2.1704e^{-16}$ on cubed-sphere grid (C grid scheme)..... 137

5.7 Relative vorticity for stationary mode with frequency $3.07873e^{-16}$ on icosahedral grid (C grid scheme)..... 138

5.8 Relative vorticity for stationary mode with frequency $2.1704e^{-16}$ on cubed-sphere grid (C grid scheme) . . . 138

5.9 Fluid height for stationary mode with frequency equal to zero on icosahedral grid (Z grid scheme) . . . 138

5.10 Relative vorticity for stationary mode with frequency equal to zero on icosahedral grid (Z grid scheme) . . . 138

5.11 Fluid height for stationary mode with frequency equal to $5.3755e^{-16}$ on icosahedral grid (Z grid scheme) . . . 139

5.12 Relative vorticity for stationary mode with frequency equal to $5.3755e^{-16}$ icosahedral grid (Z grid scheme) . . . 139

5.13 Dispersion relations for perfect square grid with $\frac{\lambda}{d} = 2.0$, without dissipation. Normalized frequency $\frac{\sigma}{f}$ versus non-dimensional wavenumbers kd and ld is plotted. Top panel is continuous system, middle panel is C grid scheme, bottom panel is Z grid scheme. . . . 143

5.14 Dispersion relations for perfect hexagonal grid with $\frac{\lambda}{d} = 2.0$, without dissipation. Normalized frequency $\frac{\sigma}{f}$ versus non-dimensional wavenumbers kd and ld is plotted. Top panel is continuous system, middle panel is C grid scheme, bottom panel is Z grid scheme. . . . 144

5.15 Real part of dispersion relations for perfect square grid with $\frac{\lambda}{d} = 2.0$, with dissipation. Normalized frequency $\frac{\sigma}{f}$ versus non-dimensional wavenumbers kd and ld is plotted. Top panel is continuous system, middle panel is C grid scheme, bottom panel is Z grid scheme. . . . 145

5.16 Real part of dispersion relations for perfect hexagonal grid with $\frac{\lambda}{d} = 2.0$, with dissipation. Normalized frequency $\frac{\sigma}{f}$ versus non-dimensional wavenumbers kd and ld is plotted. Top panel is continuous system, middle panel is C grid scheme, bottom panel is Z grid scheme. 146

5.17 Imaginary part of dispersion relations for perfect square grid with $\frac{\lambda}{d} = 2.0$, with dissipation. Normalized frequency $\frac{\sigma}{f}$ versus non-dimensional wavenumbers kd and ld is plotted. Top panel is continuous system, middle panel is C grid scheme, bottom panel is Z grid scheme. 147

5.18 Imaginary part of dispersion relations for perfect hexagonal grid with $\frac{\lambda}{d} = 2.0$, with dissipation. Normalized frequency $\frac{\sigma}{f}$ versus non-dimensional wavenumbers kd and ld is plotted. Top panel is continuous system, middle panel is C grid scheme, bottom panel is Z grid scheme. 148

5.19 Dispersion relations for f-sphere on quasi-uniform spherical grids without dissipation. Normalized frequency $\frac{\sigma}{f}$ versus mode index (see discussion) is plotted. Top panel is C grid on icosahedral grid, middle panel is C grid on cubed-sphere grid, bottom panel is Z grid scheme on icosahedral grid. 152

5.20 Real part of dispersion relations for f-sphere on quasi-uniform spherical grids with dissipation. Normalized frequency $\frac{\sigma}{f}$ versus mode index (see discussion) is plotted. Top panel is C grid on icosahedral grid, middle panel is C grid on cubed-sphere grid, bottom panel is Z grid scheme on icosahedral grid. 153

5.21 Imaginary part of dispersion relations for f-sphere on quasi-uniform spherical grids with dissipation. Frequency versus mode index (see discussion) is plotted. Top

panel is C grid on icosahedral grid, middle panel is C grid on cubed-sphere grid, bottom panel is Z grid scheme on icosahedral grid. 154

5.22 Dispersion relations for full sphere on quasi-uniform spherical grids without dissipation. Normalized frequency $\frac{\sigma}{f}$ versus mode index (see discussion) is plotted. Top panel is C grid (doubly conservative version) on icosahedral grid, middle panel is C grid (doubly conservative version) on cubed-sphere grid, bottom panel is Z grid scheme on icosahedral grid. 157

5.23 Real part of dispersion relations for full sphere on quasi-uniform spherical grids with dissipation. Normalized frequency $\frac{\sigma}{f}$ versus mode index (see discussion) is plotted. Top panel is C grid (doubly conservative version) on icosahedral grid, middle panel is C grid (doubly conservative version) on cubed-sphere grid, bottom panel is Z grid scheme on icosahedral grid. 158

5.24 Imaginary part of dispersion relations for full sphere on quasi-uniform spherical grids with dissipation. Frequency versus mode index (see discussion) is plotted. Top panel is C grid (doubly conservative version) on icosahedral grid, middle panel is C grid (doubly conservative version) on cubed-sphere grid, bottom panel is Z grid scheme on icosahedral grid. 159

5.25 Spatial structures for a selected Rossby wave for various grids and schemes. On the left is fluid height, on the right is relative vorticity. The top row is the C grid scheme on icosahedral grids, the middle row is the C grid scheme on cubed-sphere grids and the bottom row is the Z grid scheme 160

5.26 Spatial structures for the highest frequency inertia-gravity waves on the f-sphere for various grids and schemes. On the left is fluid height, on the right is relative

vorticity. The top row is the C grid scheme on icosahedral grids, the middle row is the C grid scheme on cubed-sphere grids and the bottom row is the Z grid scheme 161

5.27 Spatial structures for the highest frequency inertia-gravity waves on the full sphere for various grids and schemes. On the left is fluid height, on the right is relative vorticity. The top row is the C grid scheme on icosahedral grids, the middle row is the C grid scheme on cubed-sphere grids and the bottom row is the Z grid scheme 162

6.1 Refinement Level 4 Geodesic Grid with Tweaked Optimization (Primal) 166

6.2 Refinement Level 4 Geodesic Grid with Tweaked Optimization (Dual) 166

6.3 Refinement Level 4 Cubed Sphere Grid (Primal) 168

6.4 Refinement Level 4 Cubed Sphere Grid (Dual) 168

6.5 L_2 accuracy for the primal grid laplacian operator $\mathbf{L_p}$ 174

6.6 L_∞ accuracy for the primal grid laplacian operator $\mathbf{L_p}$ 174

6.7 L_2 accuracy for the dual grid laplacian operator $\mathbf{L_d}$ 175

6.8 L_∞ accuracy for the dual grid laplacian operator $\mathbf{L_d}$ 175

6.9 L_2 accuracy for the edge laplacian operator $\mathbf{L_e}$ 176

6.10 L_∞ accuracy for the edge laplacian operator $\mathbf{L_e}$ 176

6.11 L_2 accuracy for the $\mathbf{W}$ operator with u_e divergent 177

6.12 L_∞ accuracy for the $\mathbf{W}$ operator with u_e divergent 177

6.13 L_2 accuracy for the $\mathbf{W}$ operator with u_e rotational 177

6.14 L_∞ accuracy for the $\mathbf{W}$ operator with u_e rotational 177

6.15 L_2 accuracy for the $\mathbf{R}$ operator 178

6.16 L_∞ accuracy for the $\mathbf{R}$ operator 178

6.17 L_2 accuracy for the ϕ operator 179

6.18 L_∞ accuracy for the ϕ operator 179

6.19 L_2 accuracy for the Z grid laplacian operator 180

6.20 L_∞ accuracy for the Z grid laplacian operator 180

6.21 L_2 accuracy for the Z grid flux divergence operator 181

6.22 L_∞ accuracy for the Z grid flux divergence operator 181

6.23 L_2 accuracy for the Z grid jacobian operator 181

6.24 L_∞ accuracy for the Z grid jacobian operator 181

6.25 Potential enstrophy conservation for the C grid scheme (all three $\mathbf{Q}$ variants) on grid G8 for TC2 183

6.26 Potential enstrophy conservation for the C grid scheme (all three $\mathbf{Q}$ variants) on grid C8 for TC2 183

6.27 Total energy conservation for the C grid scheme (all three $\mathbf{Q}$ variants) on grid G8 for TC2 183

6.28 Total energy conservation for the C grid scheme (all three $\mathbf{Q}$ variants) on grid C8 for TC2 183

6.29 L_2 accuracy in fluid height h_i for TC2 with C grid scheme using enstrophy-conserving $\mathbf{Q}$ operator 184

6.30 L_∞ accuracy in fluid height h_i for TC2 with C grid scheme using enstrophy-conserving $\mathbf{Q}$ operator 184

6.31 L_2 accuracy in fluid height h_i for TC2 with C grid scheme using energy-conserving $\mathbf{Q}$ operator 184

6.32 L_∞ accuracy in fluid height h_i for TC2 with C grid scheme using energy-conserving **Q** operator 184

6.33 L_2 accuracy in fluid height h_i for TC2 with C grid scheme using doubly conservative **Q** operator 185

6.34 L_∞ accuracy in fluid height h_i for TC2 with C grid scheme using doubly conservative **Q** operator 185

6.35 L_2 accuracy in fluid height h_i for TC2 with Z grid 185

6.36 L_∞ accuracy in fluid height h_i for TC2 with Z grid 185

6.37 Potential enstrophy conservation for the Z grid and C grid (doubly conservative version) schemes on grid G8 for TC2 186

6.38 Total energy conservation for the Z grid and C grid (doubly conservative version) schemes on grid G8 for TC2 186

6.39 Potential vorticity at Day 30 for C grid scheme using doubly conservative **Q** variant on grid G6 for TC5 188

6.40 Potential vorticity at Day 30 for C grid scheme using doubly conservative **Q** variant on grid C6 for TC5 188

6.41 Potential vorticity at Day 30 for C grid scheme using energy-conserving **Q** variant on grid G6 for TC5 188

6.42 Potential vorticity at Day 30 for C grid scheme using energy-conserving **Q** variant on grid C6 for TC5 188

6.43 Potential vorticity at Day 30 for C grid scheme using enstrophy-conserving **Q** variant on grid G6 for TC5 189

6.44 Potential vorticity at Day 30 for C grid scheme using enstrophy-conserving **Q** variant on grid C6 for TC5 189

6.45 Potential vorticity at Day 30 for Z grid scheme on grid G6 for TC5 189

6.46 Absolute vorticity at Day 30 for C grid scheme using enstrophy-conserving **Q** variant on grid G7 for Rossby-Haurwitz Wave 190

6.47 Absolute vorticity at Day 30 for C grid scheme using enstrophy-conserving **Q** variant on grid C7 for Rossby-Haurwitz Wave 190

6.48 Absolute vorticity at Day 30 for C grid scheme using energy-conserving **Q** variant on grid G7 for Rossby-Haurwitz Wave 191

6.49 Absolute vorticity at Day 30 for C grid scheme using energy-conserving **Q** variant on grid C7 for Rossby-Haurwitz Wave 191

6.50 Absolute vorticity at Day 30 for C grid scheme using double conservative **Q** variant on grid G7 for Rossby-Haurwitz Wave 191

6.51 Absolute vorticity at Day 30 for C grid scheme using double conservative **Q** variant on grid C7 for Rossby-Haurwitz Wave 191

6.52 Absolute vorticity at Day 6 for Z grid scheme on grid G7 for Rossby-Haurwitz Wave 191

6.53 Absolute vorticity at Day 6 for C grid scheme using enstrophy-conserving **Q** variant on grid G8 for Galewsky without initial perturbation 193

6.54 Absolute vorticity at Day 6 for C grid scheme using enstrophy-conserving **Q** variant on grid C8 for Galewsky without initial perturbation 193

6.55 Absolute vorticity at Day 6 for C grid scheme using energy-conserving **Q** variant on grid G8 for Galewsky without initial perturbation 194

6.56 Absolute vorticity at Day 6 for C grid scheme using energy-conserving **Q** variant on grid C8 for Galewsky without initial perturbation 194

6.57 Absolute vorticity at Day 6 for C grid scheme using double conservative **Q** variant on grid G8 for Galewsky without initial perturbation 194

6.58 Absolute vorticity at Day 6 for C grid scheme using double conservative **Q** variant on grid C8 for Galewsky without initial perturbation 194

6.59 Absolute vorticity at Day 6 for Z grid scheme on grid G8 for Galewsky without initial perturbation 194

6.60 Divergence at hour 3 for C grid scheme using enstrophy conserving **Q** variant on grid G8 for Galewsky 195

6.61 Divergence at hour 3 for C grid scheme using enstrophy conserving **Q** variant on grid C8 for Galewsky 195

6.62 Divergence at hour 3 for C grid scheme using energy conserving **Q** variant on grid G8 for Galewsky 195

6.63 Divergence at hour 3 for C grid scheme using energy conserving **Q** variant on grid C8 for Galewsky 195

6.64 Divergence at hour 3 for C grid scheme using double conservative **Q** variant on grid G8 for Galewsky 196

6.65 Divergence at hour 3 for C grid scheme using double conservative **Q** variant on grid C8 for Galewsky 196

6.66 Divergence at hour 3 for Z grid scheme on grid G8 for Galewsky 196

6.67 Potential enstrophy conservation for the C grid scheme (all three **Q** variants) on grid G8 for Galewsky 199

6.68 Potential enstrophy conservation for the C grid scheme (all three **Q** variants) on grid C8 for Galewsky 199

6.69 Total energy conservation for the C grid scheme (all three **Q** variants) on grid G8 for Galewsky 199

6.70 Total energy conservation for the C grid scheme (all three **Q** variants) on grid C8 for Galewsky 199

6.71 Potential enstrophy conservation for the Z grid and C grid (doubly conservative version) schemes on grid G8 for Galewsky 200

6.72 Total energy conservation for the Z grid and C grid (doubly conservative version) schemes on grid G8 for Galewsky 200

6.73 Absolute vorticity at Day 6 for C grid scheme using enstrophy-conserving **Q** variant on grid G8 for Galewsky 200

6.74 Absolute vorticity at Day 6 for C grid scheme using enstrophy-conserving **Q** variant on grid C8 for Galewsky 200

6.75 Absolute vorticity at Day 6 for C grid scheme using energy-conserving **Q** variant on grid G8 for Galewsky 201

6.76 Absolute vorticity at Day 6 for C grid scheme using energy-conserving **Q** variant on grid C8 for Galewsky 201

6.77 Absolute vorticity at Day 6 for C grid scheme using double conservative **Q** variant on grid G8 for Galewsky 201

6.78 Absolute vorticity at Day 6 for C grid scheme using double conservative **Q** variant on grid C8 for Galewsky 201

6.79 Absolute vorticity at Day 6 for Z grid scheme on grid G8 for Galewsky 201

6.80 h_{eqm} forcing function 203

6.81 u_{eqm} forcing function 204

6.82 ψ_{eqm} forcing function 204

6.83 ζ_{eqm} forcing function 204

6.84 Zonally averaged mean fluid height for C grid scheme on the cubed-sphere grid, all three variants 207

6.85 Zonally averaged standard deviation of fluid height for C grid scheme on the cubed-sphere grid, all three variants 207

6.86 Zonally averaged mean relative vorticity for C grid scheme on the cubed-sphere grid, all three variants 207

6.87 Zonally averaged standard deviation of relative vorticity for C grid scheme on the cubed-sphere grid, all three variants 207

6.88 Zonally averaged mean divergence for C grid scheme on the cubed-sphere grid, all three variants 208

6.89 Zonally averaged standard deviation of divergence for C grid scheme on the cubed-sphere grid, all three variants 208

6.90 Zonally averaged mean fluid height for C grid scheme on the icosahedral grid, all three variants 208

6.91 Zonally averaged standard deviation of fluid height for C grid scheme on the icosahedral grid, all three variants 208

6.92 Zonally averaged mean relative vorticity for C grid scheme on the icosahedral grid, all three variants 209

6.93 Zonally averaged standard deviation of relative vorticity for C grid scheme on the icosahedral grid, all three variants 209

6.94 Zonally averaged mean divergence for C grid scheme on the icosahedral grid, all three variants 209

6.95 Zonally averaged standard deviation of divergence for C grid scheme on the icosahedral grid, all three variants 209

6.96 Standard deviation of fluid height for C grid scheme on cubed-sphere grid. Top is doubly conservative variant, middle is total energy conserving variant and bottom in potential enstrophy conserving variant 210

6.97 Mean fluid height for C grid scheme on cubed-sphere grid. Top is doubly conservative variant, middle is total energy conserving variant and bottom in potential enstrophy conserving variant 211

6.98 Standard deviation of relative vorticity for C grid scheme on cubed-sphere grid. Top is doubly conservative variant, middle is total energy conserving variant and bottom in potential enstrophy conserving variant. Note that the total energy conserving variant is producing values that exceed the plot bounds. 212

6.99 Mean relative vorticity for C grid scheme on cubed-sphere grid. Top is doubly conservative variant, middle is total energy conserving variant and bottom in potential enstrophy conserving variant 213

6.100 Standard deviation of divergence for C grid scheme on cubed-sphere grid. Top is doubly conservative variant, middle is total energy conserving variant and bottom in potential enstrophy conserving variant. Note that the total energy conserving variant is producing values that exceed the plot bounds. 214

6.101 Mean divergence for C grid scheme on cubed-sphere grid. Top is doubly conservative variant, middle is total energy conserving variant and bottom in potential enstrophy conserving variant 215

6.102 Standard deviation of fluid height for C grid scheme on icosahedral grid. Top is doubly conservative variant, middle is total energy conserving variant and bottom in potential enstrophy conserving variant 216

6.103 Mean fluid height for C grid scheme on icosahedral grid. Top is doubly conservative variant, middle is total energy conserving variant and bottom in potential enstrophy conserving variant 217

6.104 Standard deviation of relative vorticity for C grid scheme on icosahedral grid. Top is doubly conservative variant, middle is total energy conserving variant and bottom in potential enstrophy conserving variant 218

6.105 Mean relative vorticity for C grid scheme on icosahedral grid. Top is doubly conservative variant, middle is total energy conserving variant and bottom in potential enstrophy conserving variant 219

6.106 Standard deviation of divergence for C grid scheme on icosahedral grid. Top is doubly conservative variant, middle is total energy conserving variant and bottom in potential enstrophy conserving variant 220

6.107 Mean divergence for C grid scheme on icosahedral grid. Top is doubly conservative variant, middle is total energy conserving variant and bottom in potential enstrophy conserving variant 221

6.108 Zonally averaged mean fluid height for Z grid and C grid (doubly conservative variant) schemes on the icosahedral grid 223

6.109 Zonally averaged standard deviation of fluid height for Z grid and C grid (doubly conservative variant) schemes on the icosahedral grid 223

6.110 Zonally averaged mean relative vorticity for Z grid and C grid (doubly conservative variant) schemes on the icosahedral grid 223

6.111 Zonally averaged standard deviation of relative vorticity for Z grid and C grid (doubly conservative variant) schemes on the icosahedral grid 223

6.112 Zonally averaged mean divergence for Z grid and C grid (doubly conservative variant) schemes on the icosahedral grid 224

6.113 Zonally averaged standard deviation of divergence for Z grid and C grid (doubly conservative variant) schemes on the icosahedral grid 224

6.114 Standard deviation of fluid height, relative vorticity and divergence for the Z grid scheme on an icosahedral grid. 225

6.115 Mean fluid height, relative vorticity and divergence for the Z grid scheme on an icosahedral grid. 226

B.1 A general non-orthogonal polygonal grid with an associated dual grid. If m and n are parallel for every edge, then the grid is orthogonal. 254

B.2 Grid geometry 255

B.3 On the left is a Pitteway triangulation, on the right is a non-Pitteway triangulation. This figure is from http://upload.wikimedia.org/wikipedia/commons/e/ee/Pitteway.svg, obtained under a Creative Commons license 255

B.4 Triangular, square and hexagonal uniform planar grids 258

B.5 Icosahedral-hexagonal and (gnomic) cubed sphere grids 259

B.6 Various choices of grid staggering for the shallow water equations 263

C.1 The discrete DeRham cohomology induced by the incidence matrices and Hodge stars 268

D.1 Allowed wavenumbers on the hexagonal grid 275

CHAPTER 1

Introduction

1.1. Numerical Methods Should Reflect Reality

The dominant features of the large scale dry dynamics of the atmosphere (and of many important aspects of the small-scale dynamics) are:

- **Potential vorticity dynamics (Rossby waves, invertibility)**: The atmospheric state and evolution can be largely described by the potential vorticity field (subject to the assumption of various balance conditions). PV is conserved exactly for (moist) adiabatic, inviscid flow. In addition, Rossby waves dynamics also play a key role in the large-scale synoptic circulation, especially in mid-latitudes.
- **Balanced states and waves (geostrophic/hydrostatic balance and adjustment)**: The atmosphere exists (at least at synoptic scales) in a state of near-geostrophic and hydrostatic balance; and perturbations to this balance result in the processes of geostrophic and hydrostatic adjustment ([147], [95]). This occurs primarily through the radiation of inertia-gravity and sound waves.
- **Conserved quantities (mass, momentum, energy, etc.)**: The atmosphere has both primary conserved quantities such as mass and momentum, and secondary conserved quantities such as potential vorticity, potential enstrophy and total energy. On longer time scales (such as those relevant to climate), conservation laws are an important constraint on the possible phase space trajectories of the atmosphere ([114]).

Some of these features are linear (balanced states, waves); while others are non-linear (PV dynamics, conserved quantities). Since these features are so important to the dynamics

of the atmosphere, it is considered essential that the numerical methods used to build an atmospheric dynamical core (dycore) are able to accurately represent them. **The focus of this dissertation is the discrete representation of these processes**.

1.1.1. PV Dynamics.

Potential vorticity is a very important quantity in large-scale dynamics (indeed, it might be said to be THE most important quantity). Through the invertibility principle, the state and evolution of the balanced part of the flow (which is the dynamically dominant part) can be described entirely by the potential vorticity field. In addition, potential vorticity obeys the impermeability theorem ([56], [55]), which states that potential vorticity substance (PVS) cannot cross an isentropic surface; even when diabatic effects are taken into account. It is also parcel invariant (conserved following the flow) and any non-conservation of PV is due to diabatic effects such as radiation or turbulent mixing. **Therefore, an Eulerian numerical model of the atmosphere should probably conserve potential vorticity in a mass-weighted sense (this is called compatibility); and the (possibly implied) advection scheme for potential vorticity should be consistent with the mass advection scheme (this is called consistency).**

1.1.2. Balanced States and Waves.

The representation of waves in a numerical model is characterized by the dispersion relation, which determines the phase and group velocities (or temporal frequency) of the propagating modes (numerical representation of waves) in terms of their spatial frequencies. A numerical model typically has analogues of the physical wave modes, but can also have spurious branches of the dispersion relationship (extra non-physical waves) or poorly represented waves of certain frequencies (typically the high spatial frequency ones, although

higher-order finite element methods can have issues with gaps in the spectrum). There are also inertial modes that can arise from the combination of temporal and horizontal discretization ([73]). These are (purely numerical) propagating modes that do not have a wave-like structure.

Balanced states are the stationary modes of the system, which for a numerical model can include both physical and unphysical modes. The unphysical stationary modes can be especially damaging to numerical simulations, since various non-linear processes can excite them. In addition, since they do not propagate, any inherent damping in the time discretization OR advection scheme will be unable to affect them. However, a well-designed numerical scheme can be free of such modes.

Computational modes is an overloaded term, used to refer to spurious stationary modes, spurious branches of the dispersion relationship and poorly represented physical waves. A diagrammatic representation of the possible linear modes is provided in Figure 1.1. **For the remainder of this work, we will use spurious stationary modes to refer to unphysical stationary modes; spurious wave branches to refer to unphysical propagating modes; and poorly represented physical modes to refer to physical propagating modes with characteristics that are unlike those of the corresponding physical propagating mode.**

Both balanced states and the dispersion relationship are linear properties of the numerical method that depend on the choice of discrete moments (and thus analytic form of the equations used), grid staggering (placement of these moments on the elements of the mesh), specific discretization scheme and horizontal mesh. There are many possible discrete moments; common choices are volume-integrated averages over grid cells and pointwise values. Finite-difference, finite-volume and finite-element all make different choices for the discrete

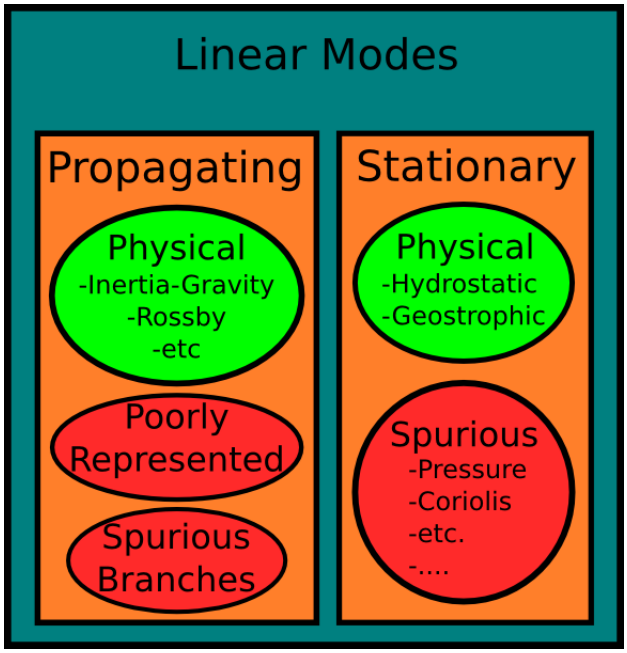

FIGURE 1.1. Diagram of the possible linear modes encountered in a numerical model of the shallow water equations. Green modes are physical, while red modes are numerical artifacts.

moments used to represent a continuous field and the ways these moments are used to represent terms in an equation. The space of possible discrete moments is very large, and there are many possibilities that have seen only cursory exploration.

The linear modes of a scheme can be investigated analytically using Fourier expansions, linear algebra, transfer functions and/or other techniques; or numerically by solving eigenvalue and nullspace problems. **This work will focus on both analytic and numerical linear algebraic techniques for investigating the linear modes of discretization schemes.**

1.1.3. Conserved Quantities.

Conserved quantities can generally be split into two types: primary and secondary. Primary conserved quantities are conservative predicted variables of an equation set. Examples include dry air mass and momentum (assuming momentum is a predicted variable).

A secondary conserved quantity is one that is a function of the primary conserved quantities: it must be diagnosed from the predicted quantities. Examples include total energy and momentum (in the vector-invariant formulation). The atmosphere possesses both types of conserved quantities, and in particular there are several secondary conserved quantities (total energy, potential vorticity, potential enstrophy) believed to provide strong constraints on the flow dynamics. It is often easy to design numerical schemes that have primary conservation, but secondary conservation is much trickier. However, on longer time scales (such as those relevant to climate), it is believed that secondary conservation properties provide an important constraint on the possible phase space trajectories of the atmosphere; and therefore help determine the long-term statistics of the system. **This work will investigate both primary and secondary conservation.**

1.1.4. Rotating Shallow Water Equations.

The rotating shallow water equations (RSW) provide a useful simplification of the full equations of the dry atmosphere since they have similar characteristics. They represent the motion of a rotating, hydrostatic, inviscid 2-D fluid for which the horizontal component of the Coriolis force has been neglected ([147], [95]). Both rotational and divergent motions are supported along with many types of waves (inertia-gravity/Poincare, Kelvin, Rossby). An excellent general overview of the types of waves supported by the shallow water equations is given in ([93]). The existence of a balanced state (geostrophic balance) and a corresponding adjustment process (inertia-gravity wave radiation/geostrophic adjustment) closely mimics similar situations in the full equations. In addition, the shallow water equations have cubic invariants (such as energy) and conserve a form of potential vorticity (and enstrophy). All of these properties make them an ideal simplified system from which to start the development of numerical models of the ocean or atmosphere. **The remainder of this**

thesis is concerned with mimetic Eulerian numerical methods for the rotating shallow water equations, on both the plane and the sphere. The discussion is restricted to schemes with a single degree of freedom per mesh element (face, edge, vertex) using either the vector invariant formulation (A/C staggering) or vorticity-divergence formulations (Z grid staggering) In addition, it considers ONLY spatial semidiscretization of underlying PDEs (assuming continuity in time). These are (necessary) simplifications, and there remains a great deal of interesting work on combined spatiotemporal discretization, other formulations of the continuous equations and multimoment discretizations.

1.2. Physics and Parameterizations

Due to the finite processing power and memory of computers, all numerical models of the atmosphere posses a truncation scale. This is the smallest scale of motions that can be explicitly represented by the dynamics. Beyond this scale, the effects of subgrid scale processes on the resolved scales must be parameterized; and these representations are termed parameterizations. A diagram of these model components and the truncation scale is found in Figures 1.2 and 1.3. Typically, an atmospheric model is split into two components: the dynamical core and the physics packages. Within the dynamical core, both the dynamics of moist air (dynamics) and the transport of other quantities (termed tracers, tracer transport) must be represented. The physics packages are the parameterizations of subgrid scale effects. Traditionally, all three components of a model (dynamics, transport and physics) have been solved on the same grid. However, the newest dynamical cores (especially those based on finite element type methods) use different grids to represent the physics, tracer transport and dynamics. **This thesis deals only with the representation**

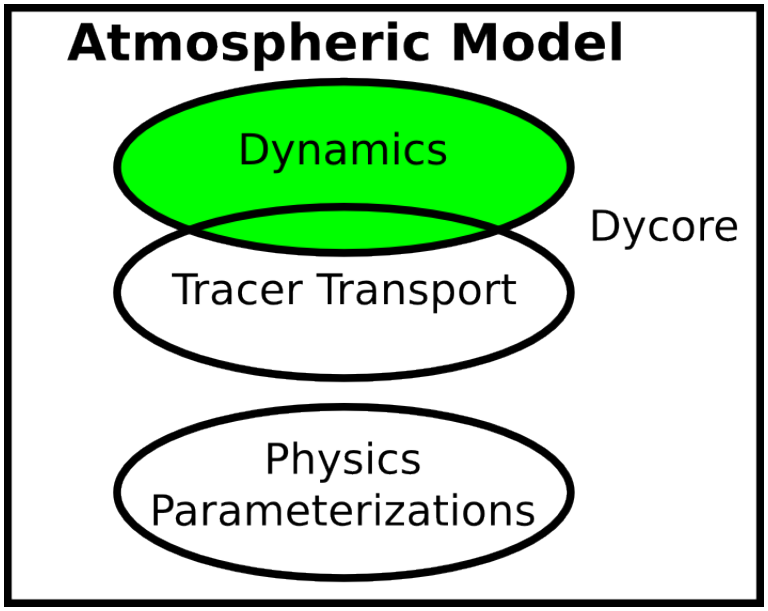

FIGURE 1.2. Diagram of the components of a modern atmospheric model. Note the overlap between tracer transport and dynamics. In practice, there should probably be overlap between all three components, but traditionally the dynamics/transport and the physics are developed largely independently. This thesis deals only with the dynamics component (shown in green).

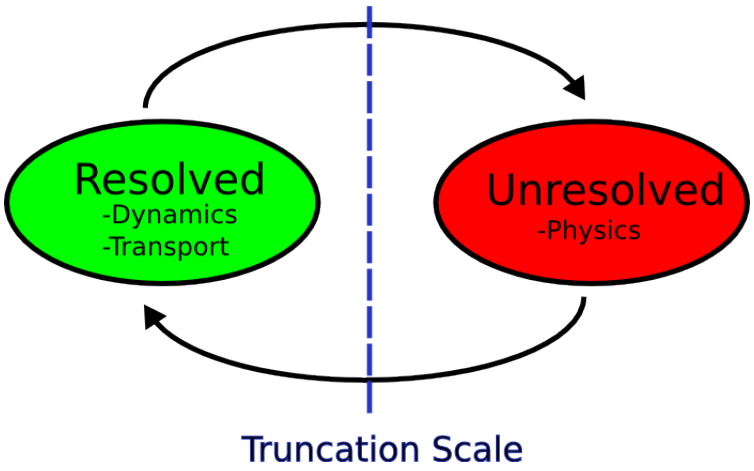

FIGURE 1.3. Image showing the interplay between physics, dynamics and transport that characterizes an atmospheric dynamical core, and the role of truncation scale in determining what constitutes the necessary physics.

of the dynamics within a dynamical core; and does not address tracer transport or physics parameterization.

1.3. Hamiltonian Structure of the Equations Governing Atmospheric Flow

The unapproximated equations that describe inviscid, rotating, (moist) adiabatic multi-component fluid flow have a very special mathematical structure: they can be derived from a Lagrangian variational principle ([122],[146]). In particular, they can be written as a (non-canonical) Hamiltonian system where the total (moist) energy is the Hamiltonian and there is a singular symplectic operator that describes all of the dynamics. This allows the full power of modern physical mechanics (which is largely based on the Lagrangian/Hamiltonian framework) to be brought to bear. Most of the interesting and important theoretical results of atmospheric dynamics can be derived in a very general way from the Hamiltonian framework. This includes (non-linear) stability theorems; wave-mean flow interaction; pseudoenergy, pseudomomentum and available potential energy; and potential vorticity conservation.

This would be quite valuable even if this were the only such system of equations which possess this special structure. However, Lagrangian/Hamiltonian expressions have been found for most of the major equation sets ([92],[32],[31]) that are used in studying atmospheric dynamics. In fact, there is a rich literature on the derivation of these equation sets through approximations in the underlying Lagrangian, which ensures that the resulting approximate equation set is consistent with the full equations. In particular, it possess similar invariants such as total energy and potential vorticity. Of special interest to us, the rotating shallow water equations in Eulerian form has such a non-canonical Hamiltonian structure.

The restrictions on the flow required to derive a Hamiltonian formulation (inviscid, (moist) adiabatic) are not as severe as first supposed, since any deviations from these restrictions represent important physical processes such as radiation, microphysics and turbulent (sub-grid scale) mixing. In fact, these deviations are precisely the processes that are parameterized within a numerical model. **Since the resolved scales of an atmospheric model**

are (moist) adiabatic and inviscid, there is a strong argument that the dynamical core of a model (the part that models the inviscid and moist adiabatic motions) should possess a discrete (quasi-)Hamiltonian structure that mimics the continuous Hamiltonian one in important ways. Deviations from inviscid and moist adiabatic flows can then be physically parameterized. This allows a clean separation between processes that are resolved by the dynamical core, and those that must be parameterized.

1.4. Desirable Properties for Discretization Schemes of the Rotating Shallow Water Equations

On the basis of the preceding features of the rotating shallow water equations (balanced states and waves, PV dynamics and conserved quantities) along with computational considerations (see [127] for more details about much of this), a detailed list of desirable properties for discretization schemes of the RSW can be developed. These are represented in pictorially in Figure 1.4. Note that many of these desirable properties carry over to the fully compressible Euler equations as well, and schemes developed for the rotating shallow water equations can be adapted to deal with the horizontal aspects of the fully compressible equations. This list has been split into five parts: linear properties (balanced states and waves), potential vorticity dynamics, conservation properties, computational properties and other properties. The focus is on vector-invariant and vorticity-divergence formulations of the RSW equations (as detailed in Chapter 2), although these considerations apply equally to all formulations of the RSW equations.

1.4.1. Linear Modes and Mimetic Properties.

The linear modes of a discretization scheme are connected to the nullspaces and eigenspaces of the resulting discrete matrix

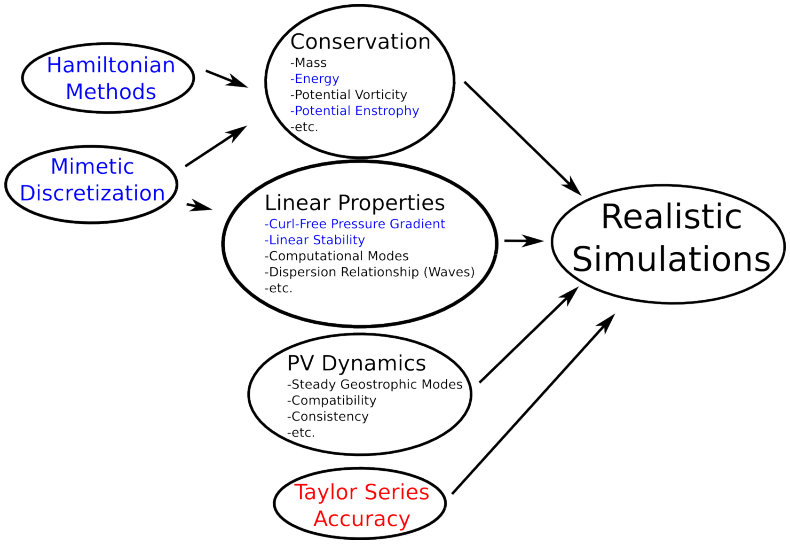

FIGURE 1.4. Diagram of (some of) the desirable properties of a model that influence its ability to achieve realistic simulations. The boxes on the far left represent two possible approaches to achieving some of these properties.

operators. In particular, the discrete dispersion relationship (stationary modes) of the numerical scheme can be determined from the eigenspaces (nullspaces) of the various operators. Desirable properties for the linear modes are:

(1) No spurious stationary modes

(2) No spurious branches of the dispersion relationship (branches which do not agree in the leading order term with a physical branch, and for which the difference between the physical branch and numerical branch does not go to zero as the discretization is refined).

(3) Good representation of inertia-gravity and Rossby waves (numerical dispersion relationship); no poorly represented physical waves

This works deals with the inertia-gravity waves and stationary modes of various discretization schemes (C grid and Z grid based) on both planar and quasi-uniform spherical grids, under the assumption of constant Coriolis force f; and

the inertia-gravity and Rossby waves for the same discretizations on quasi-uniform spherical grids with variable Coriolis force f. It also looks at the effects of dissipation on these linear modes.

1.4.1.1. *Absence of Computational Modes (1 and 2).*

It is strongly desirable that a dynamical core does not possess any spurious linear computational modes, since such modes are often excited by the non-linear and forcing terms. Generally, spurious computational modes can be grouped into two types: stationary modes and spurious linear wave branches. The first type of computational mode comes from the (possibly joint) null spaces of the various discrete operators. An example is the pressure mode that arises on unstaggered (A grid) discretizations. The second type of computational mode is a spurious linear wave branch- which is a propagating mode. These can arise when the ratio of degrees of freedom between the wind and height fields are no longer in balance (2:1 ratio). However, a correct DOF ratio is a neccessary but not sufficient condition to ensure the absence of spurious branches of the dispersion relationship ([22]). More details about this are provided in Chapter 5.

1.4.1.2. *Good Wave Representation (3).*

In addition to not possessing any spurious linear computational modes, it is desirable that the physical computational modes behave in an analogous manner to the physical modes they represent. In particular, the behaviour of the discrete dispersion relationship (and the associated group velocities) is key. For the shallow water equations (ignoring equatorial or boundary waves such as Kelvin waves) on the rotating sphere there are three types of waves: westward and eastward propagating inertia-gravity waves and westward propagating Rossby waves. The continuous dispersion relation for inertia-gravity waves is monotonically increasing with wavenumber, has a positive group velocity, is isotropic with respect to square

wavenumber and is qualitatively insensitive to Rossby radius. These are all desirable features of the discrete inertia-gravity wave dispersion relationship. Similar considerations apply to the discrete Rossby wave dispersion relationship. Again, more details are provided in Chapter 6.

Mimetic Properties. In addition to the linear mode behaviour of a scheme, there are desirable mimetic properties:

(1) Energy conserving pressure gradient force (discrete analogue of $\vec{v} \cdot \vec{\nabla}\phi + \phi\vec{\nabla} \cdot \vec{v} = \vec{\nabla} \cdot (\vec{v}\phi)$)

(2) Energy conserving Coriolis force (discrete analogue of $\vec{v} \cdot \vec{v}^{\perp} = 0$)

(3) No vorticity production due to pressure gradient force (discrete analogue of $\vec{\nabla} \times \vec{\nabla}\phi = 0$)

(4) Existence of a discrete Helmholtz decomposition (connected to steady geostrophic modes and proper treatment of slow/fast modes)

Note that 1 and 2 together ensure that a scheme for the shallow water equations is at least linearly stable. No spurious vorticity production ensures that the implied PV equation at least has the hope of being a good representation of the physical PV equation. **The general discretization schemes presented here are designed to satisfy these desirable mimetic properties, either by construction or by requirements on the properties of the various discrete operators.**

1.4.2. Potential Vorticity Dynamics.

Potential vorticity in the rotating shallow water equations has an interesting dual role: it is both a tracer (and thus is advected by the flow) and it determines the (dominant) geostrophic portion of the flow. In fact, PV plays an important role in geophysical fluid dynamics in general ([62]) and having good PV behaviour is key to a model that can faithfully

simulate reality. It is desirable that the (possibly implied) advection equation for potential vorticity possesses the following properties:

(1) Higher-order accuracy: at least 2nd order, preferably 3rd or higher

(2) Monotonicity: the advection schemes does not produce new minima or maxima

(3) No or limited spurious numerical dissipation: the amplification factor for the advection scheme is 1

(4) Shape preservation: individual Fourier components move at the same speed, a wave packet does not break into constituent components

(5) No or limited CFL condition: this allows longer time steps

(6) Compatibility: the evolution of mass-weighted potential vorticity is governed by an equation that is the divergence of a flux

(7) Consistency with the Lagrangian behaviour of PV: a uniform PV field remains uniform

(8) Conservation of potential enstrophy

(9) Conservation of total energy

(10) Steady geostrophic modes on a f-plane or f-sphere (discrete analogue of $f\vec{v}^{\perp} + \vec{\nabla}\phi = 0 \rightarrow \delta = 0 \rightarrow \frac{\partial \zeta}{\partial t} = 0$). This has to do with the implied vorticity equation for vector-invariant formulations, and ensures that the discrete dispersion relationship has steady geostrophic modes for constant f, and slow Rossby modes for variable f.

It should be noted that these characteristics cannot in general all be achieved. For example, Godunov's theorem states that a monotonic advection scheme cannot have higher accuracy than 1st order. A scheme that is dissipative cannot conserve potential enstrophy or total energy (although it might conserve mass-weighted PV). In general, advection schemes are

usually designed to satisfy **either** 1-7 (higher-order flux corrected transport schemes are a good example of this approach; OR 6-10 (Arakawa and Lamb 1981, TRiSK are good examples of this approach). Steady geostrophic modes will ensure that the model can adequately represent geostrophic balance. **The focus of this work will be on the properties 6-10.**

1.4.3. Conservation Properties.

There are an infinite number of quantities conserved by the rotating shallow water equations, however, evidence suggests ([117]) that good dynamical behaviour in a numerical simulation can be obtained by conserving only a subset of them. The main conserved quantities discussed when considering the shallow water equations are:

(1) Mass

(2) Potential Vorticity

(3) Momentum

(4) Total Energy

(5) Potential Enstrophy

(6) (Axial) Angular Momentum

Conservation of secondary conserved quantities (such as energy and potential enstrophy) has been shown ([4]) to help suppress non-linear computational instability and improve simulation fidelity, even when comparing a low-order conservative model to a higher-order non-conservative model. Of course, the real atmosphere has sources and sinks of most conserved quantities such as momentum, energy and potential enstrophy. There is debate ([133]) about the best way to handle such sources and sinks (parameterization, numerical diffusion, etc.) but a strong argument can be made on the basis of the Hamiltonian structure of the fundamental equations that at least the invsicid, adiabatic dynamical core should

conserve these quantities. **This work will concern itself only with mass, potential vorticity, total energy and potential enstrophy conservation**

1.4.4. Computational Properties.

In addition to ensuring that a dynamical core is capable of accurately simulating the fluid flow (the mimetic properties discussed above), there are practical computational concerns relating to the ability of the model to produce a simulation in a timely manner. Timely, of course, is a relative term but in general weather (climate) model users are interested in simulated days (months, years) per wallclock hour (day). An extremely accurate model that runs too slow for a given application is obviously useless. The tradeoff between speed and accuracy is a highly sensitive and application-dependent choice. **This work will not address computational properties, except for noting the order of accuracy of the proposed schemes.**

1.4.4.1. *Order of Accuracy.*

The schemes should ideally approach 2nd order accuracy on optimized grids, with higher order preferable. Higher-order accuracy is useful for:

(1) Computational intensity and scalability: Higher-order schemes tend to do more operations on each piece of data that is fetched from memory, which leads to greater computational intensity. This is useful because the cost of fetching data from memory and exchanging data between processing units is growing when compared to the cost of performing an operation. This strongly suggests that higher-order, local algorithms will scale better on future architecture, through higher computational intensity, better computation/computation ratios and better computational/memory access ratios.

(2) Grid imprinting: Higher-order schemes can reduce the impact of grid imprinting due to grid singularities. Since all of the quasi-uniform grids under consideration posses at least weak singularities, this is a desirable property.

(3) Efficiency for smooth flows: As is well-known, for smooth flows a higher-order scheme is more efficient (in terms of computational expense for a given level of accuracy) than a lower order scheme. This is primarily because a coarser grid can be used to achieve the same level of accuracy, which is much cheaper.

1.4.5. Other Properties.

1.4.5.1. *Grid Flexibility.*

There are a wide variety of quasi-uniform spherical grids under consideration (such as the icosahedral hexagonal-pentagonal, icosahedral triangular and cubed-sphere; see [127] for an excellent review) as use for the horizontal meshes in next generation weather and climate dynamical cores. Some of these grids are orthogonal; others are non-orthogonal (more discussion of grids is provided in Appendix B). In addition, there are a variety of optimization procedures (such as spring dynamics [64] and tweaking [59]) that can be applied to meshes. **The discretization schemes proposed in this work are applicable to the very general class of conformal polygonal meshes (orthogonal or non-orthogonal) on the plane or sphere.**

1.4.5.2. *Absence of Hollingsworth Instability.*

Unfortunately, non-linear stability for the single layer shallow water equations (such as energy conservation) is not sufficient to ensure that the multilayer primitive equations will also be stable. A prime example of this is the Hollingsworth instability (named after its discoverer, see [61], [85] and [70]). It has been seen in staggered grid (C grid) schemes that are both total energy and potential enstrophy conservative. Some work has been done

exploring the causes of this instability ([45]), but it is still not well understood. However, experience from the work cited above has shown it can be eliminated in several ways:

(1) Time stepping: Splitting the advection terms and inertia-gravity wave terms in the time stepping scheme seems to remove this instability.

(2) Changing the kinetic energy stencil: Enlargement of kinetic energy stencil has been shown to eliminate the Hollingsworth instability. As discussed more below, if total energy conservation is to be retained, this requires a corresponding change in the definition of the mass flux.

(3) Enstrophy conservation only: schemes that conserve only potential enstrophy do not seem to exhibit the Hollingsworth instability.

This work does not consider the Hollingsworth instability further, except to note that changes to the kinetic energy/mass flux or conservation properties of the scheme are easily accomplished within the proposed framework.

1.5. The Current State of Affairs

1.5.1. Linear Modes (Balanced States and Waves).

For finite-difference schemes the majority of work on linear properties has been the study of wave dispersion relations, with a focus on uniform grids on the f-plane or β-plane. Back in the 1960s and 1970s, there were several authors ([3],[119],[120],[118],[86]) who looked at the dispersion relationship for inertia-gravity waves on a uniform square grid for a variety of grid staggerings (descriptions of grid staggerings can be found in Appendix B, and in Figure B.6). They found that the Arakawa C-grid offers the best dispersion relationship when the Rossby radius of deformation is well-resolved, while the B-grid has moderate errors at all resolutions. However, the C-grid has poor dispersion properties when the Rossby radius

is not well-resolved. Batteen [9] looked at the computational noise for a variety of finite-difference schemes used in an ocean model and found that the B grid works best at lower resolution, while the C-grid works better at higher resolution. Since the popularization of the C-grid, much work has been done to improve its dispersion properties for lower resolution. Some examples of this can be found in ([1], [91], [27]). Due to increases in computing power and associated increases in horizontal model resolution, this is less relevant for atmospheric dynamical cores. However, it is still quite relevant for the ocean where the Rossby radius of deformation is smaller. Randall [100] extended the earlier uniform square grid dispersion relationship studies to the unstaggered vorticity-divergence grid and showed that the Z-grid had good dispersion properties independent of the horizontal resolution. Nikovic [36] looked at analogues of the B-E and Z grid on perfect planar hexagons and found that the same conclusions held for hexagons as for perfect squares. An interesting approach to improved dispersion relationships is provided by McGregor ([81]), which employs a reversible interpolation to compute inertia-gravity waves on a staggered C-grid while the rest of the calculations are done on an A-grid.

A fully discrete model has both time and space discretization. The previous studies considered only spatial discretization and assumed continuity in time. Beckers ([12]) looked at the A-D grids with 2 level forward-backward time differencing and found that the C-grid performed the best, even with low resolution (provided time steps were large enough). Fox-Rabinovitz ([42]) looked at time and horizontally staggered A-E grids for atmosphere and ocean models, again with the conclusion that the C-grid offered a good dispersion relation. These studies suggest that it is important to consider the combined effects of time and space discretization, since one can modify the effects of the other.

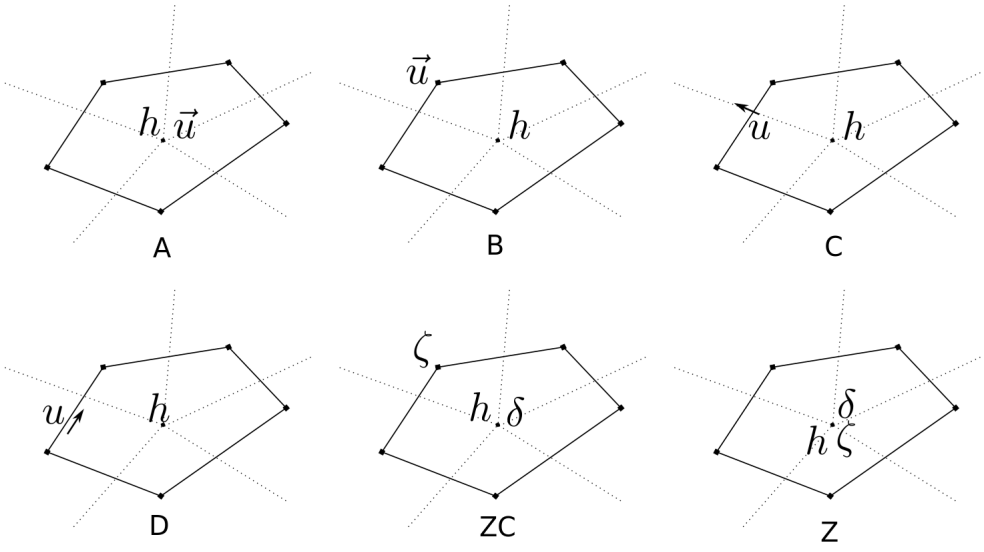

FIGURE 1.5. Various choices of grid staggering for the shallow water equations.

In addition to inertia-gravity waves, there has been some study of Rossby wave dispersion on the β-plane. Dukowicz ([33]) looked at Rossby waves on a uniform square grid and found that the B and C grids offered the best dispersion relations (of the Arakawa A-E grids), with a slight advantage for the B grid. Gavrilov ([48]) also performed a similar study and came to the same conclusion: the B and C grids were the best among the A-E grids. Thuburn ([131], [141]) looked at Rossby waves on the square and lat-lon C-grid and found that their representation was sensitive to the choice of discretization scheme. Liu ([77], [76]) looked at the dispersion relation for Rossby waves on a uniform square grid using the A-E and Z grids; and found that the C and Z grid offered the best behaviour.

When considering unstructured grids or non-uniform grids, reconstruction of the tangential velocity for C-grid models becomes non-trivial. In addition, satisfying geostrophic balance and preventing or controlling computational modes that arise due to a mismatch of degrees of freedom in the mass and wind fields also becomes difficult. Espelid ([35]) looked at the computation of the Coriolis force for triangular C-grid ocean models, while Danilov

([26]) explored errors that arise in geostrophic dynamics on triangular C-grids due to velocity divergence noise. This was further explored in Gassmann ([44]), which looked at triangular and hexagonal C-grids. Ham ([52]) also found that triangular C-grids had unstable modes. Skamarok ([124]) performed a linear analysis of the CD-grid and found that it behaved essentially like a D grid at first order. Bonaventura ([17]) looked at the C-grid on a hexagonal geodesic grid and found that it gave good dispersion properties for inertia-gravity waves. Thuburn ([132]) looked at inertia-gravity and Rossby wave dispersion on regular hexagonal grids for the f-plane and β-plane; with the conclusion that careful choice of Coriolis reconstruction could give stationary geostrophic modes. However, on the β-plane a second unphysical branch of the Rossby wave dispersion arises. This work was extended ([140]) to arbitrary polygonal C-grids with an orthogonal dual, with a focus on stationary geostrophic modes. Kleptsova ([69]) also looked at the Coriolis term on unstructured C-grids, but with a focus on properties of the corresponding discrete operator matrices.

Computational modes are also an important aspect of numerical schemes. Peixoto ([96]) looked at grid imprinting in the divergence operator on spherical geodesic grids and found that imprinting was due primarily to misalignment of opposite cell walls. Weller ([155]) looked at the computational modes for a variety of Voronoi meshes using a C-grid scheme; and also ([153]) at how to control those computational modes through appropriate choice of the potential vorticity advection scheme. Weller's work is unique because it focuses on the quasi-uniform spherical grids that are actually used in existing models, rather than perfect planar grids.

Finite-volume models have received considerably less attention in the literature, at least concerning their linear properties. Castro ([18]) performed extensive analysis of a finite-volume scheme with a focus on wave dispersion properties and balanced states. Audusse ([8])

developed a conservative finite-volume discretization from the inertial framework (instead of the rotating framework), which is an excellent example of the variety of choices that can be made in designing a numerical scheme. Mohammadian ([88]) looked at Rossby waves in 1-D upwind-based finite-volume schemes. Faure ([37]) looked at the inertia-gravity wave dispersion relationship for various finite-volume methods, and found that none of them gave a satisfactory dispersion relationship for short waves. Xiao ([157]) developed a multi-moment finite volume scheme (M grid) using both volume and surface integrated values; and found that at high resolutions it has dispersion properties similar to the Z and C grids, while at lower resolutions it is similar to an A grid.

There is a much broader and deeper body of work for locally compact Galerkin-style numerical methods (such as spectral element, discontinuous galerkin and finite element). Foreman ([39]) performed a comparison of finite element schemes to finite-difference schemes on the basis of wave dispersion for square and triangular meshes. He also investigated time discretization ([40]) and the effects of mass lumping ([41]). Hua ([63]) looked at noise-free mixed finite element methods using semi-implicit time stepping. Walters ([150]) investigated spurious oscillation modes in 1D and 2D mixed finite elements on quadrilateral and triangular grids. Atkinson ([7]) studied inertia-gravity wave dispersion in finite elements schemes for the shallow water and generalized wave continuity equations on a variety of meshes. Bernard ([13], [14]) examined Poincare, Kelvin and Rossby waves on structured and unstructured triangular meshes. Rostand ([105]) looked at the dispersion relation, spurious modes and geostrophic balance for Raviart-Thomas and BDM element on equilateral and biased triangles; and also ([106]) at discrete matrix kernels for finite-difference (B,C and CD grids) and finite-element discretizations, with a focus on stationary properties and spurious modes. Hanert ([53]) investigated the dispersion properties of a mixed finite element method

on unstructured meshes. Cotter ([21],[24],[22]) analysed the use of mixed finite elements for atmospheric and oceanic modelling, looking at the dispersion relations, ability to maintain geostrophic balance and mimetic properties. Staniforth, Melvin and others ([126],[83]) continued this research with a detailed look at the wave dispersion relationship of the RT finite element on quadrilateral meshes; along with ways to improve it via mass lumping. Melvin et. al ([84]) also investigated the dispersion relation for the spectral element method, and found that it had similar issues as the unstaggered A grid finite-difference dispersion relation for low order; along with spectral jumps and localized eigenmode structures for higher order. Walters ([151]) examined the role of semi-implicit time discretization and the Coriolis term in the propagation of inertia-gravity waves; and also ([149]) the dispersion relationships for a set of mixed schemes that use a finite-volume scheme for the continuity equation and finite-difference or finite-element schemes for the momentum equation. Boneventura ([16]) developed improved reconstruction schemes for the Coriolis terms in Raviart-Thomas elements.

Perhaps most importantly, there is an excellent series of papers by Le Roux and collaborators outlining a general framework for analysing (mixed) finite element schemes on unstructured meshes. This series outlines a linear algebra based approach to the systematic investigation of the stationary and propagating modes of an entire class of discretization schemes (finite elements) for the shallow water equations. It starts ([108]) with an early paper on spurious stationary modes through a linear algebra approach, and an associated paper ([71]) investigating the inertia-gravity dispersion relationship for a mixed finite-element scheme on triangles. These papers were followed by an intensive study of inertia-gravity ([72]) and Rossby wave ([107]) dispersion relationships for unstructured triangular grids and a variety of mixed finite element schemes. Later, the effects of mass lumping ([74]) and time

discretization ([109]) were examined. A comparison ([110]) between mixed finite element methods based on the primitive variables to the generalized wave continuity equation on the basis of the dispersion relationship was made. Recently, an investigation ([73]) into spurious inertial modes (propagating modes without a wave-like structure) was undertaken.

1.5.2. Conservation Properties.

The recognition of the Hamiltonian nature of atmospheric dynamics was made in the 1980s ([113]). However, the development of discretizations that respect this structure has been slow in coming. Salmon ([115],[117],[116]) has pioneered the application of discrete Poisson and Nambu brackets to the development of conservative numerical methods for the shallow water equations (and other inviscid hydrodynamic equations). This included energy and enstrophy conserving C-grid schemes on uniform square meshes and a Z-grid scheme for arbitrary polygonal meshes. Sommer ([125]) used the same ideas to develop an energy and enstrophy conserving scheme on the ZC-grid. Sommer and Nevir ([92]) also formalized the use of Nambu brackets in atmospheric dynamics and gave expressions for Nambu bracket forms of many equation sets used in dynamical core development. This work emphasizes the primary role that energy and vorticity play in the atmosphere. Recently, Gassmann ([46],[45]) has used the ideas of Sommer, Nevir and Salmon to develop an energetically-consistent non-hydrostatic atmospheric model called ICON-IAP. A similar project has been undertaken by Dubos et. al ([30]), termed DYNAMICO. This included careful derivation of the Hamiltonian formulation for many approximate equation sets in arbitrary vertical coordinates ([31],[32]). The Hamiltonian framework is powerful, but it is not as useful as it could be since the connection between the Hamiltonian properties necessary for conservation and the properties of various discrete operators has not been fully elucidated. Some work on this front has been done by Dubos ([29]), but additional work remains.

1.5.3. Mimetic Properties and PV Dynamics.

The pioneering work of mimetic properties for general grids was done by [140]: an energy conserving linear scheme (linearly stable) with stationary geostrophic modes and no spurious vorticity production was developed for arbitrary orthogonal polygonal grids. This was extended in [102] to consider PV dynamics along with either energy conservation or potential enstrophy conservation for the non-linear equations. A follow up paper ([135]) further extended this work to non-orthogonal grids and recognized the fact that these schemes were a type of Discrete Exterior Calculus (DEC) method. Difficulties with extension to higher-order accuracy led to the development of schemes based on Finite Element Exterior Calculus (FEEC, [25],[22],[23],[82],[136]), which can be made doubly conservative (both energy and potential enstrophy).

In particular, the use of DEC operators gives the desirable mimetic properties. Nonlinear properties such as PV dynamics and conservation amount to additional requirements on the non-standard DEC operators. Both the DEC and Hamiltonian approaches end up producing very similar schemes. One of the motivating purposes of the current work is the unification of the DEC and Hamiltonian approaches. As shown in Chapter 3, the additional requirements on the non-standard DEC operators can be understood as arising from requiring that the resulting discrete dynamics form a quasi-Hamiltonian system.

1.5.4. Arakawa and Lamb 1981 Scheme.

Advantages. The prototypical gold standard of a mimetic discretization scheme for the rotating shallow water equations is the 1981 Arakawa and Lamb scheme (AL81, [4])

(1) It has steady geostrophic modes.

(2) As long as the grid resolution is larger than the Rossby radius of deformation, it has good wave dispersion properties.

(3) The pressure gradient term does not produce any spurious vorticity.

(4) The pressure gradient and Coriolis terms are both energy conserving.

(5) There are no spurious stationary modes, spurious branches of the dispersion relationship or poorly represented physical modes.

(6) The implied potential vorticity advection equation is compatible with the height equation.

(7) It conserves mass, potential vorticity, total energy and potential enstrophy.

It is important to note that AL81 can be interpeted both as Hamiltonian-based scheme (first recognized by Salmon, [115]) and a DEC scheme (as will be shown in chapter 3). The recognition of the dual nature of this scheme was the inspiration for much of this work.

Limitations. However, there are several important limitations of the AL81 scheme. They are

(1) Restricted to a topologically square, orthogonal grid; on the sphere this means a lat-lon or equiangular cubed-sphere grid; which leads to unavoidable resolution clustering at the poles (lat-lon) or cube corners (cubed-sphere). This is a concern for two reasons: computational efficiency due to time step restrictions, and the need for a polar filter which destroys many of the desirable properties of the scheme.

(2) Low order of accuracy, especially in the advection operators. There is a 4th order version of the PV advection portion of the scheme ([129]), but the rest of the scheme remains 2nd order. Higher-order accuracy is desirable for variety of reasons, as discussed earlier.

(3) Loss of conservation properties when advection operators are changed (to be semi-lagrangian or higher order)

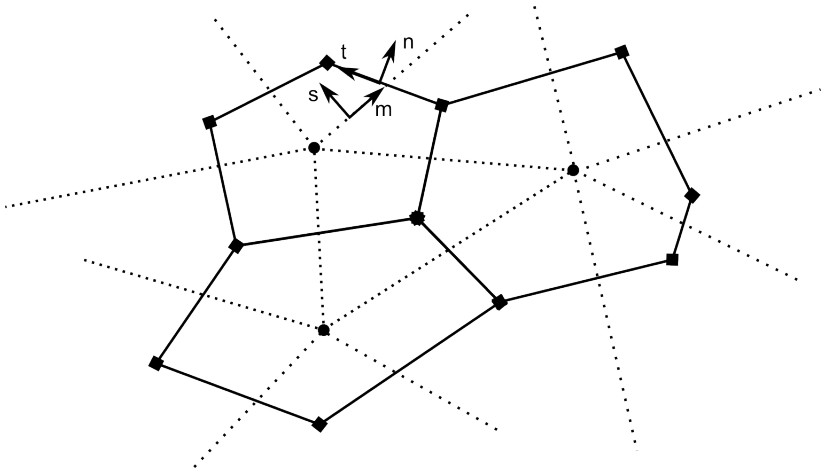

FIGURE 1.6. A general non-orthogonal polygonal grid with an associated dual grid. If m and n are parallel for every edge, then the grid is orthogonal.

(4) When used in a multilayer model, the Hollingsworth instability can occur. However, this is easily remedied by one of the methods discussed earlier.

(5) Poor wave representation for $\frac{\lambda}{\Delta x} << 1$; this is less of an issue with high model resolution. However, increased resolution for all orthogonal grids the author is aware of leads to grid cell clustering at singular points of the grid (poles for lat-lon, cell corners for cubed-sphere).

In order to ameliorate these issues, there has been substantial research in an attempt to develop a scheme that has similar properties to AL81, but enables higher-order operators (especially in advection); quasi-uniform grids (non-orthogonal cubed sphere or geodesic); or both. An example of the type of grids for which it is desirable to have AL81 apply to is shown in Figure B.1. There are three primary approaches that have been undertaken: TRiSK, FEEC and Z-Grid.

TRiSK. The TRiSK approach (named after the original designers of the scheme: Thuburn, Ringer, Skamarock and Klemp, [102]) allows the use of a general polygonal or spherical polygonal grid (either orthogonal or non-orthogonal), while preserving all of the desirable properties of AL81 with the exception of EITHER potential enstrophy conservation or total

energy conservation. This eliminates the first limitation, but fails to address the low order of convergence. There are variations on TRiSK ([137]) with higher-order advection, but they lose the secondary conservation properties (such as energy or potential enstrophy). In addition, the Coriolis operator in TRiSK is in general 0-th order accurate (inconsistent) on general grids. Interestingly, this does not seem to affect solution quality. It is not clear how (perhaps the inconsistency occurs only at isolated points of the grid?) More study of this is certainly warranted. TRiSK also suffers from the problem of spurious branches of the dispersion relationship ([44]) on geodesic or hexagonal/triangular grids, since the number of degrees of freedom in the wind and mass fields are not balanced.

FEEC. Recent work by Cotter, Thuburn and others ([22],[23],[25]) has extended the mimetic TRiSK framework to finite-element methods, using the approach of Finite Element Exterior Calculus. This retains the mesh flexibility inherent in TRiSK, but allows higher-order, doubly conservative (total energy and potential enstrophy) discretizations. In addition, it allows DOF balancing to eliminate spurious branches of the dispersion relationship. The primal-dual formulation ([136]) even allows the use of the full suite of Discontinuous Galerkin advection operators for both the mass and the potential vorticity, which is extremely useful. Of course, a dissipative advection operator will necessarily no longer conserve total energy or potential enstrophy. However, there have only been a few studies ([126],[83]) on the dispersion relationship for the finite-element families used in FEEC (with none done on quasi-uniform grids such as gnomic cubed sphere or geodesic); and no work on the Hollingsworth instability. It appears that there are spectral gaps in the dispersion relationship that must be removed through some sort of mass-lumping procedure. In addition, the mixed-finite element formulation does require a global elliptic solve at each time step. This is less of an issue when combined with a semi-implicit formulation that allows

longer time steps, and architectural trends suggest that the higher-computational intensity of finite-element methods could offset their increased communication costs. There has also been recent work ([89],[59]) on multigrid methods, which appear to offer excellent scalability on emerging architectures.

Z-Grid. A different approach is to abandon the vector-invariant formulation that underlies AL81, TRiSK and FEEC; and use the vorticity-divergence form with collocated variables (Z grid) instead. It is possible (see Chapter 4) to obtain all of the desirable mimetic properties of AL81 in this framework (including both total energy and potential enstrophy conservation), on arbitrary orthogonal (spherical) polygonal meshes. In addition, the qualitative properties of the dispersion relationship are independent of the Rossby radius; and there is proper DOF balance on any type of grid. In addition, it does not appear that the Hollingsworth instability occurs for multi-layer vorticity-divergence models. However, the vorticity-divergence formulations requires the solution of elliptic equations at each timestep to diagnose the streamfunction and velocity potential, and unlike FEEC, there is no way to avoid this. However, the existing vorticity-divergence models for quasi-uniform spherical grids either have spurious computational modes ([104]), or are not fully conservative ([57]).

1.6. What This Work Addresses

From the preceding discussion, it is easy to see several outstanding research problems:

(1) The development of a potential enstrophy AND energy conservative single moment vector-invariant C grid scheme that works on arbitrary (orthogonal or non-orthogonal) polygonal grids. As discussed in Chapter 3, most of the groundwork for this has already been done in previous work. Only the form of the potential vorticity advection remains to be determined.

(2) Development of a collocated (Z grid), total energy and potential conserving vorticity-divergence scheme based on the Hamiltonian approach that works on arbitrary spherical polygonal grids. The groundwork for this has been laid by Rick Salmon ([117]), but the specifics remain to be developed.

(3) Connecting the Hamiltonian and DEC approaches to obtaining conservative schemes; and obtaining conditions on various operators that are required for the desirable properties discussed above.

(4) Investigation of the linear modes of various discretization schemes on quasi-uniform spherical grids (geodesic and cubed-sphere). Many studies have been done on planar grids, but there is little known about the dispersion relations or stationary modes on the actual grids that are used in models (outside of [155]).

(5) Investigation of the role that diffusion (either explicitly added or numerically implicit) plays in the linear modes of various discretization schemes on both planar and quasi-uniform spherical grids.

This work aims to address these issues in the following ways:

Double Conservative C Grid Scheme. A doubly conservative potential vorticity advection operator $\mathbf{Q}$ is developed for arbitrary, orthogonal or non-orthogonal grids. When combined with the existing TRiSK framework, this completes the extension of AL81 to arbitrary polygonal grids.

Extension of $\zeta - \delta$ Schemes. The Salmon 2007 ([117]) scheme is extended to the case of arbitrary spherical polygonal grids: in particular the new scheme works on icosahedral hexagonal-pentagonal meshes.

Connection between Hamiltonian and DEC Approaches. The DEC approach is extremely useful for developing schemes that have the desirable mimetic properties and PV dynamics,

but the requirements for conservation are tricky. The Hamiltonian approach offers easy access to conservation, but it is not clear how to incorporate mimetic properties. The generalized C grid discretization shown in Chapter 3 combines these approaches in a natural and useful way. The vorticity-divergence framework presented in Chapter 4 makes use of some operators from DEC, but it is not a full DEC scheme. Instead, it is strongly believed (but not proven) that the vorticity-divergence framework presented is a mass-lumped finite element scheme (bilinear on rectangles, linear on triangles).

Linear Modes on Quasi-Uniform Spherical Grids. The numerical stationary modes and dispersion relations of the two generalized schemes (C grid and Z grid) are studied on both planar and spherical (hexagonal geodesic, cubed sphere) meshes. In addition, analytic dispersion relations and stationary modes for various planar discretization/grid combinations (such as the A grid on hexagons) are derived.

Diffusion. The effects of diffusion on the linear modes of discretizations of the shallow water are investigated. In particular, the ability of diffusion to control or remove spurious stationary modes, poorly represented physical modes and spurious branches of the dispersion relationship is quantified.

The major contribution of this work is the development of generalized single moment C and Z grid schemes that provide all of the desirable properties above (including conservation of both total energy and potential enstrophy) on arbitrary polygonal grids. Alongside this, a detailed analysis and intercomparison of their properties (such as linear modes and performance on some test cases) on two prototypical quasi-uniform spherical grids (geodesic, cubed sphere) has been performed.

As a part of this work, a software framework (Morphe) that allows rapid prototyping and intercomparison of single moment discretization schemes has been developed. Although

Morphe was designed in the context of the shallow water equations, it is useful for any 2D single moment discretization. This framework will be made available to the wider community.

1.7. What This Work Does Not Address

There are many other interesting aspects of the discretization of the shallow water equations that are not investigated in this thesis. Some relevant ones are discussed below. These are all certainly interesting and important questions, but they are beyond the scope of this work.

Time Discretization. This work does not address time discretization, and in particular the ability to obtain mimetic and conservation properties with the full spatiotemporal discretization. Also associated with time discretization are the possibility of spurious inertial modes, which are not studied.

Momentum and Angular Momentum. Although momentum and angular momentum are both conserved in the continuous equations, it seems extremely difficult to conserve them in the discrete case since they are continuous symmetry invariants of equations. In contrast, the other conserved quantities arise from anti-symmetry or Casimirs, which is much easier to discretize. When using the vector invariant formulation, it does not seem possible to conserve both momentum and potential enstrophy in the discrete case. The problem becomes even more acute on general grids. In addition, on a staggered grid using the vector invariant formulation conservation of momentum becomes very tricky. One possible approach to this is to directly predict the axial angular momentum.

Hollingsworth Instability. Full atmospheric models naturally involve multiple layers, and the Hollingsworth instability must be addressed. This work does not deal with the Hollingsworth instability, except to note that some of the existing known fixes such as modification of the

kinetic energy stencil can be incorporated into the generalized C grid framework in such a way as to maintain all of the desirable mimetic and conservation properties.

Higher Order Vorticity-Divergence Schemes. A very useful extension of the existing FEEC framework would be to incorporate the vorticity-divergence formulation. This would provide higher-order vorticity-divergence schemes that preserve the mimetic and conservation properties on arbitrary grids. As a part of this, analysis of the dispersion characteristics of higher-order vorticity-divergence schemes could be undertaken.

Flux Form Formulation. Instead of predicting $(h, \vec{u})$, we could predict $(h, h\vec{u})$. This is done in many existing models, but there has not been very much work on the theoretical underpinnings of this approach. In particular, there has been no work done on the mimetic properties, linear modes (especially connected to grid staggering choices) or PV dynamics of these types of schemes. It is possible to obtain a mass, momentum and energy conserving scheme ([148]) based on this formulation. It seems likely that these schemes are simply an anti-symmetric discretization of the underlying Lie-Poisson bracket. However, potential vorticity and potential enstrophy conservation are much trickier. From a Hamiltonian mechanics perspective, both of these are Casimirs of the Lie-Poisson bracket. An analysis of the mimetic properties, linear modes (especially relating to different choices of grid staggering), PV dynamics and conservation properties for schemes based on $(h, h\vec{u})$ would be useful. A natural extension of this would be the development of FEEC-based schemes using the $(h, h\vec{u})$ formulation. It might also be interesting to explore the prediction of the divergence $\vec{\nabla} \cdot h\vec{u}$ and curl $\vec{\nabla}^{\perp} \cdot h\vec{u}$ of the mass flux- this would be an analogue of the vorticity-divergence formulation.

1.8. Organization of Thesis

The remainder of this thesis is organized as follows. Chapter 2 presents the linear and nonlinear rotating shallow water equations in the vector-invariant and vorticity-divergence formulations. Chapter 3 presents a general discretization scheme based on single moment C grid staggering, and discusses its ability to obtain the desirable properties discussed above. Chapter 4 does the same for a single moment Z grid staggering. Chapter 5 discusses normal modes (stationary and propagating) in the context of the linear equations on an f-plane, f-sphere and full sphere, and present some numerical results from the C and Z grid schemes. Since at least part of the material in Chapters 2-5 is a review of existing literature, a summary of new results is provided at the end of each chapter. Chapter 6 presents some standard test cases from the literature that are run to evaluate the differences between the C grid and Z grid general discretizations on the basis of important physical properties such as conservation, representation of geostrophic adjustment and (physical and spurious) linear normal modes. Chapter 7 summarizes the results from Chapters 3-6 and gives some general criterion for the development of numerical discretizations schemes of the rotating shallow water equations. Finally, the Appendices covers important ancillary topics: Non-Canonical Infinite Dimensional Hamiltonian Mechanics, Horizontal Meshes, Discrete Exterior Calculus in 2D and linear mode results for uniform planar meshes (such as exact analytic dispersion relationships for various schemes and allowed wavenumbers on various horizontal meshes).

CHAPTER 2

Rotating Shallow Water Equations in Continuous Form

2.1. Continuous Shallow Water Equations

When trying to model a complex physical system such as the atmosphere or ocean, it is often useful to start with a simplified system that retains some of the key characteristics of the full system. The shallow water equations provide a useful analogue of fully compressible Euler equations- in particular they have similar conservation laws, many of the same types of waves and a similar (quasi-) balanced state. These equations represent the motion of a rotating, incompressible, inviscid 2D fluid for which the horizontal component of the coriolis force has been neglected. They support both rotational and divergent motions along with inertia-gravity and Rossby waves (geostrophic modes in the f-plane case). The existence of a balance condition (geostrophic balance) and a corresponding adjustment process (inertia-gravity wave radiation; geostrophic adjustment) closely mimics similar situations in the full equations. In addition, the shallow water equations have integral invariants (such as mass and energy) and Lagrangian invariants (such as potential vorticity and potential enstrophy). They are a (non-canonical) Hamiltonian system and can be derived from the fully compressible Euler equations via simplification of the Lagrangian. All of these properties make them an ideal system from which to start the development of numerical models of the ocean or atmosphere. The non-linear and linearized rotating shallow water equations are presented below in both vector-invariant formulation and vorticity-divergence formulation (using a momentum-based streamfunction and velocity potential). In all cases a constant value of the gravity g has been assumed. In the linearization, the height field is perturbed

about a reference height H as $h = H + h'$. The base state wind is assumed to be zero. The product of two (or more) perturbation quantities is neglected. For convenience, primes are dropped in the final form of the linearized equations.

2.1.1. Vector Invariant Formulation. The vector-invariant formulation is used primarily for two reasons: it is easy to derive a vorticity equation and associated potential vorticity equation (in particular the splitting of the advective term into a kinetic energy gradient and a "vorticity flux" cleanly separates the divergent and rotational parts of advection); and it is invariant with respect to changes in the coordinate system (hence the name).

2.1.1.1. *Nonlinear.*

Choosing fluid height h and vector wind $\vec{u}$ as our prognostic quantities, the equations of motion are given in vector-invariant form as

$$\frac{\partial h}{\partial t} = -\vec{\nabla} \cdot (h\vec{u}) = -\vec{\nabla}^{\perp} \cdot (h\vec{u}^{\perp}) \tag{1}$$

$$\frac{\partial \vec{u}}{\partial t} = -\eta\vec{u}^{\perp} - \vec{\nabla}(\Phi) \tag{2}$$

where $\eta = f + \zeta$ is the absolute vorticity, f is the Coriolis parameter, $\zeta = \vec{\nabla}^{\perp} \cdot \vec{u} = -\vec{\nabla} \cdot \vec{u}^{\perp}$ is the relative vorticity, $\vec{u}^{\perp} = \hat{k} \times \vec{u}$ is the perpendicular wind, $\hat{k}$ is the unit vector in the vertical direction, $\Phi = gh + gh_s + K$ is the Bernoulli function, $K = \frac{\vec{u}\cdot\vec{u}}{2}$ is the kinetic energy, h is the fluid height, g is the value of gravity and h_s is the topography height. We can also write an evolution equation for the perpendicular wind as

$$\frac{\partial \vec{u}^{\perp}}{\partial t} = \eta\vec{u} - \vec{\nabla}^{\perp}(\Phi) \tag{3}$$

Nonlinear Coriolis Term. The non-linear coriolis term

$$\eta\hat{k} \times \vec{u} \tag{4}$$

can be written in several alternative equivalent forms:

$$qh\hat{k} \times \vec{u} \tag{5}$$

$$q\hat{k} \times (h\vec{u}) \tag{6}$$

$$\hat{k} \times (\eta\vec{u}) \tag{7}$$

$$\hat{k} \times (qh\vec{u}) \tag{8}$$

$$h\hat{k} \times (q\vec{u}) \tag{9}$$

where $q = \frac{\eta}{h} = \frac{\zeta+f}{h}$ is the potential vorticity. These are all equivalent in the continuous system, but they lead to different discretization strategies. However, considerations from the Hamiltonian and Exterior Calculus formulations of the vector invariant equations; along with potential vorticity compatibility and consistency (see below) suggest that $q\hat{k} \times (h\vec{u})$ is the ideal form to use for discretization. In addition, the Arakawa and Lamb (AL81, REF) scheme uses this form in order to derive an energy AND potential enstrophy conserving scheme.

2.1.1.2. *Linear.*

By linearizing about a state of rest (no mean wind) with mean fluid height H, one obtains

$$\frac{\partial h}{\partial t} = -H(\vec{\nabla} \cdot \vec{u}) = -H(\vec{\nabla}^{\perp} \cdot \vec{u}^{\perp}) \tag{10}$$

$$\frac{\partial \vec{u}}{\partial t} = -f\vec{u}^{\perp} - g\vec{\nabla}h - g\vec{\nabla}h_s \tag{11}$$

$$\frac{\partial \vec{u}^{\perp}}{\partial t} = f\vec{u} - g\vec{\nabla}^{\perp}h - g\vec{\nabla}^{\perp}h_s \tag{12}$$

where H is the base state fluid height. This can be written in matrix form (without topography) as

$$\frac{\partial \vec{x}}{\partial t} = \mathbf{A}\vec{x} \tag{13}$$

where $\vec{x} = (h, \vec{u})$ and

$$\mathbf{A} = \begin{pmatrix} 0 & -H\vec{\nabla}\cdot \\ -g\vec{\nabla} & -f\hat{k}\times \end{pmatrix} \tag{14}$$

This form is useful for analysing the linear properties of a discretization, and is also strongly connected to (linear) conservation properties via the linearized Hamiltonian (see below).

2.1.1.3. *Hamiltonian.*

Define a Hamiltonian

$$\mathcal{H} = \int_{\Omega} \frac{h}{2} \left(\vec{u} \cdot \vec{u} + g(h + 2h_s)\right) d\Omega \tag{15}$$

and a symplectic operator

$$\mathbf{J} = \begin{pmatrix} 0 & -\vec{\nabla}\cdot \\ -\vec{\nabla} & -q\hat{k}\times \end{pmatrix} \tag{16}$$

Let $\vec{x} = (h, \vec{u})$. Then the vector invariant equations can be written as

$$\frac{\partial \vec{x}}{\partial t} = \mathbf{J}\frac{\delta \mathcal{H}}{\delta \vec{x}} \tag{17}$$

where

$$\frac{\delta \mathcal{H}}{\delta \vec{x}} = \begin{pmatrix} \Phi \\ h\vec{u} \end{pmatrix} = \begin{pmatrix} gh+K \\ h\vec{u} \end{pmatrix} \tag{18}$$

is the functional derivative of the Hamiltonian with respect to $\vec{x}$ and $K = \frac{\vec{u}\cdot\vec{u}}{2}$.

2.1.1.4. *Poisson Bracket.* Using the sympletic operator $\mathbf{J}$, a Poisson bracket can be defined as

$$\{\mathcal{A}, \mathcal{B}\} = (\frac{\delta \mathcal{A}}{\delta \vec{x}}, \mathbf{J}\frac{\delta \mathcal{B}}{\delta \vec{x}}) \tag{19}$$

where $\mathcal{A}$ and $\mathcal{B}$ are arbitrary functionals of $\vec{x}$. The time evolution of an arbitrary functional $\mathcal{A}$ is then given by

$$\frac{d\mathcal{A}}{dt} = \{\mathcal{A}, \mathcal{H}\} \tag{20}$$

For the nonlinear shallow water equation, the Poisson bracket is (after integration by parts)

$$\{\mathcal{A}, \mathcal{B}\} = \int_\Omega d\Omega \left(\frac{\delta \mathcal{B}}{\delta \vec{u}} \cdot \vec{\nabla}\frac{\delta \mathcal{A}}{\delta h} - \frac{\delta \mathcal{A}}{\delta \vec{u}} \cdot \vec{\nabla}\frac{\delta \mathcal{B}}{\delta h} + q\hat{k} \cdot \left(\frac{\delta \mathcal{B}}{\delta \vec{u}} \times \frac{\delta \mathcal{A}}{\delta \vec{u}} \right) \right) \tag{21}$$

It is useful to split this into two separate brackets as

$$\{\mathcal{A},\mathcal{B}\} = \{\mathcal{A},\mathcal{B}\}_R + \{\mathcal{A},\mathcal{B}\}_Q \tag{22}$$

where

$$\{\mathcal{A},\mathcal{B}\}_R = \int_\Omega d\Omega \left(\frac{\delta\mathcal{B}}{\delta\vec{u}} \cdot \vec{\nabla}\frac{\delta\mathcal{A}}{\delta h} - \frac{\delta\mathcal{A}}{\delta\vec{u}} \cdot \vec{\nabla}\frac{\delta\mathcal{B}}{\delta h} \right) = \int_\Omega d\Omega \left(\frac{\delta B}{\delta h}(\vec{\nabla} \cdot \frac{\delta A}{\delta\vec{u}}) - \frac{\delta A}{\delta h}(\vec{\nabla} \cdot \frac{\delta B}{\delta\vec{u}}) \right) \tag{23}$$

encompasses the gradient and divergence terms; and

$$\{\mathcal{A},\mathcal{B}\}_Q = \int_\Omega d\Omega \left(q\hat{k} \cdot \left(\frac{\delta\mathcal{B}}{\delta\vec{u}} \times \frac{\delta\mathcal{A}}{\delta\vec{u}} \right) \right) \tag{24}$$

encompasses the nonlinear PV flux term.

2.1.1.5. *Linearized Hamiltonian.*

As is well-known in Hamiltonian mechanics, the linearized dynamics about some steady state $\vec{x}_0$ are described by the symplectic operator $\mathbf{J}$ evaluated at that state along with the small-amplitude approximation of the pseudo-energy $\mathcal{A}$ for that state (denoted by $\tilde{\mathcal{H}}$). In symbols, we have

$$\frac{\partial\vec{x}}{\partial t} = \mathbf{J}|_{\vec{x}=\vec{x}_0} \frac{\delta\tilde{\mathcal{H}}}{\delta\vec{x}} \tag{25}$$

More details of this process can be found in the Appendix A.

In the case of the shallow water equations about the steady state $\vec{x} = (H, 0)$ where H is some constant (also dropping the topography terms), we have

$$\tilde{\mathcal{H}} = \int_\Omega \frac{1}{2} \left(H\vec{u} \cdot \vec{u} + gh^2 \right) d\Omega \tag{26}$$

and

$$\mathbb{J}|_{\vec{x}=\vec{x}_0} = \mathbb{J}_{linear} = \begin{pmatrix} 0 & -\vec{\nabla}\cdot \\ -\vec{\nabla} & -\frac{f}{H}\hat{k}\times \end{pmatrix} \tag{27}$$

with

$$\frac{\delta\tilde{\mathcal{H}}}{\delta\vec{x}} = \begin{pmatrix} gh \\ H\vec{u} \end{pmatrix} \tag{28}$$

Note that $\mathbb{J}_{linear} = \mathbf{AD}$, where $\mathbf{D} = \begin{pmatrix} g & 0 \\ 0 & H \end{pmatrix}$. This is because the functional derivative of the linearized Hamiltonian is simply $\vec{x}$ times a scaling matrix since the Hamiltonian is quadratic and does not mix variables. This is a general feature of linearized Hamiltonian dynamics. A Poisson bracket can also be defined for the linear system using $\mathbb{J}$, it is simply the non-linear Poisson bracket with q replaced by $\frac{f}{H}$.

2.1.1.6. *Schemes.*

For the reasons discussed above (vorticity, invariance) the vector invariant formulation is used by many existing schemes, including TRiSK ([103]), ICON-IAP ([45],[46]) and Dynamico ([30]).

2.1.2. Vorticity-Divergence (Helmholtz Decomposition of $h\vec{u}$) Formulation.

We start by defining the relevant kinematic properties of the velocity field: relative vorticity ζ and divergence δ:

$$\delta = \vec{\nabla}\cdot\vec{u} = \vec{\nabla}^{\perp}\cdot\vec{u}^{\perp} \tag{29}$$

$$\zeta = \vec{\nabla}^{\perp}\cdot\vec{u} = -\vec{\nabla}\cdot\vec{u}^{\perp} \tag{30}$$

One advantage of using vorticity and divergence is that δ and ζ are true or pseudo-scalars, unlike the components of the velocity vector $\vec{u}$ which change whenever the coordinate system is changed (unlike scalar/pseudo-scalars, which are invariant to changes in coordinate system with the exception of a sign reversal for pseudo-scalars when orientation is flipped). Another advantage is that only one operator (the Laplacian) appears in the linear system, which makes it easy to eliminate spurious stationary modes and have good wave propagation characteristics. In addition, all of the variables are unstaggered and thus certain types of computations can be made simpler. This also simplifies grid management and other computational issues.

However, in the nonlinear case the streamfunction and velocity potential are required (to compute the wind), which means a pair of coupled elliptic equations must be solved at each time step. Efficient (scalable) solvers such as geometric multigrid exist in the case of simply-connected domains (grids without holes or complicated boundaries). Such domains occur in models that use terrain-following coordinates or a hybrid coordinate that is terrain following at the lower boundary. However, when the vertical coordinate intersects the topography the grids contain many small islands, disconnected regions and complicated boundaries. It is an ongoing research problem as to whether there are sufficiently scalable solvers for such grids.

2.1.2.1. *Nonlinear.*

By taking the divergence ($\vec{\nabla}\cdot$) and curl ($\vec{\nabla}^{\perp}\cdot$) of the momentum equation from the vector invariant formulation, we obtain

$$\frac{\partial h}{\partial t} = -\vec{\nabla} \cdot (h\vec{u}) \tag{31}$$

$$\frac{\partial \zeta}{\partial t} = -\vec{\nabla} \cdot (\eta\vec{u}) = -\vec{\nabla} \cdot (hq\vec{u}) \tag{32}$$

$$\frac{\partial \delta}{\partial t} = \vec{\nabla}^{\perp} \cdot (\eta \vec{u}) - \nabla^2 \Phi = \vec{\nabla}^{\perp} \cdot (hq\vec{u}) - \nabla^2 \Phi \tag{33}$$

where $\eta = \zeta + f$ and $q = \frac{\eta}{h}$. The mass flux (or momentum) can always be split into rotational and divergent components (ie a Helmholtz decomposition) as:

$$h\vec{u} = h\vec{u}_{div} + h\vec{u}_{rot} = \vec{\nabla}\chi + \vec{\nabla}^{\perp}\psi \tag{34}$$

where $h\vec{u}_{div} = \vec{\nabla}\chi$ and $h\vec{u}_{rot} = \vec{\nabla}^{\perp}\psi$. The streamfunction ψ and velocity potential χ can be related to the vorticity and divergence as

$$\zeta = \eta - f = \vec{\nabla} \cdot (h^{-1}\vec{\nabla}\psi) + J(h^{-1}, \chi) \tag{35}$$

$$\delta = \vec{\nabla} \cdot (h^{-1}\vec{\nabla}\chi) + J(\psi, h^{-1}) \tag{36}$$

The tangential mass flux ($h\vec{u}^{\perp}$) also has a Helmholtz decomposition as

$$h\vec{u}^{\perp} = \vec{\nabla}^{\perp}\chi - \vec{\nabla}\psi \tag{37}$$

The Hemholtz decompositions connect the vorticity-divergence formulation and the various momentum based formulations. In the preceding, we have neglected the possibility of a harmonic component (a component A for which $\vec{\nabla}^2 A = 0$), which works because the harmonic component on the sphere is zero. On the doubly periodic plane, it would be possible to have a constant harmonic component. The equations can be re-written in terms of χ and ψ directly as

$$\frac{\partial h}{\partial t} = -\nabla^2 \chi \tag{38}$$

$$\frac{\partial \zeta}{\partial t} = J(q,\psi) - \vec{\nabla}\cdot(q\vec{\nabla}\chi) \tag{39}$$

$$\frac{\partial \delta}{\partial t} = J(q,\chi) + \vec{\nabla}\cdot(q\vec{\nabla}\psi) - \nabla^2\Phi \tag{40}$$

2.1.2.2. *Linear.*

As before, we can linearize about a state of rest with fluid height H to get:

$$\frac{\partial h}{\partial t} = -H\delta \tag{41}$$

$$\frac{\partial \zeta}{\partial t} = -\vec{\nabla}\cdot(f\vec{u}) = -\vec{\nabla}^{\perp}\cdot(f\vec{u}^{\perp}) \tag{42}$$

$$\frac{\partial \delta}{\partial t} = -\vec{\nabla}\cdot(f\vec{u}^{\perp}) - g\nabla^2 h = \vec{\nabla}^{\perp}\cdot(f\vec{u}^{\perp}) - g\nabla^2 h \tag{43}$$

In matrix form (without topography and assuming f is constant) this can be written as

$$\frac{\partial \vec{x}}{\partial t} = \mathbf{A}\vec{x} \tag{44}$$

where $\vec{x} = (h, \zeta, \delta)$ and

$$\mathbf{A} = \begin{pmatrix} 0 & 0 & -H \\ 0 & 0 & -f \\ -g\vec{\nabla}^2 & f & 0 \end{pmatrix} \tag{45}$$

2.1.2.3. *Hamiltonian.*

Define a Hamiltonian

$$\mathcal{H} = \int_{\Omega} \frac{1}{2h}\left(|\vec{\nabla}\chi|^2 + |\vec{\nabla}\psi|^2 + 2J(\chi,\psi)\right) + \frac{1}{2}gh(h+h_s)d\Omega \tag{46}$$

a symplectic operator

$$\mathbf{J} = \begin{pmatrix} 0 & 0 & \nabla^2 \\ 0 & -J(q,\bullet) & \vec{\nabla}\cdot(q\vec{\nabla}\bullet) \\ -\nabla^2 & -\vec{\nabla}\cdot(q\vec{\nabla}\bullet) & -J(q,\bullet) \end{pmatrix} \tag{47}$$

and let $\vec{x} = (h, \zeta, \delta)$. These represent the transformation of the vector invariant Hamiltonian formulation from $\vec{x} = (h, \vec{u})$ to $\vec{x} = (h, \zeta, \delta)$ (ie the vorticity-divergence formulation). As before, the evolution of the system is governed by

$$\frac{\partial \vec{x}}{\partial t} = \mathbf{J}\frac{\delta \mathcal{H}}{\delta \vec{x}} \tag{48}$$

Note that

$$\delta\mathcal{H} = \int_\Omega d\Omega \left(-\psi\delta\zeta - \chi\delta\delta + \Phi\delta h\right) \tag{49}$$

where

$$\Phi = K + gh = \frac{|\vec{\nabla}\chi|^2 + |\vec{\nabla}\psi|^2 + 2J(\chi,\psi)}{2h^2} + gh \tag{50}$$

which gives

$$\frac{\delta\mathcal{H}}{\delta\vec{x}} = \begin{pmatrix} \Phi \\ -\psi \\ -\chi \end{pmatrix} \tag{51}$$

(this is the functional derivative of the Hamiltonian with respect to $\vec{x}$). The functional derivative of the Hamiltonian is intimately connected to the Helmholtz decomposition of the momentum. An alternative derivation of this is as follows. Note that for a general functional

$\mathcal{F}$, we have:

$$\frac{\delta \mathcal{F}}{\delta \vec{u}} = \vec{\nabla} \frac{\delta \mathcal{F}}{\delta \delta} + \vec{\nabla}^{\perp} \frac{\delta \mathcal{F}}{\delta \zeta} \tag{52}$$

Since

$$\frac{\delta \mathcal{H}_{kin}}{\delta \vec{u}} = h\vec{u} = \vec{\nabla}\chi + \vec{\nabla}^{\perp}\psi \tag{53}$$

it is immediately clear that

$$\frac{\delta \mathcal{H}}{\delta \vec{x}} = \begin{pmatrix} \Phi \\ -\psi \\ -\chi \end{pmatrix} \tag{54}$$

The minus signs come from integration by parts.

2.1.2.4. *Poisson Bracket.*

Using the sympletic operator $\mathbf{J}$, a Poisson bracket can be defined as

$$\{\mathcal{A}, \mathcal{B}\} = (\frac{\delta \mathcal{A}}{\delta \vec{x}}, \mathbf{J} \frac{\delta \mathcal{B}}{\delta \vec{x}}) \tag{55}$$

where $\mathcal{A}$ and $\mathcal{B}$ are arbitrary functionals of $\vec{x}$. The time evolution of an arbitrary functional $\mathcal{A}$ is then given by

$$\frac{d\mathcal{A}}{dt} = \{\mathcal{A}, \mathcal{H}\} \tag{56}$$

For the nonlinear shallow water equation, the Poisson bracket for the vorticity-divergence form is best expressed as the sum of three separate brackets:

$$\{\mathcal{A}, \mathcal{B}\} = \{\mathcal{A}, \mathcal{B}\}_{\delta\delta} + \{\mathcal{A}, \mathcal{B}\}_{\zeta\zeta} + \{\mathcal{A}, \mathcal{B}\}_{\delta\zeta h} \tag{57}$$

where

$$\{\mathcal{A},\mathcal{B}\}_{\zeta\zeta} = \int_\Omega d\Omega q J(\mathcal{A}_\zeta,\mathcal{B}_\zeta) \tag{58}$$

$$\{\mathcal{A},\mathcal{B}\}_{\delta\delta} = \int_\Omega d\Omega q J(\mathcal{A}_\delta,\mathcal{B}_\delta) \tag{59}$$

$$\{\mathcal{A},\mathcal{B}\}_{\zeta\delta h} = \int_\Omega d\Omega q(\vec{\nabla}\mathcal{A}_\delta\cdot\vec{\nabla}\mathcal{B}_\zeta - \vec{\nabla}\mathcal{A}_\zeta\cdot\vec{\nabla}\mathcal{B}_\delta) + (\vec{\nabla}\mathcal{A}_\delta\cdot\vec{\nabla}\mathcal{B}_h - \vec{\nabla}\mathcal{A}_h\cdot\vec{\nabla}\mathcal{B}_\delta) \tag{60}$$

Note that each of these brackets is anti-symmetric and has the correct general Casimir functional from above.

2.1.2.5. *Nambu Bracket.*

As shown in REF, each of these Poisson brackets has as associated Nambu bracket:

$$\{\mathcal{F},\mathcal{H},\mathcal{Z}\}_{\zeta\zeta\zeta} = \int_\Omega d\Omega \mathcal{Z}_\zeta J(\mathcal{F}_\zeta,\mathcal{H}_\zeta) \tag{61}$$

$$\{\mathcal{F},\mathcal{H},\mathcal{Z}\}_{\delta\delta\zeta} = \int_\Omega d\Omega \mathcal{Z}_\zeta J(\mathcal{F}_\delta,\mathcal{H}_\delta) \tag{62}$$

(63)

$$\{\mathcal{F},\mathcal{H},\mathcal{Z}\}_{\delta\zeta h} = \int_\Omega d\Omega \left(\vec{\nabla}\mathcal{Z}_h\cdot\vec{\nabla}\mathcal{F}_\delta\cdot\vec{\nabla}\mathcal{H}_\zeta\cdot\frac{1}{\vec{\nabla}q} - \vec{\nabla}\mathcal{Z}_h\cdot\vec{\nabla}\mathcal{F}_\zeta\cdot\vec{\nabla}\mathcal{H}_\delta\cdot\frac{1}{\vec{\nabla}q}\right) + \text{cyc}(\mathcal{F},\mathcal{H},\mathcal{Z})$$

where $Z_C = \int_\Omega d\Omega h\frac{q^2}{2}$ is the potential enstrophy, and the multipart dot product is simply the product of the individual components, summed over each basis (ie the first term is

$\frac{\partial_x \mathcal{Z}_h \partial_x \mathcal{F}_\delta \partial_x \mathcal{H}_\zeta}{\partial_x q}$). These are useful because they are triply anti-symmetric (which ensures the conservation of $\mathcal{H}$ and $\mathcal{Z}$) and non-degenerate (no Casimirs). It would of course be possible to generalize these brackets to ANY Casimir, but since we are interested mostly in potential enstrophy conservation it is not necessary. These brackets will form the basis of the general discretization method discussed below.

2.1.2.6. *Linearized Hamiltonian.*

As before, in the case of the shallow water equations about the steady state $\vec{x} = (H, 0, 0)$ where H is some constant (also dropping the topography terms and assuming f is constant), we have

$$\tilde{\mathcal{A}} = \int_\Omega \frac{1}{2}\left(|\vec{\nabla}\chi|^2 + |\vec{\nabla}\psi|^2\right) + \frac{1}{2}gh^2 d\Omega \tag{64}$$

and

$$\mathbf{J}\big|_{\vec{x}=\vec{x}_0} = \begin{pmatrix} 0 & 0 & \nabla^2 \\ 0 & -J(\frac{f}{H},\bullet) & \vec{\nabla}\cdot(\frac{f}{H}\vec{\nabla}\bullet) \\ -\nabla^2 & -\vec{\nabla}\cdot(\frac{f}{H}\vec{\nabla}\bullet) & -J(\frac{f}{H},\bullet) \end{pmatrix} \tag{65}$$

with

$$\frac{\delta\tilde{\mathcal{A}}}{\delta\vec{x}} = \begin{pmatrix} gh \\ -\psi \\ -\chi \end{pmatrix} \tag{66}$$

where $x = (h, \zeta, \delta)$ (we have changed from η to ζ since f is constant). Note also that the Hemholtz decomposition simplifies to

$$H\vec{u} = \vec{\nabla}\chi + \vec{\nabla}^\perp\psi \tag{67}$$

which yields

$$\delta = \frac{\nabla^2 \chi}{H} \tag{68}$$

$$\zeta = \frac{\nabla^2 \psi}{H} \tag{69}$$

In the case of constant f, this reduces to

$$\mathbf{J}\big|_{\vec{x}=\vec{x}_0} = \begin{pmatrix} 0 & 0 & \nabla^2 \\ 0 & 0 & \frac{f}{H}\nabla^2 \\ -\nabla^2 & -\frac{f}{H}\nabla^2 & 0 \end{pmatrix} \tag{70}$$

2.1.2.7. *Schemes.*

There is only one class of schemes that use the vorticity-divergence form of the shallow water equations (with a momentum-based Helmholtz decomposition): those based on Nambu brackets using the approach pioneered by Rick Salmon in [116] and [117]. They include the single moment collocated (Z grid) schemes developed in those references; and the staggered (ZC grid) scheme developed by Sommer and Nevir in [125].

There are also several schemes that use the vorticity-divergence form with a velocity based Helmholtz decomposition (such as [57] and [104]; or a closely related PV-divergence form [130]); however it seems quite difficult to derive a Hamiltonian formulation of this approach. In particular, the expression of the functional derivatives of the Hamiltonian in terms of χ and ψ from a Helmholtz decomposition of $\vec{u}$ is very complicated, whereas the expression in terms of χ and ψ from a Helmholtz decomposition of $\vec{hu}$ is quite simple. The symplectic operator $\mathbf{J}$ is of course the same in both cases, since we have the same prognostic variables.

2.2. Potential Vorticity

Take the curl of the wind equation and note that $\eta = \zeta + f = qh$ where $q = \frac{\eta}{h}$ is the rotating shallow water potential vorticity to get

$$\frac{\partial(hq)}{\partial t} = -\vec{\nabla} \cdot (hq\vec{u}) = -\vec{\nabla}^{\perp} \cdot \left(hq\vec{u}^{\perp}\right) \tag{71}$$

This is the flux form of the PV equation, it can be combined with the mass equation to get

$$\frac{Dq}{Dt} = 0 \tag{72}$$

which is the advective (or Lagrangian) PV equation. Typically, numerical models developed from the vorticity-divergence or vector-invariant formulation will have an explicit equation for the height evolution and either an implied or explicit equation for the flux-form PV evolution. It is highly desirable that these schemes possess two properties related to the PV (among others):

(1) Compatibility: The (possibly implied) flux-form PV equation can be written as the divergence of a flux. This ensures both local and global conservation of mass-weighted PV.

(2) Consistency: When PV is constant, the flux-form PV equation reduces to the height equation. This ensures that an initially uniform PV field will remain so for all time.

2.3. Conserved Quantities

Since the rotating shallow water equations form a (non-canonical) Hamiltonian system, we know from Noether's theorem and other considerations (such as the singular nature of the

symplectic operator) that there are three categories of conserved quantities: Hamiltonian, Casimirs and Symmetry Invariants.

2.3.0.8. *Energy (Hamiltonian).* The first is simply the Hamiltonian itself. In this case, the Hamiltonian is the total energy of the system. Conservation of the Hamiltonian arises due to the skew-symmetric nature of the symplectic operator $\mathbf{J}$. In particular, the evolution of any functional $\mathcal{F}$ is given by

$$\frac{d\mathcal{F}}{dt} = (\frac{\delta \mathcal{F}}{\delta \vec{x}}, \mathbf{J}\frac{\delta \mathcal{H}}{\delta \vec{x}}) \tag{73}$$

where $(,)$ is the inner product associated with the function spaces that $\mathcal{H}$ is defined on. When $\mathcal{F} = \mathcal{H}$, we get

$$\frac{d\mathcal{H}}{dt} = (\frac{\delta \mathcal{H}}{\delta \vec{x}}, \mathbf{J}\frac{\delta \mathcal{H}}{\delta \vec{x}}) = 0 \tag{74}$$

since $\mathbf{J}$ is skew-symmetric. For the rotating shallow water equations, the Hamiltonian is the total energy of the system. The elegant derivation of energy conservation and its simplicity (relying ONLY on the skew-symmetry of $\mathbf{J}$) has lead to the development of powerful discrete methods for ensuring energy conservation (see Chapter 4).

Kinetic Energy Equation. The local rate of change of mass-weighted kinetic energy is given by

(75)
$$\frac{\partial (hK)}{\partial t} = \frac{\delta \mathcal{H}_{kin}}{\delta \vec{u}} \cdot \frac{\partial \vec{u}}{\partial t} + \frac{\delta \mathcal{H}_{kin}}{\delta h}\frac{\partial h}{\partial t} = -K\vec{\nabla}\cdot(h\vec{u}) - h\vec{u}\cdot\vec{\nabla}K - h\vec{u}\cdot\vec{\nabla}(gh) = -\vec{\nabla}\cdot(h\vec{u}K) - h\vec{u}\cdot\vec{\nabla}(gh)$$

where $K = \frac{\vec{u}\cdot\vec{u}}{2}$. Note that there are two terms here: an advection of kinetic energy term $(-\vec{\nabla}\cdot(h\vec{u}K))$ and a conversion term $(-h\vec{u}\cdot\vec{\nabla}(gh))$ that (reversibly) transforms kinetic energy into potential energy.

Potential Energy Equation. The local rate of change of mass-weighted potential energy is given by

$$\frac{\partial(gh^2/2)}{\partial t} = \frac{\delta \mathcal{H}_{pot}}{\delta h}\frac{\partial h}{\partial t} = -gh\vec{\nabla}\cdot(h\vec{u}) \tag{76}$$

which is entirely a conversion term between kinetic and potential energy. It is useful to split the potential energy into available and unavailable parts as:

$$\mathcal{H}_{UPE} = \int_\Omega \frac{g}{2}H_0(2h + H_0)d\Omega = \frac{gH_0^2}{2}\int_\Omega d\Omega \tag{77}$$

$$\mathcal{H}_{APE} = KE + \int_\Omega \frac{g}{2}(h - H_0)^2 d\Omega \tag{78}$$

$$\mathcal{H}_{PE} = \int_\Omega \frac{gh^2}{2}d\Omega = \mathcal{H}_{UPE} + \mathcal{H}_{APE} \tag{79}$$

where $H_0 = \frac{\int_\Omega h d\Omega}{\int_\Omega d\Omega}$ is the domain averaged height (constant with time due to mass conservation), and $\mathcal{H}_{UPE}$ is a constant. Since

$$\frac{\delta \mathcal{H}_{APE}}{\delta h} = g(h - H_0) \tag{80}$$

$$\frac{\delta \mathcal{H}_{UPE}}{\delta h} = 0 \tag{81}$$

we can write the local rates of change of APE and UPE as

$$\frac{\partial(APE)}{\partial t} = -g(h - H_0)\vec{\nabla}\cdot(h\vec{u}) \tag{82}$$

$$\frac{\partial(UPE)}{\partial t} = 0 \tag{83}$$

The inclusion of topography simply replaces h with $h + h_s$ in the equations for $\mathcal{H}_{APE}$ and H_0.

Total Energy Equation. The preceding equations can be combined into a mass-weighted total energy equation as

$$\frac{\partial(hK + hgh)}{\partial t} = \frac{\delta \mathcal{H}_{kin}}{\delta \vec{u}} \cdot \frac{\partial \vec{u}}{\partial t} + \frac{\delta \mathcal{H}_{kin}}{\delta h}\frac{\partial h}{\partial t} + \frac{\delta \mathcal{H}_{pot}}{\delta h}\frac{\partial h}{\partial t} = -\vec{\nabla} \cdot (h\vec{u}K) - g\vec{\nabla} \cdot (h\vec{u}h) \tag{84}$$

2.3.0.9. *Casimir Invariants.* The second category of conserved quantities consists of Casimir invariants. Since the rotating shallow water equations are a non-canonical Hamiltonian system, the symplectic operator **J** is singular and thus it posseses Casimir invariants that satisfy

$$\mathbf{J}\frac{\delta \mathcal{C}}{\delta \vec{x}} = 0 \tag{85}$$

Note that from above, this implies that

$$\frac{d\mathcal{C}}{dt} = 0 \tag{86}$$

For the rotating shallow water equations, the Casimirs take the form

$$\mathcal{C} = \int_\Omega hF(q)d\Omega \tag{87}$$

where $F(q)$ is an arbitrary function of the potential vorticity and

$$\frac{\delta \mathcal{C}}{\delta \vec{x}} = \begin{pmatrix} F(q) - qF'(q) \\ \vec{\nabla}^T F'(q) \end{pmatrix} \tag{88}$$

Important cases include $F = 1$ (mass conservation), $F = q$ (circulation or mass-weighted potential vorticity) and $F = \frac{q^2}{2}$ (potential enstrophy).

2.3.0.10. *Symmetry Invariants.* The third type of conserved quantity is the Symmetry invariant. Consider an arbitrary translation of some independent coordinate y^k. If $\mathbf{J}$ and $\mathcal{H}$ are invariant under this translation, and there is some functional $\mathcal{M}$ that satisfies

$$\mathbf{J}\frac{\delta \mathcal{M}}{\delta \vec{x}} = -\frac{\partial \vec{x}}{\partial y^k} \tag{89}$$

then $\mathcal{M}$ is conserved ($\frac{d\mathcal{M}}{dt} = 0$). For the rotating shallow water equations, the symmetry invariants are momentum and angular momentum, which arise from translational and rotational symmetry, respectively. It is easy to see that momentum is given by

$$\mathcal{M}_{\vec{u}} = \int_{\Omega} h(\vec{u} + \vec{R}) d\Omega \tag{90}$$

where $\vec{R} = \vec{\Omega} \times \vec{x}$ and $\vec{x}$ is the position vector. In the absence of pressure torques exerted by the bottom topography, this will be conserved. The angular momentum is given by

$$\mathcal{M}_M = \int_{\Omega} \vec{x} \times (\vec{u} + \vec{R}) d\Omega \tag{91}$$

It too is conserved in the absence of pressure torques exerted by the bottom topography.

2.4. Subgrid Turbulence Operators

Due to limited computational resources, numerical models naturally have a finite resolution. That is, there are scales of motion that are not resolved, and since this is a non-linear system, these scales interact with the resolved scales. A major thrust of this research is the development of schemes that are nonlinearly stable WITHOUT any added dissipation, and

conserve both total energy and potential enstrophy in an analogous manner to the continuous equations. This allows the representation of the interaction between the resolved and unresolved scales to be parameterized on a purely physical basis, instead of being at least partly a band-aid for poor numerics.

Fundamental considerations from inviscid, incompressible 2D turbulence ([38]) imply that the conservation of both energy and enstrophy ensure that energy is cascaded upscale, while enstrophy cascades downscale (and in the case of a viscous flow, ultimately removed). A numerical model with a finite resolution will therefore see a build-up of enstrophy at the grid scale. This suggests that our dissipation operator should conserve resolved energy and dissipate resolved potential enstrophy, with a focus on removing grid-scale enstrophy. Similar considerations apply to many geophysical flows with the enstropy/vorticity replaced by the potential enstrophy/potential vorticity (such as the shallow water equations), which are stratified, quasi-2D turbulence.

Essentially all numerical models of the atmosphere are an example of large-eddy simulations, since the effective resolution of models is far coarser than the viscous scale. In particular, this means that the effects of molecular viscosity can be neglected- the resolved portion of the flow is inviscid. However, there exist very important interactions between the resolved and unresolved scales . These can be parameterized as a viscous interaction (and therefore represented using some form of dissipation), but there is growing evidence ([68],[138]) that such parameterizations ignore important effects such as the upscale cascade of energy in 2D turbulence.

There are many possible ways to parameterize the subgrid interaction term. Implicit LES models use numerical dissipation from the advection operator as a representation of the subgrid interaction. Explicit LES models use an explicit representation of the subgrid term,

typically either hyperviscosity or Smagorinsky-type diffusion. However, these parameterizations usually break other desirable features of the discretizations (such as steady geostrophic modes, energy conservation etc.). In addition, they are unable to represent the upscale cascade of energy from unresolved to resolved scales. An alternative to hyper-diffusion and divergence damping is the anticipated potential vorticity method ([111],[20],[49]), which conserves energy, dissipates enstrophy and preserves all of the other properties of the flow (such as linear waves, steady geostrophic modes and PV compatibility). However, work by Gassmann and Gilbert ([47],[50]) suggests that from an energetic perspective, Smagorinsky-type diffusion is the correct physical representation of subgrid turbulence, especially in the case of 3D flow.

2.4.1. Hyperviscosity.

For the purposes of simplicity and comparison with other models, when dissipation is required in the various test cases in Chapter 8, simple hyperviscosity is used. This is given by:

$$\frac{\partial \vec{u}}{\partial t} = \nu \vec{\nabla}^2 \vec{u} \tag{92}$$

where

$$\vec{\nabla}^2 \vec{u} = \vec{\nabla}(\vec{\nabla} \cdot \vec{u}) - \vec{\nabla}^T \cdot (\vec{\nabla}^T \cdot \vec{u}) = \vec{\nabla}\delta - \vec{\nabla}^T \zeta \tag{93}$$

It is easy to see (by taking divergence and curl of the equation above) that this is equivalent to

$$\frac{\partial \zeta}{\partial t} = \nu \vec{\nabla}^2 \zeta \tag{94}$$

$$\frac{\partial \delta}{\partial t} = \nu \vec{\nabla}^2 \delta \tag{95}$$

since

$$\vec{\nabla} \cdot \vec{\nabla}^2 \vec{u} = \vec{\nabla}^2 \delta \tag{96}$$

$$\vec{\nabla}^T \cdot \vec{\nabla}^2 \vec{u} = \vec{\nabla}^2 \zeta \tag{97}$$

Hyperviscosity of order $2p$ is obtained by simply iterating the relevant Laplacian operators an additional p times.

2.5. Chapter Summary

The material in this chapter is entirely review (with the possible exception of the symplectic operator for the vorticity-divergence formulation, but that is a trivial derivation from the existing Poisson brackets in the literature) and no claims to originality are made.

CHAPTER 3

Generalized C Grid Scheme

3.1. General Nonlinear Formulation (Discrete Exterior Calculus and Discrete Hamiltonian)

As shown in the previous section, the rotating shallow water equations can be expressed in terms of Hamiltonian mechanics. The Hamiltonian framework is very useful for looking at conserved quantities. Therefore, presented below is a generalized scheme based on a combination of discrete exterior calculus and Hamiltonian methods, that extends the 1981 Arakawa and Lamb scheme to arbitrary grids. This C grid framework draws heavily from work by Todd Ringler, Joe Klemp, Bill Skamarock, John Thuburn, Collin Cotter, Thomas Dubos and Hilary Weller (see [140],[102],[103] [135],[137],[153],[155] and [154]); and much of the material presented is a combination of existing work in the literature.

Generally, the discrete exterior calculus aspect of the discretization is used to obtain desirable linear mimetic properties, while the Hamiltonian aspect of the discretization is used to obtain conservation properties. The combination of these two represents the realization of Salmon's desire for a constructive method for the development of total energy and potential enstrophy conserving schemes. It gives a very general, extremely powerful framework for the creation of discrete models on arbitrary grids that possess linear mimetic and conservation properties. More details about Hamiltonian mechanics and Discrete Exterior Calculus are provided in Appendices A and C, respectively.

3.1.1. Grids and choice of variables.

Consider a general polygonal grid and its associated dual grid, as described more in Appendix B. The method outlined below places NO restrictions on the dual grid, provided

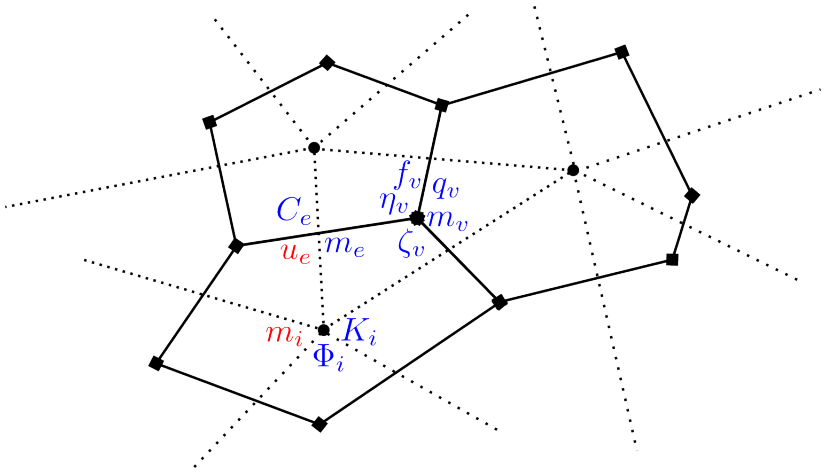

FIGURE 3.1. Discrete variables and their staggering on the horizontal mesh

operators (really discrete Hodge stars) can be found that possess the required properties. Generally, a choice of discrete Hodge star is equivalent to a choice of dual grid. Examples of grid systems that are covered under this framework are: Voronoi-Delauney (and spherical Voronoi-Delauney), including both hexagonal-pentagonal and triangular icosahedral grids; and gnomic non-orthogonal cubed sphere grids. These are the vast majority of quasi-uniform horizontal grids that are under consideration for next-generation weather and climate dynamical cores.

This approach is naturally a C grid type discretization, since vectors are associated with a 1-forms (and n-1 forms, but we are in 2 dimensions so vectors are ONLY associated with 1-forms). Therefore, the mass variable m_i lives on cells (as a primal 2-form), and the wind variable u_e lives at cell edges (as a dual 1-form). A detailed list of discrete variables is given in Table 3.1, and diagram of their staggering on the grid is given in Figure 3.1. In Table 3.1, p refers to variables that live on the primal grid; while d refers to variables that live on the dual grid. The number refer to the mesh element each variable is associated with (0 for vertices, 1 for edges and 2 for cells). For example, p-2 is a variable that lives on primal cells; while d-0 is a variable that lives on dual vertices.

TABLE 3.1. List of discrete variables and their diagnostic equations

Variable	**Type**	**Equation**	**Description**
m_i	p-2	Prognostic	Mass
u_e	d-1	Prognostic	Wind
b_i	p-2	Constant	Topography
f_v	d-2	Constant	Coriolis Force
C_e	d-1	$\mathbf{H}C_e = F_e$	Mass Flux
F_e	p-1	$F_e = \frac{\delta \mathcal{H}_{kin}}{\delta u_e}$	Mass Flux
q_v	p-0	$q_v = \eta_v / h_v$	Potential Vorticity
ζ_v	d-2	$\zeta_v = D_2 u_e$	Relative Vorticity
η_v	d-2	$\eta_v = \zeta_v + f_v$	Absolute Vorticity
Φ_i	p-2	$\Phi_i = K_i + g h_i$	Poisson Energy
h_v	d-2	$h_v = \mathbf{R} h_i$	Mass
δ_i	p-2	$\delta_i = D_2 \mathbf{H} u_e$	Divergence
K_i	p-2	$\mathbf{I}K_i = \frac{\delta \mathcal{H}_{kin}}{\delta m_i}$	Kinetic Energy
χ_i	d-0	$D_2 \mathbf{H} D_1 \chi_i = \delta_i$	Velocity Potential
ψ_v	p-0	$-D_2 \mathbf{H}^{-1} D_1 \psi_v = \zeta_v$	Streamfunction

3.1.1.1. *Operators.*

Incidence Matrices. Incidence matrices describe the topological relationships between geometric elements on the same (primal or dual) grid. Since we are working in two dimensions, there are four: D_1,D_2,$\bar{D}_1$,$\bar{D}_2$; where for example D_1 maps from primal 0-form to primal 1-form, and D_2 maps from dual 1-forms to dual 2-forms. They are a discrete analogue of the differential operator d, and therefore represent discrete divergence, gradient and curl. Continuous properties such as $\vec{\nabla}^T \cdot \vec{\nabla} = 0$ are automatically enforced by construction (ex $D_2 D_1 = 0$). These operators are defined purely topologically using the cell complex structure from algebraic topology. Specifically, they are defined as:

$$D_2 = \sum_{e \in EC(i)} n_{e,i} \tag{98}$$

$$\bar{D}_1 = \sum_{i \in CE(e)} -n_{e,i} \tag{99}$$

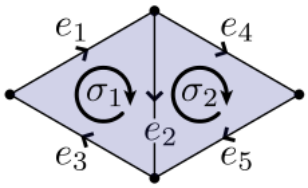

FIGURE 3.2. Diagram of the discrete exterior derivative D_2 on a triangular mesh. Obtained from http://brickisland.net/cs177/?p=274

$$\bar{D}_2 = \sum_{e \in EV(v)} t_{e,v} \tag{100}$$

$$D_1 = \sum_{v \in VE(e)} t_{e,v} \tag{101}$$

The following properties hold:

$$D_2 D_1 = 0 \tag{102}$$

$$\bar{D}_2 \bar{D}_1 = 0 \tag{103}$$

$$D_2 = -\bar{D}_1^{\,T} \tag{104}$$

$$\bar{D}_2 = D_1^T \tag{105}$$

The action of the discrete exterior derivative is shown in Figure 3.2.

Hodge Star Operators. The discrete Hodge Star operators map between variables defined on the primal grid and variables defined on the dual grid (in fact, they DEFINE the dual grid). There are two types of discrete Hodge stars that are typically used: circumcentric (or

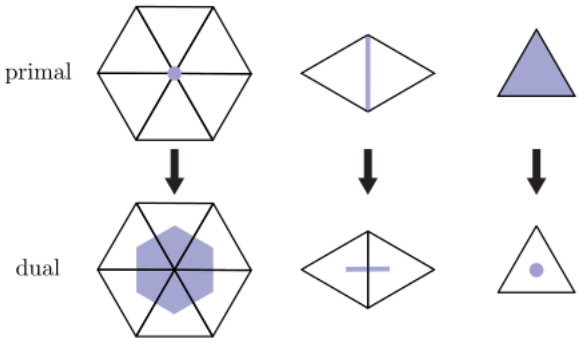

FIGURE 3.3. Depiction of the action of the various Hodge star operators on a uniform triangular grid. Obtained from http://brickisland.net/cs177/?p=274

Voronoi) and barycentric. In this work, we will use exclusively circumcentric Hodge stars (which are diagonal) with the exception of the dual 1-form circulations to primal 1-form fluxes Hodge star $\mathbf{H}$ for cubed-sphere grids. Note that a discrete Hodge star induces a discrete inner product. Of course, this process could be reversed: an inner product could be used to define a Hodge star. This leads to mixed finite-element methods and is the basis of the FEEC approach ([94]). The action of the Hodge star operators is shown in Figure 3.3.

The combination of the discrete exterior derivatives and the Hodge star operators induces a De-Rham cohomology, shown in Figure C.1.

R and **W**. In addition to incidence matrices and Hodge stars described in Appendix C, the rotating shallow water equations require two additional operators: $\mathbf{R}$ (which maps from primal 2-forms to dual 2-forms, and is an analogue of the identity operator) and $\mathbf{W}$ (which maps from primal 1-form fluxes to dual 1-form fluxes, and is an analogue of the contraction operator plus sharp/flat operators, see [10] for more details). Note that the transpose $\mathbf{R}^T$ maps from primal 0-forms to dual 0-forms. Also note that $\mathbf{W}$ is distinct from $\mathbf{H}^{-1}$, which maps from primal 1-form fluxes to dual 1-form circulations. The correct discretization of the contraction and sharp/flat operators (to form a discrete calculus with analogous properties to the continuous one) is an open research question. $\mathbf{R}$ is arbitrary, provided that it preserves

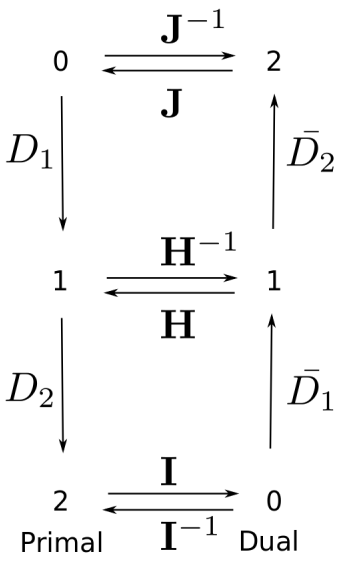

FIGURE 3.4. The discrete DeRham cohomology induced by the incidence matrices and Hodge stars

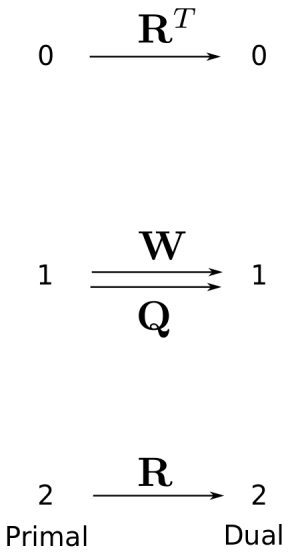

FIGURE 3.5. Actions of $\mathbf{R}$ and $\mathbf{W}$ for the C grid scheme

the global integral of the operand, and ensures that a constant operand remains constant. For an $\mathbf{R}$ with a stencil given by CV, these reduce to $\sum_{v \in VC(i)} R_{i,v} = 1$ and $\frac{1}{A_v} \sum_{i \in CV(v)} R_{i,v} A_i = 1$. The actions of $\mathbf{R}$ and $\mathbf{W}$ are shown in Figure 3.5.

Q. The final operator required is the non-linear Coriolis operator **Q**, which maps from primal 1-form fluxes to dual 1-form fluxes. There are many properties it should posses, which are discussed in more detail below. Since this is the non-linear version of **W**, its continuous counterpart is also a combination of the contraction operator and the sharp/flat operators.

Mass Flux and Kinetic Energy. We will also need an operator to construct the primal mass flux from the staggered variables m_i and u_e. As discussed below, this flux reconstruction must be compatible with the associated definition of kinetic energy (if total energy is to be preserved). Fundamentally, the mass flux and kinetic energy both come from discrete variational derivatives of the Hamiltonian (which implies the compatibility condition between them).

3.1.2. Discretization.

Starting from the vector invariant equations in Hamiltonian form, we write a general discretization as follows:

$$\mathbb{J} = \begin{pmatrix} 0 & -D_2 \\ -\bar{D}_1 & \mathbf{Q} \end{pmatrix} \tag{106}$$

$$\mathcal{H} = \frac{1}{2} g(m_i, m_i + b_i)_{\mathbf{I}} + \frac{1}{2}(C_e, u_e)_{\mathbf{H}} = \mathcal{H}_{pot} + \mathcal{H}_{kin} \tag{107}$$

$$\frac{\delta \mathcal{H}}{\delta \vec{x}} = \begin{pmatrix} \mathbf{I}\Phi_i \\ F_e \end{pmatrix} = \begin{pmatrix} \mathbf{I}K_i + g\mathbf{I}(m_i + b_i) \\ \mathbf{H}C_e \end{pmatrix} = \begin{pmatrix} \frac{\delta \mathcal{H}_{kin}}{\delta m_i} + \frac{\delta \mathcal{H}_{pot}}{\delta m_i} \\ \frac{\delta \mathcal{H}_{kin}}{\delta u_e} \end{pmatrix} \tag{108}$$

$$\vec{x} = (m_i, u_e) \tag{109}$$

where $\mathbb{J}$ is the discrete symplectic operator and $\mathcal{H}$ is the discrete Hamiltonian; D_1, D_2, $\bar{D}_1$ and $\bar{D}_2$ are discrete exterior derivatives (incidence matrices) that satisfy various properties (see below); **I**,**H** and **J** are discrete Hodge star operators (diagonal for orthogonal grids, non-diagonal for non-orthogonal grids); and F_e (primal 1-form) is the discrete mass flux, C_e (dual 1-form) is the discrete mass circulation, Φ_i (primal 2-form) the discrete Bernoulli function and K_i (primal 2-form) the discrete kinetic energy, respectively. As shown below, F_e and K_i must be compatible in order for the resulting scheme to conserve total energy. Note that the discrete functional derivative produces a dual 0-form and a primal 1-form, as is required. These are the associated dual form counterparts of the predicted variables (primal 2-form and dual 1-form).

Note that we can define

$$C_e^{\perp} = \mathbf{W}F_e = \mathbf{WH}C_e \tag{110}$$

and

$$F_e^{\perp} = \mathbf{H}C^{\perp} = \mathbf{HW}F_e = \mathbf{HWH}C_e \tag{111}$$

where $C_e^{\perp}$ is the dual edge mass flux (dual 1-form) and $F_e^{\perp}$ is the primal edge circulation (primal 1-form). These various fluxes are defined by the choice of primal and dual grid advection schemes. Careful selection of advection scheme will give total energy and potential vorticity conservation. However, this is often at the cost of accurate advection, which is discussed more below.

Putting all of this together, the governing equations are therefore given as

$$\frac{\partial m_i}{\partial t} + D_2 \mathbf{H} C_e = 0 \tag{112}$$

$$\frac{\partial u_e}{\partial t} - \mathbf{Q}\mathbf{H} C_e + \bar{D}_1 \mathbf{I}(K_i + g m_i + g b_i) = 0 \tag{113}$$

3.1.2.1. *Available Energy.*

$$\mathcal{H}_{APE} = \frac{1}{2} g(m_i + b_i, m_i + b_i)_{\mathbf{I}} - \frac{1}{2} g(\bar{m_i} + \bar{b_i}, \bar{m_i} - \bar{b_i})_{\mathbf{I}} \tag{114}$$

$$\mathcal{H}_{UPE} = \frac{1}{2} g(\bar{m_i} + \bar{b_i}, \bar{m_i} - \bar{b_i})_{\mathbf{I}} \tag{115}$$

$$\bar{m_i} = \mathbf{I}^{-}1 \frac{\sum_i m_i}{\sum_i \mathbf{I}^{-}1} \tag{116}$$

$$\bar{b_i} = \mathbf{I}^{-}1 \frac{\sum_i b_i}{\sum_i \mathbf{I}^{-}1} \tag{117}$$

3.1.2.2. *Functionals.*

Note that functionals such as total energy or potential enstrophy in this discretization are expressed as discrete inner products (or the sum of several inner products). A discrete functional derivative with respect to a particular form produces a result that is the associated dual form. For example, the functional derivative of

$$\mathcal{A} = (A_i, B_i)_{\mathbf{I}} \tag{118}$$

with respect to A_i (where A_i and B_i are primal 2 forms) is

$$\frac{\delta \mathcal{A}}{\delta A_i} = \mathbf{I} B_i \tag{119}$$

which is a dual 0-form.

3.1.2.3. *Discrete Hodge Decomposition.*

As done in [135], all of the wind variables can be decomposed into non-divergent and irrotational parts:

$$u_e = \bar{D}_1 \chi_i - \mathbf{H}^{-1} D_1 \psi_v \tag{120}$$

is the dual 1-form circulation and

$$\mathbf{H} u_e = v_e = \mathbf{H} \bar{D}_1 \chi_i - D_1 \psi_v \tag{121}$$

is the primal 1-form flux. Note that χ_i is a dual 0-form and ψ_v is a primal 0-form (rather than working in terms of 2-forms). This is useful, since many times initial conditions are given in terms of functions (which are 0-forms). It would be trivial to work in terms of 2-forms (by adding $\mathbf{I}$ and $\mathbf{J}$ as needed). Also note that these can be calculated from the divergence primal 2-form and vorticity dual 2-form as

$$\delta_i = D_2 \mathbf{H} u_e = D_2 \mathbf{H} \bar{D}_1 \chi_i \tag{122}$$

$$\zeta_v = \bar{D}_2 u_e = -\bar{D}_2 \mathbf{H}^{-1} D_1 \psi_v \tag{123}$$

A similar decomposition can be made for the other wind variables as

$$u_e^{\perp} = \mathbf{W} v_e = \mathbf{W}\mathbf{H} u_e = \mathbf{H}^{-1} D_1 \chi_v + \bar{D}_1 \psi_i \tag{124}$$

is the dual 1-form flux and

$$v_e^{\perp} = \mathbf{H} u_e^{\perp} = \mathbf{H}\mathbf{W}\mathbf{H} u_e = D_1 \chi_v + \mathbf{H}\bar{D}_1 \psi_i \tag{125}$$

is the primal 1-form circulation. Note that χ_v is a primal 0-form and ψ_i is a dual 0-form. Also note that these can be calculated from the divergence dual 2-form and vorticity primal 2-form as

$$\zeta_i = D_2 v_e^{\perp} = D_2 \mathbf{H} \bar{D}_1 \psi_i \tag{126}$$

$$\delta_v = -\bar{D}_2 u_e^{\perp} = -\bar{D}_2 \mathbf{H}^{-1} D_1 \chi_v \tag{127}$$

One key feature of the discretization above is that

$$\delta_v = \mathbf{R} \delta_i \tag{128}$$

Continuous Wind Analogues. As also done in [135], we can associate each of the wind variables (u_e,v_e,$u_e^{\perp}$ and $v_e^{\perp}$) with line integrals of the continuous wind $\vec{u}$ over primal or dual edges:

$$u_e = \int_{dual} \vec{u} \cdot \hat{m} dl \tag{129}$$

$$v_e = \int_{primal} \vec{u} \cdot \hat{m} dl \tag{130}$$

$$u_e^p erp = \int_{dual} \vec{u} \cdot \hat{s} dl = -\int_{dual} \vec{u}^{\perp} \cdot \hat{m} dl \tag{131}$$

$$v_e^{\perp} = \int_{primal} \vec{u} \cdot \hat{t} dl = -\int_{primal} \vec{u}^{\perp} \cdot \hat{n} dl \tag{132}$$

where $\vec{u}^{\perp} = \hat{k} \times \vec{u}$; and $\hat{m}$ is the unit tangent to the dual edge, $\hat{n}$ is the unit normal to the primal edge, $\hat{s}$ is the unit normal to the dual edge and $\hat{t}$ is the unit tangent to the primal edge (see Appendix B for more details).

Non-Divergent Flow. If $\delta_i = 0$ (and therefore $\chi_i = 0$) then

$$u_e^{\perp} = \bar{D}_1 \mathbf{R}^T \psi_v \tag{133}$$

and therefore

$$\psi_i = \mathbf{R}^T \psi_v \tag{134}$$

Thus, the streamfunction at cell centers is a (convex) interpolation of the streamfunction at vertices.

Choice of Predicted Wind Component. The shallow water equations require u_e, v_e and $u_e^{\perp}$. We choose to predict u_e and reconstruct v_e (through $\mathbf{H}$) and $u_e^{\perp}$ (through $\mathbf{W}$). It would be possible to work in terms of v_e, but this would require $\mathbf{H}^{-1}$ in the nonlinear equations (specifically, in K_i and in the diagnosis of q_v from $\zeta_v = \bar{D}_2 u_e$.). This is an issue, because $\mathbf{H}^{-1}$ is dense for certain grids (such as the non-orthogonal cubed sphere).

3.1.2.4. *Poisson Bracket.*

From this discretization, a discrete Poisson bracket can be constructed as

$$\{\mathcal{A},\mathcal{B}\} = \{\mathcal{A},\mathcal{B}\}_R + \{\mathcal{A},\mathcal{B}\}_Q \tag{135}$$

where

$$\{\mathcal{A},\mathcal{B}\}_R = \sum_i \frac{\delta A}{\delta m_i} D_2 \frac{\delta B}{\delta u_e} + \sum_e \frac{\delta A}{\delta u_e} \bar{D}_1 \frac{\delta B}{\delta m_i} \tag{136}$$

and

$$\{\mathcal{A},\mathcal{B}\}_Q = \sum_e \frac{\delta A}{\delta u_e} \mathbf{Q} \frac{\delta B}{\delta u_e} \tag{137}$$

As in the continuous case, the time evolution of a general functional $\mathcal{A}$ is given by

$$\frac{d\mathcal{A}}{dt} = \{\mathcal{A},\mathcal{H}\} \tag{138}$$

The anti-symmetry of each of these brackets is manifest, using the fact that $D_2^T = -\bar{D}_1$, along with $\mathbf{Q} = -\mathbf{Q}^T$. The choice of $\mathbf{Q}$ is arbitrary, provided it satisfies the conditions discussed below.

3.1.2.5. *Linearized Version (f = const).*

As in continuous case, to get the linearized discrete system about a particular steady state $\vec{x}_0$ (in our case, $\vec{x}_0 = (H, 0)$) we simply need to linearize the psuedo-energy associated with that steady state (this gives the Hamiltonian of the linear system, see Appendix A)

and evaluate $\mathbb{J}$ at $\vec{x}_0$. This yields:

$$\mathbb{J} = \begin{pmatrix} 0 & -D_2 \\ -\bar{D}_1 & \frac{f}{H}\mathbf{W} \end{pmatrix} \tag{139}$$

$$\mathcal{H} = \frac{1}{2}g(m_i + b_i, m_i + bi)_{\mathbf{I}} + \frac{1}{2}H(u_e, u_e)_{\mathbf{H}} \tag{140}$$

$$\frac{\delta \mathcal{H}}{\delta \vec{x}} = \begin{pmatrix} g\mathbf{I}m_i + b_i \\ H\mathbf{H}u_e \end{pmatrix} \tag{141}$$

$$\vec{x} = (m_i, u_e) \tag{142}$$

where we have assumed that $\mathbf{Q}|_{q=q_0} \rightarrow q_0\mathbf{W}$, and $\mathbf{W}$ is defined below (it maps between primal 1-forms and dual 1-forms, and is a discretization of the $\hat{k}\times$ or perp operator). This assumption is in fact a requirement for steady geostrophic modes and PV compatibility. Note that we have also assumed that $F_e \rightarrow Hu_e$ when linearized (this is embedded in the form of the Hamiltonian given above); and that f is a constant. Putting this all together yields:

$$\frac{\partial m_i}{\partial t} + HD_2\mathbf{H}u_e = 0 \tag{143}$$

$$\frac{\partial u_e}{\partial t} + g\bar{D}_1\mathbf{I}(m_i + b_i) - \frac{f}{H}\mathbf{W}\mathbf{H}u_e = 0 \tag{144}$$

for the linear evolution equations.

$\zeta - \delta$ Equivalent Equations. Following the procedure in [19], we can also derive equivalent vorticity-divergence equations for the discrete linearized system. Define $\zeta_v = \bar{D}_2 u_e$ and $\delta_i = D_2 \mathbf{H} u_e$. By taking $D_2\mathbf{H}$ and $\bar{D}_2$ of the linear u_e evolution equation we obtain

$$\frac{\partial \zeta_v}{\partial t} - f\bar{D}_2 \mathbf{W}\mathbf{H} u_e = 0 \tag{145}$$

and

$$\frac{\partial \delta_i}{\partial t} - f D_2 \mathbf{H}\mathbf{W}\mathbf{H} u_e + g D_2 \mathbf{H}\bar{D}_1 \mathbf{I}(m_i + b_i) = 0 \tag{146}$$

Now define $\zeta_i = D_2\mathbf{H}\mathbf{W}\mathbf{H}u_e$ and $\delta_v = \bar{D}_2\mathbf{W}\mathbf{H}u_e$ so that these reduce to

$$\frac{\partial \zeta_v}{\partial t} - f\delta_v = 0 \tag{147}$$

and

$$\frac{\partial \delta_i}{\partial t} - f\zeta_i + g\mathbf{L}(m_i + b_i) = 0 \tag{148}$$

where $\mathbf{L} = D_2\mathbf{H}\bar{D}_1\mathbf{I}$. A key feature of the discretization above is that δ_v is a linear convex combination of δ_i (128). However, in general ζ_i is NOT a linear convex combination of ζ_v, unless the wind is non-divergent. These equations can inverted to obtain the original u_e evolution equation using the discrete Hemholtz decompositions, discrete gradient (D_1 and $\bar{D}_1$) and inverse discrete Laplacian operators. In fact, we can either predict δ_i and ζ_v using the equations above, or predict u_e and diagnose ζ_v and δ_i using $\zeta_v = \bar{D}_2 u_e$ and $\delta_i = D_2\mathbf{H}u_e$; and the results will be the same.

Poisson Bracket. A linearized Poisson bracket can also be constructed. It is identical to the non-linear one, except that

$$\{\mathcal{A},\mathcal{B}\}_Q = \{\mathcal{A},\mathcal{B}\}_W = \frac{f}{H}\sum_e \frac{\delta A}{\delta u_e}\mathbf{W}\frac{\delta B}{\delta u_e} \tag{149}$$

3.1.2.6. *Linearized Version (f = variable).*

The previous analysis can be be repeated for the case of variable f (as for example, occurs on the sphere or the β-plane). The only change occurs in the Coriolis term, which becomes

$$\mathbf{Q} \to \mathbf{Q}|_{q_v=\frac{f}{H}} = \mathbf{Q}_L \neq \frac{f}{H}\mathbf{W} \tag{150}$$

The specific form that this takes depends on the expression for $\mathbf{Q}$. The choice of $\mathbf{Q}$ will influence the propagation behaviour of discrete Rossby waves, but not the discrete inertia-gravity waves.

3.2. Linear Mimetic Properties

3.2.1. Linear Stability.

The conditions for linear stability are almost the same as those for non-linear energy conservation: $\mathbb{J} = \mathbb{J}^T$ (div and grad are adjoints, Coriolis is self-adjoint) and the discrete Hodge stars are symmetric-positive definite (total energy exists and is positive-definite). There is no condition on the compatibility of the mass flux and kinetic energy, since functional derivatives of the linearized Hamiltonian come directly from the Hodge stars (ie the mass flux in the Hamiltonian is Hu_e instead of F_e). Another way of saying this is that the Hamiltonian is now quadratic and does not contain mixed terms that require reconstruction when using a staggered grid.

The conditions on $\mathbb{J}$ are

$$\bar{D_1}^T = -D_2 \tag{151}$$

which is a topological identity enforced by the construction of the incidence matrices (equivalent to the adjointness of divergence and gradient operators in the continuous case); and

$$\mathbf{W}^T = -\mathbf{W} \tag{152}$$

which is just anti-symmetry of the Coriolis operator.

3.2.2. Geostrophic Balance and Vorticity Production.

Consider the general linearized discrete system and let $\zeta_v = \bar{D}_2 u_e$ be the vorticity dual 2-form. Its evolution equation (from above) is

$$\frac{\partial \zeta_v}{\partial t} - f\bar{D}_2\mathbf{W}\mathbf{H}u_e + g\bar{D}_2\bar{D}_1\mathbf{I}h = 0 \tag{153}$$

Vorticity Production. The third term in this equation vanishes since $\bar{D}_2\bar{D}_1 = 0$ (this the discrete analogue of $\vec{\nabla}^T \cdot \vec{\nabla} = 0$, or that curl grad $= 0$). If it did not vanish, then the gradient term would be an unphysical source of vorticity.

Geostrophic Balance/Steady Geostrophic Modes. The second term in this equation should be an approximation to $f\delta$, where δ is the divergence. In particular it should be zero when $D_2\mathbf{H}u_e = 0$. This is enforced by requiring that the divergence seen in the implied vorticity equation is a weighted average of the divergence seen in the mass equation:

$$\mathbf{R}D_2 = -\bar{D}_2\mathbf{W} \tag{154}$$

In fact, this condition (which implies that $\bar{D}_2 \mathbf{W} D_1 = 0$, and $\mathbf{W} D_1 = -\bar{D}_1 \mathbf{R}$) is enough to ensure that ANY non-divergent wind field can be balanced by a corresponding height field, such that the resulting state is steady for the linear equations. Start by assuming that the wind field is non-divergent ($D_2 \mathbf{H} u_e = 0$). Then it is immediately clear that $\frac{\partial m_i}{\partial t} = 0$. From the discrete Helmholtz decomposition, the wind can be written as

$$\mathbf{H} u_e = -D_1 \psi_v \tag{155}$$

In order for $\frac{\partial u_e}{\partial t} = 0$, both the vorticity and the divergence must be steady. The vorticity equation is

$$\frac{\partial \zeta_v}{\partial t} = f \bar{D}_2 \mathbf{W} D_1 \psi_v \tag{156}$$

This is zero if $\bar{D}_2 \mathbf{W} D_1 = 0$. The divergence equation can be written as

$$\frac{\partial \delta}{\partial t} = f D_2 \mathbf{H} \mathbf{W} D_1 \psi_v - g D_2 \mathbf{H} \bar{D}_1 \mathbf{I} m_i \tag{157}$$

which is zero if

$$\mathbf{W} D_1 \psi_v = \frac{g}{f} \bar{D}_1 \mathbf{I} m_i \tag{158}$$

Note that

$$\mathbf{W} D_1 = -\bar{D}_1 \mathbf{R} \tag{159}$$

and therefore if we define

$$m_i = -\frac{f}{g}\mathbf{I}^{-1}\mathbf{R}^T\psi_v \tag{160}$$

this equation is satisfied. Although any given non-divergent wind field can be balanced by some height field, the converse is not necessarily true (see [136] for more discussion of this). Particular choices of $\mathbf{R}$ and the resulting $\mathbf{W}$ are discussed in [140]. Note that the convexity condition on $\mathbf{R}$ ensures that the global integral of both divergences will be the same, and that a unique solution for $\mathbf{W}$ can be found.

3.3. Discrete Conservation

3.3.1. Mass.

Mass is automatically conserved (in local and global form) by the form of the discretization above, for ANY choice of F_e. Similarly a dual grid mass equation can be defined as

$$\frac{\partial m_v}{\partial t} + \mathbf{R}D_2\mathbf{H}C_e = 0 \tag{161}$$

where $m_v = \mathbf{R}m_i$ is a dual 2-form, and $\mathbf{R}$ is a convex interpolation operator that converts from primal 2-forms to dual 2-forms. Since $\mathbf{R}$ is chosen to preserve the global integral of quantities that it operates on, the dual grid mass is also globally conserved. In addition, the relation between $\mathbf{W}$ and $\mathbf{R}$ ensures that the dual grid mass equation can be written an

$$\frac{\partial m_v}{\partial t} + \mathbf{D_2}\mathbf{W}\mathbf{H}C_e = 0 \tag{162}$$

which is in flux form and therefore conserves dual grid mass both locally and globally. Note that we can predict m_v directly, or diagnose it as $\mathbf{R}m_i$ at each timestep, and the result will be the same. In practice, of course, only m_i is predicted.

3.3.2. Total Energy.

Total energy conservation occurs in the same way as in the continuous system: by ensuring that $\mathbb{J}$ is anti-symmetric, and that the Hamiltonian functional derivatives are compatible (basically that the mass flux F_e and kinetic energy K_i both come from a functional derivative of the same Hamiltonian). The first of these conditions is satisfied by requiring that

(1) $\bar{D}_1$ and D_2 are adjoints ($D_2^T = -\bar{D}_1$; this is automatic when using incidence matrices)

(2) $Q = -Q^T$ (this is trickier)

The second of these conditions is satisfied by requiring that

(1) F_e and K_i are compatible (that is, $\frac{\delta \mathcal{H}_{kin}}{\delta m_i} = \mathbf{I}K_i$ and $\frac{\delta \mathcal{H}_{kin}}{\delta u_e} = F_e = \mathbf{H}C_e$ for the same $\mathcal{H}$)

(2) Hodge stars ($\mathbf{I}$,$\mathbf{J}$,$\mathbf{H}$) are symmetric and positive definite

Note that is is enough to specify an $\mathcal{H}$ and simply ensure that $\mathbb{J}$ is anti-symmetric: the system will then conserve energy for ANY choice of $\mathcal{H}$. However, it is often useful to be able to make changes to F_e or K_i independently (to eliminate the Hollingsworth instability, for example). Then energetic consistency can be restored by simply modifying F_e or K_i to ensure compatibility. This is of course equivalent to defining a new Hamiltonian $\mathcal{H}$. It is also possible to relax strict energy conservation by choosing a more accurate definition of F_e or K_i. This might be useful, for example, in cases where accurate advection of mass is more important than energy conservation. The framework is flexible enough to allow this.

3.3.3. Potential Vorticity.

3.3.3.1. *Discrete PV Equation.*

The absolute vorticity equation is given by

$$\frac{\partial \eta_v}{\partial t} - \bar{D}_2 \mathbf{Q}\mathbf{H} C_e = 0 \tag{163}$$

which can be re-written as the mass-weighted potential vorticity equation

$$\frac{\partial m_v q_v}{\partial t} - \bar{D}_2 \mathbf{Q}\mathbf{H} C_e = 0 \tag{164}$$

where $\eta_v = \zeta_v + f = m_v q_v$ is the absolute vorticity dual 2-form, $\zeta_v = D_2 u_e$ is the relative vorticity dual 2-form, q_v is the potential vorticity primal 0-form and $m_v = \mathbf{R} m_i$ is the height dual 2-form.

Compatibility. Compatibility is provided by the form of the discrete mass-weighted PV equation, independent of the choice of $\mathbf{Q}$. That is, the mass-weighted potential vorticity equation is written in terms of a flux divergence.

Consistency. By combining the dual grid mass equation and the mass-weighted potential vorticity equation (with $q_v = c$ a constant), it is easy to see that in order to obtain consistency that $\bar{D}_2 \mathbf{Q}_{q_v=c} = -\mathbf{R} D_2$ must hold. Denote $\mathbf{Q}_{q_v=c} = \mathbf{W}$, as before. Therefore consistency requires that $\bar{D}_2 \mathbf{W} = -\mathbf{R} D_2$. This is sufficient to ensure that an initially uniform q_v field will remain uniform for all time. Interestingly, this is same as the requirement earlier for stationary geostrophic modes.

3.3.4. Potential Enstrophy.

Using the discrete potential vorticity q_v defined earlier, discrete potential enstrophy can be defined as

$$\mathcal{Z}_C = \frac{1}{2}(\zeta_v, q_v)_{\mathbf{J}} \tag{165}$$

Taking functional derivatives of this yields

$$\frac{\delta \mathcal{Z}_{\mathcal{C}}}{\delta \vec{x}} = \begin{pmatrix} -\mathbf{R}^T \frac{q_v^2}{2} \\ \bar{D_2}^T q_v \end{pmatrix} = \begin{pmatrix} -\mathbf{R}^T \frac{q_v^2}{2} \\ D_1 q_v \end{pmatrix} \tag{166}$$

Combining this with the general discrete $\mathbb{J}$ gives

$$D_2 D_1 q_v = 0 \tag{167}$$

and

$$-\bar{D_1}\mathbf{R}^T \frac{q_v^2}{2} + \mathbf{Q} D_1 q_v = 0 \tag{168}$$

The first equation is satisfied INDEPENDENT of the choice for $\mathbf{R}$, it is purely topological. The second equation is more complicated, and requires a careful choice for $\mathbf{Q}$ for a given $\mathbf{R}$. Using the relation $\mathbf{R}D_2 = -\bar{D_2}\mathbf{W}$ along with $\mathbf{W} = -\mathbf{W}^T$, the second equation can be re-written as

$$\mathbf{W} D_1 \frac{q_v^2}{2} + \mathbf{Q} D_1 q_v = 0 \tag{169}$$

Using this form, it is easy to show that $\mathbf{Q} = q_e \mathbf{W}$ conserves potential enstrophy when q_e is the well-known arithmetic mean between values across an edge. However, this form is not

energy conservative. Deriving a form for $\mathbf{Q}$ that is both total energy and potential enstrophy conserving is much trickier, and has only been done for logically square orthogonal grids (for which $\mathbf{R} = \frac{1}{4}$; see [4],[129],[115]). A solution method for variable $\mathbf{R}$ is given below.

3.4. Summary of Required Operator Properties

The preceding discussion outlined the requirements on the various operators in order to obtain desirable linear and nonlinear properties. These requirements are now summarized.

3.4.1. Incidence Matrices.

Using the discrete exterior calculus framework (incidence matrices) gives the following four properties automatically for ANY grid:

(1) $D_2 D_1 = 0$ (divergence of skew-gradient is zero)

(2) $\bar{D}_2 \bar{D}_1 = 0$ (curl of gradient is zero)

(3) $D_2 = -\bar{D}_1^{\,T}$ (divergence and gradient are adjoints)

(4) $D_1^T = \bar{D}_2$ (curl and skew-gradient are adjoints)

These properties ensure that a scheme does not have any spurious vorticity production, and also that the linear pressure gradient terms conserve energy. They are also useful for both total energy and potential enstrophy conservation. In addition, the flux-form formulation of D_1 and D_2 ensure PV compatibility along with local and global conservation of mass and dual mass.

3.4.2. Hodge Stars- $\mathbf{I}$, $\mathbf{J}$ and $\mathbf{H}$.

In order to obtain linear stability and total energy conservation (and more generally, to ensure that discrete inner products exist and are positive definite), the discrete Hodge stars $\mathbf{I}$, $\mathbf{J}$ and $\mathbf{H}$ must be symmetric positive definite.

3.4.3. $\mathbf{R}$ AND $\mathbf{W}$.

In order obtain steady geostrophic modes on an f-plane (along with a flux-form dual mass equation, PV consistency AND linear PV conservation), then $\bar{D}_2\mathbf{W} = -\mathbf{R}D_2$. In order for the Coriolis force to be linearly energy conserving, $\mathbf{W} = -\mathbf{W}^T$. Since $\mathbf{R}$ is a convex interpolation function, there exists a unique solution for $\mathbf{W}$.

3.4.4. $\mathbf{Q}$.

There are three desirable properties that $\mathbf{Q}$ should posses:

(1) $\mathbf{Q} = -\mathbf{Q}^T$ (gives total energy conservation)

(2) $\mathbf{Q}|_{q_v=c} \rightarrow c\mathbf{W}$ (for various linear properties to hold, along with PV consistency)

(3) $-\bar{D}_1\mathbf{R}^T\frac{q_v^2}{2} + \mathbf{Q}D_1 q_v = 0 \forall q_v$ (gives potential enstrophy conservation)

Versions of $\mathbf{Q}$ that posses either properties 1 and 2 OR 2 and 3 for general non-orthogonal polygonal grids have been previously developed. However, thus far, a $\mathbf{Q}$ that posses all three of these properties has only been developed for orthogonal, logically square grids where $\mathbf{R} = \frac{1}{4}$. Note that this representation of potential enstrophy conservation shows that the stumbling block is variable $\mathbf{R}$, and not the orthogonality of the grid (which is encoded in $\mathbf{H}$). A generalization of $\mathbf{Q}$ for the case of variable $\mathbf{R}$ is discussed below.

3.4.5. F_e AND K_i.

In order for there to be total energy conservation, F_e and K_i must be compatible in the sense that

$$F_e = \mathbf{H}C_e = \frac{\delta \mathcal{H}_{kin}}{\delta u_e} \tag{170}$$

and

$$\mathbf{I}K_i = \frac{\delta \mathcal{H}_{kin}}{\delta h_i} \tag{171}$$

for the SAME $\mathcal{H}_{kin} = \frac{1}{2}(C_e, u_e)_{\mathbf{H}}$. Additional discussion of this compatibility and an example for a specific choice of $\mathcal{H}$ can be found in [135].

TABLE 3.2. Summary of required operator properties

Operator	**Properties**	**Notes**	**Mapping**
$\mathbf{I}$	SPD	Hodge Star	p2 ->d0
$\mathbf{J}$	SPD	Hodge star	d2 ->p0
$\mathbf{H}$	SPD	Hodge star	d1 ->p1
$\mathbf{W}$	$\mathbf{R}D_2 = \bar{D}_2\mathbf{W}$	Interior product (contraction)	p1 ->d1
$\mathbf{R}$	$\mathbf{W} = -\mathbf{W}^T$	Identity operator	p2 ->d2
$\mathbf{Q}$	$\mathbf{Q} = -\mathbf{Q}^T$ $\mathbf{Q} \to q_0\mathbf{Q}$ when $q_v = q_0$ is constant $-\bar{D}_1\mathbf{R}^T\frac{q_v^2}{2} + \mathbf{Q}D_1 q_v = 0 \quad \forall q_v$	Interior product (contraction)	p1 ->d1

Importance of Various Properties. It is generally agreed that the mimetic properties (linear stability, steady geostrophic modes on an f-plane, no spurious vorticity production from the gradient term); mass and potential vorticity conservation; and PV compatibility/consistency plus a consistent dual mass equation are the most important characteristics of for a numerical scheme to posses. These are encapsulated by the requirements 3.4.1-3.4.3 along with $\mathbf{Q}|_{q_v=c} \to c\mathbf{W}$. There is less consensus on the importance of total energy and potential enstrophy conservation, and within this framework a choice must be made between accurate mass and PV advection; and conservation. Some choices made in existing schemes that fall under this framework are discussed below.

3.5. Specific Schemes

The determination of a specific scheme requires choices for the Hodge star operators (**I**, **J** and **H**), nonlinear Coriolis operator **Q**, interpolation operator **R** (which will determine **W**), mass flux F_e and the kinetic energy K_i. There are many possible choices for these operators that satisfy the properties discussed above.

Common Operators. All of the scheme discussed below make some common choices:

(1) $\mathbf{I} = \frac{1}{A_i}$

(2) $\mathbf{J} = \frac{1}{A_v}$

(3) $\mathbf{R} = \sum_{i \in CV(v)} \frac{A_{iv}}{A_i}$

(4) $\mathbf{W}$ defined from $\mathbf{R}$ using $\bar{D}_2 \mathbf{W} = -\mathbf{R} D_2$

The first two are the diagonal Voronoi (circumcentric) Hodge stars, the third one is an interpolation operator (1st order for general grids, 2nd order for (SCVT grids?), and the fourth is an analogue of the contraction operator (converts primal 1-form fluxes to dual 1-form fluxes). Although **R** and **W** are 2nd order on uniform planar grids, **W** is 0th order on quasi-uniform grids. As discussed in [137], there are O(1) errors that occur in **W** along the lines joining pentagons on the geodesic grid, and along the panel edges on the cubed sphere grid.

In general, provided **H** is symmetric positive-definite and $\mathbf{Q} \to c\mathbf{W}$ when $q_v = c$ is constant), the schemes below posses all of the linear mimetic properties (linear stability, steady geostrophic modes on an f-plane, no spurious vorticity production from the gradient term), mass and potential vorticity conservation; and PV compatibility/consistency plus a consistent dual mass equation (with the exception of the non-symmetric **H** version of Weller 2014, see below). They differ in their ability to handle different types of meshes (Voronoi, general orthogonal non-voronoi, non-orthogonal polygonal, etc.) and their treatment of the

non-linear aspects such as $\mathbf{Q}$, F_e and K_i, which influence their ability to obtain total energy and potential enstrophy conservation.

3.5.1. TRiSK 2010/Thuburn 2012.

For TRiSK 2010 ([102]), the following choices are made:

(1) $\mathbf{H} = \frac{l_e}{d_e}$

(2) $F_e = m_e u_e$ and $K_i = \sum_{e \in EC(i)} \frac{u_e^2}{4}$; with $m_e = \frac{1}{2} \sum_{i \in CE(e)} m_i$

(3) $\mathbf{Q} = \frac{1}{2}\mathbf{Q_e W} + \frac{1}{2}\mathbf{W Q_e}$ OR $\mathbf{Q} = \mathbf{Q_e W}$

This scheme works only for an orthogonal grid. Note that A_e is defined as $A_e = \frac{lede}{2}$ in order to ensure energy conservation. The first choice for $\mathbf{Q}$ gives an energy-conserving scheme, while the second choice gives a potential enstrophy conserving scheme. $\mathbf{Q_e}$ is a diagonal operator on edges. In the total energy conserving scheme, it is arbitrary. Various choices have been explored, including simple linear averaging and anticipated potential vorticity. In the potential enstrophy conserving scheme, it must be midpoint averaging: $\mathbf{Q}_e = \frac{1}{2} \sum_{v \in VE(e)} q_v$.

3.5.2. Weller 2012.

For the Weller 2012 ([155]) scheme, the following choices are made:

(1) $\mathbf{H} = \frac{l_e}{d_e}$

(2) $F_e = m_e u_e$ and $K_i = \sum_{e \in EC(i)} A_{ie} u_e^2$; with $m_e = \frac{A_{ie} h_i + A_{je} h_j}{A_e}$

(3) $\mathbf{Q} = \frac{1}{2}\mathbf{Q_e W} + \frac{1}{2}\mathbf{W Q_e}$ OR $\mathbf{Q} = \mathbf{Q_e W}$

This scheme works only for an orthogonal grid. These are essentially the same choices as made in TRiSK 2010, but with slightly different definitions for mass flux and kinetic energy. The scheme actually reduces to TRiSK 2010 on a Voronoi grid, but it more accurate for non-Voronoi grids. Note that spherical geometry is used for area calculations (which requires the grid to be Pitteway, see Appendix B for more information). Also note that $de = \frac{2A_e}{le}$, instead

of defining A_e through le and de. For the total energy conserving variant, $\mathbf{Q}_e$ is defined using either APVM or CLUST.

3.5.3. Weller 2014.

The Weller 2014 ([154]) scheme is identical to the Weller 2012 scheme (using the energy conserving version of $\mathbf{Q}$) except for the following:

(1) m_e is calculated using CLUST or some other advection scheme. Note that without corresponding changes in the calculation of kinetic energy, this breaks total energy conservation. However, since $\mathbf{Q} = -\mathbf{Q}^T$, the nonlinear Coriolis term still conserves energy.

(2) q_e is calculated using CLUST or some other advection scheme. This helps smooth PV advection (and deal with the spurious Rossby wave modes on hexagonal or geodesic grids).

(3) $\mathbf{H}$ is either the Thuburn 2014 symmetric $\mathbf{H}$ ([137]) or a non-symmetric $\mathbf{H}$ discussed in ([154]) (this $\mathbf{H}$ becomes diagonal as grid becomes orthogonal).

This scheme works for both orthogonal and non-orthogonal grids. It does not conserve total energy (unless the kinetic energy calculation is changed to be compatible with the definition of m_e AND the symmetric $\mathbf{H}$ is used) or potential enstrophy. If the symmetric $\mathbf{H}$ is used, it has all of the desirable linear mimetic properties. If the non-symmetric $\mathbf{H}$ is used, it no longer has linear stability. However, the eigenvalues of the resulting linearized scheme are very similar to the eigenvalues of the symmetric $\mathbf{H}$ linearized scheme. It is possible here that the resulting instability is very weak, and therefore the scheme is stable in practical situations (especially if any dissipation is added). This would be similar to the situation with the 2nd order Adams-Bashford time stepping scheme, which has a weak linear instability but is usable in practice.

3.5.4. Thuburn 2014.

The Thuburn 2014 ([137]) scheme uses the following definitions:

(1) F_e comes from $\mathbf{H}u_e$ and m_i using the primal grid advection scheme

(2) $C_e^{\perp} = \mathbf{W}F_e$ and $\mathbf{J}^{-1}q_v$ are used to define $\mathbf{Q_e^{\perp}} = \mathbf{Q}F_e$ using the dual grid advection scheme

(3) K_i defined either via the TRISK 2010 approach (which is only 1st order on Voronoi meshes, 0th order on CS meshes) or as $K_i = \frac{|\vec{u}_i|^2}{2}A_i$, where $\vec{u}_i$ is a constant vector for each cell constructed to give a least-square best fit to the u_e's at the edges of that cell.

(4) $\mathbf{H}$ is constructed to be symmetric positive definite, but does not become diagonal as the grid becomes orthogonal.

This scheme works for both orthogonal and non-orthogonal grids. It provides a high degree of flexibility in advection schemes for both m_i and q_v; and posses all of the desirable mimetic properties. However, it does not conserve total energy or potential enstrophy.

3.5.5. Arakawa and Lamb 1981.

Although it was not recognized at the time (since the generalized framework was not developed until 30 years later), the Arakawa and Lamb 1981 energy and potential enstrophy conserving scheme (which works only for logically square orthogonal meshes) is a member of the above general discretization family. By making the same choices as TRiSK 2010/2012, with the exception of a different $\mathbf{Q}$, one obtains both the square grid and logically square orthogonal versions of AL1981. Note that one must also choose particular values for the orientation of grid elements that define D_1,D_2 (although they are the logical ones for a square grid).

3.5.6. Arakawa and Lamb 1981 Extension (AL81-E).

The schemes above are interesting, but they do not represent a full extension of AL81 to arbitrary grids (primarily due to a lack of double conservation properties). What follows reproduces all the desirable features of AL81 on arbitrary polygonal grids (except for extra branches of the dispersion relationship on non-quadrilateral grids, which are unavoidable with C grid schemes). The following definitions are used for kinetic energy and mass flux:

$$K_i = \phi^T \frac{u_e^T \mathbf{H} u_e}{2} \tag{172}$$

$$m_e = \phi \mathbf{I} m_i \tag{173}$$

$$C_e = m_e u_e \tag{174}$$

where $\phi = \sum_{i \in CE(e)} \frac{A_{ie}}{A_e}$, and A_{ie} and A_e are spherical triangular areas, and other geometric quantities are similarly defined. Note that these reduce to the original AL81 scheme on logically square, orthogonal meshes. All of the Hodge star operators are the circumcentric Voronoi ones discussed above, except the $\mathbf{H}$ operator on cubed sphere grids which follows Thuburn 2014. Three different variants of $\mathbf{Q}$ are chosen: one that conserves just total energy, one that conserves just potential enstrophy and one that conserves both. They are given as

$$\mathbf{Q} = Q_e \mathbf{W} \tag{175}$$

for the version that conserves only potential enstrophy, and

$$\mathbf{Q} = \frac{1}{2} Q_e \mathbf{W} + \frac{1}{2} \mathbf{W} Q_e \tag{176}$$

for the version that conserves only total energy, where Q_e is the arithmetic mean of q_v across dual edge. Note that both of these also satisfy

$$\mathbf{Q} \rightarrow c_0 \mathbf{W} \tag{177}$$

when $q_v = c_0$ is a constant. The version that conserves both total energy and potential enstrophy is discussed below.

3.6. Doubly Conservative Version of $\mathbf{Q}$

The only remaining piece of the puzzle is the generalization of $\mathbf{Q}$ to arbitrary grids. $\mathbf{Q}$ must be generalized because the derivation given in AL81 works only for the case of $\mathbf{R} = \frac{1}{4}$, which is valid for logically square orthogonal grids but not more general ones. AL1981 achieves its desirable properties (total energy and potential enstrophy conservation, mimeticity, etc.) by requiring that $\mathbf{Q}$ satisfies:

(1) Total Energy Conservation: $\mathbf{Q} = -\mathbf{Q}^T$

(2) PV Consistency: $\mathbf{Q}_{q=q_0} \rightarrow q_0 \mathbf{W}$

(3) Potential Enstrophy Conservation $-\bar{D_1}\mathbf{R}^T \frac{q_v^2}{2} + \mathbf{Q} D_1 q_v = 0$

General Form. Start from the Salmon 2005 ([116]) definition of $\mathbf{Q}$ via a discrete Poisson bracket as

$$\{\mathcal{A}, \mathcal{B}\}_Q = \sum_i \sum_{(e,e') \in EP(i)} \sum_{v \in VC(i)} q_v \alpha_{e,e',v} \frac{\partial(\mathcal{A}, \mathcal{B})}{\partial(u_e, u_{e'})} \tag{178}$$

where $\alpha_{e,e',v} = \alpha_{e',e,v}$. The coefficients will be determined in a manner that ensures that the three desirable properties from above hold. A diagram of this operator is shown in Figure 3.6.

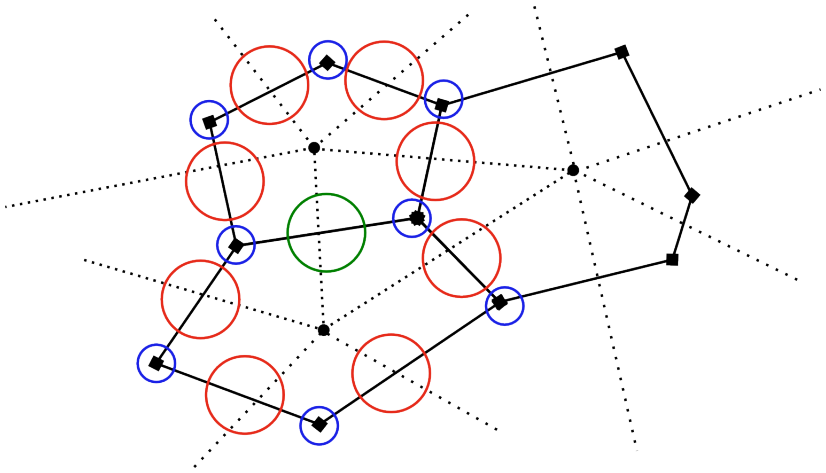

FIGURE 3.6. Diagram of doubly conservative $\mathbf{Q}$ operator. For a given edge (denoted by the green circle), the potential vorticity flux is a weighted sum of the mass flux at each red circled edge, where the weights are a linear combination of the potential vorticity at each blue circled vertex.

Energy Conservation. This form is automatically energy conserving due to anti-symmetry of the $\frac{\delta(,)}{\delta(,)}$ operator, INDEPENDENT of the choices of $\alpha_{e,e',v}$.

PV Consistency. Ensuring PV consistency simply means that

$$\{\mathcal{A},\mathcal{B}\}_Q \to q_0\{\mathcal{A},\mathcal{B}\}_W \tag{179}$$

when $q_v = q_0 =$ constant. This is equivalent to requiring that

$$\sum_{v\in VC(i)} \alpha_{e,e',v} = w_{e,e'} \tag{180}$$

for every edge pair.

Potential Enstrophy Conservation. Start by noting that potential enstrophy conservation implies that $\{\mathcal{F},\mathcal{Z}\} = 0$ for ANY functional $\mathcal{F}$. By the chain rule, it will suffice to show this for $\mathcal{F} = u_e$ and $\mathcal{F} = m_i$. In fact, the condition that comes from m_i reduces to $D_2D_1 = 0$ (as

discussed in section 3.3.4) and will not be discussed further. So letting $\mathcal{F} = u_e$ we have

$$\{u_e, \mathcal{Z}\} = \{u_e, \mathcal{Z}\}_Q + \{u_e, \mathcal{Z}\}_R = 0 \tag{181}$$

where

$$\{u_e, \mathcal{Z}\}_Q = \mathbf{Q} D_1 q_v \tag{182}$$

$$\{u_e, \mathcal{Z}\}_R = -\bar{D}_1 \mathbf{R}^T \frac{q_v^2}{2} \tag{183}$$

using $\frac{\delta \mathcal{Z}}{\delta u_e} = D_1 q_v$ and $\frac{\delta \mathcal{Z}}{\delta m_i} = -\mathbf{R}^T \frac{q_v^2}{2}$. In particular, this must hold at each edge (for each u_e). This yields

$$\sum_{e' \in ECP(e)} \left(\sum_{v \in EVC(e,e')} \alpha_{e,e',v} q_v \right) \sum_{v' \in VE(e')} t_{e',v'} q'_v = \sum_{i \in CE(e)} (-n_{e,i}) \sum_{v \in VC(i)} R_{i,v} \frac{q_v^2}{2} \tag{184}$$

for every e. Both the left and right hand side of these equations are quadratic polynomials in $\{v \in CVE(e)\}$ where $CVE(e) = VE(i1) \cup VE(i2)$ and $(i1, i2) = CE(e)$. The coefficients in these polynomial are linear combinations of the α's. Since these equations must hold for arbitrary q_v, each coefficient in the polynomial for the LHS must be equal to the corresponding coefficient for the RHS polynomial. This gives a large matrix system

$$\mathbf{A} \vec{\alpha} = \vec{b} \tag{185}$$

where each row in $\mathbf{A}$ and corresponding entry in $\vec{b}$ are ONE of the coefficients in the LHS/RHS polynomials; and $\vec{\alpha}$ is the vector of unknown coefficients. This system can be solved (via a least-squares approach) to yield a set of coefficients $\vec{\alpha}$ such that $\mathbf{Q}$ conserves potential

enstrophy. This procedure is essentially identical to the one employed in Salmon 2005. Specifically, for each grid cell i, we have

$$A_{v,v} = \sum_{e' \in EVE(v,e,i)} \alpha_{e,e',v} t_{e',v} sgn(e,e') \tag{186}$$

$$B_{v,v} = \sum_i n_{e,i} \frac{R_{i,v}}{2} = \frac{R_{i,v}}{2} \tag{187}$$

where the sum occurs only when $v \in VE(e)$;

$$A_{v,v'} = \sum_{e' \in EVE(v',e,i)} \alpha_{e,e',v} t_{e',v'} sgn(e,e') + \sum_{e' \in EVE(v,e,i)} \alpha_{e,e',v'} t_{e',v} sgn(e,e') \tag{188}$$

$$B_{v,v'} = 0 \tag{189}$$

where e loops over each edge in i and (v, v') is the set of vertex pairs in $VC(i)xVC(i)$; and $EVE(v,e,i) = EC(i) \cap EV(v) - e$. Note that $sgn(e,e') = 1 = -sgn(e',e)$, which ensures that the scheme is energy conservative. Also note that coefficients in one cell are coupled with adjacent cells when $v \in VE(e)$ or $v' \in VE(e)$.

Number of Equations. For each edge e, there are $\frac{n_v 1(n_v 1-1)}{2} + \frac{n_v 2(n_v 2-1)}{2} - 3$ equations, where $n_v 1$ is the number of vertices for cell $i1$ and $n_v 2$ is the number of vertices for cell $i2$, and $(i1, i2) = CE(e)$.

Number of Unknowns. For each cell i, there are $\frac{n_e(n_e-1)}{2} * n_v$ coefficients, where n_e is the number of edges for cell i and n_v is the number of vertices for cell i.

In practice, although there can be more equations than unknowns, the resulting system in underdetermined since the equations are not all linearly independent. This results in

there being a large number of free parameters. This freedom is dealt with in different ways, depending on the grid (see below).

3.7. Results for Doubly Conservative **Q**

3.7.1. Uniform Grids.

On a uniform grid, the simplest possible schemes are homogeneous: they are the same for each cell i. This means that the coefficients are the same for every cell i, which greatly reduces the number of unknowns. In addition, it makes sense for a scheme to be symmetric with respect to the underlying symmetries of the grid. This means, for example that a uniform square grid scheme is symmetric with respect to 90 degree rotations, and that a hexagonal grid scheme in symmetric with respect to 120 degree rotations. Note that these symmetry properties are NOT required for potential enstrophy conservation (or the other desirable properties of $\mathbf{Q}$), but they help reduce the number of free parameters. They are added on as additional equations in the matrix-vector system that is solved.

3.7.2. Uniform Square Grid.

As expected, the solution procedure reproduces the AL81 scheme, including its one free parameter. This can be set as in AL81.

3.7.3. Uniform Hexagonal Grid.

The same procedure can be applied to the uniform hexagonal grid (with 120 degree symmetry instead of 90 degree symmetry), and it yields a scheme with 8 free parameters. These free parameters could be optimized to improve the dispersion relation for Rossby waves, or for other purposes. However, instead they are allowed to take arbitrary values dictated by the least-squares solver. Much effort was devoted to finding analytic values for the parameters that could inspire a general analytic solution, but this was not found.

3.7.4. PV Compatibility.

The astute reader will note that nothing has been said yet about enforcing PV compatibility: $\mathbf{Q}_L = \mathbf{W}$. It was originally believed that PV compatibility would have to added as additional equations in the matrix-vector system. However, it was found that $\mathbf{Q}$ was PV compatible when ONLY potential enstrophy conservation is enforced (without symmetry even). This corresponds with the results of Salmon 2004 ([115]), who did not explicitly add PV compatibility, yet ALL of his schemes had this property.

3.7.5. Quasi-Uniform Spherical Grids.

On a quasi-uniform grid, the scheme is no longer homogenous; and the coupling between coefficients in each grid cell becomes strongly undesirable due to computational concerns. On realistic grids, the sparse linear least squares problem can be O(100 million) coefficients, and is ill-conditioned. Following [140], the coefficients can be uncoupled by defining

$$B_{v,v} = (\frac{R_{i,v}}{2} - C)n_{e,i} \tag{190}$$

$$B_{v,v'} = Cn_{e,i} \tag{191}$$

when $v \in VE(e)$ or $v' \in VE(e)$, where $C = -1/6$. On all meshes tested (including uniform square and uniform grid) there are enough degrees of freedom to do this, and the least-squares problem has a unique, exact solution.

3.8. Other Desirable Properties

In addition to mimetic properties and conservation properties, it is desirable that a discretization scheme posses other useful properties.

3.8.1. Linear Modes.

A detailed study of the linear modes for this generalized C grid scheme on both planar and quasi-uniform spherical grids is provided in Chapter 6. Some results are summarized below.

Absence of Computational Modes. The discrete framework discussed above does not posses any spurious stationary modes; at least on the grids investigated. On certain grids (such as planar hexagonal or hexagonal icosahedral), it has spurious linear wave branches ([44]). On a hexagonal grid, the spurious branch will be low frequency Rossby waves, which can be controlled through the use of proper choices in potential vorticity advection (see [153]). However, on the triangular grid, there are two spurious branches of inertia-gravity waves which are much harder to control. For this reason, it is advisable to use either square or hexagonal based grids; and not triangular ones.

Good Wave Representation. The dispersion relation of the discretization above is determined by a combination of the discrete gradient and discrete Coriolis operators. For all of the operator and grid combinations studied, the discrete dispersion relation exhibited some of the same essential characteristics as the continuous one: monotonic increase of frequency with wavenumber and a positive-definite group velocity. The isotropy of the resulting dispersion relationship is a function of grid (as expected), with the hexagonal grid being the most isotropic. The well-resolved Rossby radius grid dispersion relationship did show artificial reductions in phase speed for higher-frequency waves, but this is an expected feature for a finite-difference scheme. However, the dispersion relations all had a strong dependence on Rossby radius (specifically, the ratio of the Rossby radius to the grid spacing). When the Rossby radius was poorly resolved, the schemes exhibited pathological behaviour: the

group velocity had the wrong sign and the dispersion relation decreased monotonically with increasing wavenumber. This is a disadvantage of staggered grid schemes.

3.8.2. Grid Flexibility.

The general discretization scheme introduced above works on practically all quasi-uniform spherical meshes under consideration (including both orthogonal and non-orthogonal geodesic grids and cubed sphere grids), primarily through the choice of discrete Hodge star operators (specifically, the **H** operator).

3.8.3. Order of Accuracy.

As shown in [96], using the type of schemes chosen above (nearest-neighbour finite volume/difference) it is not possible to achieve higher than first-order accuracy on the type of grids chosen (spherical polygons with geodesics for edges). Even this requires careful grid optimization, and for the given operator choices has only been achieved on hexagonal-icosahedral grids using the tweaking optimziation from [59]. In addition, the **W** operator (and therefore all the given variants of the **Q** operator) is inconsistent on general grids.

3.9. Chapter Summary

The general discretization scheme presented above is an extension of the TRiSK scheme (in particular, the approach presented in [135]). The scheme from [135] is shown to be a quasi-Hamiltonian scheme, and the connections between the Hamiltonian approach and the DEC approach are made explicit. In addition to clarifying and unifying existing work, two major new contributions are made: conditions on the **Q** operator to obtain total energy conservation, potential enstrophy conservation and PV consistency; and the development of a version of the **Q** operator with these properties for variable **R**. This completes the extension of AL81 to arbitrary, non-orthogonal polygonal grids started by the TRiSK team.

A detailed study of the linear and non-linear properties of the resulting scheme is performed in Chapters 5 and 6.

CHAPTER 4

Generalized Z Grid Scheme

4.1. General Nonlinear Formulation

As shown in section 2.1, the rotating shallow water equations can be expressed in terms of both exterior calculus and Hamiltonian mechanics. These are more natural frameworks than vector calculus, since they generalize to arbitrary manifolds. In addition, the Hamiltonian framework is very useful for looking at conserved quantities. Therefore, presented below is a generalized discrete framework based on the vorticity-divergence formulation and the Hamiltonian approach. It is inspired (and draws heavily) from the work of Rick Salmon ([117]).

This framework is not based on discrete exterior calculus (since we are dealing with all collocated quantities, this makes sense). A DEC based vorticity-divergence framework would place vorticity staggered from height/divergence, which would then suffer from similar computational mode problems as the generalized C grid. A major motivation for using the Z grid framework is the elimination of computational modes. Since DEC is used mostly to obtain desirable linear mimetic properties, and those properties are automatically enforced in the vorticity-divergence framework due to form, it does not seem necessary to incorporate the full mechanics of DEC. Instead, the framework is based purely on the Hamiltonian approach, which lends itself naturally to conservation properties. In fact, it is believed (but not proven) that this framework is a mass-lumped version of P_1 finite elements (which are an example of finite element exterior calculus for the equations under consideration). However, it is written in terms of incidence matrices on the primal and dual meshes (D_2, $\bar{D}_1$ and D_1)

and also uses the same geometric quantities (A_i, le, de, $n_{e,i}$ and $t_{e,v}$) as the DEC scheme in Chapter 3.

There are three discrete objects that must be defined: the discrete variable set $\vec{x}$, a discrete Hamiltonian $\mathcal{H}$ and a discrete symplectic operator (or equivalently, a discrete Poisson bracket) $\mathbb{J}$. The scheme is designed to work on orthogonal grids. Most of the motivation for using non-orthogonal grids (specifically, the cubed-sphere grid) stems from a desire to avoid computational modes associated with a mismatch of degrees of freedom, which are not an issue on the Z grid. Since the icosahedral grid has is more uniform and has better operator convergence, the inability to use the cubed-sphere grid does not seem to be a serious issue.

This discretization draws heavily from the work of Rick Salmon (Salmon 2007, [117]) and the discretization below collapses to his for specific choices of grids (such as orthogonal planar polygonal with a triangular dual or the perfect planar square grid). However, this framework extends his results to icosahedral hexagonal-pentagonal grids. It is important to note that the desirable properties of the scheme (mimetic, conservation, etc.) are entirely contained in the discrete symplectic operator $\mathbb{J}$ and are independent of the choice of Hamiltonian $\mathcal{H}$.

4.1.1. Discrete Variable Set.

The discrete prognostic variable set is given by

$$\vec{x} = (h_i, \zeta_i, \delta_i) \tag{192}$$

Note that the height h_i, divergence δ_i and vorticity ζ_i are all co-located at the same points. In addition to these prognostic variables, four diagnostic variables (Φ_i, χ_i, ψ_i and q_i) are also used. These variables are defined below, and their staggering on the grid is shown in Figure 4.1.

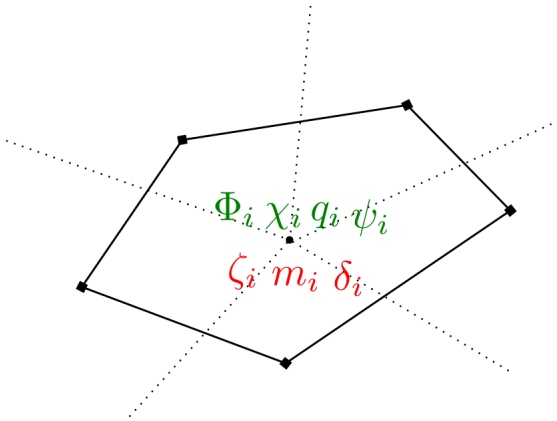

FIGURE 4.1. Discrete variables and staggering for the generalized Z grid scheme

4.1.2. FUNCTIONAL DERIVATIVES.

The functional derivative of a general functional $\mathcal{F}$ is defined as

$$\frac{\delta \mathcal{F}}{\delta x_i} = \mathcal{F}_{x_i} = \frac{1}{A_i}\frac{\partial \mathcal{F}}{\partial x_i} \tag{193}$$

The diagnostic variables (Φ_i, χ_i, ψ_i and q_i) are defined through the functional derivatives of the discrete Hamiltonian $\mathcal{H}$ and discrete Potential Enstrophy $\mathcal{Z}$ as

$$\frac{\delta \mathcal{H}}{\delta h_i} = \Phi_i \tag{194}$$

$$\frac{\delta \mathcal{H}}{\delta \zeta_i} = -\psi_i \tag{195}$$

$$\frac{\delta \mathcal{H}}{\delta \delta_i} = -\chi_i \tag{196}$$

$$\frac{\delta \mathcal{Z}}{\delta h_i} = -\frac{1}{2}q_i^2 \tag{197}$$

$$\frac{\delta \mathcal{Z}}{\delta \zeta_i} = q_i = h_i \eta_i = h_i(\zeta_i + f_i) \tag{198}$$

$$\frac{\delta \mathcal{Z}}{\delta \delta_i} = 0 \tag{199}$$

where the discrete Potential enstrophy is defined as

$$\mathcal{Z} = \frac{1}{2} \sum_{cells} A_i h_i q_i^2 = \frac{1}{2} \sum_{cells} A_i \frac{\eta_i^2}{h_i} \tag{200}$$

4.1.3. Discrete Poisson/Nambu Brackets.

Following Salmon 2007, the general discretization starts from the Nambu brackets for the shallow water equations in vorticity-divergence form. As long as these brackets retain their triply anti-symmetric structure when discretized, total energy and potential enstrophy will be automatically conserved for any definition of the total energy and potential enstrophy (with one caveat explained below). In addition, the bracket structure ensures that this conservation is local as well as global. That is, the evolution of a conserved quantity can be written in flux-form for each grid cell, where cancellation of fluxes between adjacent cells leads to the global integral being invariant. This is in contrast to a method that conserves the global integral, but cannot be written in flux-form for each grid cell. Finite-element methods are examples of methods for which this is true. The existence of local flux-form conservation is a useful feature of discretization using Nambu brackets. In what follows below, we will consider only the case where $\mathcal{Z}$ is the potential enstrophy, although this approach could be easily generalized to arbitrary Casimirs (see [116] for an example of this on a uniform square grid).

Jacobian Brackets. Start by defining a "Jacobian" along edges as

$$J_\zeta(A,B) = n_{e,2}\frac{\delta A}{\delta\zeta_2}\frac{\delta B}{\delta\zeta_1} + n_{e,1}\frac{\delta A}{\delta\zeta_1}\frac{\delta B}{\delta\zeta_2} \tag{201}$$

where ζ_1, ζ_2 are the values at either side of an edge. Then the $\{\mathcal{F},\mathcal{H},\mathcal{Z}\}_{\zeta\zeta\zeta}$ bracket can be discretized as

$$\{\mathcal{F},\mathcal{H},\mathcal{Z}\}_{\zeta\zeta\zeta} = \frac{1}{3}\sum_{edges}\frac{1}{2}(D_1\mathbf{R}\mathcal{Z}_\zeta)J_\zeta(F,H) + \text{cyc}(\mathcal{F},\mathcal{H},\mathcal{Z}) \tag{202}$$

where $\mathbf{R} = \sum_{i\in CV(v)} C$ maps from cells to vertices, and C is a constant that depends on the grid. Note that this bracket is triply anti-symmetric, as required. The $\{\mathcal{F},\mathcal{H},\mathcal{Z}\}_{\delta\delta\zeta}$ bracket can be similarly discretized as

$$\{\mathcal{F},\mathcal{H},\mathcal{Z}\}_{\delta\delta\zeta} = \sum_{edges}\frac{1}{2}(D_1\mathbf{R}\mathcal{Z}_\zeta)J_\delta(F,H) \tag{203}$$

using the same $\mathbf{R}$ operator. This bracket is only doubly-antisymmetric, but it will conserve $\mathcal{Z}$ also on account of the fact that $\frac{\delta\mathcal{Z}}{\delta\delta_i} = 0$. These brackets are essentially those encountered when discretizing the Arakawa Jacobian, as detailed in [116].

Mixed Bracket. The mixed bracket is trickier since it contains an apparent singularity. On closer inspection, this singularity cancels out when combined with the functional derivative of the potential enstrophy. This is the caveat mentioned above- the discrete mixed bracket must be constructed such that the apparent singularity cancels out with the functional derivative of the potential enstrophy. With this in mind, the general form of the discrete mixed bracket is given as:

$$\{\mathcal{F},\mathcal{H},\mathcal{Z}\}_{\delta\zeta h} = \sum_{edges}\frac{\bar{D}_1(\mathcal{Z}_h)_i}{\bar{D}_1 q_i}\frac{le}{de}\left[(\bar{D}_1\mathcal{F}_\delta)(\bar{D}_1\mathcal{H}_\zeta) - (\bar{D}_1\mathcal{F}_\zeta)(\bar{D}_1\mathcal{H}_\delta)\right] + \text{cyc}(\mathcal{F},\mathcal{H},\mathcal{Z}) \tag{204}$$

By using a spherical geometry definition of le and de, this scheme works on arbitrary spherical polygon grids, provided that they are orthogonal. Note that the definition of $\mathcal{Z}$ given above (or more precisely, the definition of q_i as a functional derivative of $\mathcal{Z}$) ensures that the apparent singularity $\frac{\bar{D}_1(\mathcal{Z}_h)_i}{\bar{D}_1 q_i}$ cancels. By inspection, this bracket is triply anti-symmetric (and therefore, as shown below, will conserve total energy and potential enstrophy).

4.1.4. Discrete Hamiltonian and Helmholtz Decomposition.

The Hamiltonian $\mathcal{H}$ can be split into three parts: $\mathcal{H}_{FD}$, $\mathcal{H}_J$ and $\mathcal{H}_{PE}$. In the continuous system we have

$$\mathcal{H} = \mathcal{H}_{FD} + \mathcal{H}_J + \mathcal{H}_{PE} \tag{205}$$

where

$$\mathcal{H}_{FD} = \int_\Omega d\Omega \frac{1}{2h}\left[\vec{\nabla}\chi \cdot \vec{\nabla}\chi + \vec{\nabla}\psi \cdot \vec{\nabla}\psi\right] \tag{206}$$

$$\mathcal{H}_J = \int_\Omega d\Omega \frac{2J(\chi,\psi)}{2h} = \int_\Omega d\Omega \frac{J(\chi,\psi) - J(\psi,\chi)}{2h} \tag{207}$$

$$\mathcal{H}_{PE} = \int_\Omega d\Omega \frac{1}{2} gh(h + 2h_s) \tag{208}$$

These can be discretized as

$$\mathcal{H}_{FD} = \frac{1}{2}\sum_{edges} \frac{le}{de}\frac{(\bar{D}_1\chi_i)^2}{h_e} + \frac{le}{de}\frac{(\bar{D}_1\psi_i)^2}{h_e} \tag{209}$$

$$\mathcal{H}_{PE} = \frac{1}{2}\sum_{cells} A_i g h_i (h_i + b_i) \tag{210}$$

$$\mathcal{H}_{J} = \frac{1}{2}\sum_{edges} (D_1 \frac{1}{\mathbf{R}h_i}) J(\chi_i, \psi_i) \tag{211}$$

with

$$J(\chi_i, \psi_i) = n_{e,2}\chi_1\psi_2 + n_{e,1}\psi_1\chi_2 \tag{212}$$

where $h_e = \sum_{i \in CE(e)} \frac{1}{2} h_i$ and $\mathbf{R}$ is the cell to vertex interpolation operator from above.

Helmholtz Decompositions and Bernoulli Function. By taking variations of $\mathcal{H}$ we obtain

$$\delta\mathcal{H}_{PE} = \sum_{cells} g A_i (h_i + b_i)\delta h_i \tag{213}$$

(214)
$$\delta\mathcal{H}_{FD} = \frac{1}{2}\sum_{edges} \frac{le}{de}\frac{(\bar{D}_1\chi_i)^2 + (\bar{D}_1\psi_i)^2}{h_e^2}\delta h_e + \sum_{edges} \frac{le}{de}\frac{(\bar{D}_1\chi_i)(\bar{D}_1\delta\chi_i)}{h_e} + \sum_{edges} \frac{le}{de}\frac{(\bar{D}_1\psi_i)(\bar{D}_1\delta\psi_i)}{h_e}$$

$$\delta\mathcal{H}_{J} = \frac{1}{2}\sum_{edges} D_1 \frac{1}{(\mathbf{R}h_i)^2}\mathbf{R}\delta h_i J(\chi, \psi) + \frac{1}{2}\sum_{edges} D_1 \frac{1}{\mathbf{R}h_i}\delta J(\chi, \psi) \tag{215}$$

These can be grouped (half of each term involving δh_i goes to Φ_i and half to δ_i/ζ_i) to obtain

$$\delta\mathcal{H} = -\chi_i\delta\delta_i + -\psi_i\delta\zeta_i + \Phi_i\delta h_i \tag{216}$$

where (using the definition of functional derivative)

$$\Phi_i = \frac{\delta\mathcal{H}}{\delta h_i} = \frac{1}{A_i} g(h_i + b_i) + \frac{1}{4}\frac{1}{A_i}\mathbf{K}\frac{le}{de}\frac{(\bar{D}_1\chi_i)^2 + (\bar{D}_1\psi_i)^2}{h_e^2} + \frac{C}{2}\frac{1}{A_i}\mathbf{K}D_1\frac{1}{(\mathbf{R}h_i)^2}J(\chi, \psi) \tag{217}$$

$$\delta_i = \frac{1}{A_i} D_2 \frac{1}{h_e} \frac{le}{de} \bar{D}_1 \chi_i - \frac{1}{2} \frac{1}{A_i} D_2 (D_1 \frac{1}{\mathbf{R} h_i}) \psi_e \tag{218}$$

$$\zeta_i = \frac{1}{A_i} D_2 \frac{1}{h_e} \frac{le}{de} \bar{D}_1 \psi_i + \frac{1}{2} \frac{1}{A_i} D_2 (D_1 \frac{1}{\mathbf{R} h_i}) \chi_e \tag{219}$$

where $\mathbf{K} = \sum_{e \in EC(i)}$. The last two equations are the discrete version of the Helmholtz decomposition, and form a pair of non-singular elliptic equations. They can be combined into a single equation as

$$\mathbf{A} \begin{pmatrix} \chi_i \\ \psi_i \end{pmatrix} = \begin{pmatrix} \mathbf{FD} & -\mathbf{JA} \\ \mathbf{JA} & \mathbf{FD} \end{pmatrix} \begin{pmatrix} \chi_i \\ \psi_i \end{pmatrix} = \begin{pmatrix} \delta_i \\ \zeta_i \end{pmatrix} \tag{220}$$

where, for example, $\mathbf{FD}\chi_i = \frac{1}{A_i} D_2 \frac{1}{h_e} \frac{le}{de} \bar{D}_1 \chi_i$ and $\mathbf{JA}\psi_i = \frac{1}{2} \frac{1}{A_i} D_2 (D_1 \frac{1}{\mathbf{R} h_i}) \psi_e$. Note that (without the $\frac{1}{A_i}$ factors) $\mathbf{FD}$ is symmetric and $\mathbf{JA}$ is anti-symmetric, which means that $\mathbf{A} = -\mathbf{A}^T$ (ie $\mathbf{A}$ itself is skew-symmetric).Also note that when $h_i = H$ is a constant (and therefore $h_e = H$), they reduce to

$$\delta_i = \frac{1}{H} \frac{1}{A_i} D_2 \frac{le}{de} \bar{D}_1 \chi_i = \frac{1}{H} \mathbf{L} \chi_i \tag{221}$$

$$\zeta_i = \frac{1}{H} \frac{1}{A_i} D_2 \frac{le}{de} \bar{D}_1 \psi_i = \frac{1}{H} \mathbf{L} \psi_i \tag{222}$$

which is the correct linearization behavior.

Independence between choice of $\mathcal{H}$ and Nambu Brackets. It is important to note that the mimetic and conservation properties of the discrete scheme are completely independent of the choice of discrete Hamiltonian, provided the Hamiltonian is positive definite and produces invertible elliptic equations for the Helmholtz decomposition. If the resulting elliptic

equations were singular, then the scheme would have a computational mode (as discussed in Salmon 2007). Additionally, the discrete Helmholtz decomposition should also simplify to a pair of uncoupled Poisson problems when linearized.

4.1.5. Discrete Evolution Equations.

By setting $F = (h_i, \zeta_i, \delta_i)$, the following evolution equations are obtained:

$$\frac{\partial h_i}{\partial t} = -\mathbf{L}\chi_i \tag{223}$$

$$\frac{\partial \zeta_i}{\partial t} = \mathbf{J}_\zeta(q, \psi_i) - \mathbf{FD}(q_i, \chi_i) \tag{224}$$

$$\frac{\partial \delta_i}{\partial t} = -\mathbf{L}\Phi_i + \mathbf{J}_\delta(q_i, \chi_i) + \mathbf{FD}(q_i, \psi_i) \tag{225}$$

where $\mathbf{L}$ is the Laplacian, $\mathbf{FD}$ is the Flux-Divergence and $\mathbf{J}$ is the Jacobian. Note that these operators on an icosahedral hexagonal-pentagonal grid are the same as those from [57]. The only difference is in the arguments (q_i instead of η_i, and different χ_i and ψ_i.)

Laplacian and Flux-Div Operators. The Laplacian and Flux-Divergence operators (which come from the mixed bracket) can be written as

$$\mathbf{L}\alpha_i = \frac{1}{A_i} D_2 \frac{le}{de} \bar{D}_1 \alpha_i \tag{226}$$

$$\mathbf{FD}(\alpha_i, \beta_i) = \frac{1}{A_i} D_2 \alpha_e \frac{le}{de} \bar{D}_1 \beta_i \tag{227}$$

where $\alpha_e = \sum_{i \in CE(e)} \frac{\alpha_i}{2}$. Note that when $\alpha_i = \alpha_0$ is a constant, then

$$\mathbf{FD}(\alpha_i, \beta_i) \to \alpha_0 \mathbf{L} \beta_i \tag{228}$$

Jacobian Operators. The Jacobian operators (which come from the Jacobian brackets) can be written as

$$\mathbf{J}_\delta(q_i, \chi_i) = -\frac{1}{A_i} D_2[(D_1 \mathbf{R} q_i)(\chi_e)] \tag{229}$$

$$\mathbf{J}_\zeta(q_i, \psi_i) = \frac{-1}{3} \frac{1}{A_i} D_2[(D_1 \mathbf{R} q_i)(\psi_e)] + \frac{1}{3} \frac{1}{A_i} D_2[(D_1 \mathbf{R} \psi_i)(q_e)] \tag{230}$$

It is easy to see that both of these operators are zero if either argument is zero. In addition J_δ will conserve kinetic energy. J_ζ is anti-symmetric under interchange of its arugments, and will conserve vorticity, kinetic energy and enstrophy: it is an Arakawa-Jacobian. These properties suffice to ensure that the general discretization scheme conserves PV, total energy and potential enstrophy. Note that on certain grids with certain choices of $\mathbf{R}$, these operators might have additional properties. For example, on a polygonal grid with a triangular dual, using the choice $C = \frac{1}{3}$, J_δ is also an Arakawa Jacobian (in fact, $J_\delta = J_\zeta$).

4.1.6. Discrete Sympletic Operator.

From the evolution equations and the definition of the discrete functional derivatives of the Hamiltonian, it is clear that the discrete symplectic operator can be recovered from the brackets as

$$\mathbb{J} = \begin{pmatrix} 0 & 0 & \mathbf{L} \\ 0 & -J_\zeta(q,\bullet) & FD(q,\bullet) \\ -\mathbf{L} & -FD(q,\bullet) & -J_\delta(q,\bullet) \end{pmatrix} \tag{231}$$

where $\mathbf{L} = \frac{1}{A_i} D_2 \frac{le}{de} \bar{D}_1$ is the discrete Laplacian, $FD(q, \bullet) = \frac{1}{A_i} D_2 q_e \frac{le}{de} \bar{D}_1$ is the discrete flux-divergence and $J(q, \bullet)$ is a discrete Jacobian. Note that there are two different Jacobian operators- one that is used in the divergence equation and one that is used in the vorticity equation.

4.1.7. Linear Version (f = constant).

As before, the linear version of the scheme is obtained by linearizing the Hamiltonian $\mathcal{H}$ and the sympletic operator $\mathbb{J}$ about the point $(h_i, \delta_i, \zeta_i) = (H, 0, 0)$ (which implies that $q_i = \frac{f}{H}$), to yield

$$\mathbb{J}_{linear} = \begin{pmatrix} 0 & 0 & \mathbf{L} \\ 0 & 0 & \frac{f}{H}\mathbf{L} \\ -\mathbf{L} & -\frac{f}{H}\mathbf{L} & 0 \end{pmatrix} \tag{232}$$

$$\mathcal{H}_{linear} = \frac{1}{2} \sum_{cells} \frac{1}{A_i} g h_i^2 + \frac{1}{2H} \sum_{edges} \frac{le}{de} \left[(\bar{D}_1 \chi_i)^2 + (\bar{D}_1 \psi_i)^2 \right] \tag{233}$$

where we have used the fact that discrete Jacobian operators are zero when one of their arguments (q in this case) is constant; and that the flux-divergence operators become Laplacian operators when q is a constant. This is easy to see by contracting the discrete Nambu brackets with respect to $\mathcal{Z}$ (to make discrete Poisson brackets) and then applying the condition $q = \frac{f}{H}$. The functional derivatives of the linear Hamiltonian are given as

$$\frac{\delta \mathcal{H}}{\delta h_i} = g h_i \tag{234}$$

$$\frac{\delta \mathcal{H}}{\delta \zeta_i} = -\psi_i \tag{235}$$

$$\frac{\delta \mathcal{H}}{\delta \delta_i} = -\chi_i \tag{236}$$

where

$$\mathbf{L}\chi_i = H\delta_i \tag{237}$$

$$\mathbf{L}\psi_i = H\zeta_i \tag{238}$$

Putting this all together yields the following evolution equations:

$$\frac{\partial h_i}{\partial t} + H\delta_i = 0 \tag{239}$$

$$\frac{\partial \zeta_i}{\partial t} + f\delta_i = 0 \tag{240}$$

$$\frac{\partial \delta_i}{\partial t} - f\zeta_i + g\mathbf{L}h_i = 0 \tag{241}$$

These are an exact analogue of the corresponding continuous equations, and do not require the solution of elliptic equations.

4.1.8. Linear Version (f = variable).

The same analysis holds as before, except $\mathbb{J}$ will be different:

$$\mathbb{J} = \begin{pmatrix} 0 & 0 & \mathbf{L} \\ 0 & -\frac{1}{H}\mathbf{J}_\zeta(f_i,\bullet) & \frac{1}{H}\mathbf{FD}(f_i,\bullet) \\ -\mathbf{L} & -\frac{1}{H}\mathbf{FD}(f_i,\bullet) & -\frac{1}{H}\mathbf{J}_\delta(f_i,\bullet) \end{pmatrix} \tag{242}$$

In this case, elliptic equations must be solved to get χ_i and ψ_i.

4.2. Linear Mimetic Properties

4.2.1. Linear Stability.

There are two conditions that must be fulfilled for linear stability: an anti-symmetric $\mathbb{J}_{linear}$, and a positive-definite linear Hamiltonian $\mathcal{H}_{linear}$. Inspection of both reveals that these are satisfied for arbitrary orthogonal polygonal grids.

4.2.2. Geostrophic Balance and Vorticity Production.

In contrast to the C-grid models, Z-grid models have geostrophic balance and no spurious vorticity production "built-in". The linear vorticity and mass equations are given by

$$\frac{\partial h_i}{\partial t} + H\delta_i = 0 \tag{243}$$

$$\frac{\partial \zeta_i}{\partial t} + f\delta_i = 0 \tag{244}$$

where $H\delta_i = \mathbf{L}\chi_i$. Since the δ_i is the same in both equation, geostrophic modes are automatically stationary. In addition, the vorticity equation does not have any spurious production terms.

Existence of Geostrophic Balance. In fact, any non-divergent wind field can be balanced by a corresponding height field. Let $\delta_i = 0$ and $\frac{\partial \delta_i}{\partial t} = 0$, then

$$\frac{\partial \zeta_i}{\partial t} = 0 \tag{245}$$

and

$$\frac{\partial h_i}{\partial t} = 0 \tag{246}$$

The divergence equation becomes

$$-f\zeta_i + \mathbf{L}h_i = 0 \tag{247}$$

which can be rewritten as

$$\mathbf{L}h_i = \frac{f}{g}\zeta_i \tag{248}$$

The solvability of this easy to determine- since the Laplacian operator is negative (semi-)definite (semi in domains with topology that supports a nullspace), there will be a unique solution up to the nullspace of $\mathbf{L}$.

4.3. Discrete Conservation

4.3.1. Mass.

The discrete mass equation is given by

$$\frac{\partial h_i}{\partial t} + \mathbf{L}\chi_i = 0 \tag{249}$$

Since $\mathbf{L}$ can be written as $D_2 A_e$, where A_e is some quantity defined at edges, mass will be automatically conserved (both locally and globally) by form regardless of what A_e is.

4.3.2. Energy and Potential Enstrophy.

Note that the discrete dynamics (by virtue of their triply anti-symmetric construction) will conserve $\mathcal{H}$ AND $\mathcal{Z}$ for ANY definition of $\mathcal{H}$ and $\mathcal{Z}$ (subject to the caveat regarding $\mathcal{Z}$ and the mixed bracket singularity discussed above), provided that $\mathbf{H}$ is symmetric positive definite. As discussed in Salmon 2007, this conservation occurs due to flux exchange between

adjacent cells (along with a discrete analogue of the conversion between potential energy and kinetic energy).

Both the Jacobian and mixed brackets are written as a sum over edges, such that the edge fluxes for a given grid cell are equal and opposite for adjacent cells. This ensures that the energy and potential enstrophy are conserved locally as well as globally: in both cases the time evolution of the total energy or potential enstrophy in a grid cell can be written as the divergence of a flux, where the flux is equal and opposite between two adjacent grid cells. In fact, both a kinetic energy and a potential energy equation can written for each grid cell that share this property (there is of course a conversion term in each equation between kinetic and potential energy that cancels when the total energy equation is formed).

The Hamiltonian above is positive-definite and leads to invertible elliptic equations for the Helmholtz decomposition, which when combined with an anti-symmetric $\mathbb{J}$ ensures that energy is conserved.

4.3.3. Potential Vorticity.

Discrete PV Equation. The discrete height and vorticity equations are given as

$$\frac{\partial h_i}{\partial t} + \mathbf{L}\chi_i = 0 \tag{250}$$

$$\frac{\partial \eta_i}{\partial t} - J_\zeta(q, \psi_i) + FD_\zeta(q, \chi_i) = 0 \tag{251}$$

Noting that $q_i h_i = \eta_i$, a mass-weighted PV equation can be written as

$$\frac{\partial q_i h_i}{\partial t} - J_\zeta(q, \psi_i) + FD_\zeta(q, \chi_i) = 0 \tag{252}$$

Compatibility. Compatibility requires that the mass-weighted PV equation can be written as the divergence of a flux; or as the divergence of a set of fluxes such that each flux is equal and opposite between cells that share said flux. This will be sufficient to ensure both local and global conservation of mass-weighted PV. Just as in the case of total energy and potential enstrophy, the form of the Jacobian and Mixed Brackets ensures that this is the case.

Consistency. Consider the mass-weighted PV equation when $q_i = q_0 =$ constant. We have

$$q_0 \frac{\partial h_i}{\partial t} + J_\zeta(q, \psi_i)|_{q=q_0} + FD_\zeta(q, \chi_i)|_{q=q_0} = 0 \tag{253}$$

Note that (by construction) $J_\zeta(q, \psi_i) = 0$ when q_i is constant; and that $FD_\zeta(q, \chi_i) \to q_0 \mathbf{L}\chi_i$ when q_i is constant; therefore the mass-weighted PV equations will reduce to

$$q_0 \frac{\partial h_i}{\partial t} + q_0 \mathbf{L}\chi_i = 0 \tag{254}$$

which corresponds with the discrete mass equation. Note that these are the same conditions as those required to ensure that the fully nonlinear system collapses down to the linear system. This makes sense, since the linear symplectic operator is obtained by evaluating the full symplectic operator at the point of linearization (which has constant q).

4.4. Schemes

The specification of a scheme from this general family requires a process for determining geometric quantities (A_i, le and de) and the constant C (from $\mathbf{R}$). In all of the schemes presented below, A_i is determined by decomposing the polygonal element into planar (or spherical) triangles, and then applying the relevant formulas. The edge lengths are simply

the geodesic distances between the relevant points (straight lines on the plane, geodesic arcs on the sphere). The constant C is given by $\frac{1}{n}$, where n is the number of grid elements in $CV(v)$ (equal to 4 for quadrilateral elements and 3 for triangular elements).

4.4.1. Salmon 2007 Perfect Square Grid (PS).

On a perfect square grid with spacing Δ (which is orthogonal and logically square), the geometric quantities are very simple: $A_i = \Delta^2$ and $le = de = \Delta$. Also, since the dual grid is composed purely of quadrilaterals, $C = \frac{1}{4}$. Plugging these choices into the general scheme above recovers the first scheme presented in Salmon 2007 (with the caveat that a particular orientation of grid elements has been assumed).

4.4.2. Salmon 2007 Triangular Grid (TG).

For a general orthogonal polygonal grid with a triangular dual, the geometric quantities must be computed for each grid element. However, the dual grid is composed purely of triangles and thus $C = \frac{1}{3}$. Again, by plugging these operators into the general scheme above we recover the second scheme presented in Salmon 2007. Our scheme is written using le and de instead of $\cot\theta$ (and in terms of A_i instead of A_v), but is is well known that the DEC Laplacian using the Voronoi dual (which is our scheme) is equivalent to the cotangeant formulation of the Laplacian (which is the Salmon 2007 triangular grid scheme). Salmon did not present a form for the Hamiltonian in this scheme, while we do. Our scheme also works on icosahedral hexagonal-pentagonal grids, not just planar grids.

4.4.3. Future.

The scheme discussed above is generally first order on icosahedral grids (and the Jacobian is 0th order), and it would be desirable to have an extension of it to higher-order. Although it would certainly be possible to do this using the existing finite-difference framework, it is likely

that the grids would have to have special properties. A more general approach is to use finite or spectral element methods instead, which have much more geometric flexibility. In fact, considerations from finite element exterior calculus suggest that it would be possible to derive an energy and potential enstrophy conserving scheme on both simplices and quadrilaterals using either P_n continous elements, or DG_n discontinous elements. In particular, both the spectral element and Discontinuous Galerkin methods should be feasible on the cubed-sphere, in a manner that conserves both energy and potential enstrophy. It is believed (but not proven) that the generalized scheme described above is in fact a mass-lumped, P_1 finite element scheme (on simplices) of precisely this type.

4.5. Other Desirable Properties

In addition to mimetic properties and conservation properties, it is desirable that a discretization scheme posses other useful properties.

4.5.1. Linear Modes.

A detailed study of the linear modes for this generalized Z grid scheme on both planar (constant f) and quasi-uniform spherical grids (both constant and variable f) is provided in Chapter 5. Some results are summarized below.

Absence of Computational Modes. The discrete framework discussed above does not posses any spurious stationary modes OR spurious linear wave branches; at least on the grids investigated. This is a strong advantage of the Z grid formulation.

Good Wave Representation. The inertia-gravity wave dispersion relationship of the unstaggered vorticity-divergence scheme presented above is determined ENTIRELY by the spectrum of the discrete Laplacian (exactly as in the continuous case). For all of the Laplacian/Grid combinations studied, the discrete dispersion relationship exhibited the same

essential characteristics as the continuous one: monotonic increase with wavenumber, a positive-definite group velocity, and insensitivity to Rossby radius. The isotropy of the resulting dispersion relationship is a function of grid (as expected), with the hexagonal grid being the most isotropic. This is in strong contrast to the A and C grid dispersion relationships, which had issues with at least one of these features. The Z grid dispersion relationship does show artificial reductions in phase speed for higher-frequency waves, is expected from a finite-difference scheme.

4.5.2. Grid Flexibility.

The general discretization scheme introduced above works only on icosahedral hexagonal-pentagonal meshes (more generally on orthogonal polygonal meshes with a triangular dual); and on perfect planar square meshes; it does not work on non-orthogonal grids such as the cubed sphere. However, the main motivation for using a cubed-sphere grid is the avoidance of spurious branches of the dispersion relationship associated with a mismatch of wind/height dofs. Since the Z grid does not suffer from this, and the icosahedral hexagonal-pentagonal grid offers better accuracy, there seems to be little motivation for using a cubed sphere grid.

4.5.3. Order of Accuracy.

The general discretization scheme presented above is approximately first order on optimized quasi-uniform spherical grids, while the Jacobian operator is 0th order. However, the general approach of using triply anti-symmetric Nambu brackets along with some discrete Hamiltonian (whose precise definition does not effect the conservation or mimetic properties of the scheme) is amenable to higher order-discretizations. It would be fairly trivial to extended the approach presented above to fourth-order on logically square, orthogonal grids (as discussed in Salmon 2007). Non-orthogonal grids and general polygonal grids would be

trickier, and as discussed above it is likely that a finite-element based approach would be preferable for that type of grid.

4.5.4. Absence of Hollingsworth Instability.

There is no evidence of the emergence of Hollingsworth Instability in multi-level vorticity-divergence models. This is probably because there is no error term in the discrete quasi-geostrophic equations that are derived from the full equations.

4.6. Chapter Summary

The generalized scheme presented above extends the work of Salmon 2007 to spherical orthogonal polygonal grids, including the icosahedral grid. In particular Salmon 2007 only presented a full scheme for perfect square grids, and gave only the brackets (not the Hamiltonian) for the case of a general planar orthogonal polygonal grid. This work also shows that the generalized scheme posses the desirable mimetic and PV dynamics properties.

CHAPTER 5

Linear Modes

An important component of a numerical scheme for the rotating shallow water equations are the linear modes associated with the scheme. This includes both the discrete representation of the continuous linear modes (inertia-gravity and Rossby waves; also physical stationary modes such as the hydrostatic mode and geostrophic modes), and any spurious linear modes. This chapter investigates the linear modes of the generalized schemes presented in Chapter 3 and Chapter 4, with a focus on the linear modes for quasi-uniform spherical grids. It also incorporates the effects of dissipation (in the form of viscosity). Investigation of the linear modes for quasi-uniform grids using a very similar discretization scheme has been done before in Weller 2012 ([155]). However, this work extends that study in several key ways:

(1) More accurate determination of the linear system matrix $\mathbf{A}$

(2) Uses a true cubed-sphere grid (instead of a "Voronoized" cube)

(3) Looks at the effects of dissipation (in the form of viscosity)

Where possible, comparison will be made between the results obtained in [155] and the results obtained here.

5.1. Continuous Equations

From Chapter 2, the linearized rotating shallow water equations without topography can be written as

$$\frac{\partial h}{\partial t} + H\vec{\nabla} \cdot \vec{u} = 0 \tag{255}$$

$$\frac{\partial \vec{u}}{\partial t} + f\hat{k} \times \vec{u} + g\vec{\nabla}h = 0 \tag{256}$$

which in vorticity-divergence form are

$$\frac{\partial h}{\partial t} + H\delta = 0 \tag{257}$$

$$\frac{\partial \zeta}{\partial t} - J(f, \psi) + \vec{\nabla} \cdot (f\vec{\nabla}\chi) = 0 \tag{258}$$

$$\frac{\partial \delta}{\partial t} - J(f, \chi) - \vec{\nabla} \cdot (f\vec{\nabla}\psi) + g\vec{\nabla}^2 h = 0 \tag{259}$$

In the case of constant f the latter two equations reduce to

$$\frac{\partial \zeta}{\partial t} + f\delta = 0 \tag{260}$$

$$\frac{\partial \delta}{\partial t} - f\zeta + g\vec{\nabla}^2 h = 0 \tag{261}$$

5.1.1. Stationary Modes (Constant f).

A stationary mode occurs when the time derivatives of the evolutions equations are all equal to zero: in other words, it is a steady state.

5.1.1.1. $\frac{\partial \vec{u}}{\partial t} = 0 \rightarrow$ *Geostrophic Balance.*

Geostrophic balance occurs when the time derivative of the wind is zero, or in the vorticity-divergence formulation, when the time derivative of the divergence is zero. This implies that:

$$g\vec{\nabla}h + f\vec{u}^{\perp}_{geo} = 0 \tag{262}$$

or equivalently that

$$\vec{u}_{geo} = \hat{k} \times \vec{\nabla}(\frac{hg}{f}) \tag{263}$$

In the vorticity-divergence formulation, we have

$$f\zeta_{geo} - g\nabla^2 h = 0 \tag{264}$$

or equivalently that

$$\zeta_{geo} = \nabla^2(\frac{hg}{f}) \tag{265}$$

These two formulations are equivalent, which can be seen by computing the vorticity from the geostrophic wind. Alternatively, one could compute the streamfunction from the vorticity, and then the geostrophic wind from the streamfunction.

5.1.1.2. $\frac{\partial h}{\partial t} = 0 \rightarrow$ *Non-Divergent Flow.*

Non divergent flow occurs when the divergence is set to zero, which means that the time derivative of the height and vorticity equations are both zero. Thus by the Helmholtz decomposition we have

$$\vec{u}_{nd} = \hat{k} \times \vec{\nabla}\psi \tag{266}$$

where ψ is the streamfunction.

5.1.1.3. $\frac{\partial \vec{u}}{\partial t} = 0 \leftrightarrow \frac{\partial h}{\partial t} = 0$ *(Existence of Geostrophic Balance).*

Start by taking the divergence of the geostrophic wind. This is:

$$\vec{\nabla} \cdot \vec{u}_{geo} = \vec{\nabla} \cdot (\hat{k} \times \vec{\nabla}(\frac{hg}{f})) \tag{267}$$

$$= \frac{g}{f}\vec{\nabla}h \cdot (\vec{\nabla} \times \hat{k}) - \frac{g}{f}\hat{k} \cdot (\vec{\nabla} \times \vec{\nabla}h) \tag{268}$$

$$= 0 \tag{269}$$

since the first term is zero because $\hat{k}$ is a constant and the second term is zero because $\vec{\nabla} \times \vec{\nabla}A = 0$ for any scalar field A. So the geostrophic wind is non-divergent.

Now consider a general non-divergent wind field. Note that $\nabla^2\psi = \zeta = \vec{\nabla}^{\perp} \cdot \vec{u}$ by definition and that $\vec{u}^{\perp} = -\vec{\nabla}\psi$, where ψ is the streamfunction. Plugging this into the wind equation gives

$$\vec{\nabla}\psi = \vec{\nabla}\left(\frac{gh}{f}\right) \tag{270}$$

Therefore, there is a corresponding non-unique height field such that geostrophic balance holds. The non-uniqueness of the height field comes from the fact that the kernel of the gradient operator will in general be non-zero (on the doubly periodic plane or sphere, it contains constant functions).

5.1.1.4. *Geostrophic and Hydrostatic Adjustment.*

On large scales, the real atmosphere exists in a state of near-geostrophic and hydrostatic balance. Perturbations to this balance result in the radiation of inertia-gravity and sound waves that act to restore the atmosphere to the balanced state. This is an important physical

process and it is widely believed that a dynamical core needs to be able to simulate this process correctly. Accurate representation of inertia-gravity waves is an important first step.

5.1.1.5. *Hydrostatic Mode.*

A special case of the geostrophic mode is the hydrostatic mode, which corresponds to $\vec{u} = 0$ and $h = \text{const}$. It reflects the fact that only differences in fluid height play a physical role in the linearized shallow water system, not the absolute height of the fluid. Note that the geostrophic and hydrostatic mode are the ONLY physical stationary modes.

5.1.2. Propagating Modes (Inertia-Gravity Waves).

The other type of linear mode for physical systems is a propagating mode, that is, one that changes in time. Typically, these modes are assumed to be decomposable into the appropriate spatial and temporal basis functions for a given spacetime configuration. For the rotating shallow water equations, this means time variation that looks like $e^{i\sigma t}$. Combined with our assumption about continuity in time, this gives $\frac{\partial}{\partial t} \to i\sigma$. We will consider both the f-plane/f-sphere (which admits only inertia-gravity waves) and the full-sphere (which admits both inertia-gravity and Rossby waves), again without topography.

5.1.2.1. *Wave Dynamics: Phase and Group Velocity.*

Consider a standard one dimensional spatiotemporal plane wave of the form:

$$A(x,t) = \hat{A}e^{i(kx-\omega t)} \tag{271}$$

with spatial wavenumber k, temporal frequency w and amplitude $\hat{A}$. Note that the wavenumber is related to the wavelength λ by $k = \frac{2\pi}{\lambda}$; and the frequency is related to the period T by $T = \frac{2\pi}{\omega}$. The phase speed or velocity of such a wave is described by

$$c_p = \frac{\omega}{k} \tag{272}$$

Now consider a group of such waves where $\omega = \omega(k)$. The group velocity c_g is defined by

$$c_g = \frac{d\omega}{dk} \tag{273}$$

Waves whose phase velocity does not depend on wavenumber are called non-dispersive, since a group of such waves will retain their initial structure. If the individual wavenumbers travelled at different speeds, the packet would tend to spread out (disperse) over time. It is well known that the energy associated with a wave packet travels at the group velocity, not the phase velocity. Shallow water waves are non-dispersive: their phase velocity is independent of wave number. As will be seen, this is no longer the case for a numerical scheme. Such numerical dispersion is a hallmark of all discrete approximations (with the exception of a spectral model that explicitly decomposes a solution in terms of the basis functions that represent individual waves).

5.1.2.2. *Continuous RSW.*

The propagating normal modes of the shallow water system are analysed by first linearising about a reference state (ignoring topography), then assuming wave-like solutions. Physically, these are the various types of waves in the system: intertia-gravity and Rossby waves. Plugging this assumed solution into the linearised equations gives the dispersion relation. Three cases are examined below: the f-plane, the f-sphere and full sphere.

5.1.2.3. *f-plane.*

The f-plane is a doubly periodic plane with constant f. Assume plane wave solutions of the form:

$$\theta(x, y, t) = \theta_0 e^{ikx} e^{ily} e^{-i\sigma t} \tag{274}$$

where θ is some variable, θ_0 is a constant, k and l are the horizontal wavenumbers in the x and y directions and σ is the frequency. These wave solutions are appropriate since the natural Laplacian basis for the double periodic plane is a double Fourier series. By plugging these assumed solutions into the linearized shallow water equations we get the dispersion relation:

$$\sigma(\sigma^2 - f^2 - gH(k^2 + l^2)) = 0 \tag{275}$$

or equivalently

$$(\frac{\sigma}{f})^2 = 1 + (\frac{\lambda}{d})^2((kd)^2 + (ld)^2) \tag{276}$$

where $\lambda^2 = \frac{gH}{f^2}$ is the Rossby radius of deformation (this is the conventional non-dimensionalization of the problem) and the $\sigma = 0$ root has been dropped (it corresponds to geostrophic modes). For comparison with numerical methods later, a factor of d (grid spacing) has been introduced. These waves are inertia-gravity waves, since the restoring force is a combination of gravity and the Coriolis force. The number $C = \frac{\lambda}{d}$ measures the ratio of the Rossby radius of deformation to the grid spacing: it is a measure of how well-resolved waves are on the grid. A large value indicates well-resolved modes, a small value poorly resolved modes. Modern horizontal resolutions imply that most intertia-gravity waves are well-resolved. However, as the shallow water equations can be regarded as an analogue for the primitive equations in isentropic coordinates, it is still important to consider small values of C since high wavenumber, vertical, internal modes are often still poorly resolved at current resolutions.

General Properties. By convention, $k > 0$ and $l > 0$, which means that the $K = 0$ case is unphysical (where $K^2 = k^2 + l^2$. This can also be seen simply from the assumed form

of the waves: $K = 0$ implies a wave that has infinite wavelength (and is therefore constant everywhere). However, such by plugging such a wave into the original equations, it is easy to see that it will not propagate. This is not consistent with the dispersion relation, which states that such waves will have a frequency of f. The positive-definiteness of K implies that ALL inertia-gravity waves on an f-plane have a frequency greater than the Coriolis frequency f. Since the domain is bounded, there will be a minimal wavenumber in each direction given by the size of the domain in that dimension; however, there is no maximal wavenumber. The frequency increases monotonically with increasing wavenumber and is isotropic in wavenumber space. However, the dispersion relation solution is not unique- a given frequency has multiple wavenumber pairs associated with it (these wavenumber pairs are found by interchanging k and l; this is another consequence of isotropy). On the plane, every wavenumber pair with an equal value of $K^2 = k^2 + l^2$ will have the same frequency. In addition, each frequency comes in a positive and negative sign. In the case that $f = 0$, the inertia-gravity waves become non-dispersive. These are all properties that a numerical model should replicate (or there should be good reasons for not satisfying them; in particular there will always be a maximal wavenumber that is resolvable on a grid due to the finite nature of computational meshes).

Non-Rotating Case. In the case that $f = 0$ (non rotating gravity waves), the dispersion relation becomes

$$\sigma^2 = gHK^2 \tag{277}$$

where $K^2 = k^2 + l^2$ and there are no longer any geostrophic modes. Note that the phase speed becomes

$$c_p = \frac{\omega}{k} = \sqrt{gH} \tag{278}$$

ie the non rotating gravity waves are non-dispersive. In addition, the flow is purely divergent; more correctly, any vortical portion of the flow does not contribute to the linearized dynamics.

5.1.2.4. *f-sphere.*

The f-sphere is a spherical surface with constant f- note that this is a mathematical construct that has no physical analogue, since such a sphere would have to rotate infinitely fast at the equator in order to have a non-zero value of f there. The advantage of this construct is that the effects of spherical geometry can be taken into account without having to deal with latitudinal variation of the Coriolis parameter. In particular, there are still stationary geostrophic modes and the only physical propagating modes are inertia-gravity waves.

A similar procedure to that utilized for the f-plane can be carried out using the spherical harmonics $Y_m^n(\lambda, \sin\phi)$ as spatial basis functions (again since they are the natural laplacian basis), where λ is the longitude and ϕ is the latitude. This yields a dispersion relationship ([140]) of

$$\sigma(\sigma^2 - f^2 - \frac{n(n+1)}{a^2} gH) = 0 \tag{279}$$

where a is the radius of the Earth and n must be an non-negative integer. There are two cases to consider. The first is $n = 0$, for which only the $\sigma = 0$ root is physical (corresponds to the hydrostatic mode). When $n = 0$ and $\sigma \neq 0$, there is again the problem of a propagating

solution that is constant in space everywhere (which is not consistent with the evolution equations). The second case is $n \geqslant 1$, in which case there are $2n+1$ linearly independent spherical harmonics corresponding to $m = -n, \ldots, 0, \ldots, n$. For each pair of (n, m), all three roots are physical with the $\sigma = 0$ root a geostrophic mode and the others inertia-gravity waves.

General Properties. By convention, the spherical harmonics have $n \geqslant 0$ and $m = -n, \ldots, 0, \ldots, n$, with both m and n integers. The minimal wavenumber for propagating modes is $n = 1$. The frequency increases monotonically with increasing n but it is independent of m. Therefore, there are $2n+1$ linearly independent propagating modes, each with the same frequency. Each frequency also comes in a positive and negative pair. In the case that $f = 0$, the inertia-gravity waves become non-dispersive. These are all properties that a numerical model should replicate (or there should be good reasons for not satisfying them; in particular there will always be a maximum wavenumber that is resolvable on a grid due to the finite nature of computers).

5.2. Discrete Equations

For convenience, presented below are the linearized versions of the general C and Z grid schemes from Chapters 3 and 4 (**without topography**). These general formulations will be useful in analysing the linear modes (stationary and propagating) of various schemes.

5.2.1. Linear Schemes.

By definition, the time evolution of a linearized scheme can be written as

$$\frac{\partial \vec{x}}{\partial t} = \mathbf{A}\vec{x} \tag{280}$$

where $\vec{x}$ is the vector of discrete degrees of freedom, and $\mathbf{A}$ is the evolution matrix. This equation forms the basis of analyzing the linear modes of the discrete system, since they are determined entirely by the properties of $\mathbf{A}$. Specific examples of $\vec{x}$ and $\mathbf{A}$ for various schemes are presented below.

5.2.2. C Grid Scheme.

The linearized version of the generalized C grid scheme from Chapter 4 is

$$\frac{\partial m_i}{\partial t} = -H\bar{D}_2\mathbf{H}u_e \tag{281}$$

$$\frac{\partial u_e}{\partial t} = H\mathbf{Q}_L\mathbf{H}u_e - \bar{D}_1\mathbf{I}m_i \tag{282}$$

where **QL** is the discrete bilinear Coriolis operator. For the three variants discussed in Chapter 3, it is given as

$$\mathbf{Q}_{L,TE} = \mathbf{W}\frac{fv_e + fv_{e'}}{2} \tag{283}$$

$$\mathbf{Q}_{L,Q} = fv_e\mathbf{W} \tag{284}$$

$$\mathbf{Q}_{L,TEQ} = \sum_{e' \in ECP(e)} \Big(\sum_{v \in VC(i)} \alpha_{e,e',v} f_v \Big) \tag{285}$$

Note that when $f_v = f$ is a constant, all three variants reduce to

$$\mathbf{Q}_L = f\mathbf{W} \tag{286}$$

This is a side-effect of the condition of PV compatibility. In matrix form, this can be written as

$$\frac{\partial \vec{x}}{\partial t} = i\omega \vec{x} = \mathbf{A}\vec{x} \tag{287}$$

where $\vec{x} = (m_i, u_e)$ and

$$\mathbf{A} = \begin{pmatrix} 0 & -H\mathbf{D} \\ -g\mathbf{G} & \mathbf{Q} \end{pmatrix} \tag{288}$$

and

$$\mathbf{D} = D_2\mathbf{H} \tag{289}$$

$$\mathbf{G} = \bar{D}_1\mathbf{I} \tag{290}$$

$$\mathbf{Q} = \mathbf{Q}_L\mathbf{H} \tag{291}$$

Scaling. For comparison with other schemes (that use point values), these matrices are scaled by

$$\mathbf{D} = \mathbf{I}\mathbf{D}\mathbf{E}^{-1} \tag{292}$$

$$\mathbf{G} = \mathbf{E}\mathbf{G}\mathbf{I}^{-1} \tag{293}$$

$$\mathbf{Q} = \mathbf{E}\mathbf{Q}\mathbf{E}^{-1} \tag{294}$$

which ensures that we are working with point values for all variables. Then $\vec{x}$ becomes (h_i, v_e) where $h_i = \mathbf{I}m_i$ and $v_e = \mathbf{E}u_e$.

5.2.2.1. *Dissipation.*

Momentum dissipation in the form of viscosity can be added to the scheme as

$$\mathbf{A}_{new} = \mathbf{A}_{old} + \mathbf{A}_{dissip} \tag{295}$$

where

$$\mathbf{A}_{dissip} = \begin{pmatrix} 0 & 0 \\ 0 & \nu_{cc}\mathbf{CC} + \nu_{gd}\mathbf{GD} \end{pmatrix} \tag{296}$$

where $\mathbf{CC} = -\mathbf{H}^{-1}D_1\mathbf{J}\bar{D}_2$ and $\mathbf{GD} = \bar{D}_1\mathbf{I}D_2\mathbf{H}$. The generalization to hyperviscosity $\vec{\nabla}^{2p}$ is

$$\mathbf{A}_{dissip} = \begin{pmatrix} 0 & 0 \\ 0 & \nu_{cc}\mathbf{CC}^p + \nu_{gd}\mathbf{GD}^p \end{pmatrix} \tag{297}$$

which relies on the relations $D_2D_1 = 0$ and $\bar{D}_2\bar{D}_1 = 0$.

5.2.3. Z Grid Scheme.

The linearized scheme from Chapter 4 can be written (assuming no topography) as

$$\mathbb{J} = \begin{pmatrix} 0 & 0 & H \\ 0 & -\frac{1}{H}J_\zeta(f_i,\bullet) & \frac{1}{H}FD(f_i,\bullet) \\ -g\mathbf{L} & -\frac{1}{H}FD(f_i,\bullet) & -\frac{1}{H}J_\delta(f_i,\bullet) \end{pmatrix} \tag{298}$$

with Hamiltonian functional derivatives given as

$$\frac{\delta\mathcal{H}}{\delta\vec{x}} = \begin{pmatrix} gh_i \\ -\psi \\ -\chi \end{pmatrix} \tag{299}$$

and

$$\mathbf{L}^{-1}\bar{H}\delta = -\chi \tag{300}$$

and

$$\mathbf{L}^{-1}\bar{H}\zeta = -\psi \tag{301}$$

where $\vec{x} = (h_i, \zeta_i, \delta_i)$. This can all be put together to yield

$$\mathbf{A} = \begin{pmatrix} 0 & 0 & -H \\ 0 & J_\zeta(f_i, \mathbf{L}^{-1}\bullet) & -FD(f_i, \mathbf{L}^{-1}\bullet) \\ -g\mathbf{L} & FD(f_i, \mathbf{L}^{-1}\bullet) & J_\delta(f_i, \mathbf{L}^{-1}\bullet) \end{pmatrix} \tag{302}$$

In the case of constant f this reduces to

$$\mathbf{A} = \begin{pmatrix} 0 & 0 & -H \\ 0 & 0 & -f \\ -g\mathbf{L} & f & 0 \end{pmatrix} \tag{303}$$

5.2.3.1. *Dissipation.*

Momentum dissipation in the form of viscosity can be added to the scheme as

$$\mathbf{A}_{new} = \mathbf{A}_{old} + \mathbf{A}_{dissip} \tag{304}$$

where

$$\mathbf{A}_{dissip} = \begin{pmatrix} 0 & 0 & 0 \\ 0 & \nu_{cc}\mathbf{L} & 0 \\ 0 & 0 & \nu_{gd}\mathbf{L} \end{pmatrix} \tag{305}$$

The generalization to hyperviscosity $\vec{\nabla}^{2p}$ is

$$\mathbf{A}_{dissip} = \begin{pmatrix} 0 & 0 & 0 \\ 0 & \nu_{cc}\mathbf{L}^p & 0 \\ 0 & 0 & \nu_{gd}\mathbf{L}^p \end{pmatrix} \tag{306}$$

5.3. Numerical Stationary Modes

Numerical stationary modes of a general linear system exist when

$$\frac{\partial \vec{x}}{\partial t} = \mathbf{A}\vec{x} = 0 \tag{307}$$

where $\mathbf{A}$ is the evolution operator matrix for the system. Thus we see that the stationary modes of a particular scheme are connected to the nullspaces of various discrete operators.

As discussed prior, a discretization scheme might posses spurious stationary modes. These are non-propagating modes (typically around grid-scale) that do not have a corresponding physical counterpart. Such modes are often damaging, since non-linear processes can lead to a build-up of energy in these modes which contaminates the solution. Generally, spurious stationary modes arise when the kernel dimension of the discrete operator matrix is not the same as the kernel dimension of the corresponding continuous operator.

5.3.1. Stationary Modes for Vector Invariant Formulation.

General Form for Stationary Modes. Starting from 288 and assuming $\frac{\partial}{\partial t} = 0$, the vector invariant linear shallow water equations in discrete matrix form reduce to

$$H\mathbf{D}\vec{u} = 0 \tag{308}$$

$$f\mathbf{Q}\vec{u} + g\mathbf{G}\vec{h} = 0 \tag{309}$$

This is equivalent to the requirement that $\mathbf{A}\vec{x} = 0$. In order for these equations to hold, both $\vec{u}$ and $\vec{h}$ must satisfy them. The first one gives that either $\vec{u} = 0$ or $\vec{u} \in K(\mathbf{D})$. The second one gives that either $\vec{h} = 0$, $\vec{h} = \text{const}$ or $\vec{h} = \text{geostrophic}$; and that either $\vec{u} = 0$,

$\vec{u} \in K(\mathbf{T})$ or $\vec{u}$ = geostrophic. Putting these possibilities together gives a classification of the stationary modes.

5.3.1.1. *Zero Mode/Hydrostatic Mode.*

When $\vec{u} = 0$ and $\vec{h} = 0$ or $\vec{h}$ = const (assuming that the gradient operator gives zero when $\vec{h} = const$, which is a condition for 0-th order consistency of the gradient operator), this is the hydrostatic mode. Ideally $\mathbf{G}$ will have rank 1 and the only mode will be the hydrostatic mode. This is the case for C grid models, but not for A grid models. This is a physical mode.

5.3.1.2. *Geostrophic Mode.*

When $\vec{u} \in K(\mathbf{D})$ and $-f\mathbf{C}\vec{u} = g\mathbf{G}\vec{h}$ (ie discrete geostrophic balance), we have a geostrophic mode. The conditions for the existence of stationary geostrophic modes in the C grid model are discussed further in Chapter 3.

5.3.1.3. *Spurious Pressure Modes.*

When $\vec{u} = 0$ and $\vec{h} \in K(\mathbf{G})$, we have a (spurious) pressure mode. There are $K_{dim}(\mathbf{G}) - 1$ of these modes. Since $K_{dim}(\mathbf{G}) = 1$ for C grid schemes (this is one of the motivations for the use of a staggered grid), these modes typically only occur for A grid models. They arise from the unavoidable averaging in the gradient operator that occurs for collocated quantities.

5.3.1.4. *Spurious TD Modes.*

When $\vec{u} \in K(\mathbf{D}) \cap \vec{u} \in K(\mathbf{T})$ and $\vec{h} = 0$, we have a (spurious) TD mode. Since $K_{dim}(\mathbf{T}) = 1$ for A grid schemes (since the wind components are collocated), these modes typically only occur for C grid models. However, a well-designed (energy-conserving) C grid scheme has $\mathbf{D} = -\mathbf{G}^T$, and therefore $K_{dim}(D) = K_{dim}(G)$. Since one of the motivations for using a staggered grid is that $K_{dim}(G) = 1$, energy conserving C grid models will be free of spurious TD modes (and therefore free of spurious stationary modes in general).

5.3.1.5. *Spurious Mixed Pressure-TD Modes.*

When $\vec{u} \in K(\mathbf{D}) \cap \vec{u} \in K(\mathbf{T})$ and $\vec{h} \in K(\mathbf{G})$, we have a (spurious) mixed pressure-TD mode. This is really a combination of a pressure mode and a TD-mode. Generally, these modes do not exist in practice since schemes will have either pressure modes (A grids) or TD modes (C grids).

5.3.2. Stationary Modes for Vorticity-Divergence Formulation.

The situation is markedly different for the vorticity-divergence formulation. Only one discrete operator appears- the Laplacian. Starting with 302, we obtain

$$H\vec{\delta} = 0 \tag{310}$$

$$f\vec{\delta} = 0 \tag{311}$$

$$-f\vec{\zeta} + g\mathbf{L}\vec{h} = 0 \tag{312}$$

In order for these equations to hold, $\vec{h}$, $\vec{\delta}$ and $\vec{\zeta}$ must satisfy them. The first two give $\delta = 0$. The last one gives either $\vec{\zeta} = 0$ or $\vec{\zeta}$ = geostrophic; and either $\vec{h} = 0$, $\vec{h}$ = const, $\vec{h} \in K(\mathbf{L})$ or $\vec{h}$ = geostrophic. Putting these possibilities together gives a classification of the stationary modes.

5.3.2.1. *Zero Mode/Hydrostatic Mode.*

When $\vec{\delta} = 0$, $\vec{\zeta} = 0$ and $\vec{h} = 0$ or $\vec{h}$ = const, we have the hydrostatic mode (this is physical). Again $\mathbf{L} = 0$ when $\vec{h}$ = const since this is a condition for 0-th order consistency of the Laplacian operator.

5.3.2.2. *Geostrophic Modes.*

When $\vec{\delta} = 0$ and $-f\vec{\zeta} + g\mathbf{L}\vec{h} = 0$, we have a (physical) geostrophic mode. The conditions for the existence of stationary geostrophic modes in the Z grid model are discussed further in Chapter 4.

5.3.2.3. *Spurious Pressure Modes.*

When $\vec{\delta} = 0$, $\vec{\zeta} = 0$ and $\vec{h} \in K(\mathbf{L})$ we have a (spurious) pressure mode. There are $K_{dim}(\mathbf{L}) - 1$ of these modes. Note that if the kernel of the Laplacian is non-trivial (contains non-constant functions) then there is not longer a unique (up to a constant) geostrophic height field for a given non-constant. In practice, however, the kernel of the discrete Laplacian usually only contains constant functions (an exception would the the X stencil laplaian for a square grid, for example); and therefore pressure modes are absent.

5.3.3. Spurious Stationary Modes for C and Z Grid Schemes.

On the basis of the above analysis, it is expected that both the C and Z grid schemes will be free of spurious stationary modes, on ANY grid. This result is investigated numerically on quasi-uniform spherical grids (icosahedral and cubed-sphere) below. Additionally, the stationary modes of the full sphere; and the effects of dissipation are also investigated.

5.3.4. Quasi-Uniform Spherical Grid Results.

The null space of a numerical matrix $\mathbf{A}$ is tricky to calculate, since in practice a floating point representation of a matrix is almost always full-rank even when the true matrix is low-rank. For this reason, the null space is calculated using a Singular Value Decomposition. For the true matrix, the zero singular values represent the null space. For a floating point matrix, there will instead be singular values that are much smaller (1e12 or more times smaller in double precision) than the other singular values. The singular vectors associated with these

singular values form a basis for the null space of the matrix. The SVD is computed using SciPy ([67]) by generating the linear matrix of the various schemes from their definitions. Only results from the doubly-conservative C grid scheme are shown, the other variants are similar. Parameters used were the same as those below, in the study of propagating modes on the f-sphere and fullsphere.

The singular vectors are decomposed into h_i and u_e (from which ζ_v and δ_i are computed) for the C grid scheme, and h_i, ζ_i and δ_i for the Z grid scheme. ζ_v and δ_i are computed as:

$$\zeta_v = \mathbf{J}\bar{D}_2\mathbf{E}^{-1}v_e \tag{313}$$

$$\delta_i = \mathbf{i}D)_2\mathbf{H}\mathbf{E}^{-1}v_e \tag{314}$$

5.3.4.1. *f-sphere.*

On the f-sphere, several important conclusions can be drawn:

(1) Without dissipation, there are n_v stationary modes for the C grid scheme and n_f stationary modes for the Z grid scheme. This fits with theory, which says that there should be that many geostrophic modes. Inspection of the decomposed singular vectors reveals that each of these modes has zero divergence, and the height/relative vorticity fields are a linear combination of spherical harmonics (as expected).

(2) With dissipation, the only stationary mode for the C grid scheme has constant height and zero relative vorticity and divergence. However, the zero frequency modes from the eigensolver did have the same structure as those found without dissipation. Essentially, dissipation is acting exactly as it did in the planar case: no change in mode structure, but the modes are damped.

(3) There were no stationary modes found for the Z grid scheme with dissipation. It appears that the numerical SVD solver used is not converging properly in this case, since a constant height field with zero relative vorticity and divergence is a steady state of the numerical scheme (this has been checked). However, the eigensolver did converge, and the resulting zero frequency modes were found to match the expected behaviour of the geostrophic modes.

5.3.4.2. *full-sphere.*

The same analysis can be repeated on the full sphere to yield:

(1) For the C grid scheme without dissipation, there are 16 "stationary" modes for the icosahedral grid and 24 "stationary" modes for the cubed sphere grid. Closer inspection reveals that these modes have spatial frequencies either exactly equal to 0, or around 10^{-16}. Furthermore, they have $\delta = 0$ and zonally symmetric height and relative vorticity. Therefore, they can be categorized as physical stationary modes. Plots of them can be found in Figures 5.5, 5.6, 5.1, 5.2, 5.7, 5.8, 5.3 and 5.4. Note that although the magnitude of the singular vectors is arbitrary, the spatial structure is not. Furthermore, the relative magnitudes of the decomposed singular vector parts are not arbitrary (for example, if the height is scaled by x, the relative vorticity must be scaled by x as well).

(2) For the C grid scheme with dissipation, the only stationary mode found is one with constant height with zero relative vorticity and divergence.

(3) Again, there were no stationary modes found for the Z grid scheme with or without dissipation. However, the zero frequency modes from the eigensolver did converge, and they can be found in Figures 5.11, 5.9, 5.12 and 5.10. Their spatial structure was very similar to that found in the C grid case.

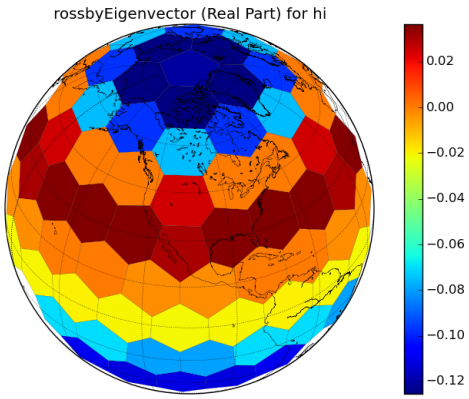

FIGURE 5.1. Fluid height for stationary mode with frequency equal to zero on icosahedral grid (C grid scheme)

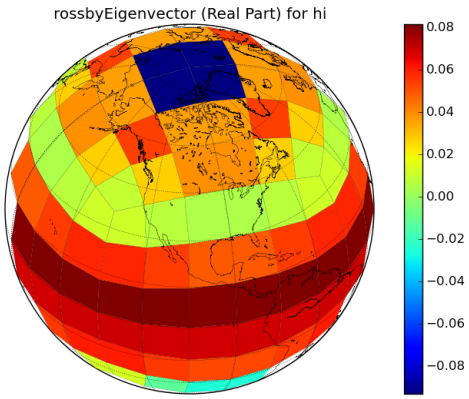

FIGURE 5.2. Fluid height for stationary mode with frequency equal to zero on cubed-sphere grid (C grid scheme)

(4) In contrast with the results in Weller 2012, all of the stationary ($\omega = 0$) and quasi-stationary ($\omega \approx 0$) modes for the schemes without dissipation were zonally symmetric. This is probably due to two reasons: one, the use of an actual cubed sphere grid instead of the "Voronoized" cube; and two, a more accurate determination of $\mathbf{A}$. Weller 2012 determined $\mathbf{A}$ by running the nonlinear model, which is approximate. Our approach uses the analytic definition of the schemes to get an exact $\mathbf{A}$ for the linearized model.

5.3.4.3. *Conclusions.*

From the above analysis, it is clear that the schemes on quasi-uniform planar grids are behaving in the expected manner. Both the icosahedral and cubed-sphere grids support zonally symmetric stationary modes in the case of variable f, and have geostrophic modes in the case of constant f. In addition, no spurious stationary modes were found for either scheme, for both constant f and variable f. This accords with the theoretical results above.

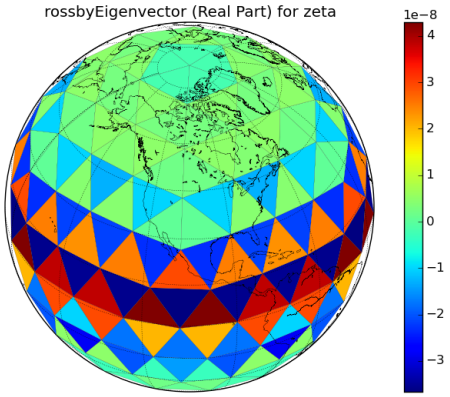

FIGURE 5.3. Relative vorticity for stationary mode with frequency equal to zero on icosahedral grid (C grid scheme)

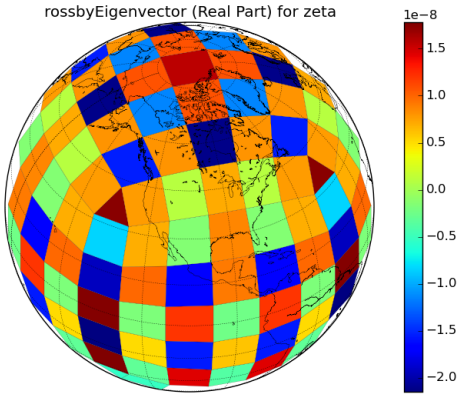

FIGURE 5.4. Relative vorticity for stationary mode with frequency equal to zero on cubed-sphere grid (C grid scheme)

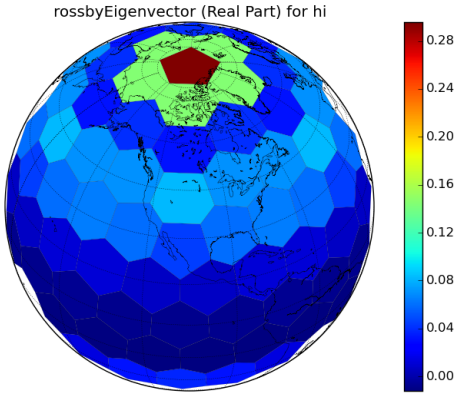

FIGURE 5.5. Fluid height for stationary mode with frequency $3.07873e^{-16}$ on icosahedral grid (C grid scheme)

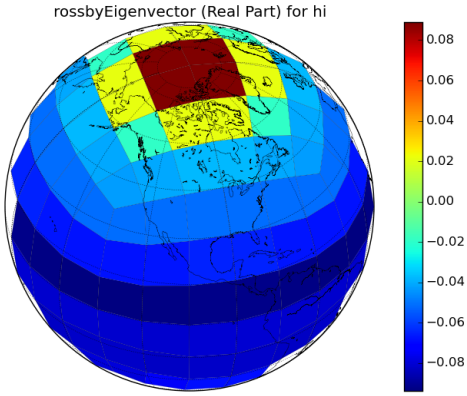

FIGURE 5.6. Fluid height for stationary mode with frequency $2.1704e^{-16}$ on cubed-sphere grid (C grid scheme)

As predicted from the planar grid results, dissipation does not alter the mode structures. It simply leads to damping of the stationary modes.

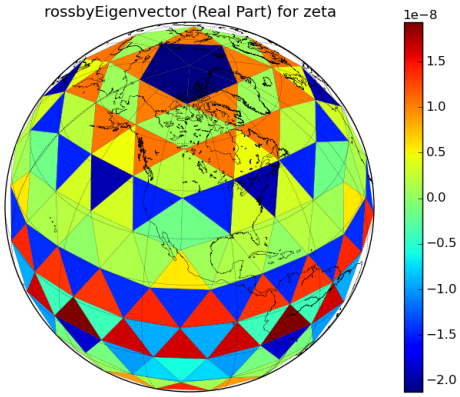

FIGURE 5.7. Relative vorticity for stationary mode with frequency $3.07873e^{-16}$ on icosahedral grid (C grid scheme)

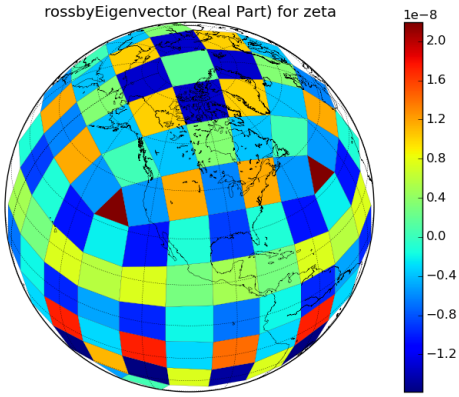

FIGURE 5.8. Relative vorticity for stationary mode with frequency $2.1704e^{-16}$ on cubed-sphere grid (C grid scheme)

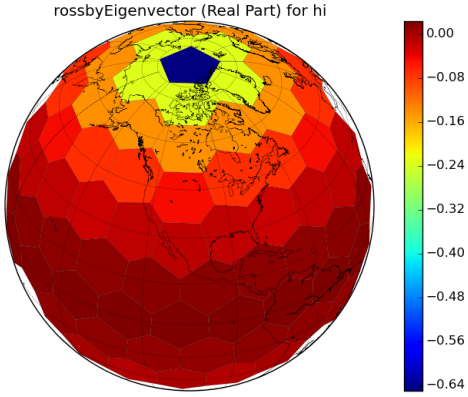

FIGURE 5.9. Fluid height for stationary mode with frequency equal to zero on icosahedral grid (Z grid scheme)

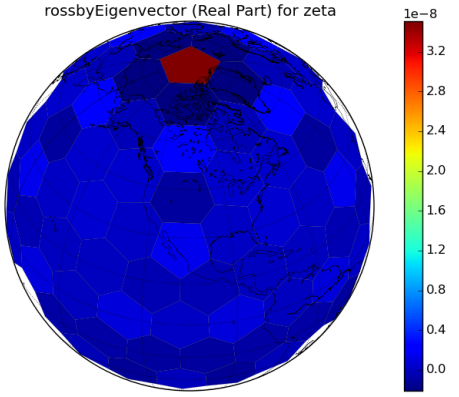

FIGURE 5.10. Relative vorticity for stationary mode with frequency equal to zero on icosahedral grid (Z grid scheme)

5.4. NUMERICAL PROPAGATING MODES

5.4.0.4. *Discrete in Space, Continuous in Time.*

The propagating linear modes of a numerical scheme are the solution of

$$i\sigma\vec{x} = \mathbf{A}\vec{x} \tag{315}$$

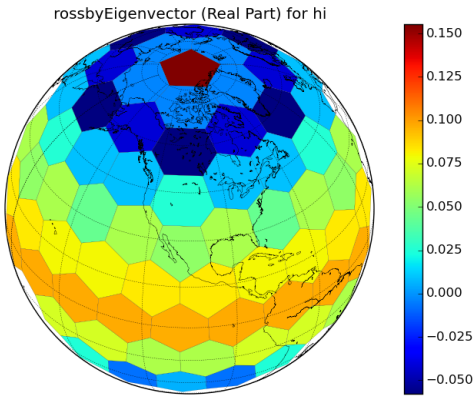

FIGURE 5.11. Fluid height for stationary mode with frequency equal to $5.3755e^{-16}$ on icosahedral grid (Z grid scheme)

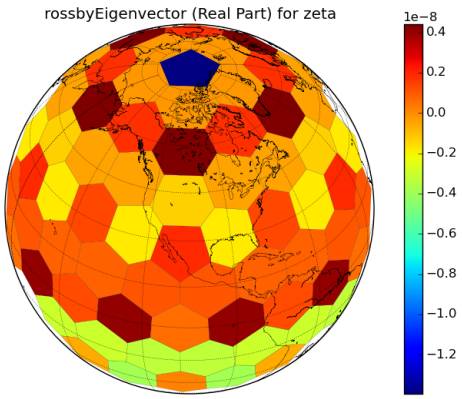

FIGURE 5.12. Relative vorticity for stationary mode with frequency equal to $5.3755e^{-16}$ icosahedral grid (Z grid scheme)

where continuity in time as $e^{i\sigma t}$ has been assumed. Thus the propagating modes are associated with the eigendecomposition (eigenvalues and eigenvectors) of the matrix $\mathbf{A}$. In practice, this system is solved as

$$\omega\vec{x} = \mathbf{A}\vec{x} \tag{316}$$

Equating $i\sigma$ and ω, and splitting each into real and imaginary parts gives

$$\sigma_r = \omega_i \tag{317}$$

$$\sigma_i = -\omega_r \tag{318}$$

Therefore growing modes are characterized by

$$\omega_r > 0 \rightarrow \sigma_i < 0 \tag{319}$$

and damped modes are characterized by

$$\omega_r < 0 \rightarrow \sigma_i > 0 \tag{320}$$

This will be useful when analysing the results of adding dissipation.

5.4.1. Z Grid Scheme.

By assuming wave-like solutions in time ($e^{-i\sigma t}$) and using 302, an expression for the discrete wave dispersion relation is obtained as:

$$\frac{\sigma^2}{f^2}\hat{\delta} = (\mathbf{I} - \lambda^2 \mathbf{L})\hat{\delta} \tag{321}$$

This is an eigenvalue problem for the non-dimensional frequencies $\frac{\sigma}{f}$. This can also be written as

$$(\frac{\sigma^2 - f^2}{f^2\lambda^2})\hat{\delta} = \mathbf{L}\hat{\delta} \tag{322}$$

Perfect correspondence with the continuous case (for the plane) would imply that $\mathbf{L}\hat{\delta} = -K^2\hat{\delta}$ is satisfied for the eigenvectors: the eigenvalues of $\mathbf{L}$ are simply the (squared) sum of squares of the spatial wavenumbers of the eigenvector. For the sphere, it would require that $\mathbf{L}\hat{\delta} = \frac{n(n+1)}{a^2}\hat{\delta}$. The eigenspectrum of discrete Laplacian operators on various grids has been very well studied, and in general it is a good approximation to the above requirements. This explains why the Z grid dispersion relation is uniformly good independent of $\frac{\lambda}{d}$.

5.4.2. C Grid Scheme.

Again assuming wave-like solutions in time ($e^{-i\sigma t}$), and by using 288 we obtain:

$$H\mathbf{D}\hat{u} + i\sigma\hat{h} = 0 \tag{323}$$

$$f\mathbf{Q}\hat{u} + g\mathbf{G}\hat{h} + i\sigma\hat{u} = 0 \tag{324}$$

This can be solved to yield

$$\frac{\sigma^2}{f^2}\mathbf{I} - \frac{i\sigma}{f}\mathbf{Q} - \lambda^2\mathbf{GD} = 0 \tag{325}$$

Unfortunately, unlike the Z grid case, this does not have a clean solution.

5.4.3. Planar Grid Results.

To begin, the propagating modes are investigated analytically on uniform planar grids for the case of constant f with $\frac{\lambda}{d} = 2.0$. Dispersion relationships are obtained by simply substituting spatial solutions proportional to $e^{ikx+ily}$ into the governing equations (continuous, C grid or Z grid), and solving the resulting system using a computer algebra system (SymPy, [128]). Figures 5.13 and 5.14 show the results on square and hexagonal grids without dissipation. These results are well known (they can be found in [100] and [132]), but their reproducibility is a useful check of the code. More details (including specific equations) about the analytic dispersion relationships and allowed wavenumbers on various grids can be found in Appendix C. Figures 5.15 and 5.16 show the real part of the dispersion relationship for square and hexagonal grids when dissipation is added; and Figure 5.17 and 5.18 show the imaginary part of the dispersion relationship when dissipation is added. Only the positive branch of inertia-gravity waves is shown (results from the negative branch are identical).

The following parameters were used to make the plots below: $g = 9.81ms^{-1}$, $f = 0.0001s^{-1}$, $\bar{H} = 400m$, $\nu = 1000.0m^2s^{-1}$ and dx chosen such that $\frac{\lambda}{d} = 2.0$, which gives $dx \approx 313.209km$.

The primary results of this sub-section are the effects of dissipation on the dispersion relationship. Some key points are summarized below:

(1) The addition of dissipation does not noticeably alter the real part of the dispersion relationships.

(2) The imaginary part of all of the dispersion relations is positive, and therefore is damping.

(3) The Z grid scheme is slightly more isotropic than the C grid scheme, especially at higher wavenumber.

(4) The hexagonal grid is more isotropic than the square grid, for all schemes and for both real and imaginary parts.

(5) Higher frequencies are more damped than lower frequencies.

(6) The C and Z grid damping appears to be almost identical in magnitude

(7) All three schemes (continuous, C and Z) retain geostrophic modes that have zero real frequency and therefore do not propagate. However, the modes now have non-zero imaginary frequencies, and are therefore damped. In addition, the damping appears to be an increasing function of spatial wavenumber (not shown)

It will be interesting to see if these conclusions hold on quasi-uniform spherical grids, and in the case of variable f.

5.4.4. Quasi-Uniform Spherical Grid Results.

As in the previous section, only results from the doubly-conservative C and Z grid schemes are shown. The results from the total energy and potential enstrophy conserving variants are similar. The numerical eigenvalues and eigenvectors are computed using Scipy by the same procedure as used for the SVD calculation. Just like the singular vectors, the eigenvectors are decomposed into h_i and u_e (from which ζ_v and δ_i are computed) for the C grid scheme, and h_i, ζ_i and δ_i for the Z grid scheme.

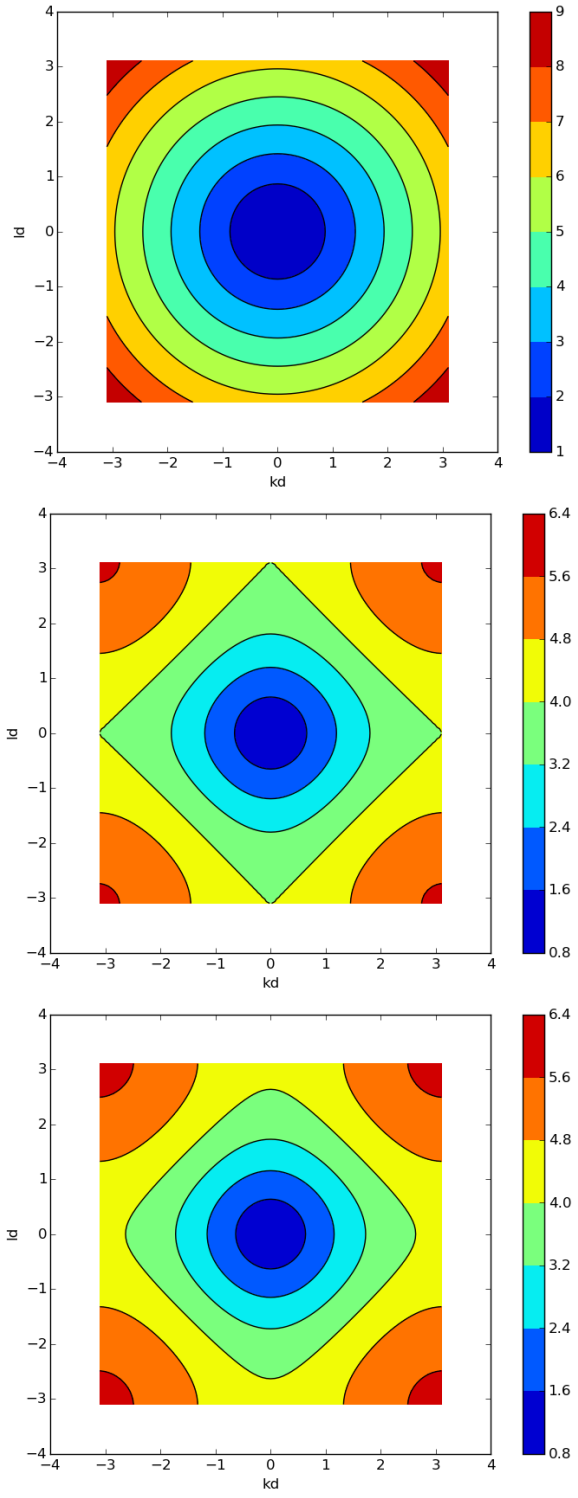

FIGURE 5.13. Dispersion relations for perfect square grid with $\frac{\lambda}{d} = 2.0$, without dissipation. Normalized frequency $\frac{\sigma}{f}$ versus non-dimensional wavenumbers kd and ld is plotted. Top panel is continuous system, middle panel is C grid scheme, bottom panel is Z grid scheme.

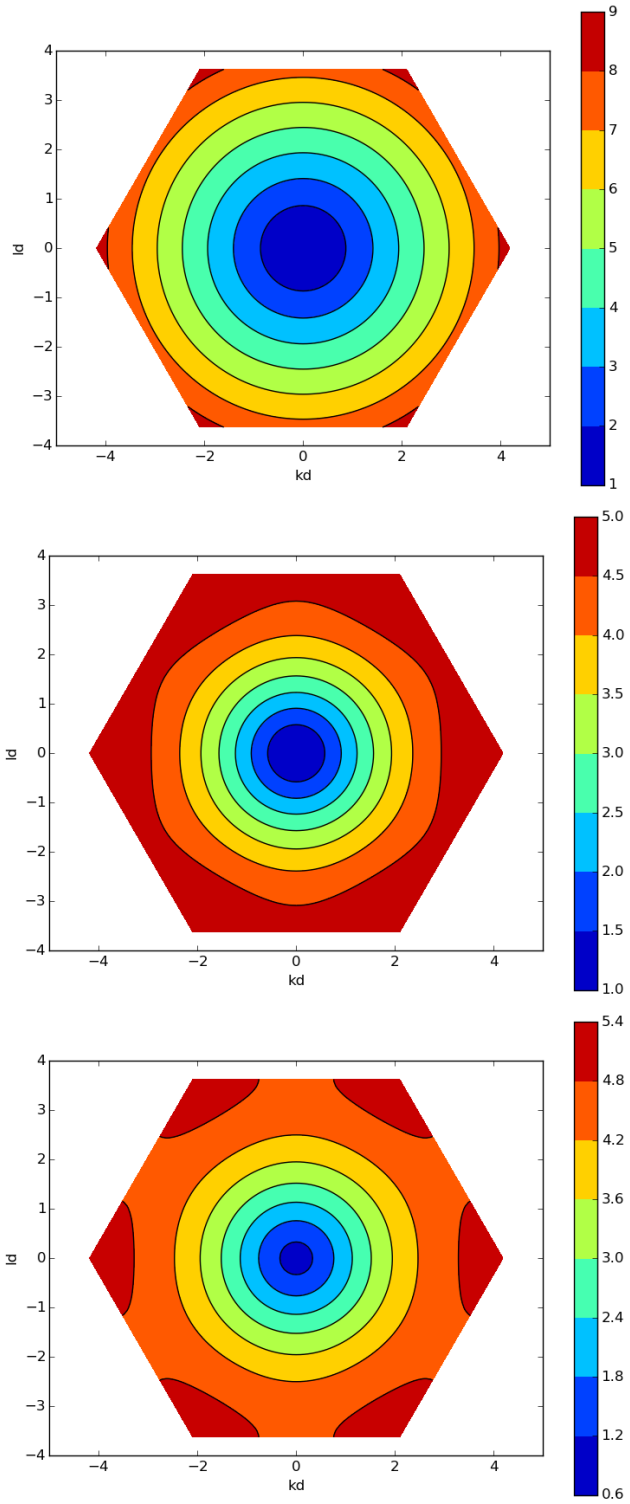

FIGURE 5.14. Dispersion relations for perfect hexagonal grid with $\frac{\lambda}{d} = 2.0$, without dissipation. Normalized frequency $\frac{\sigma}{f}$ versus non-dimensional wavenumbers kd and ld is plotted. Top panel is continuous system, middle panel is C grid scheme, bottom panel is Z grid scheme.

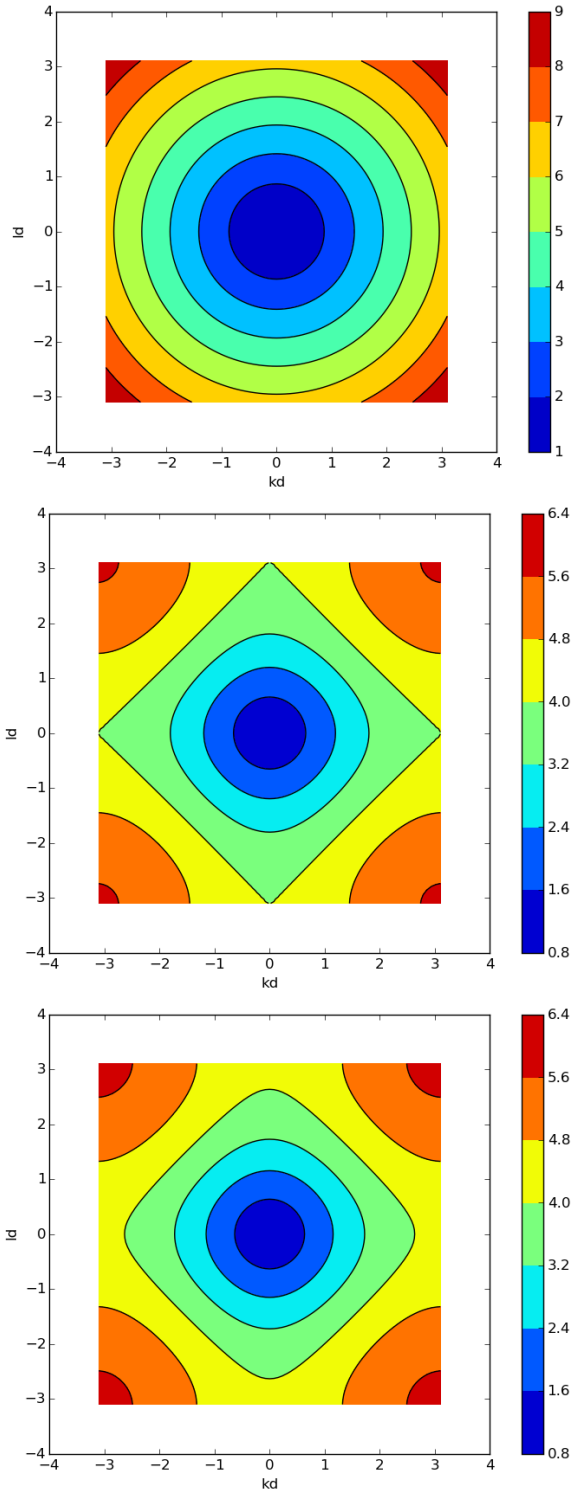

FIGURE 5.15. Real part of dispersion relations for perfect square grid with $\frac{\lambda}{d} = 2.0$, with dissipation. Normalized frequency $\frac{\sigma}{f}$ versus non-dimensional wavenumbers kd and ld is plotted. Top panel is continuous system, middle panel is C grid scheme, bottom panel is Z grid scheme.

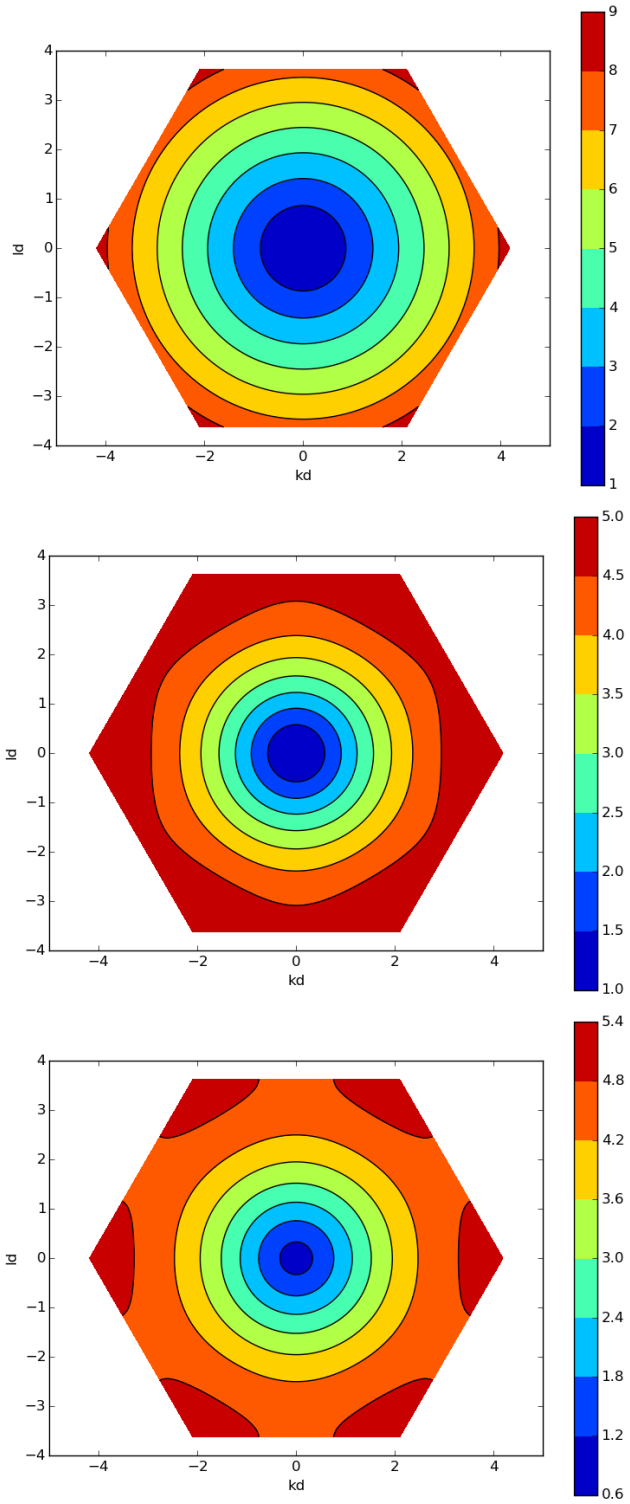

FIGURE 5.16. Real part of dispersion relations for perfect hexagonal grid with $\frac{\lambda}{d} = 2.0$, with dissipation. Normalized frequency $\frac{\sigma}{f}$ versus non-dimensional wavenumbers kd and ld is plotted. Top panel is continuous system, middle panel is C grid scheme, bottom panel is Z grid scheme.

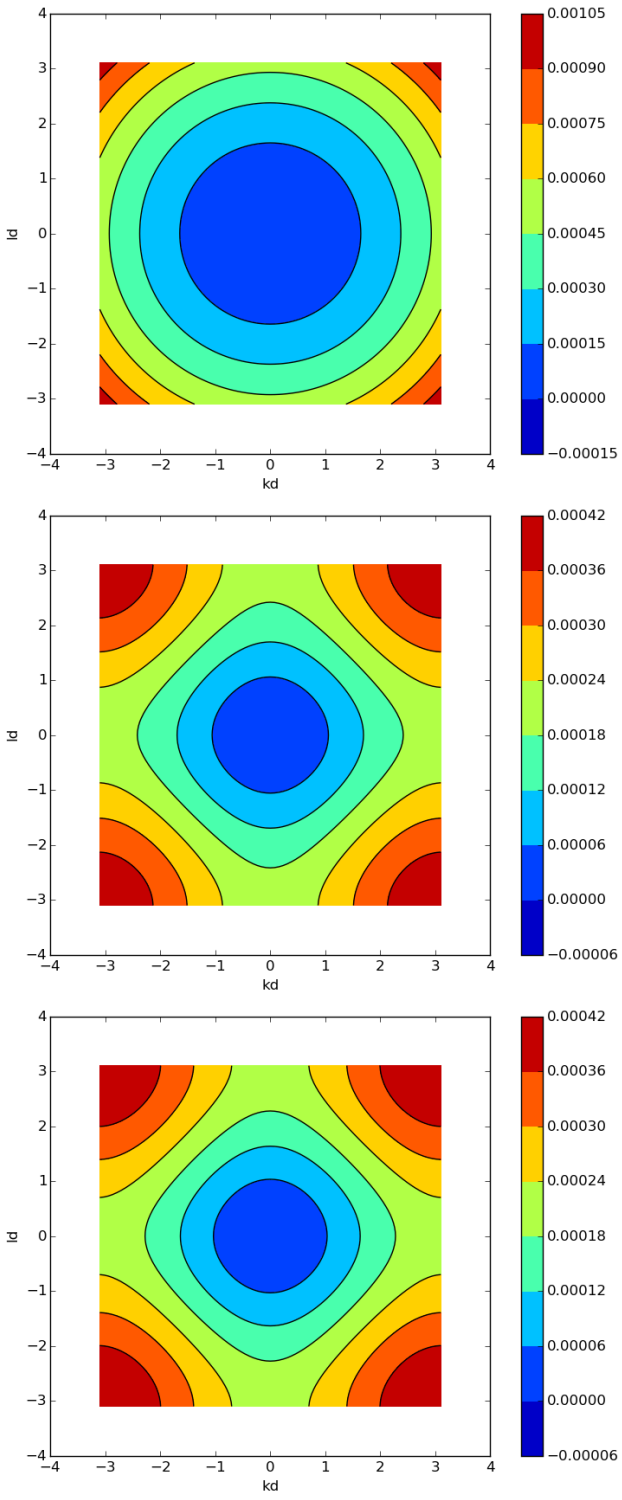

FIGURE 5.17. Imaginary part of dispersion relations for perfect square grid with $\frac{\lambda}{d} = 2.0$, with dissipation. Normalized frequency $\frac{\sigma}{f}$ versus non-dimensional wavenumbers kd and ld is plotted. Top panel is continuous system, middle panel is C grid scheme, bottom panel is Z grid scheme.

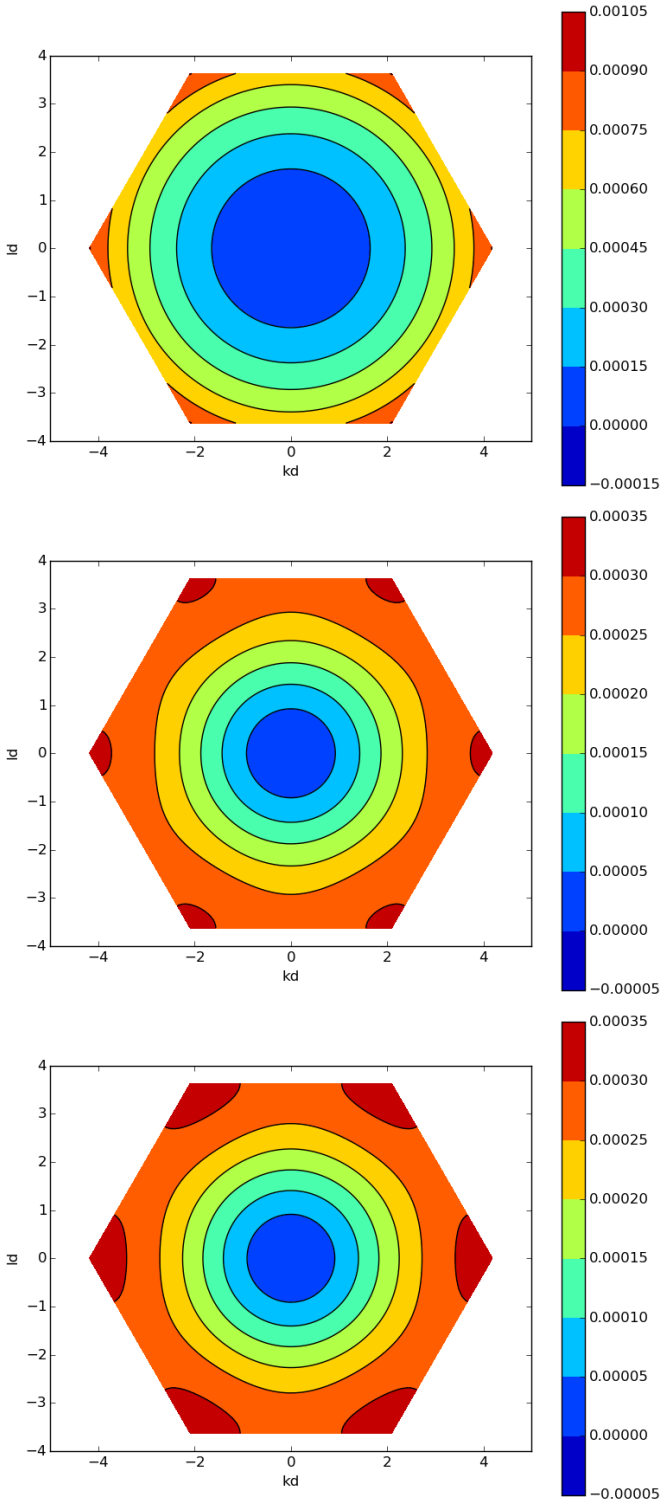

FIGURE 5.18. Imaginary part of dispersion relations for perfect hexagonal grid with $\frac{\lambda}{d} = 2.0$, with dissipation. Normalized frequency $\frac{\sigma}{f}$ versus non-dimensional wavenumbers kd and ld is plotted. Top panel is continuous system, middle panel is C grid scheme, bottom panel is Z grid scheme.

5.4.4.1. *f-sphere results.*

Figure 5.19 shows the numerical dispersion relationship on the f-sphere without dissipation for the C grid scheme (which is the same for all three variants in the constant f case) on icosahedral (G2) and cubed-sphere (C2) grids, and the Z grid scheme on icosahedral grids (G2). Only the positive mode branches are shown. Red crosses indicate stationary modes, black crosses indicate inertia-gravity modes and green circles indicate the theoretical frequencies obtained from equation 279. Plots were obtained by sorting the numerical eigenvalues by frequency, and assuming that all zero frequency modes were geostrophic modes. This follows the approach used in Weller 2012 and [140], and the results for the C grid on icosahedral grids agree with those papers. In correspondence with those papers, the following parameters were used: $g = 9.80616ms^{-1}$, $a = 6371220m$, $\nu = 10^5 m^2 s^{-1}$ and $f = 0.0001s^{-1}$. $\bar{H}$ was chosen such that $\frac{\lambda}{d} = 2.0$, where d is the average grid spacing. The average grid spacing and other characteristics of the grids (including the number of inertia-gravity wave and stationary modes found) used in this Chapter can be found in Table 5.1.

TABLE 5.1. Grid Details

Grid	n_f	n_v	average de	IGW	Stationary	H	λ
G2	162	320	1916km	322	320	14974m	3832km
C2	216	218	1542km	430	218	9699m	3084km

Some key points from Figure 5.19 are summarized below:

(1) The number of modes obtained following the above procedure is correct. There are $2n_f - 2$ inertia-gravity modes and n_v stationary modes for the C grid scheme, and $2n_f$ inertia-gravity and n_f stationary modes for the Z grid scheme.

(2) The agreement between the theoretical mode frequencies and the numerical mode frequencies gets worse as frequency increases. This is the expected behaviour for a numerical method.

(3) The mode frequencies are quantized, especially at low frequency.

(4) The C grid on the cubed-sphere grid has higher frequency inertia-gravity waves, but this is expected since the resolution is a little better.

(5) The spectrum is well behaved for all schemes on all grids: there are no spectral gaps, and increasing frequency is associated with increasing spatial wavenumber.

(6) The frequency spectrum is flattening out as wavenumber increases for the C grid on icosahedral grids and the Z grid on icosahedral grids, as expected from the theory of C grids on hexagonal grids. However, it is linearly increasing for the C grid scheme on cubed-sphere grids. This is in correspondence with the continuous system, but disagrees with the theory for C grids on square grids. Closer inspection of the highest frequency modes reveals that they are localized in structure around the singular points of the cubed sphere. Therefore, as discussed in Weller 2012, such modes will simply propagate around the singular points, which is not physical. The highest frequency modes on the icosahedral grids (both C and Z) are also somewhat localized, but not nearly as bad as that seen on the cubed-sphere grid.

The numerical dispersion relations for the same system, but with dissipation added are plotted in Figures 5.20 and 5.21. As before, the key points are summarized below:

(1) Dissipation does not appear to change the real part of the spectrum. In particular, the stationary modes still exist, and the inertia-gravity wave frequencies are essentially the same.

(2) The imaginary part of the spectrum is positive everywhere, which means that the waves are damped.

(3) The values in the imaginary part of the spectrum are broadly comparable between C and Z grid schemes.

(4) The dissipation increases monotonically with mode index for inertia-gravity waves (and thus increase monotically with frequency). In addition, the dissipation is also quantized in the same manner as the real part of the spectrum.

(5) Dissipation is randomly distributed for stationary modes. This is probably due to the fact that mode index is no longer a measure of spatial frequency in the case of geostrophic modes, unlike the inertia-gravity waves.

(6) Dissipation does not change the spatial structure of the inertia-gravity waves. In particular, the localized mode structures seen at the highest frequencies on the cubed-sphere grid remain. A plot of mode structures for the highest frequency inertia-gravity waves can be found in Figure 5.26. Note that all grid have localized mode structures, although they are worst for the cubed-sphere.

These conclusions (with the exception of the distribution of dissipation for stationary modes) are basically the same as those found in the planar case.

5.4.4.2. *fullsphere results.*

Figure 5.22 shows the numerical dispersion relationship on the full sphere without dissipation for the C grid scheme (only the doubly-conservative version) on icosahedral and cubed-sphere grids, and the Z grid scheme on icosahedral grids. Only the positive mode branches are shown. Red crosses indicate Rossby modes and black crosses indicate inertia-gravity modes. Plots were obtained by sorting the numerical eigenvalues by frequency, and assuming that all zero frequency modes from the f-sphere case became Rossby modes. Although this undoubtedly means that some modes are mis-characterized, the approach follows that used in Weller 2012 and the results for the C grid on icosahedral grids agree with that paper. In correspondence with those papers, the following parameters were used: $g = 9.80616ms^{-1}$, $a = 6371220m$, $\nu = 10^5 m^2 s^{-1}$, $\bar{H} = \frac{10^5 m^2 s^{-1}}{g}$ and $\Omega = 0.0000729 2s^{-1}$. The

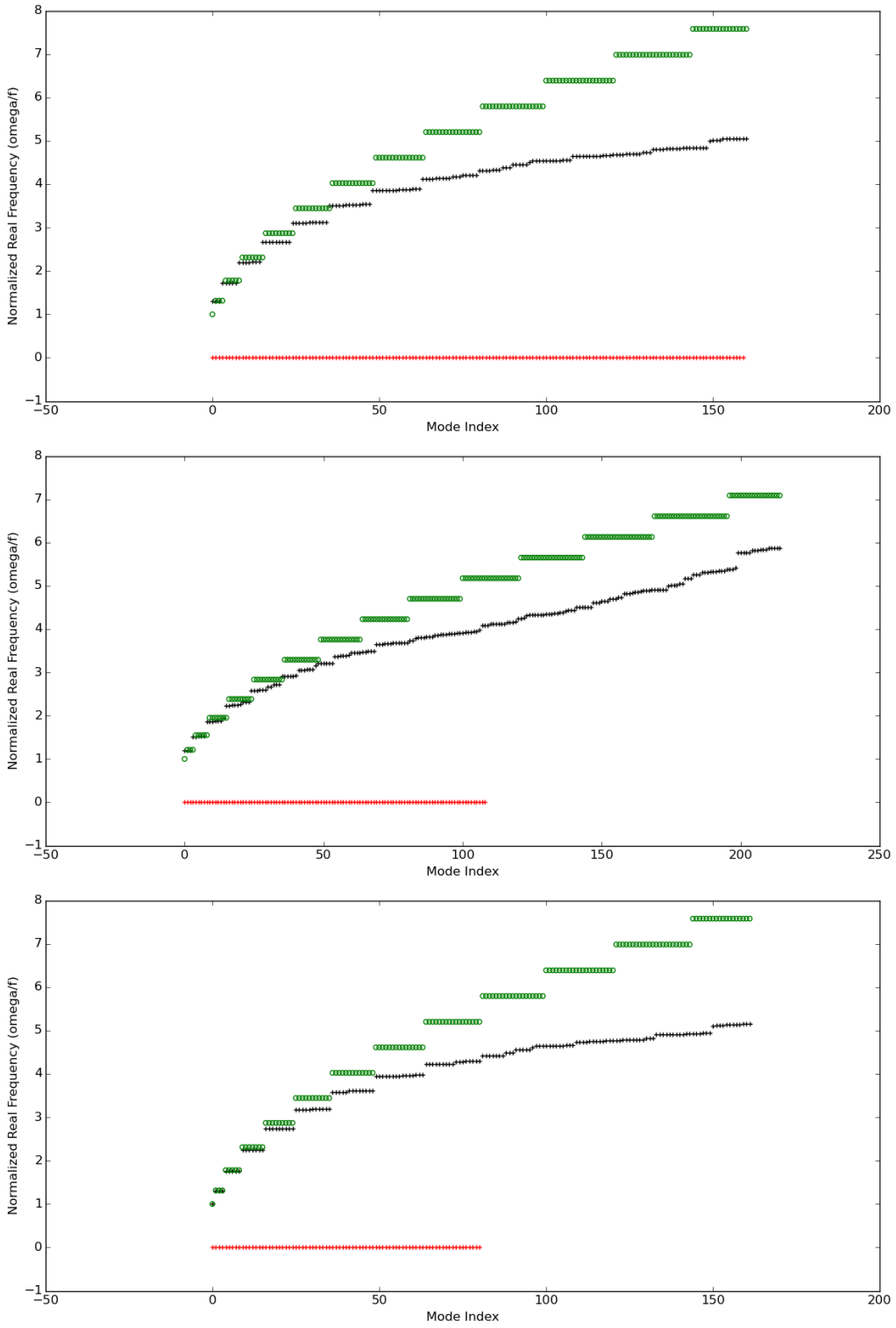

FIGURE 5.19. Dispersion relations for f-sphere on quasi-uniform spherical grids without dissipation. Normalized frequency $\frac{\sigma}{f}$ versus mode index (see discussion) is plotted. Top panel is C grid on icosahedral grid, middle panel is C grid on cubed-sphere grid, bottom panel is Z grid scheme on icosahedral grid.

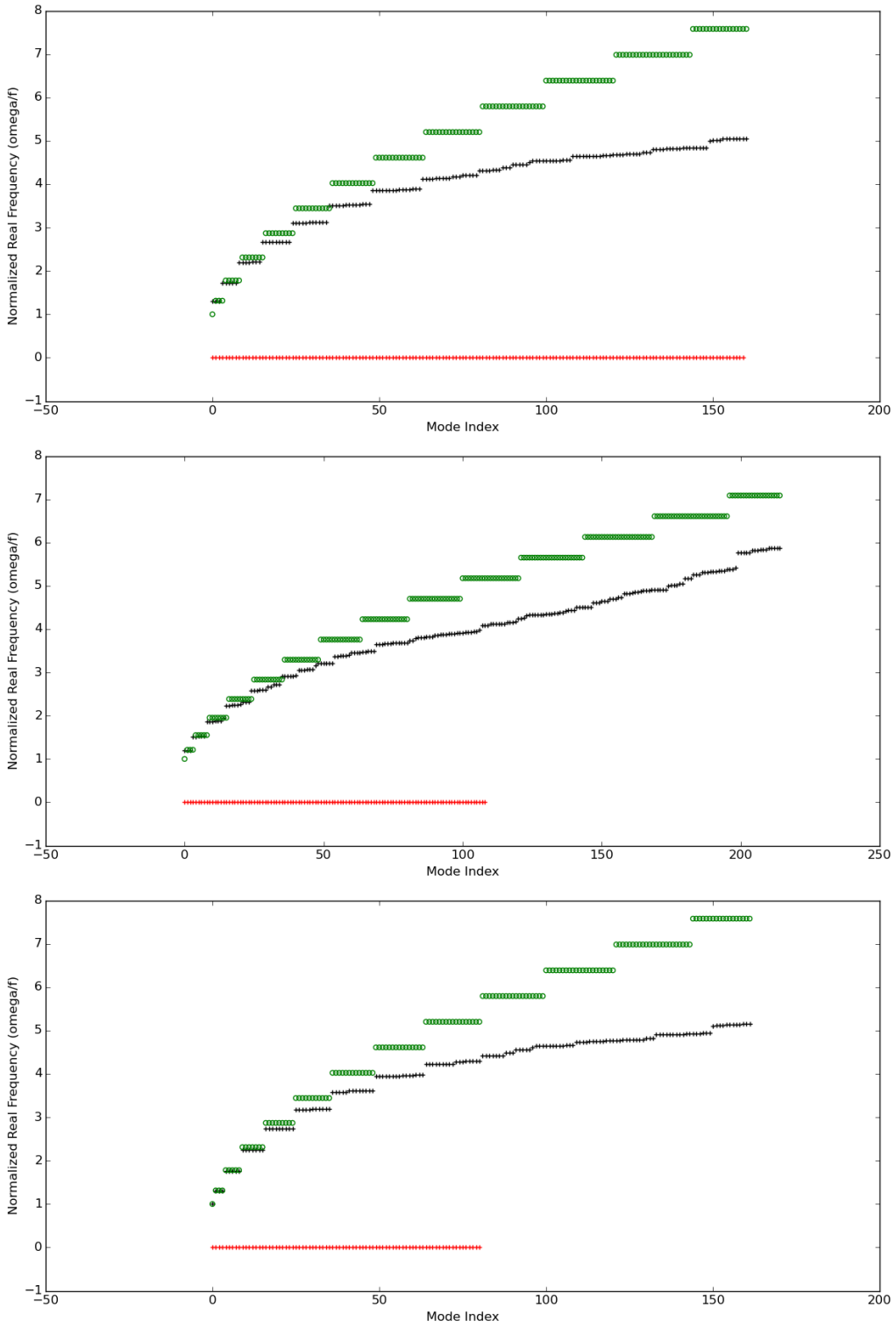

FIGURE 5.20. Real part of dispersion relations for f-sphere on quasi-uniform spherical grids with dissipation. Normalized frequency $\frac{\sigma}{f}$ versus mode index (see discussion) is plotted. Top panel is C grid on icosahedral grid, middle panel is C grid on cubed-sphere grid, bottom panel is Z grid scheme on icosahedral grid.

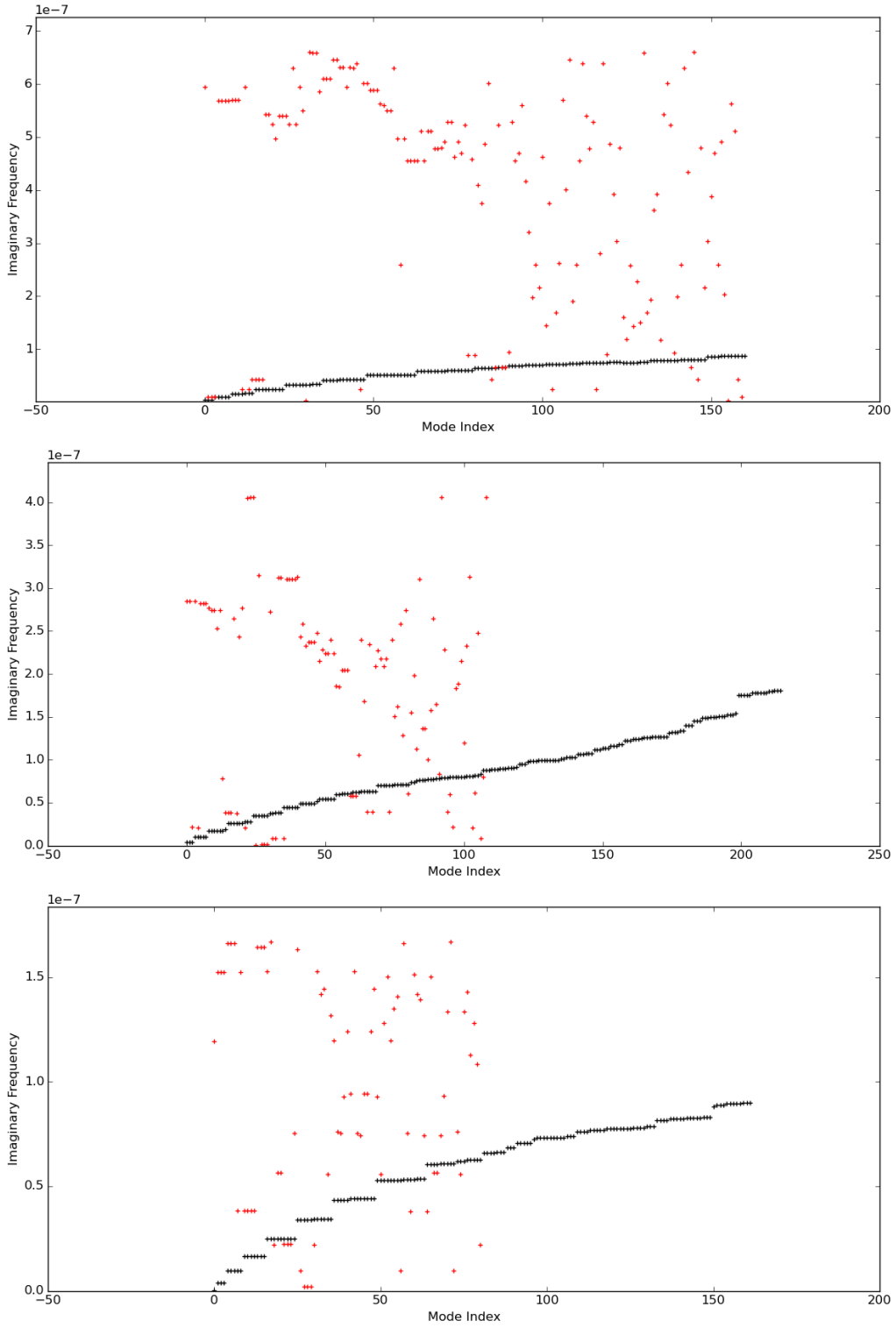

FIGURE 5.21. Imaginary part of dispersion relations for f-sphere on quasi-uniform spherical grids with dissipation. Frequency versus mode index (see discussion) is plotted. Top panel is C grid on icosahedral grid, middle panel is C grid on cubed-sphere grid, bottom panel is Z grid scheme on icosahedral grid.

smallest Rossby radius occurs at the poles, and is equal to $2168.32km$. This is marginally resolved for the grid resolution chosen.

Some key points from Figure 5.22 are summarized below:

(1) The mode frequencies are less quantized than in the f-sphere case, probably due to the influence of variable f

(2) Rossby wave frequency is comparable between schemes, as is inertia-gravity wave frequency.

(3) The spectrum is well behaved for all schemes on all grids: there are no spectral gaps, and increasing frequency is associated with increasing spatial wavenumber.

(4) The spurious Rossby modes on the icosahedral C grid scheme are all low frequency, as predicted for theoretical considerations on the β plane.

(5) The spectrum is again flattening with increasing wavenumber for the icosahedral grid schemes, and linear with wavenumber for the cubed-sphere grid scheme. As before, the highest frequency modes on both grids are localized, with the cubed-sphere being noticeably worse than the icosahedral grids.

(6) A plot of mode structures for the highest frequency inertia-gravity waves can be found in Figure 5.27, and for a representative Rossby wave in Figure 5.25. Note that all grids have localized modes for the high frequency inertia-gravity wave structures, although they are worst for the cubed-sphere. In addition, all of the grids are capable of producing realistic looking low wavenumber Rossby wave mode structures. Visual inspection of the full set of Rossby wave mode structures for the C grid scheme does not reveal any immediately obvious spurious mode structures on the icosahedral grid when compared to the C grid scheme, although such structures must be present.

The numerical dispersion relations for the same system, but with dissipation added are plotted in Figures 5.23 and 5.24. As before, the key points are summarized below:

(1) Dissipation does not appear to change the real part of the spectrum. In particular, both the inertia-gravity wave and Rossby wave frequencies are essentially the same.

(2) The imaginary part of the spectrum is positive everywhere, which means that the waves are damped.

(3) The values in the imaginary part of the spectrum are broadly comparable between C and Z grid schemes.

(4) The dissipation increases monotonically with mode index for inertia-gravity waves (and thus increases monotonically with frequency). In addition, the dissipation is also quantized in the same manner as the real part of the spectrum.

(5) Dissipation appears to be decreasing with increasing mode index for Rossby modes, although it is not monotonic. This is NOT due to the spurious Rossby modes on the icosahedral C grid, since the same effect is observed for the C grid on the cubed-sphere grid, and for the Z grid on the icosahedral grid.

(6) Yet again, dissipation does not change the mode structures seen.

These conclusions (with the exception of the distribution of dissipation for Rossby modes) are basically the same as those found in the planar case for constant f, and also those found numerically for the f-sphere.

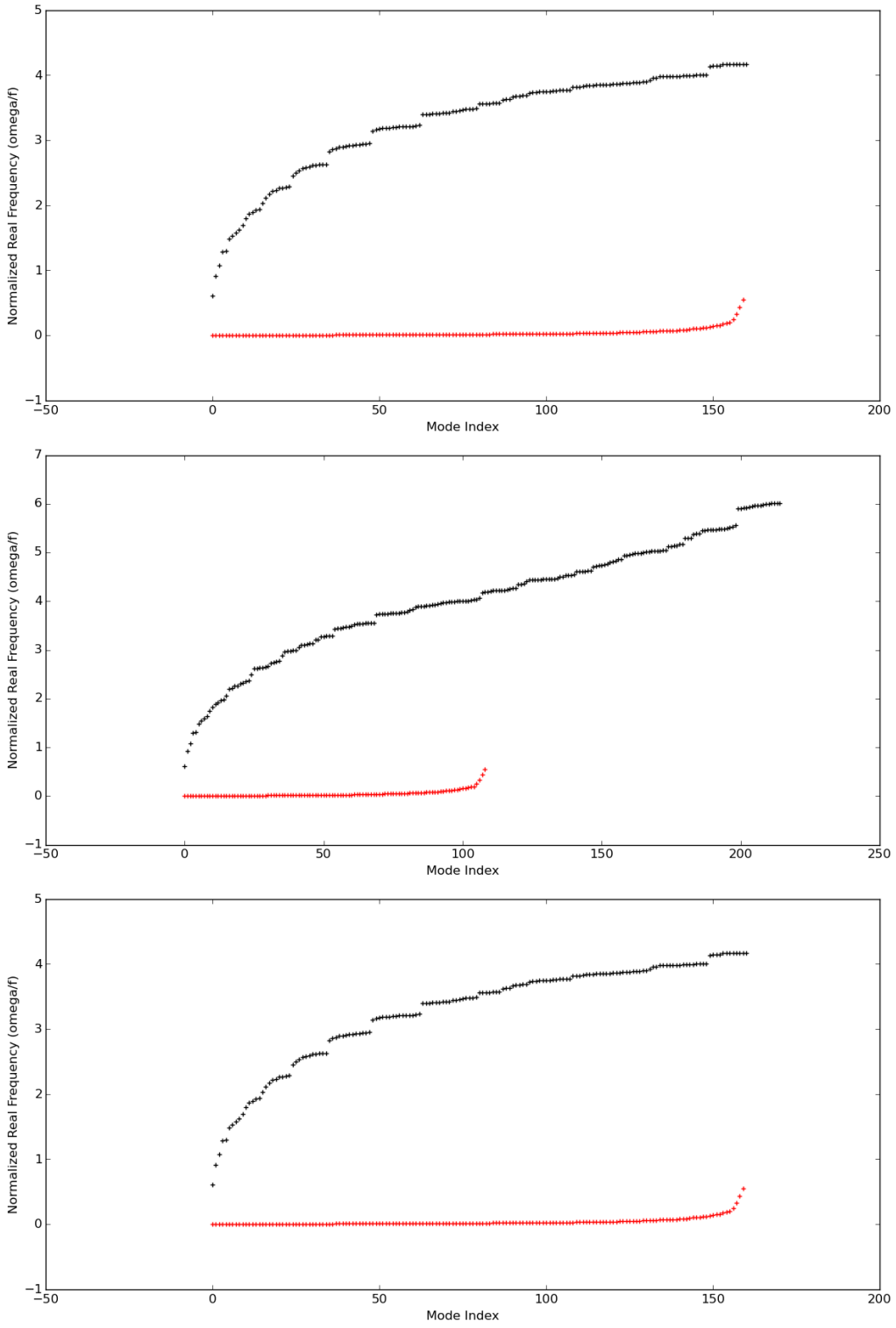

FIGURE 5.22. Dispersion relations for full sphere on quasi-uniform spherical grids without dissipation. Normalized frequency $\frac{\sigma}{f}$ versus mode index (see discussion) is plotted. Top panel is C grid (doubly conservative version) on icosahedral grid, middle panel is C grid (doubly conservative version) on cubed-sphere grid, bottom panel is Z grid scheme on icosahedral grid.

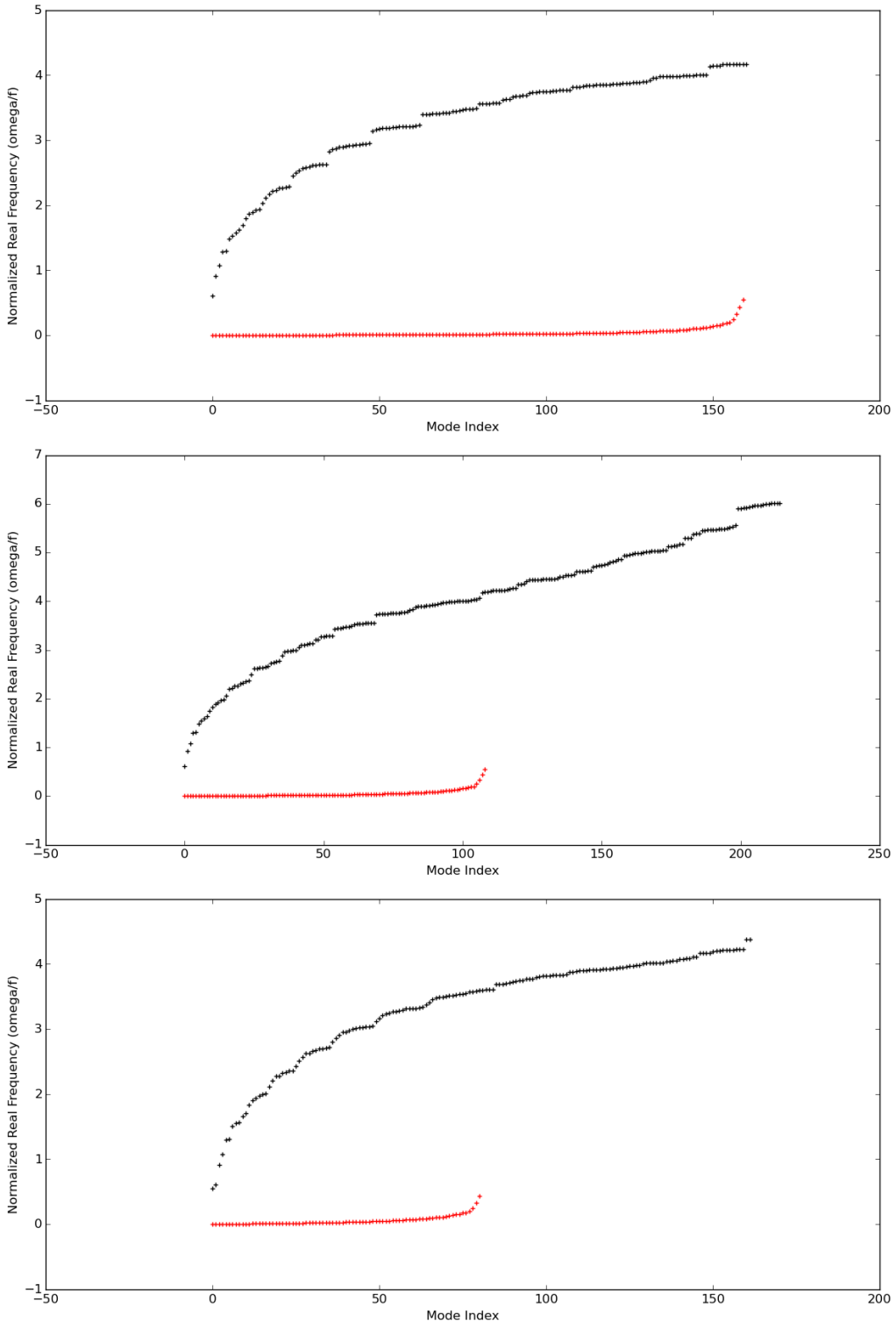

FIGURE 5.23. Real part of dispersion relations for full sphere on quasi-uniform spherical grids with dissipation. Normalized frequency $\frac{\sigma}{f}$ versus mode index (see discussion) is plotted. Top panel is C grid (doubly conservative version) on icosahedral grid, middle panel is C grid (doubly conservative version) on cubed-sphere grid, bottom panel is Z grid scheme on icosahedral grid.

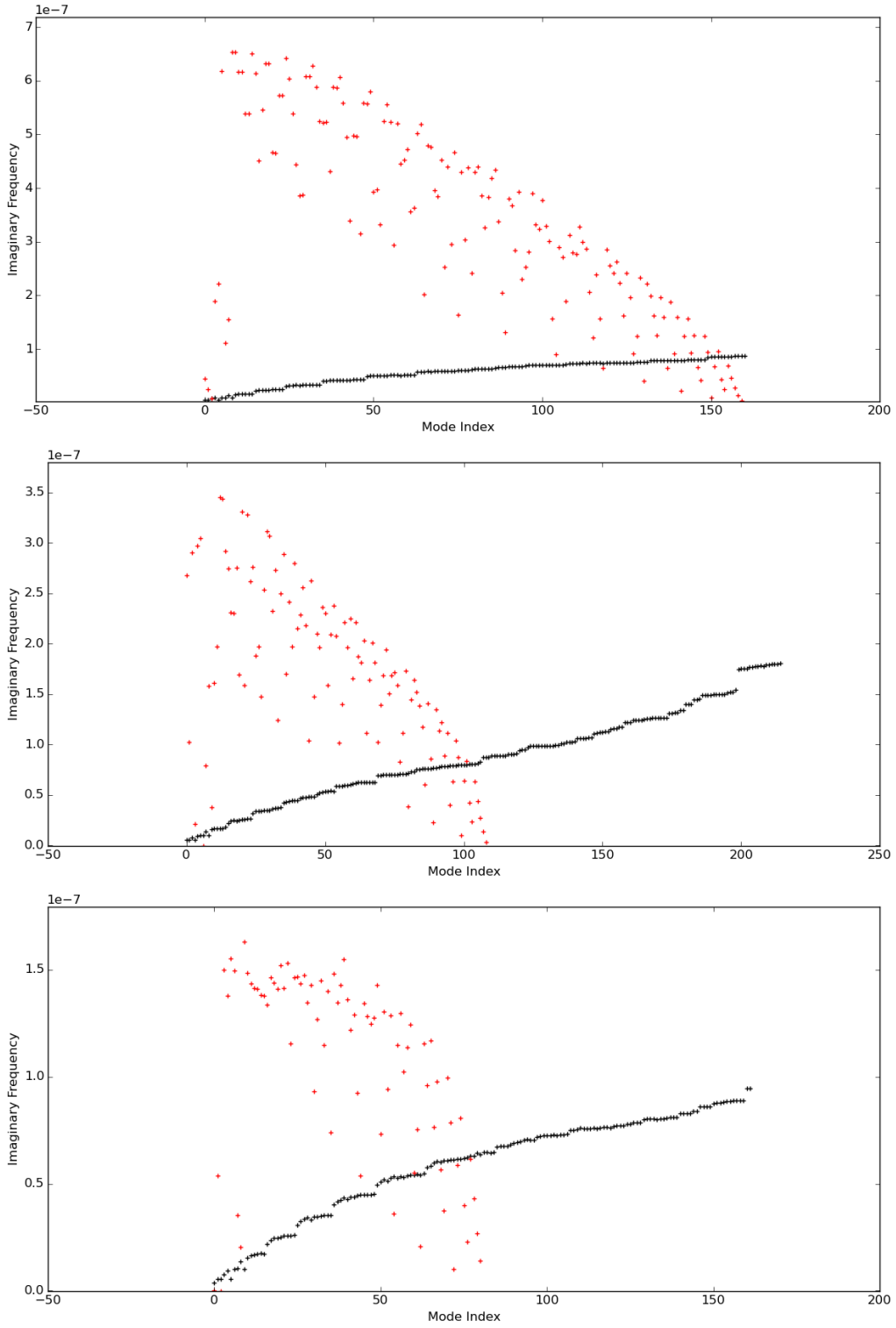

FIGURE 5.24. Imaginary part of dispersion relations for full sphere on quasi-uniform spherical grids with dissipation. Frequency versus mode index (see discussion) is plotted. Top panel is C grid (doubly conservative version) on icosahedral grid, middle panel is C grid (doubly conservative version) on cubed-sphere grid, bottom panel is Z grid scheme on icosahedral grid.

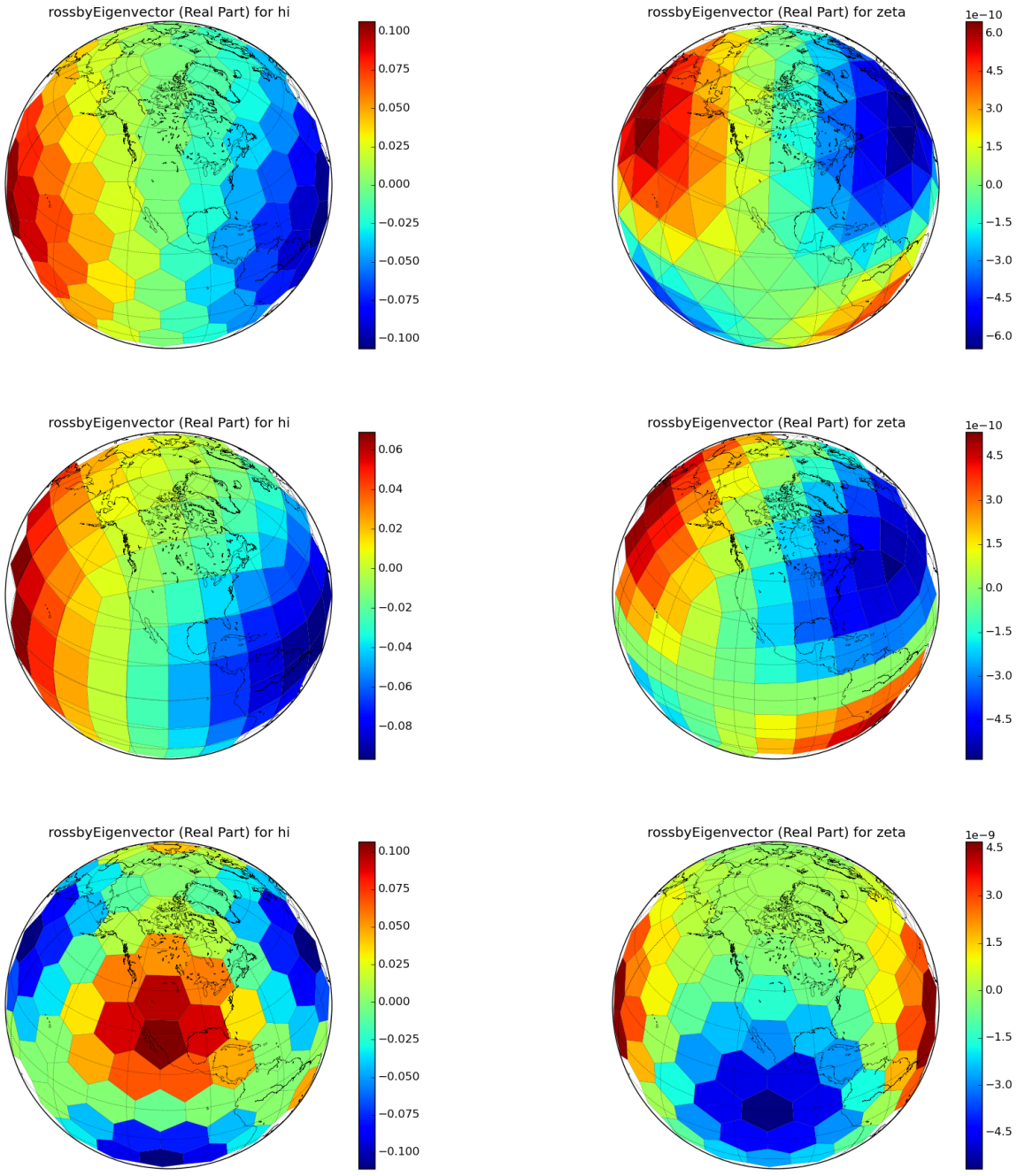

FIGURE 5.25. Spatial structures for a selected Rossby wave for various grids and schemes. On the left is fluid height, on the right is relative vorticity. The top row is the C grid scheme on icosahedral grids, the middle row is the C grid scheme on cubed-sphere grids and the bottom row is the Z grid scheme

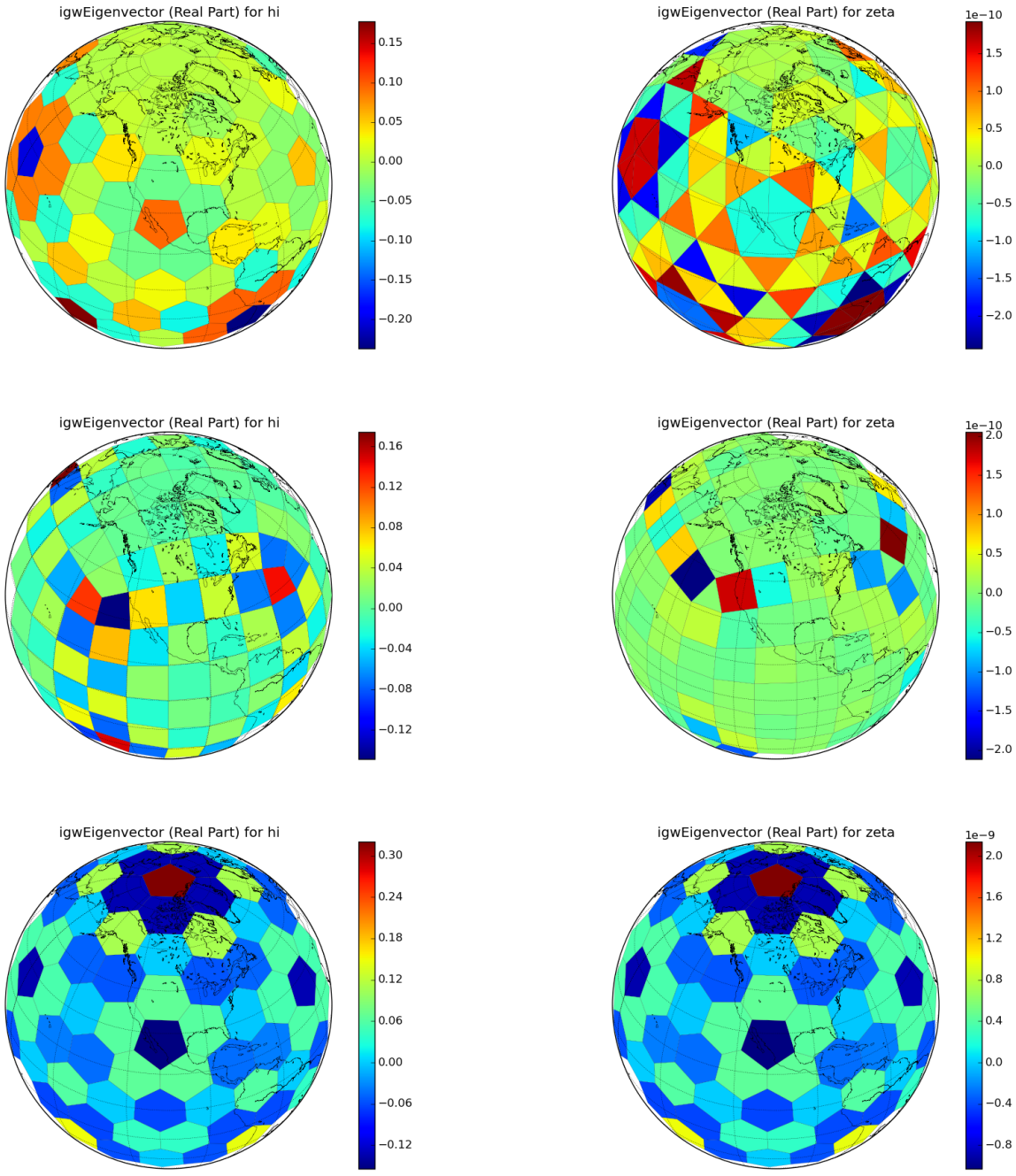

FIGURE 5.26. Spatial structures for the highest frequency inertia-gravity waves on the f-sphere for various grids and schemes. On the left is fluid height, on the right is relative vorticity. The top row is the C grid scheme on icosahedral grids, the middle row is the C grid scheme on cubed-sphere grids and the bottom row is the Z grid scheme

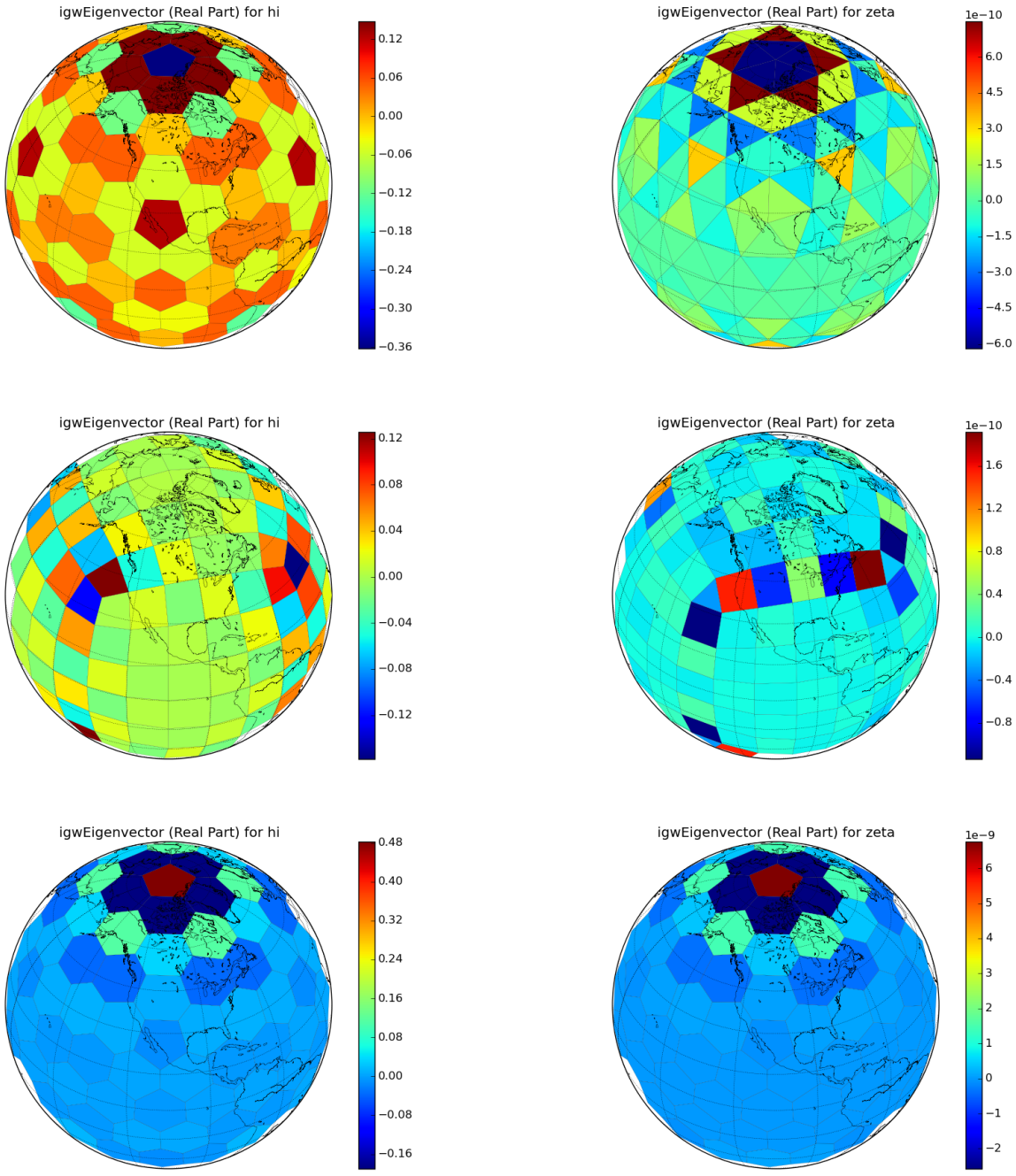

FIGURE 5.27. Spatial structures for the highest frequency inertia-gravity waves on the full sphere for various grids and schemes. On the left is fluid height, on the right is relative vorticity. The top row is the C grid scheme on icosahedral grids, the middle row is the C grid scheme on cubed-sphere grids and the bottom row is the Z grid scheme

5.5. Chapter Summary

A detailed examination of the linear modes for both the C and Z grid schemes was performed, from a theoretical basis and numerically through the eigendecomposition and singular value decomposition of $\mathbf{A}$. The results were broadly similar to those found in Weller 2012, with the exception of all stationary modes being zonally symmetric for both grids. The theoretical predictions about stationary modes, and the planar grid results for C and Z grid scheme on uniform square or hexagonal grids were all found to carry over to the case of quasi-uniform grids. In addition, the effects of dissipation were quantified. The majority of this material is new, with the exception of planar grid dispersion relationships.

CHAPTER 6

Evaluation and Comparison of the Generalized C and Z Grid Schemes

This chapter concerns itself with the evaluation and comparison of the generalized C grid and Z grid schemes presented in Chapter 3 and Chapter 4 , with a focus on their non-linear properties (the linear properties have been explored in Chapter 5). This is done through the running of various test cases from the literature (described in more detail below), and determining the order of accuracy for various operators.

6.1. Details of Runs

A wide range of test cases were run to evaluate the two schemes. These include test cases 2 (Solid Body Rotation/Zonal Flow), 5 (Flow over a Mountain) and 6 (Rossby-Haurwitz Wave) from the Williamson set ([156]), the Galewsky et. al barotropically unstable jet ([43]) and a forced dissipative turbulence test case from John Thuburn (personal communication and [134]). Table 6.1 and the discussion below summarizes the grids, run lengths and other details. In all cases, gravity was set equal to $g = 9.80616ms^{-1}$, the Earth's radius was set equal to $a = 6371220m$ and rotation was set equal to $\Omega = 0.00007292s^{-1}$, with Coriolis force equal to $2\Omega \sin\theta$, where θ is latitude.

Table 6.1. Simulation Details

Simulation	**Length (Days)**	**Output (Hours)**	**Grids**	**Dissipation**
TC2	10	6	G 2-8, C 2-8	None
TC5	50	6	G 6,7 C 6,7	None
TC6	50	6	G 6,7 C 6,7	None
Galewsky	10	6	G 6,7,8 C 6,7,8	None
GalewskyInit	1	1	G 6,7 C 6,7	None
GalewskyNoPerturb	10	6	G 2-8, C 2-8	None
Held Suarez	2400	24	G 6, C6	None

6.1.1. Grids.

Two quasi-uniform spherical grids were used: the icosahedral hexagonal-pentagonal grid, and the gnomonic non-orthogonal cubed-sphere grid. More details about the grids are provided in Appendix B. For the C grid scheme, both the icosahedral and the cubed-sphere grid were used. For the Z grid scheme, only the icosahedral grid was used.

6.1.1.1. *Icosahedral Hexagonal (G).*

This grid is based on the subdivision of each triangular face of an icosahedron into smaller triangles, which is repeated until the desired resolution is reached. This gives the icosahedral triangular grid, while the dual of this grid gives the icosahedral hexagonal-pentagonal. This process produces a highly uniform grid, but the primal grid is composed of 12 pentagons with the remaining cells hexagons. The dual grid is entirely triangles. This leads to a mismatch in the degrees of freedom between the wind and the mass field when using a C grid discretization, which manifests itself as spurious branches of the dispersion relationship. There are many possibly ways of constructing such a grid, see [87], [152], [11] and Appendix B for more information. There are also many possible optimizations, the three considered here are spherical centroidal voronoi tesselation (SCVT, [78], [66] and [28]), tweaking ([59],[58]) and spring dynamics ($\beta = 0.8$ and $\beta = 1.1$, [142] and [64]). In all cases, the resulting grids are orthogonal. Additionally, all of these optimizations preserve the property that the primal grid vertices (triangle "centers") are located at the centroid of the dual grid cells (triangles). This is required by the non-orthogonal $\mathbf{H}$ operator. Various grid properties are summarized in the table below. Results for most test cases (except the order of accuracy for individual operators and Williamson Test Case 2) are shown only for the tweaked grids, since they are the only ones to produce consistent operators (see below). Tables 6.2, 6.3, 6.4 and 6.5

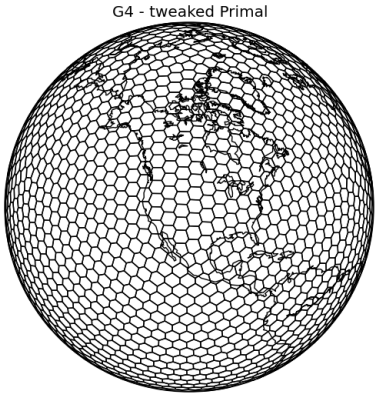

FIGURE 6.1. Refinement Level 4 Geodesic Grid with Tweaked Optimization (Primal)

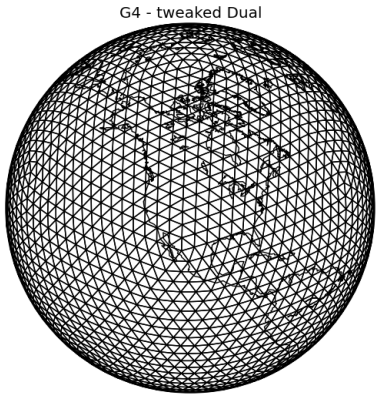

FIGURE 6.2. Refinement Level 4 Geodesic Grid with Tweaked Optimization (Dual)

outline various grid properties, , while Figures 6.1 and 6.2 show refinement level 4 (2562 cells) icosahedral grids.

TABLE 6.2. Grid Properties for Tweaked Geodesic Grids

Grid	Cells	Max de (km)	Max/Min de	Max/Min le	Max/Min Ai	$\Delta t(s)$
G2-HR	162	2101	1.21879	1.64446	1.09143	1440
G3-HR	642	1073	1.25213	1.84172	1.06141	720
G4-HR	2562	541	1.2647	1.93143	1.05475	360
G5-HR	10242	271	1.26931	1.97294	1.05208	180
G6-HR	40962	136	1.27096	1.99271	1.05036	90
G7-HR	163842	68	1.27153	2.00232	1.04988	45
G8-HR	655362	34	1.27171	2.00705	1.04965	22.5

TABLE 6.3. Grid Properties for SCVT Geodesic Grids

Grid	Cells	Max de (km)	Max/Min de	Max/Min le	Max/Min Ai	$\Delta t(s)$
G2-CVT	162	2027	1.16595	1.52553	1.19193	1440
G3-CVT	642	1016	1.19683	1.64997	1.25628	720
G4-CVT	2562	509	1.23354	1.71255	1.33178	360
G5-CVT	10242	254	1.27087	1.76735	1.41406	180
G6-CVT	40962	127	1.30997	1.82211	1.50195	90
G7-CVT	163842	64	1.35012	1.87814	1.59545	45
G8-CVT	655362	32	1.39154	1.93578	1.69481	22.5

TABLE 6.4. Grid Properties for Spring Dynamics $\beta = 0.8$ Geodesic Grids

Grid	Cells	Max de (km)	Max/Min de	Max/Min le	Max/Min Ai	$\Delta t(s)$
G2-SB0.8	162	2003	1.18668	1.4393	1.27855	1440
G3-SB0.8	642	1003	1.25416	1.56135	1.4431	720
G4-SB0.8	2562	502	1.32205	1.67179	1.60309	360
G5-SB0.8	10242	251	1.38455	1.77793	1.75933	180

TABLE 6.5. Grid Properties for Spring Dynamics $\beta = 1.1$ Geodesic Grids

Grid	Cells	Max de (km)	Max/Min de	Max/Min le	Max/Min Ai	$\Delta t(s)$
G2-SB1.1	162	2034	1.16588	1.5364	1.18257	1440
G3-SB1.1	642	1017	1.1853	1.66707	1.228	720
G4-SB1.1	2562	509	1.20847	1.73271	1.27162	360
G5-SB1.1	10242	255	1.22606	1.78558	1.30953	180

6.1.1.2. *Cubed Sphere (C).*

This grid is based on equiangular, central projection of a cube onto the sphere. Grid refinement is accomplished by subdivision of each face of the cubed prior to projection. For the grids used here, each face is equally subdivided into X^2 cells, where $X = 3 * 2^{n-1}$ and n is the refinement level. This process produces a less uniform grid than the icosahedral discretization, however the resulting primal grid is now quadrilateral. Unfortunately, it is also non-orthogonal. The dual grid is also quadrilateral, with the exception of the original 8 vertices of the cube that are triangles. In addition, once generated, the primal grid vertices are moved to the centroid of the dual grid cells. As before, this is required by the non-orthogonal **H** operator. Various grid properties are summarized in the table below. Table 6.6 outlines various grid properties, while Figures 6.3 and 6.3 show refinement level 4 (3456) cubed sphere grids.

6.1.2. ELLIPTIC SOLVER.

The Z grid scheme requires the solution of an elliptic equation at each timestep to determine the streamfunction and velocity potential. This was done via multigrid ([89], [90] and [59]), which is a scalable method that offers O(n) performance, where n is the number of

TABLE 6.6. Grid Properties for Cubed Sphere Grids

Grid	Cells	Max de (km)	Max/Min de	Max/Min le	Max/Min Ai	$\Delta t(s)$
C2-TH	216	1661	1.24518	1.46956	1.63319	1200
C3-TH	864	834	1.32607	1.45848	1.72167	480
C4-TH	3456	417	1.36911	1.44069	1.73851	240
C5-TH	13824	208	1.39138	1.42855	1.73835	120
C6-TH	55296	104	1.40272	1.42165	1.73598	60
C7-TH	221184	52	1.40845	1.418	1.73421	30
C8-TH	884736	26	1.41133	1.41612	1.73318	15

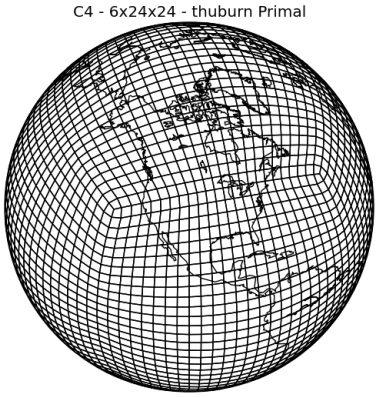

FIGURE 6.3. Refinement Level 4 Cubed Sphere Grid (Primal)

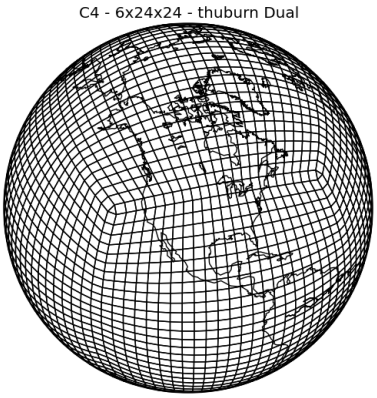

FIGURE 6.4. Refinement Level 4 Cubed Sphere Grid (Dual)

degrees of freedom in the problem. The restriction and prolongation operators were the same as those used by [137], and the full multigrid algorithm using a Jacobi smoother was employed for cycling. Three passes of the algorithm were made, with 2 iterations of the smoother at each level and 10 iterations of the smoother as a coarse grid solver. There is room for improvement of the smoother here, and certainly optimization of the multigrid parameters. However, the given settings gave satisfactory results for the grids under consideration.

6.1.3. TIME STEPPING.

Time stepping was done using the third order Adams Bashford scheme (AB3, [34]). Since this is a multilevel time scheme, it admits a computational mode in time. However, this mode is damped, and there was no evidence of interaction between the computational mode in time

and any spatial computational modes in either scheme (of which there is only the spurious Rossby wave branches for the C grid scheme on icosahedral grids). Unfortunately, the AB3 scheme does no preserve the conservation properties of the scheme, and full conservation is lost. A better choice of time stepping scheme would have been a single step scheme such as a Runge-Kutta scheme, but such a scheme would have been significantly more computationally expensive (requiring multiple evaluations of the RHS, which for the Z grid scheme would have been multiple elliptic solves per time step). Another strong alternative would have been a semi-implicit or even fully implicit scheme, both for improved time step length and conservation properties. There is some work ([46], [75] and [45]) indicating that a fully conservative scheme would be possible by combining a conservative spatial discretization with the appropriate implicit time stepping scheme. This possibility merits further exploration.

6.1.4. Auxiliary Variables.

To facilitate the analysis of results from the various test cases, auxiliary variables were computed from prognostic variables at each output step. Many of them are actually used in the discretization schemes, and the full set is detailed below.

6.1.4.1. *C Grid.*

Analysis of results from the C grid scheme requires the relative vorticity primal 0-form:

$$\zeta_v = \mathbf{J}\bar{D}_2 u_e \tag{326}$$

the absolute vorticity primal 0-form:

$$\eta_v = \mathbf{J}(\zeta_v + f_v) \tag{327}$$

(where f_v is the Coriolis 2-form), the potential vorticity primal 0-form:

$$q_v = \frac{\bar{D}_2 u_e + f_v}{\mathbf{R} m_i} \tag{328}$$

the dual cell-integrated fluid height primal 0-form:

$$m_v = \mathbf{JR} m_i \tag{329}$$

and the divergence dual 0-form:

$$\delta_i = \mathbf{I} D_2 \mathbf{H} u_e \tag{330}$$

Note that 0-forms (instead of 2-forms) are used here for ζ_v, η_v, m_v and δ_i. This allows easy comparison with Z grid results, and other models that use pointwise values.

6.1.4.2. *Z Grid.*

Since the Z grid directly predicts many quantities of interest (ζ_i and δ_i) and does not require an auxiliary fluid height, the only auxiliary variables are the pointwise absolute vorticity

$$\eta_i = \zeta_i + f_i \tag{331}$$

and the pointwise potential vorticity

$$q_i = \frac{\eta_i}{h_i} \tag{332}$$

6.1.5. Choice of $\mathbf{Q}$ in C Grid Scheme.

Three different version of $\mathbf{Q}$ were used, corresponding to choices conserving only total energy, only potential enstrophy or conserving both. They are (where $\mathbf{Q_e} = \sum_{v \in VE(e)} q_v$):

$$\mathbf{Q} = \mathbf{W}\mathbf{Q_e} \tag{333}$$

for the enstrophy conserving version

$$\mathbf{Q} = \frac{1}{2}\mathbf{Q_e}\mathbf{W} + \frac{1}{2}\mathbf{W}\mathbf{Q_e} \tag{334}$$

for the energy conserving version, and

$$\mathbf{Q} = \sum_{e' \in ECP(e)} \sum_{v \in VC(i)} \alpha_{e,e',v} q_v \tag{335}$$

for the doubly conservative version.

6.2. Order of Accuracy

An important component of testing the C and Z grid schemes is determining the order of accuracy of the individual operators, as well as the overall scheme. To determine the accuracy of individual operators, various test functions were used. In all of the order of accuracy plots that follow, the dashed line indicates first-order accuracy.

C Grid Test Functions. For the C grid operators, a simple test function was used:

$$\psi = \cos(\theta)\cos(\lambda) \tag{336}$$

where a is the radius of the Earth, θ is the latitude, and λ is the longitude. This has a laplacian equal to

$$\vec{\nabla}^2\psi = -\frac{2}{a^2}\psi = -\frac{2}{a^2}\cos(\theta)\cos(\lambda) \tag{337}$$

Z Grid Test Functions. For the Z grid operators, two test functions were needed:

$$\alpha = \cos^3(\theta)\sin(5\lambda) \tag{338}$$

and

$$\beta = \frac{-a^2}{2}\cos^3(\theta)\sin(3\lambda) \tag{339}$$

where a is the radius of the Earth, θ is the latitude, and λ is the longitude.

Norms. Two norms are used: the L_2 norm

$$||B||_{L_2} = \frac{\sum_i (B_i^2 d\Omega_i)}{\sum_i (d\Omega_i)} \tag{340}$$

and the L_∞ norm

$$||B||_{L_\infty} = |B_i|_{max} \tag{341}$$

where $d\Omega_i$ is the area (or length) associated with whatever element the norm is being taken over. For the C grid scheme, this can be A_i, A_v, de or le, depending on whether the norm involves 2-forms or 1-forms. For the Z grid scheme, it is just A_i.

6.2.1. C Grid.

In general, using the tweaked optimization, the C grid scheme operators on the icosahedral grid are approximately first order accurate in both the L_2 and L_∞ norms, with the exception of $\mathbf{W}/\mathbf{Q}$. First order accuracy corresponds with the findings of [96],[137] and [154]. However, both the spring dynamics and SCVT optimizations fail to produce consistent operators- in particular, both the dual grid laplacian and edge laplacian fail to converge in the L_∞ norm.

On the cubed sphere grid, all of the laplacian operators along with the $\mathbf{W}/\mathbf{Q}$ operators are inconsistent in the L_∞ norm. In addition, even for the norms and operators that do converge, the rate of convergence and absolute error magnitudes are much worse than for the icosahedral grid.

In what follows, ψ_v, ψ_i and ψ_e are simply $\cos(\theta)\cos(\lambda)$ sampled at the appropriate points (primal vertices, dual vertices and edges).

6.2.1.1. *Primal Grid Laplacian.*

The primal grid Laplacian is defined by

$$\mathbf{L_p} = \mathbf{I}D_2\mathbf{H}\bar{D}_1 \tag{342}$$

and its error e can be computed as

$$e = \mathbf{L_p}\psi_i + \frac{2}{a^2}\psi_i \tag{343}$$

As seen in Figures 6.5 and 6.6, the primal grid Laplacian is approximately first order accurate in the L_2 and L_∞ norms for icosahedral grids, and somewhat less than first order accurate in

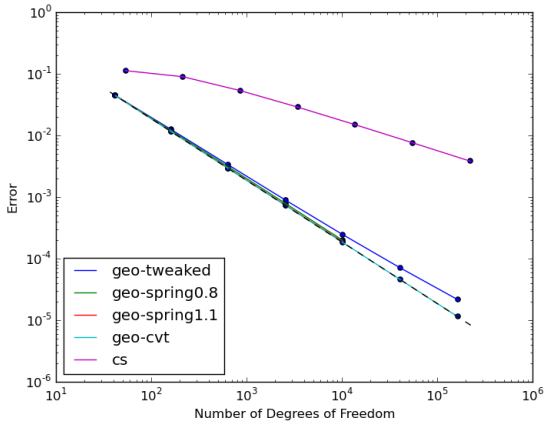

FIGURE 6.5. L_2 accuracy for the primal grid laplacian operator $\mathbf{L_p}$

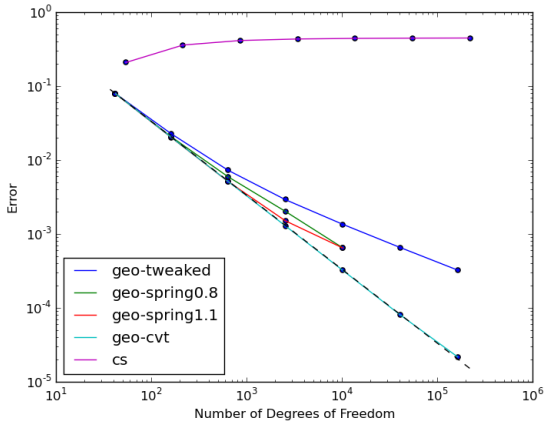

FIGURE 6.6. L_∞ accuracy for the primal grid laplacian operator $\mathbf{L_p}$

L_2 for cubed sphere grids. However, it is inconsistent in the L_∞ norm for the cubed sphere grid.

6.2.1.2. *Dual Grid Laplacian.*

The dual grid laplacian is defined as

$$\mathbf{L_d} = -\mathbf{J}\bar{D}_2\mathbf{H}^{-1}D_1 \tag{344}$$

and its error e can be computed as

$$e = \mathbf{L_d}\psi_v + \frac{2}{a^2}\psi_v \tag{345}$$

The L_2 norm results (Figure 6.7) for the dual grid laplacian are broadly similar to those of the primal grid laplacian. However, unlike the primal grid laplacian, the dual grid laplacian is inconsistent in L_∞ (Figure 6.8) for both icosahedral and cubed-sphere grids, except when the tweaked optimization is used on the icosahedral grid.

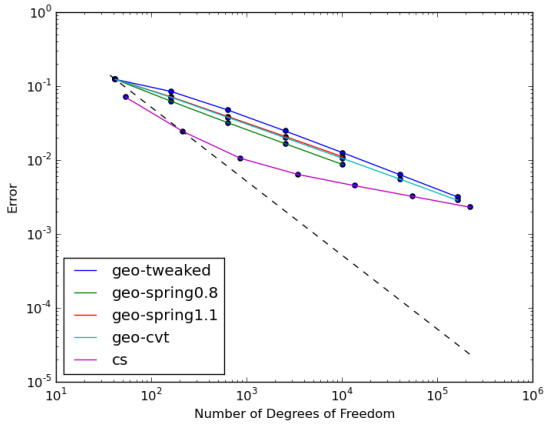

FIGURE 6.7. L_2 accuracy for the dual grid laplacian operator $\mathbf{L_d}$

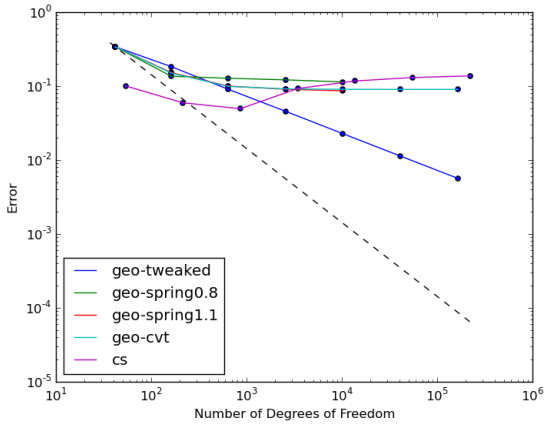

FIGURE 6.8. L_∞ accuracy for the dual grid laplacian operator $\mathbf{L_d}$

6.2.1.3. *Edge Laplacian.*

The edge laplacian is defined as

$$\mathbf{L_e} = -\mathbf{H}^-1 D_1 \mathbf{J} \bar{D}_2 + \bar{D}_1 \mathbf{I} D_2 \mathbf{H} \tag{346}$$

and its error e can be computed as

$$e = \mathbf{L_e}\psi_e + \frac{2}{a^2}\psi_e \tag{347}$$

The results (Figures 6.9 and 6.10) are essentially the same as those obtained for the dual grid laplacian.

6.2.1.4. $\mathbf{W}$ *Operator.*

To assess the accuracy of the $\mathbf{W}$ operator, the wind was defined using either

$$u_e = -\mathbf{H}\bar{D}_1\psi_i \tag{348}$$

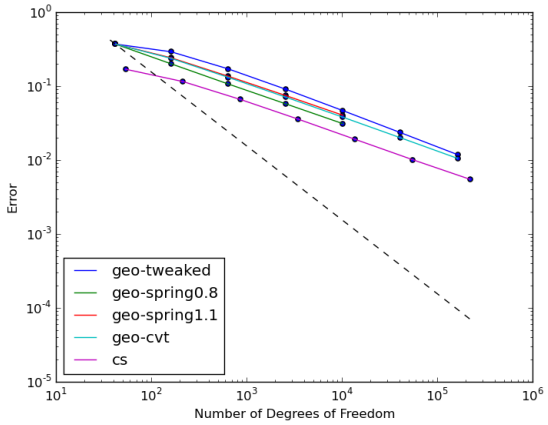

FIGURE 6.9. L_2 accuracy for the edge laplacian operator $\mathbf{L_e}$

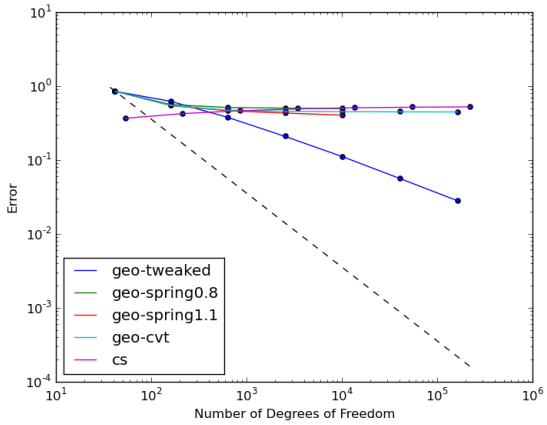

FIGURE 6.10. L_∞ accuracy for the edge laplacian operator $\mathbf{L_e}$

(the divergent wind) or

$$u_e = D_1 \psi_v \tag{349}$$

(the rotational wind). With the divergent wind, the error e was defined as

$$e = D_1 \psi + \mathbf{HWH} \bar{D}_1 \psi_v \tag{350}$$

, while with the rotational wind the error e was defined as

$$e = \bar{D}_1 \psi_i - \mathbf{W} D_1 \psi_v \tag{351}$$

The results (Figures 6.11, 6.12, 6.13 and 6.14) indicate somewhat less than first order accuracy in L_2 on all grids. However, the L_∞ norm is inconsistent for all grids. This is a major shortcoming of the C grid scheme.

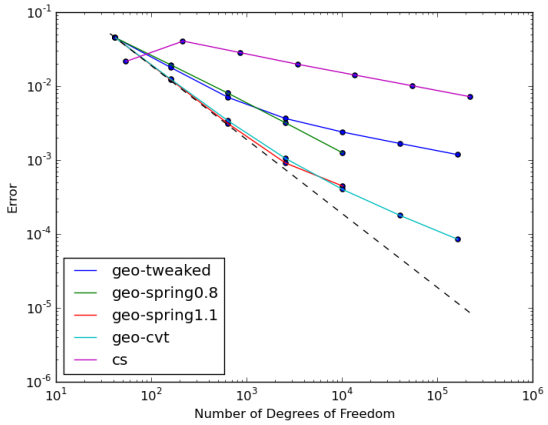

FIGURE 6.11. L_2 accuracy for the $\mathbf{W}$ operator with u_e divergent

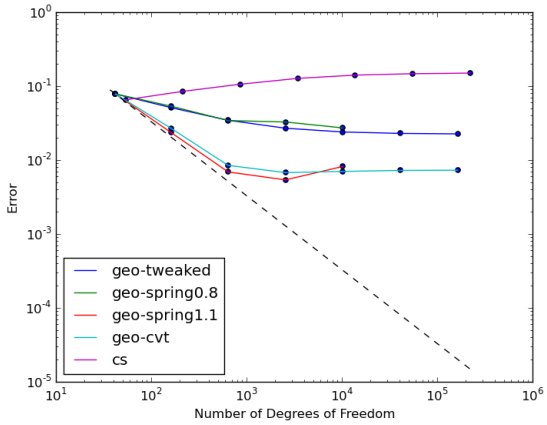

FIGURE 6.12. L_∞ accuracy for the $\mathbf{W}$ operator with u_e divergent

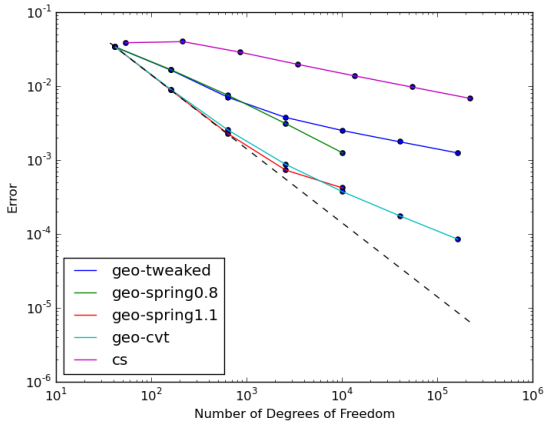

FIGURE 6.13. L_2 accuracy for the $\mathbf{W}$ operator with u_e rotational

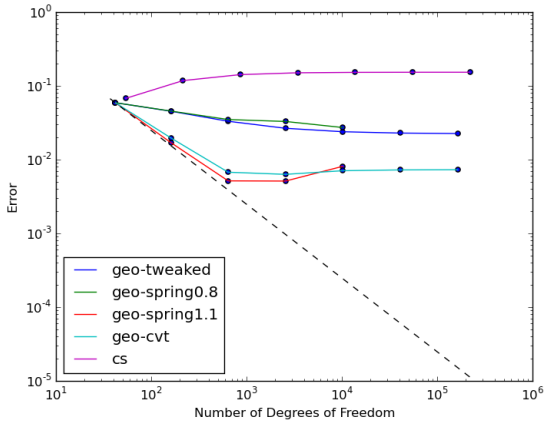

FIGURE 6.14. L_∞ accuracy for the $\mathbf{W}$ operator with u_e rotational

6.2.1.5. $\mathbf{Q}$ *Operator.*

Essentially the same approach to assessing accuracy for the $\mathbf{W}$ operator can be employed for the $\mathbf{Q}$ operator, with the error for the divergent wind defined as

$$e = \psi_e * D_1\psi - \mathbf{HQ}(\psi_e, \mathbf{H}\bar{D}_1\psi_v) \tag{352}$$

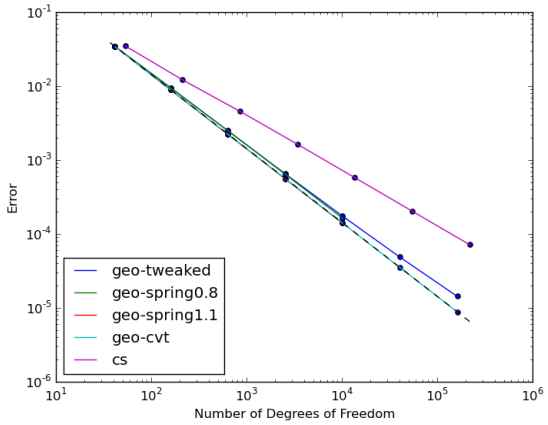

FIGURE 6.15. L_2 accuracy for the $\mathbf{R}$ operator

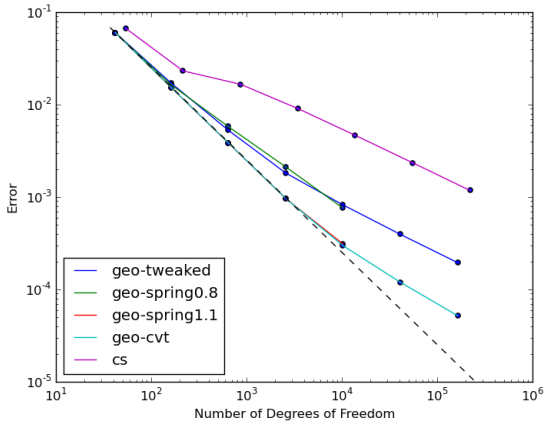

FIGURE 6.16. L_∞ accuracy for the $\mathbf{R}$ operator

and the error for the rotational wind defined as

$$e = \psi_e * \bar{D}_1 \psi_i - \mathbf{Q}(\psi_e, D_1 \psi_v) \tag{353}$$

The results (not shown) are the same.

6.2.1.6. $\mathbf{R}$ *Operator.*

The error e in the $\mathbf{R}$ operator can be computed as

$$e = \mathbf{R}^T \psi_v - \psi_i \tag{354}$$

As seen in Figures 6.15 and 6.16, $\mathbf{R}$ is approximately first order in L_2 for icosahedral grids and somewhat less than first order for cubed-sphere grids. In L_∞, it is somewhat less than first order for all grids.

6.2.1.7. ϕ *Operator.*

The error e in the ϕ operator can be computed as

$$e = \phi \psi_i - \psi_e \tag{355}$$

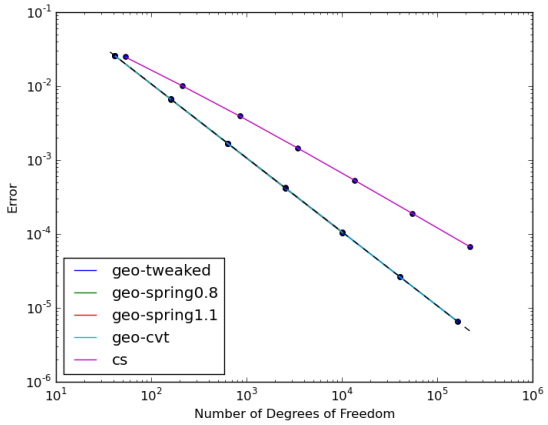

FIGURE 6.17. L_2 accuracy for the ϕ operator

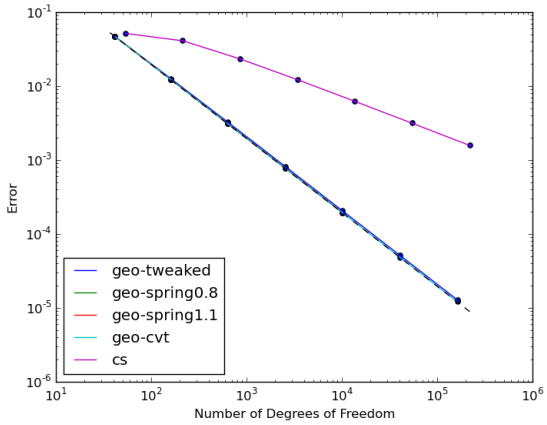

FIGURE 6.18. L_∞ accuracy for the ϕ operator

Figures 6.17 and 6.18 clearly show first order accuracy in both L_2 and L_∞ for icosahedral grids, and somewhat less than first order accuracy for cubed-sphere grids.

6.2.2. Z GRID.

In general, using the tweaked optimization, the Z grid scheme operators on the icosahedral grid are approximately first order accurate in both the L_2 and L_∞ norms, with the exception of the Jacobian operator $\mathbf{J}$. First order accuracy (and inconsistency of the Jacobian) corresponds with the findings of [96] and [59]. Recent work by Ross Heikes (personal communication) suggests that the Laplacian and Flux-Divergence operators might also be inconsistent. In all cases, both the spring dynamics and SCVT optimizations fail to produce consistent operators- in particular, all three operators fail to converge in the L_∞ norm.

6.2.2.1. $\mathbf{L}$ *Operator.*

The error e in the Laplacian operator can be computed as

$$e = \mathbf{L}\beta_i - (\vec{\nabla}^2\beta)_i \tag{356}$$

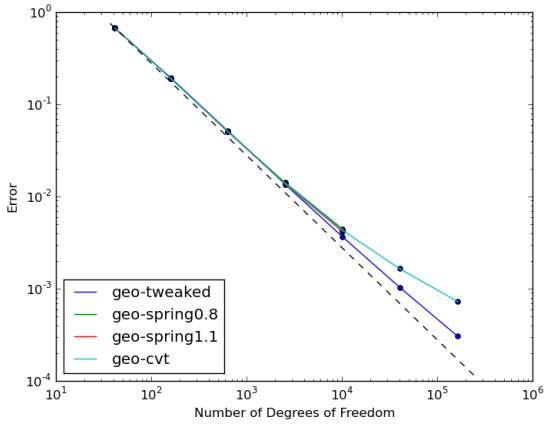

FIGURE 6.19. L_2 accuracy for the Z grid laplacian operator

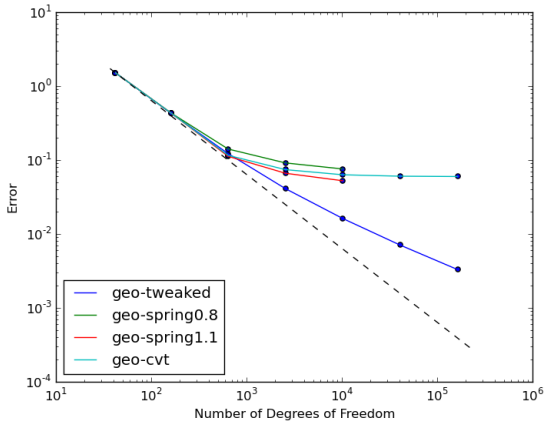

FIGURE 6.20. L_∞ accuracy for the Z grid laplacian operator

where $(\vec{\nabla}^2\beta)_i$ is the analytic Laplacian sampled at cell centers. From Figures 6.19 and 6.20, it is easy to see that the Z grid laplacian is first order in L_2 on all grids, and inconsistent in L_∞ except on the tweaked grid.

6.2.2.2. **FD** *Operator.*

The error e in the flux-divergence operator can be computed as

$$e = \mathbf{FD}(\alpha_i, \beta_i) - (\vec{\nabla} \cdot (\alpha\vec{\nabla}\beta))_i \tag{357}$$

where $(\vec{\nabla} \cdot (\alpha\vec{\nabla}\beta))_i$ is the analytic flux-divergence sampled at cell centers. The results (6.21 and 6.22) are the same as the laplacian operator, except that tweaked grid flux-divergence might be getting inconsistent at the highest resolutions.

6.2.2.3. **J** *Operator.*

The error e in the Jacobian operator can be computed as

$$e = \mathbf{J}(\alpha_i, \beta_i) - (J(\alpha, \beta))_i \tag{358}$$

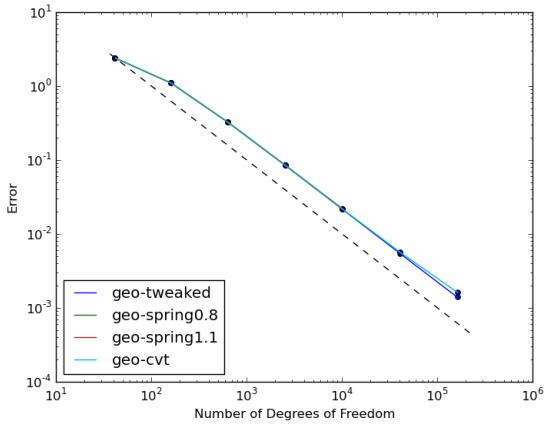

FIGURE 6.21. L_2 accuracy for the Z grid flux divergence operator

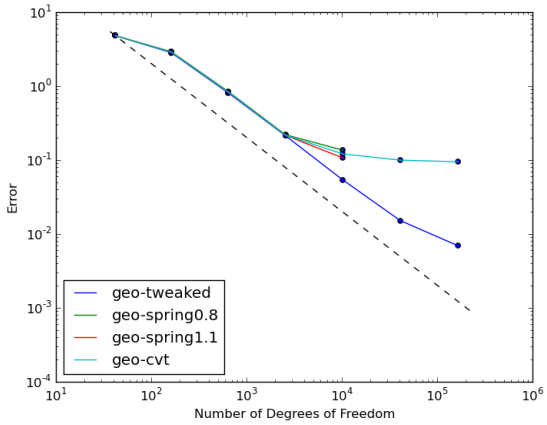

FIGURE 6.22. L_∞ accuracy for the Z grid flux divergence operator

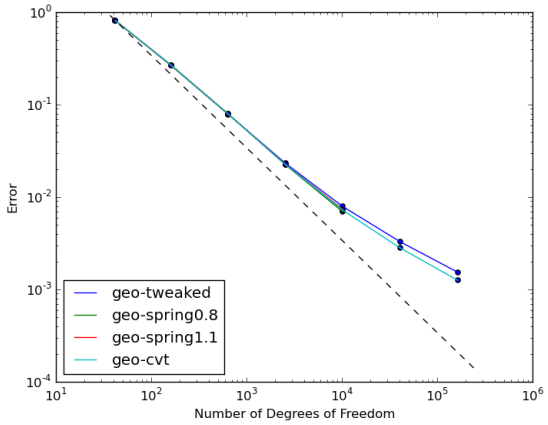

FIGURE 6.23. L_2 accuracy for the Z grid jacobian operator

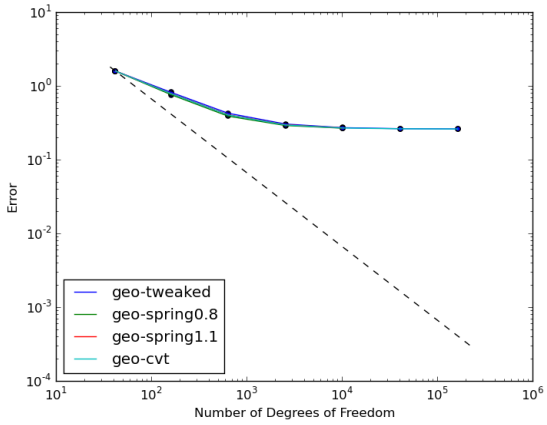

FIGURE 6.24. L_∞ accuracy for the Z grid jacobian operator

where $(J(\alpha, \beta))_i$ is the analytic Jacobian sampled at cell centers. Unlike the flux-divergence and laplacian operators, the Jacobian operator (Figures 6.23 and 6.24) is inconsistent in L_∞ on all grids, including the tweaked optimization.

6.3. Williamson Test Case 2- Solid Body Rotation (TC2)

The first test case is quite simple: solid body rotation (a special case of purely zonal flow) on the sphere. This test case is used primarily to determine the ability of the schemes

to maintain a steady state solution, and to assess the accuracy of the overall scheme (since the analytic solution is known). It does not reflect the complexity of realistic flows in the atmosphere. The details of the setup can be found in [156]. For the C grid scheme, variables were initialized using

$$u_e = -\mathbf{H}^{-}1D_1\psi_v \tag{359}$$

$$m_i = \mathbf{I}^{-}1h_i \tag{360}$$

where ψ_v was the prescribed streamfunction sampled at primal vertices, and h_i was the prescribed fluid height sampled at dual vertices. For the Z grid scheme, variables were initialized using

$$\zeta_i = \mathbf{L}\psi_i \tag{361}$$

where ψ_i was the prescribed streamfunction sampled at cell centers (dual vertices).

C Grid Results. Conservation properties for the C grid scheme are illustrated in Figures 6.25, 6.26, 6.27 and 6.28. This confirms that the scheme is working as expected, with each version conserving the relevant quantities. The only exception appears to the total energy conserving variant on cubed-sphere grids. This inaccuracy is probably related to the inconsistency of the cubed-sphere model in general. The order of accuracy of the scheme (determined as the difference between the initial fluid height and fluid height at Day 5) is detailed in Figures 6.29, 6.30, 6.31, 6.32, 6.33 and 6.34. The schemes (all variants) are

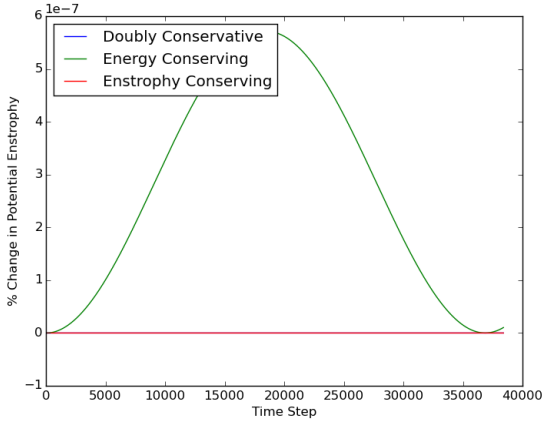

FIGURE 6.25. Potential enstrophy conservation for the C grid scheme (all three **Q** variants) on grid G8 for TC2

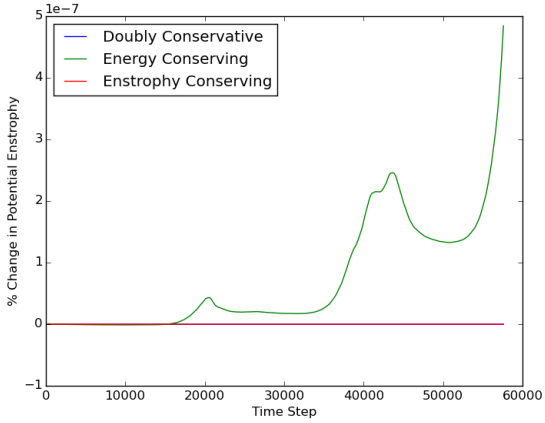

FIGURE 6.26. Potential enstrophy conservation for the C grid scheme (all three **Q** variants) on grid C8 for TC2

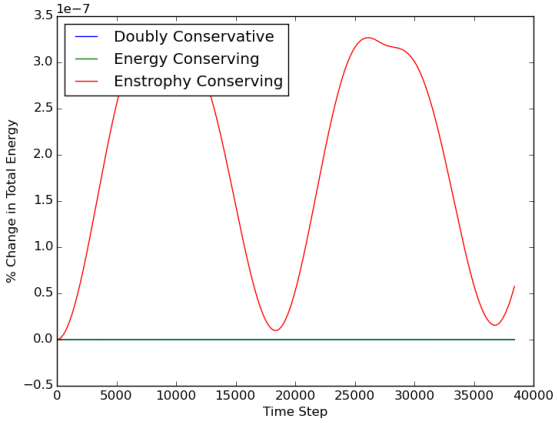

FIGURE 6.27. Total energy conservation for the C grid scheme (all three **Q** variants) on grid G8 for TC2

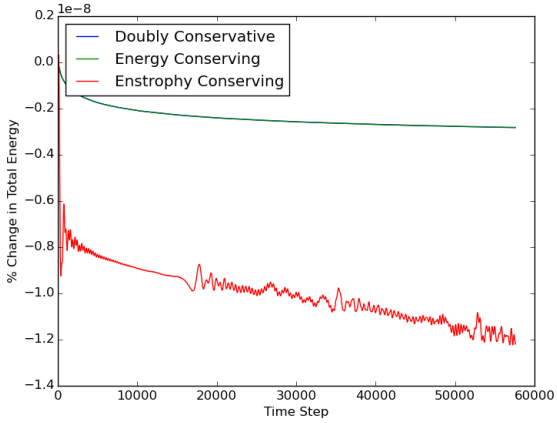

FIGURE 6.28. Total energy conservation for the C grid scheme (all three **Q** variants) on grid C8 for TC2

approximately first order accurate in L_2 on all grids, with the icosahedral grids being significantly more accurate than the cubed sphere. However, in L_∞ only the tweaked icosahedral grid is first order accurate- the remaining grids (including the cubed sphere) are inconsistent.

Z Grid Results. Conservation properties for the Z grid scheme are illustrated in Figures 6.37 and 6.38. This confirms that the scheme is working as expected and conserving the

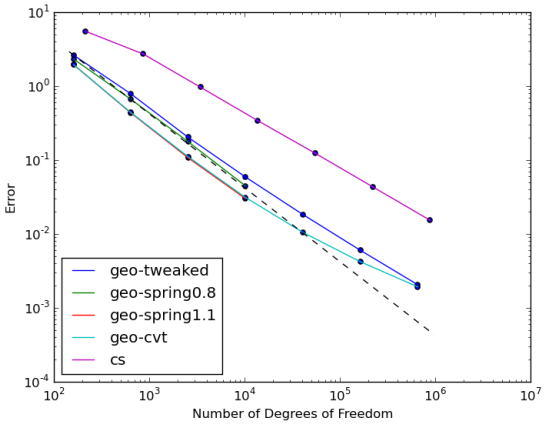

FIGURE 6.29. L_2 accuracy in fluid height h_i for TC2 with C grid scheme using enstrophy-conserving $\mathbf{Q}$ operator

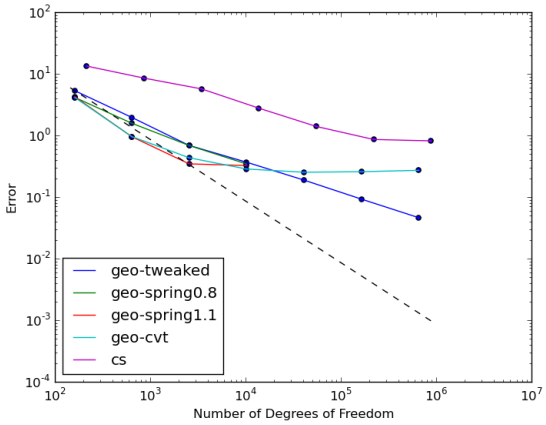

FIGURE 6.30. L_∞ accuracy in fluid height h_i for TC2 with C grid scheme using enstrophy-conserving $\mathbf{Q}$ operator

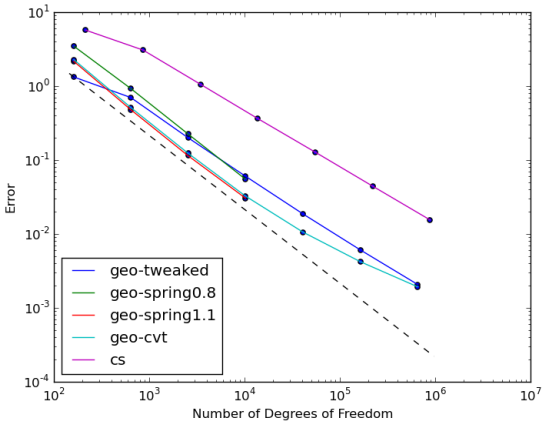

FIGURE 6.31. L_2 accuracy in fluid height h_i for TC2 with C grid scheme using energy-conserving $\mathbf{Q}$ operator

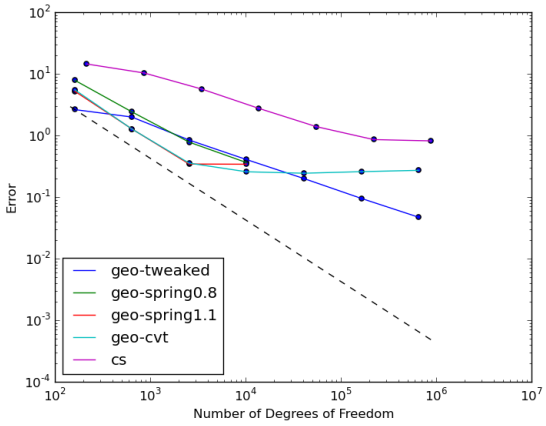

FIGURE 6.32. L_∞ accuracy in fluid height h_i for TC2 with C grid scheme using energy-conserving $\mathbf{Q}$ operator

relevant quantities. In addition, it is clear that the doubly conservative C grid and Z grid scheme are conserving to roughly the same order of accuracy, with slighly better conservation in the Z grid case. The order of accuracy of the scheme (determined as the difference between the initial fluid height and fluid height at Day 5) is detailed in Figures 6.35 and 6.36. The Z grid scheme is approximately first order accurate in both L_2 and L_∞.

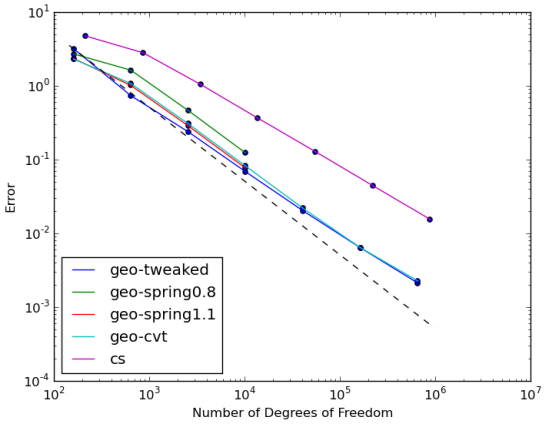

FIGURE 6.33. L_2 accuracy in fluid height h_i for TC2 with C grid scheme using doubly conservative **Q** operator

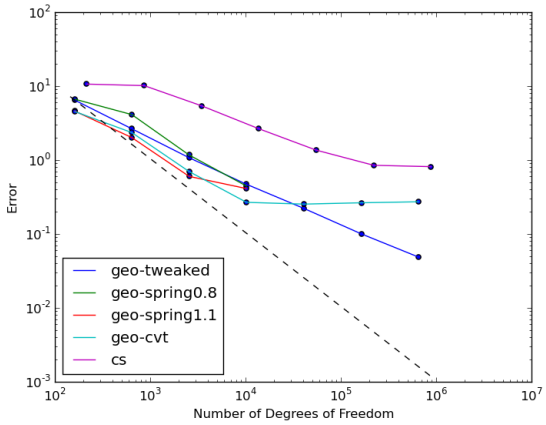

FIGURE 6.34. L_∞ accuracy in fluid height h_i for TC2 with C grid scheme using doubly conservative **Q** operator

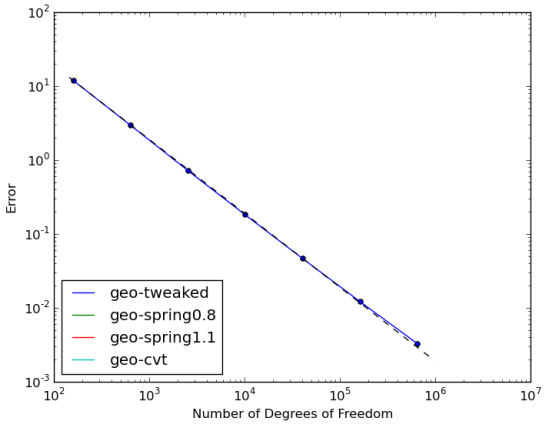

FIGURE 6.35. L_2 accuracy in fluid height h_i for TC2 with Z grid

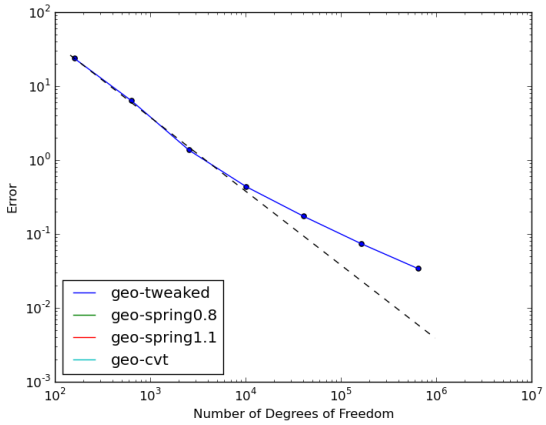

FIGURE 6.36. L_∞ accuracy in fluid height h_i for TC2 with Z grid

Comparing the two schemes, it is interesting to note that the Z grid scheme appears to have much better conservation properties than the C grid. Since other test cases (see below) do not show this effect, it is hypothesized that this might be due to a better representation of balance for this test in the Z grid scheme than the C grid scheme. More importantly, the inconsistency of the **W** and Jacobian operators does not seem to affect results, provided the tweaked grid is used.

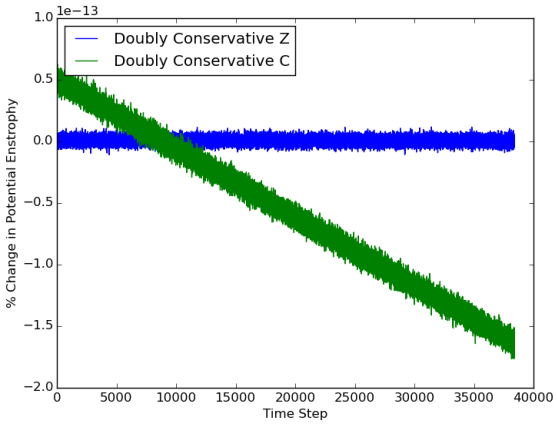

FIGURE 6.37. Potential enstrophy conservation for the Z grid and C grid (doubly conservative version) schemes on grid G8 for TC2

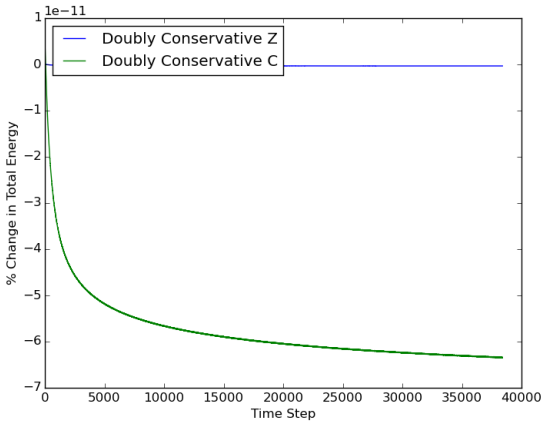

FIGURE 6.38. Total energy conservation for the Z grid and C grid (doubly conservative version) schemes on grid G8 for TC2

6.4. WILLIAMSON TEST CASE 5- FLOW OVER A MOUNTAIN (TC5)

The second test case involves the zonal flow field from TC2, but introduces a non-differentiable "mountain" in the topography field. There is no longer an analytic solution, and therefore comparison with high-resolution reference solutions is the only way to assess correctness. In addition, the initial flow is highly unbalanced and requires short time steps to resolve the resulting intertia-gravity waves. The non-differentiable mountain also produces difficulties for spectral-type methods, and can lead to Gibbs oscillations around the mountain. However, the resulting structures in the flow field (especially after 15-20 days of development) are representative of realistic atmospheric complexity. The details of the setup can be found in [156]. For the C grid scheme, variables were initialized using

$$u_e = -\mathbf{H}^{-}1 D_1 \psi_v \tag{362}$$

$$m_i = \mathbf{I}^{-}1 h_i \tag{363}$$

where ψ_v was the prescribed streamfunction sampled at primal vertices, and h_i was the prescribed fluid height sampled at dual vertices. For the Z grid scheme, variables were initialized using

$$\zeta_i = \mathbf{L}\psi_i \tag{364}$$

where ψ_i was the prescribed streamfunction sampled at cell centers (dual vertices).

Plots of the potential vorticity at Day 30 for all the schemes tested are found in Figures 6.39, 6.40, 6.41, 6.42, 6.43, 6.44 and 6.45. They give essentially the same large scale results, but there is a marked difference in small scale structure between the different schemes. In particular, it appears that the C grid icosahedral schemes have much more small scale structure than the C grid cubed sphere schemes. This difference probably indicates the presence of the spurious Rossby wave modes on the icosahedral C grid, which are close to grid scale. This is especially apparent by comparing the C grid icosahedral schemes to the Z grid iscohedral schemes (which do NOT have any computational modes). However, the presence of these modes does not seem to be affecting the larger scale features in the flow, which is consistent with the idea that the spurious Rossby modes are quasi-passively advected by the flow. Similar small scale structures in the flow field for the TC5 test case can be seen in [155].

6.5. Rossby-Haurwitz Wave (TC6)

The third test is a Rossby-Haurwitz wave, which is an analytic solution to the barotropic vorticity equation (BVE). In the BVE case, the wave is simply advected around the globe. It is NOT an analytic solution of the shallow water equations, but it is still widely used as a test case. Again, since there is no analytic solution, comparison with high-resolution reference

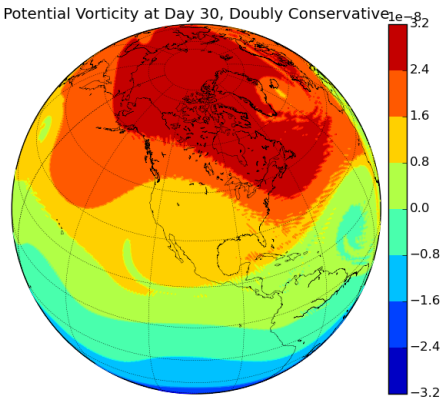

FIGURE 6.39. Potential vorticity at Day 30 for C grid scheme using doubly conservative **Q** variant on grid G6 for TC5

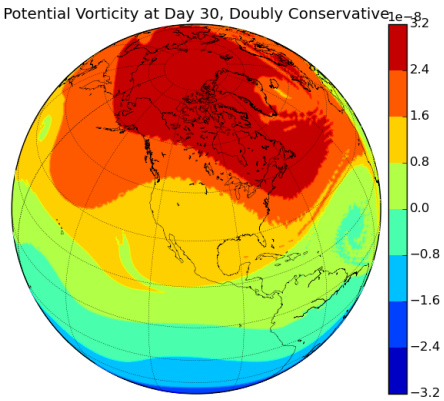

FIGURE 6.40. Potential vorticity at Day 30 for C grid scheme using doubly conservative **Q** variant on grid C6 for TC5

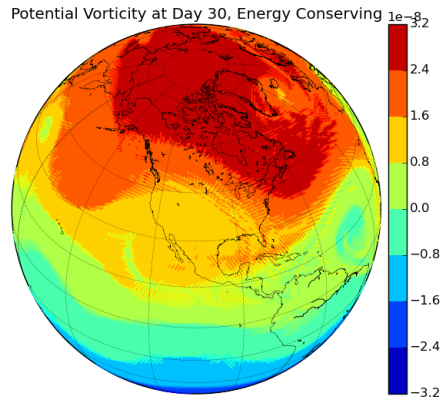

FIGURE 6.41. Potential vorticity at Day 30 for C grid scheme using energy-conserving **Q** variant on grid G6 for TC5

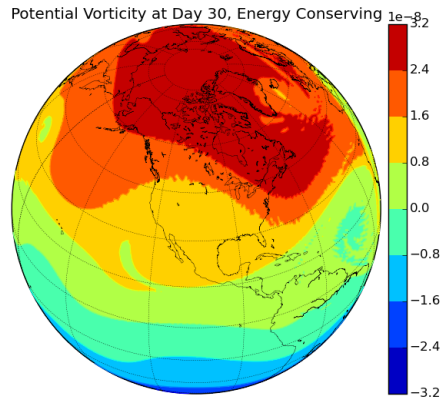

FIGURE 6.42. Potential vorticity at Day 30 for C grid scheme using energy-conserving **Q** variant on grid C6 for TC5

solutions is the only way to assess correctness. Unfortunately, as was discovered later, the particular choice of Rossby-Haurwitz wave advocated in [156] is dynamically unstable to a triad interaction ([139]). This limits its utility as a test case, since unavoidable truncation errors can trigger the instability, especially when they project onto the relevant wavenumbers (1, 3 and 5). The details of the setup can be found in [156]. For the C grid scheme, variables

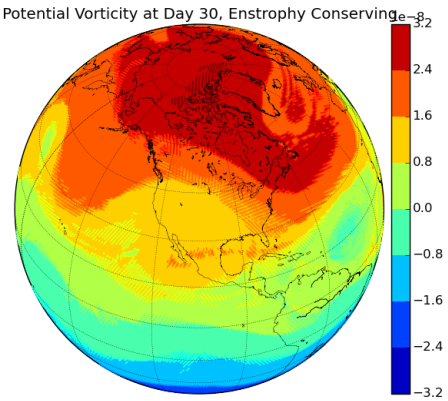

FIGURE 6.43. Potential vorticity at Day 30 for C grid scheme using enstrophy-conserving **Q** variant on grid G6 for TC5

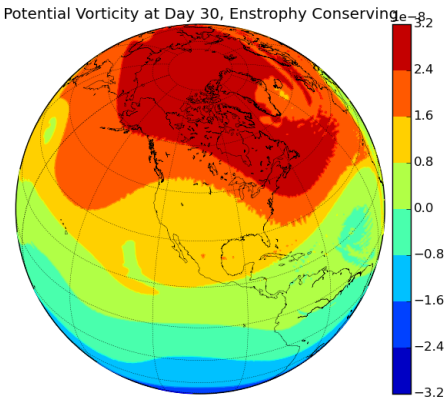

FIGURE 6.44. Potential vorticity at Day 30 for C grid scheme using enstrophy-conserving **Q** variant on grid C6 for TC5

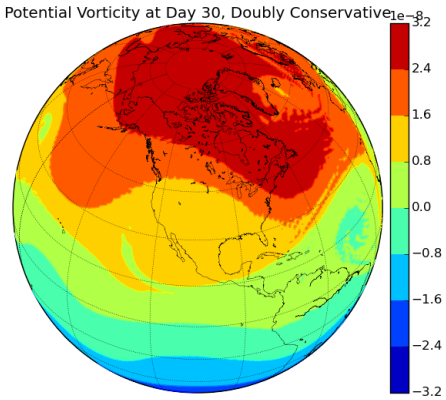

FIGURE 6.45. Potential vorticity at Day 30 for Z grid scheme on grid G6 for TC5

were initialized using

$$u_e = -\mathbf{H}^{-}1D_1\psi_v \tag{365}$$

$$m_i = \mathbf{I}^{-}1h_i \tag{366}$$

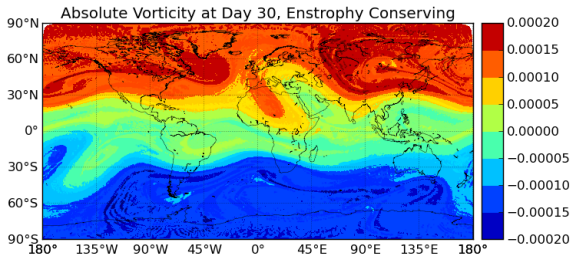

FIGURE 6.46. Absolute vorticity at Day 30 for C grid scheme using enstrophy-conserving **Q** variant on grid G7 for Rossby-Haurwitz Wave

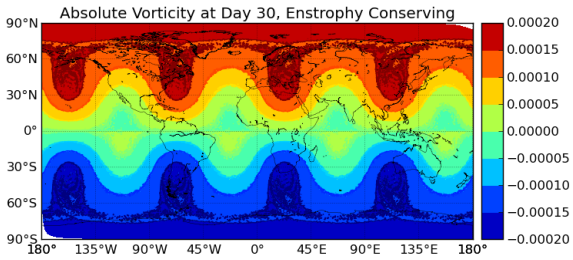

FIGURE 6.47. Absolute vorticity at Day 30 for C grid scheme using enstrophy-conserving **Q** variant on grid C7 for Rossby-Haurwitz Wave

where ψ_v was the prescribed streamfunction sampled at primal vertices, and h_i was the prescribed fluid height sampled at dual vertices. For the Z grid scheme, variables were just sampled at cell centers (dual vertices).

Figures 6.46, 6.47, 6.48, 6.49, 6.50, 6.51 and 6.52 plot the absolute vorticity η for all of the schemes tested. Two features immediately emerge: the first is the inability of the icosahedral grid schemes to maintain the Rossby-Haurwitz wave. They all experience breakdown of the wave by Day 35, with the enstrophy-conserving variant breaking down earlier (around Day 25). By Day 50 (not shown) all of the icosahedral grid schemes have broken down completely, while the cubed-sphere grid schemes continue to maintain the initial Rossby-Haurwitz wave through day 50. These results are consistent with the idea that the Rossby-Haurwitz wave is strongly unstable to wavenumber 5 perturbations, which are forced by the singular points of the icosahedral grid. However, the cubed sphere grid singular points generate a wavenumber 4 forcing, and therefore the Rossby-Haurwitz is much more stable on that grid.

The second is the presence of small scale structures in all schemes, similar to the results found for TC5. However, unlike the TC5 test, it does not appear that the C grid scheme on icosahedral grids is any noisier than the other schemes.

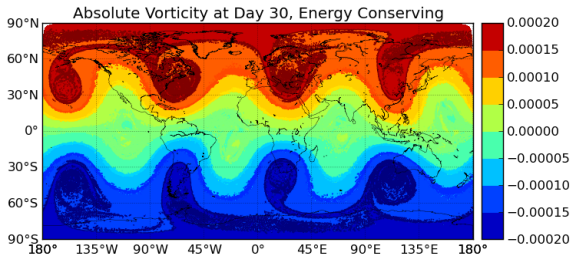

FIGURE 6.48. Absolute vorticity at Day 30 for C grid scheme using energy-conserving **Q** variant on grid G7 for Rossby-Haurwitz Wave

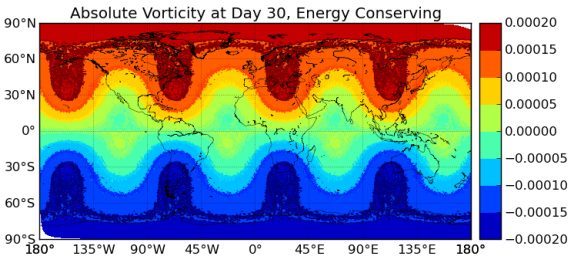

FIGURE 6.49. Absolute vorticity at Day 30 for C grid scheme using energy-conserving **Q** variant on grid C7 for Rossby-Haurwitz Wave

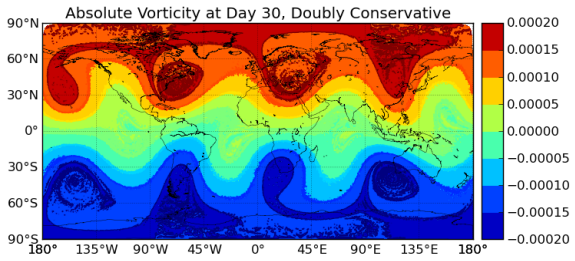

FIGURE 6.50. Absolute vorticity at Day 30 for C grid scheme using double conservative **Q** variant on grid G7 for Rossby-Haurwitz Wave

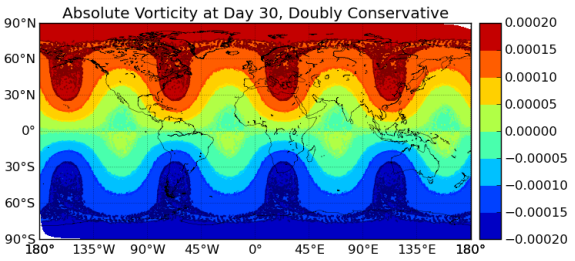

FIGURE 6.51. Absolute vorticity at Day 30 for C grid scheme using double conservative **Q** variant on grid C7 for Rossby-Haurwitz Wave

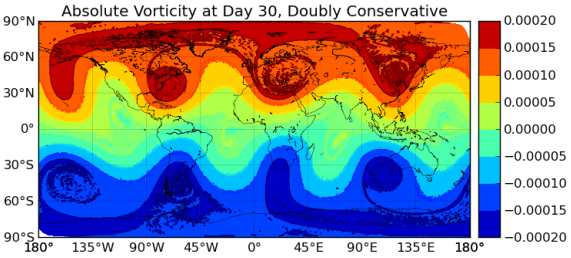

FIGURE 6.52. Absolute vorticity at Day 6 for Z grid scheme on grid G7 for Rossby-Haurwitz Wave

6.6. BAROTROPICALLY UNSTABLE JET (GALEWSKY)

As discussed in [43], the preceding three test cases have issues: TC2 is too simple to represent realistic atmospheric flows, the mountain in TC5 is only C_0 continuous and

requires very short time steps due to initialization shocks, and the particular Rossby wave in TC6 is dynamically unstable to a triad interaction. For these reasons, a new test case was developed by Galewsky et al ([43]). It is a barotropically unstable but balanced zonal jet. To this balanced but unstable initial condition a perturbation is added that triggers the instability. Both the balanced state and the perturbation have analytic expressions and are C_∞ continuous. The details of the setup can be found in the paper mentioned above. For the C grid scheme, variables were initialized using

$$u_e = -\mathbf{H}^{-}1 D_1 \psi_v \tag{367}$$

$$m_i = \mathbf{I}^{-}1 h_i \tag{368}$$

where ψ_v was the prescribed streamfunction sampled at primal vertices, and h_i was the prescribed fluid height sampled at dual vertices. For the Z grid scheme, variables were initialized using

$$\zeta_i = \mathbf{L}\psi_i \tag{369}$$

where ψ_i was the prescribed streamfunction sampled at cell centers (dual vertices). The height was set using h_i (sampled at cell centers, which are dual vertices).

6.6.1. Unperturbed Version (GalewskyNoPerturb).

The simplest realization of this test case is the initial balanced state, without any perturbation. The correct solution is simply a maintenance of the initial state. As is well known, this is a difficult test for models built on quasi-uniform grids, since the flow field is not aligned with grid cell walls. As shown in Figures 6.53, 6.54, 6.55, 6.56, 6.57, 6.58 and

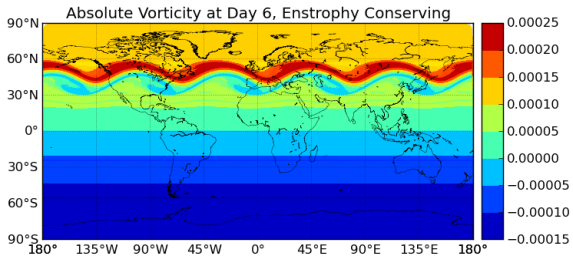

FIGURE 6.53. Absolute vorticity at Day 6 for C grid scheme using enstrophy-conserving **Q** variant on grid G8 for Galewsky without initial perturbation

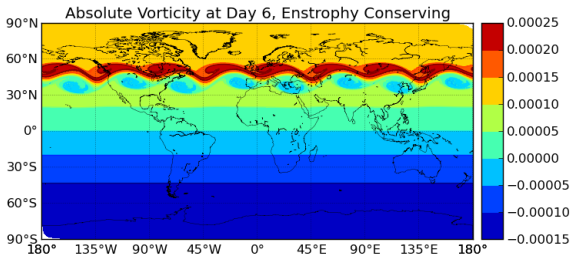

FIGURE 6.54. Absolute vorticity at Day 6 for C grid scheme using enstrophy-conserving **Q** variant on grid C8 for Galewsky without initial perturbation

6.59; none of the tested schemes were able to maintain the initial steady state. However, it is clear that the icosahedral grid schemes are superior to the cubed-sphere grid schemes. It is also evident that the total energy and doubly conservative variants of the C grid scheme, and the Z grid scheme, are better than the potential enstrophy conserving variant. In particular, the doubly conservative C grid scheme on the icosahedral grid and the Z grid scheme are extremely similar, despite being based on completely different numerics.

These results can be contrasted with those found in [123], [79] and [65]. All of the grid-based schemes described in the preceding papers are based on quasi-uniform spherical grids, and they all exhibit the same inability to maintain the balanced but unstable initial state. This problem is exacerbated by lower resolution. At higher resolutions, especially for the higher-order schemes ([79], [65]), the models are much better at maintaining the initial condition. [79] found that the icosahedral grid also did a better job at maintaining balance than the cubed-sphere grid, although both had issues at lower resolution. [79] also found that the addition of viscosity with $\nu = 10^5 m^2 s^{-1}$ helped control the instability, but it did not remove it.

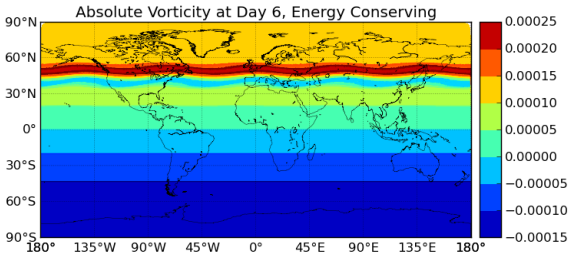

FIGURE 6.55. Absolute vorticity at Day 6 for C grid scheme using energy-conserving **Q** variant on grid G8 for Galewsky without initial perturbation

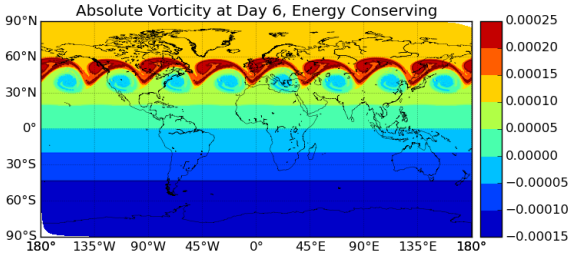

FIGURE 6.56. Absolute vorticity at Day 6 for C grid scheme using energy-conserving **Q** variant on grid C8 for Galewsky without initial perturbation

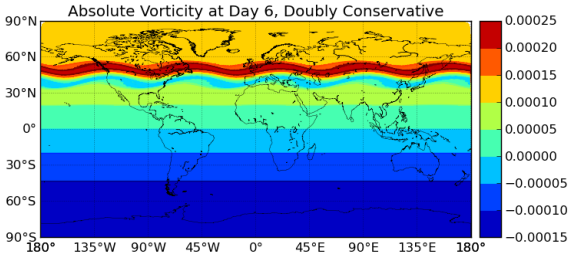

FIGURE 6.57. Absolute vorticity at Day 6 for C grid scheme using double conservative **Q** variant on grid G8 for Galewsky without initial perturbation

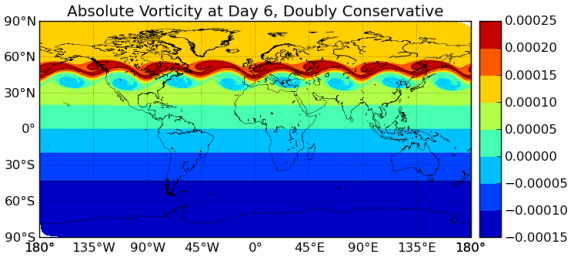

FIGURE 6.58. Absolute vorticity at Day 6 for C grid scheme using double conservative **Q** variant on grid C8 for Galewsky without initial perturbation

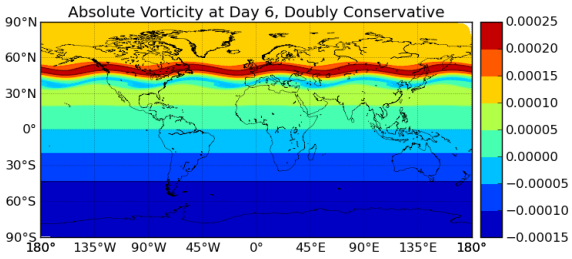

FIGURE 6.59. Absolute vorticity at Day 6 for Z grid scheme on grid G8 for Galewsky without initial perturbation

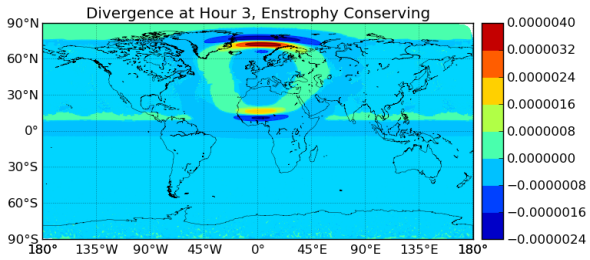

FIGURE 6.60. Divergence at hour 3 for C grid scheme using enstrophy conserving **Q** variant on grid G8 for Galewsky

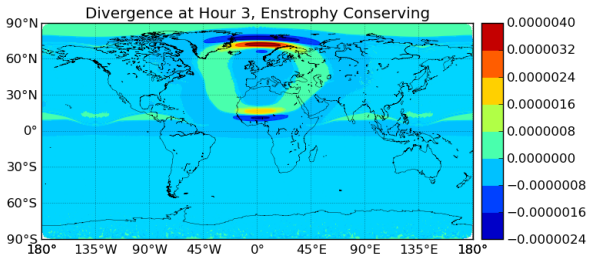

FIGURE 6.61. Divergence at hour 3 for C grid scheme using enstrophy conserving **Q** variant on grid C8 for Galewsky

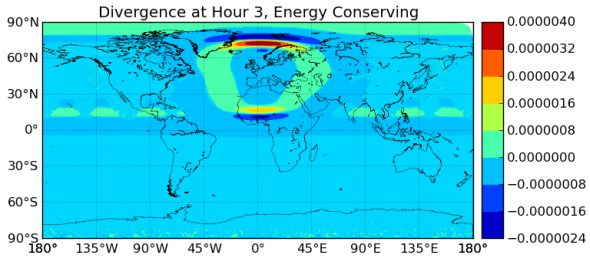

FIGURE 6.62. Divergence at hour 3 for C grid scheme using energy conserving **Q** variant on grid G8 for Galewsky

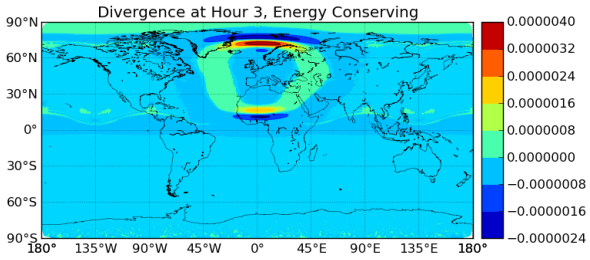

FIGURE 6.63. Divergence at hour 3 for C grid scheme using energy conserving **Q** variant on grid C8 for Galewsky

6.6.2. Initial Response (GalewskyInit).

When the perturbation is added, a markedly different response in observed. Plotting in Figures 6.60, 6.61, 6.62, 6.63, 6.64, 6.65 and 6.66 is the divergence δ after 3 hours of simulation. There is a clearly defined inertia-gravity wave spreading out from the initial height perturbation. This wave is very similar for all of the schemes tested. There are some slight differences in the divergence field away from the wavefront, but the main wave itself appears the same between schemes. The divergence field can be compared to that obtained in [43], and they are extremely similar. This confirms that the initial perturbation has been implemented correctly, and that the models are behaving as expected.

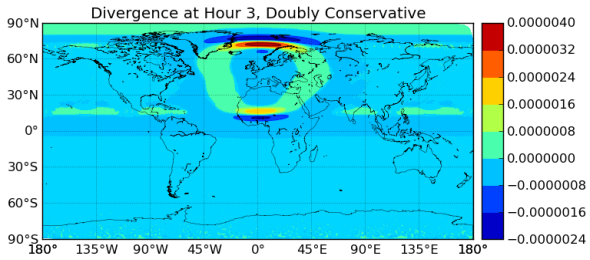

FIGURE 6.64. Divergence at hour 3 for C grid scheme using double conservative **Q** variant on grid G8 for Galewsky

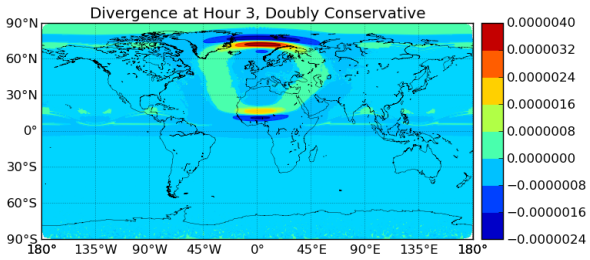

FIGURE 6.65. Divergence at hour 3 for C grid scheme using double conservative **Q** variant on grid C8 for Galewsky

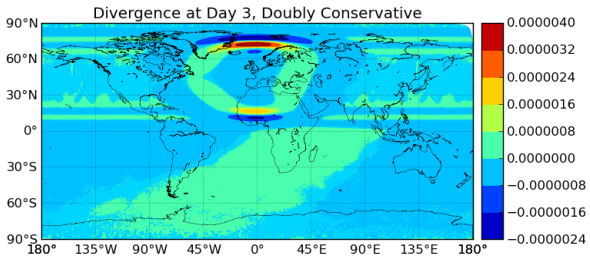

FIGURE 6.66. Divergence at hour 3 for Z grid scheme on grid G8 for Galewsky

6.6.3. Fully Developed Jet (Galewsky).

In addition to the initial response, it is useful to examine the fully developed jet. The absolute vorticity at Day 6 for all of the schemes tested is shown in Figures 6.73, 6.74, 6.75, 6.76, 6.77, 6.78 and 6.79. The main jet structure between 0° and 180° W is very similar between all of the schemes (except for the C grid total energy conserving variant), with some differences in the depth of the trough around 110° W. The main jet structure is also very similar to the inviscid jet solution from the original Galewsky et. al paper. As noted, the C grid total energy conserving variant is unstable, and the solution is quite bad. The undeveloped portion of the jet between 0° and 180° E is markedly different from scheme to scheme. The two stables C grid schemes (potential enstrophy and doubly conservative) on the cubed-sphere grid show similar behaviour, while the doubly-conservative, total energy

and Z grid scheme on icosahedral grids are also similar. The enstrophy conserving variant on icosahedral grids is similar to none of these schemes.

Close inspection does reveal that the doubly conservative C grid scheme and the Z grid scheme are extremely similar. This is an interesting result, because the schemes are built using very different numerics. It suggests that conservation properties can have an influence even in shorter-term simulations, an unexpected result.

The differences between the schemes (in particular the different variants of $\mathbf{Q}$, and the two types of grid) do not appear to be going away with increasing resolution. Since this testcase represents the complicated evolution of a unstable initial state, this is not unexpected. Nonlinear feedbacks between scales imply that small scale features in the flow (which are strongly sensitive to the choice of scheme and grid) can influence the evolution of the larger scales. Additionally, lower resolution runs of this testcase (not shown) had very strong wavenumber 4 (for the cubed sphere) or wavenumber 5 (for the icosahedral grid) patterns.

These results can be contrasted with the many examinations of this test case in the literature using a variety of schemes. Hilary Weller ([154]) and Thuburn et. al ([137]) used a very similar scheme on both icosahedral and cubed-sphere grid, and found broadly the same results. A high resolution was required to eliminate the spurious wavenumber 4 (cubed-sphere) or 5 (icosahedral) patterns. In addition, unlike Weller's results, both we and Thuburn et. al found that the cubed-sphere grid gave comparable results to the icosahedral grid at sufficiently high resolution. Xiao et. al ([65], using a higher-order multi-moment finite volume scheme on icosahedral grids), Maras et. al ([79], using a continuous/discontinuous Galerkin method on both cubed-sphere and icosahedral grids), Shin et. al ([123], using low-order finite volume methods on icosahedral grids) and Salehipour et. al ([112], using

a discontinuous Galerkin method on icosahedral grids) and obtained similar conclusions regarding the neccessity of high resolution to control the wavenumber 4/5 forcing. In addition, Salehipour et. al also found that the implicit diffusion in the DG method helped control the spurious release of instability associated with low resolution. Ringler e.t. al ([103], using a very similar low-order finite volume method on icosahedral grids) obtained a similar main jet structure on variable resolution grids, with the solution in the coarse region exhibiting a strong wavenumber 5 pattern as resolution decreased. From our results and these other results in the literature, it appears some combination of high resolution and higher-order approximations is required to prevent spurious release of instability associated with the singular points on icosahedral and cubed-sphere grids.

Conservation properties for this test case are plotted in Figures 6.67, 6.68, 6.69, 6.70, 6.71 and 6.72. They show broadly the same results as TC2: each variant of $\mathbf{Q}$ is conserving the expected quantities. However, the total energy conserving C grid scheme on the cubed-sphere grid is no longer conserving energy. In addition, it also shows a lot of potential enstrophy growth (around 30% by the end of the simulation), while the remaining schemes show little growth for the non-conserved quantities. This makes sense, since that scheme is unstable (see above). In addition, the differences in conservation between the doubly-conservative C grid scheme and the Z grid scheme have gone away. This suggests that the interpretation of this effect given early (better ability of the Z grid scheme to maintain the balanced state of TC2) is correct.

6.7. Shallow Water Held-Suarez Analogue (Held Suarez)

The preceding test cases focus on the ability of the schemes to accurately simulate the evolution of a given initial condition, and on their ability to maintain a balanced initial

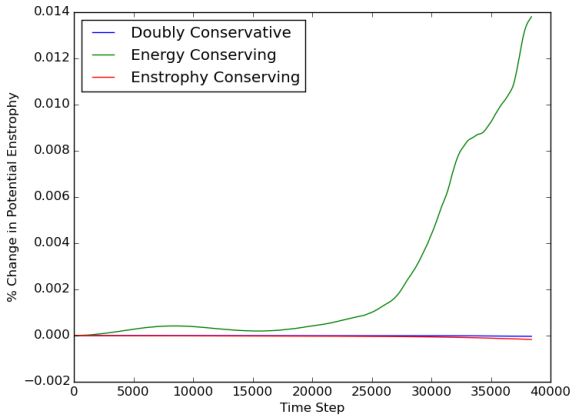

FIGURE 6.67. Potential enstrophy conservation for the C grid scheme (all three **Q** variants) on grid G8 for Galewsky

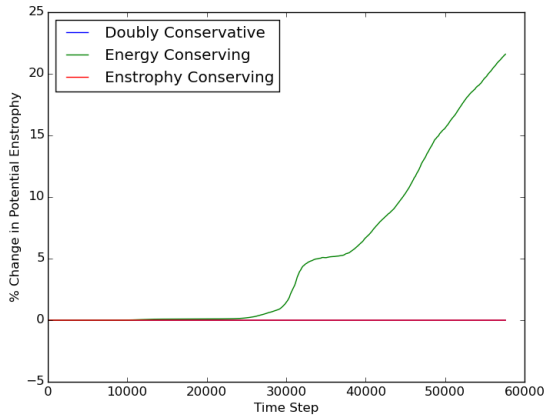

FIGURE 6.68. Potential enstrophy conservation for the C grid scheme (all three **Q** variants) on grid C8 for Galewsky

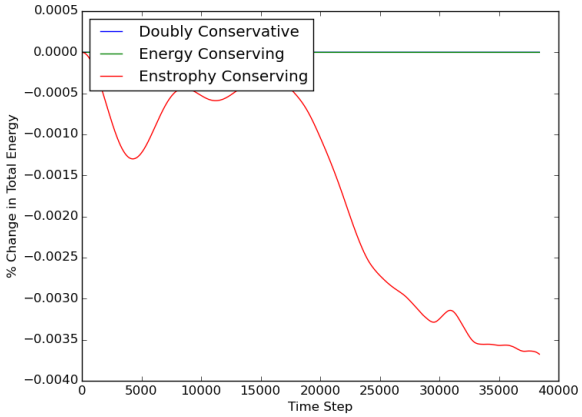

FIGURE 6.69. Total energy conservation for the C grid scheme (all three **Q** variants) on grid G8 for Galewsky

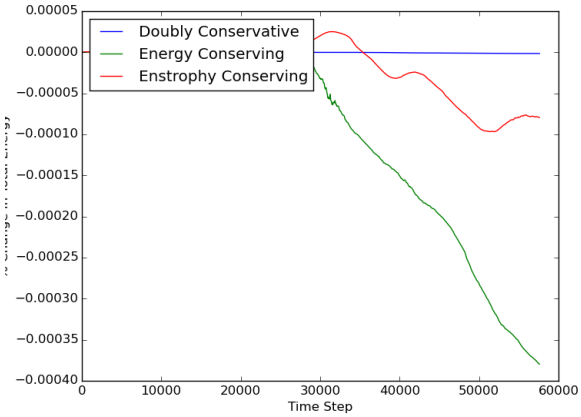

FIGURE 6.70. Total energy conservation for the C grid scheme (all three **Q** variants) on grid C8 for Galewsky

condition. These situations are characteristic of the types of problems that a weather forecasting model is used to solve. However, climate simulations rely on the ability of a model to correctly simulate the long-term statistics of the dynamical system under a (possibly time-varying) forcing. This is markedly different from the test cases above. To evaluate the ability of the schemes to simulate long-term statistics, a shallow water analogue of the Held-Suarez

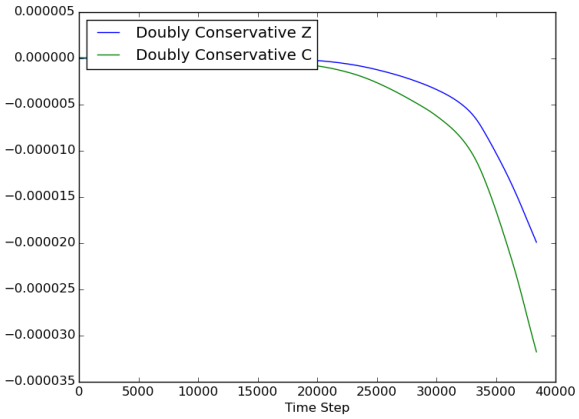

FIGURE 6.71. Potential enstrophy conservation for the Z grid and C grid (doubly conservative version) schemes on grid G8 for Galewsky

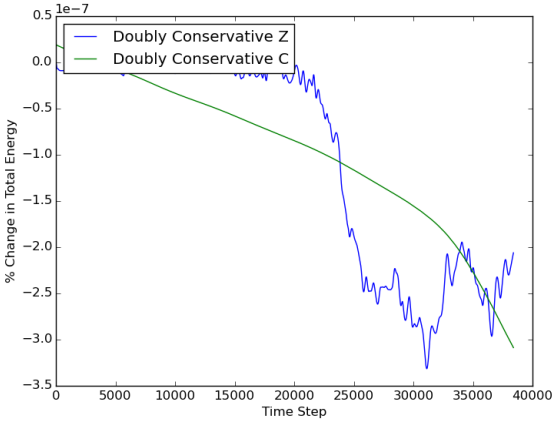

FIGURE 6.72. Total energy conservation for the Z grid and C grid (doubly conservative version) schemes on grid G8 for Galewsky

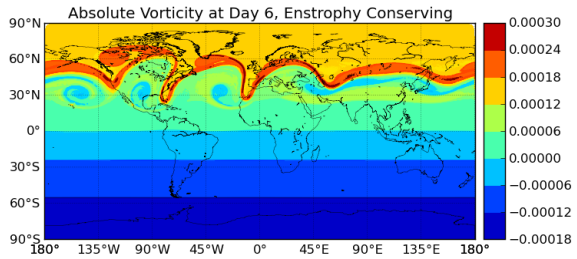

FIGURE 6.73. Absolute vorticity at Day 6 for C grid scheme using enstrophy-conserving **Q** variant on grid G8 for Galewsky

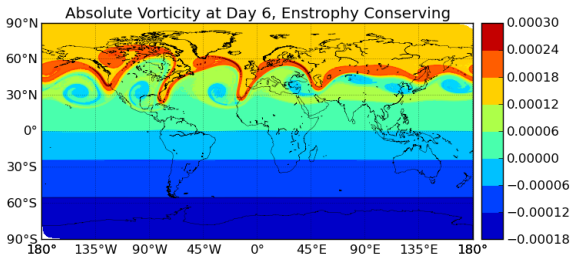

FIGURE 6.74. Absolute vorticity at Day 6 for C grid scheme using enstrophy-conserving **Q** variant on grid C8 for Galewsky

test case has been developed by John Thuburn ([134], and personal communication). It is essentially a forced-dissipative turbulence test case.

Description of Test Case. A forcing is added to the shallow water equations as

$$\frac{\partial u}{\partial t} = \cdots + \frac{\vec{u}_{eqm} - \vec{u}}{\tau_u} \tag{370}$$

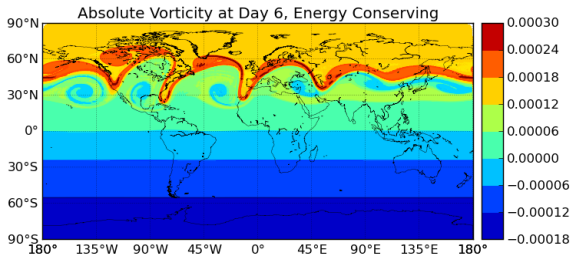

FIGURE 6.75. Absolute vorticity at Day 6 for C grid scheme using energy-conserving **Q** variant on grid G8 for Galewsky

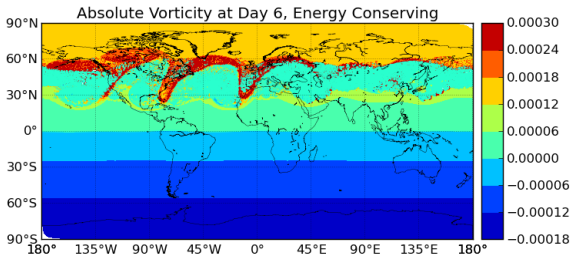

FIGURE 6.76. Absolute vorticity at Day 6 for C grid scheme using energy-conserving **Q** variant on grid C8 for Galewsky

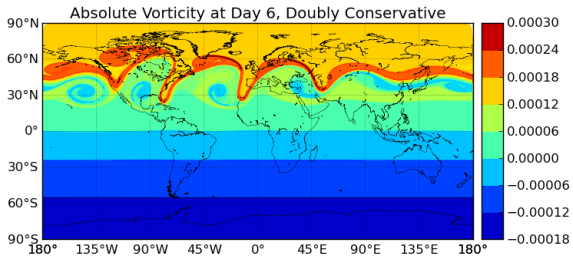

FIGURE 6.77. Absolute vorticity at Day 6 for C grid scheme using double conservative **Q** variant on grid G8 for Galewsky

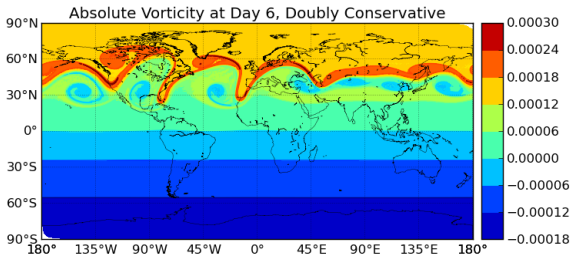

FIGURE 6.78. Absolute vorticity at Day 6 for C grid scheme using double conservative **Q** variant on grid C8 for Galewsky

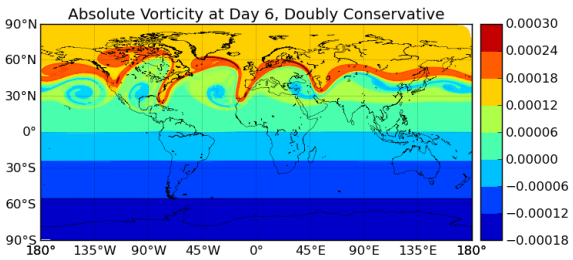

FIGURE 6.79. Absolute vorticity at Day 6 for Z grid scheme on grid G8 for Galewsky

$$\frac{\partial h}{\partial t} = \cdots + \frac{h_{eqm} - h}{\tau_h} \tag{371}$$

or in vorticity-divergence form as

$$\frac{\partial \delta}{\partial t} = \cdots + \frac{\delta_{eqm} - \delta}{\tau_u} \tag{372}$$

$$\frac{\partial \zeta}{\partial t} = \cdots + \frac{\zeta_{eqm} - \zeta}{\tau_u} \tag{373}$$

The equilibrium profiles (with θ latitude, λ longitude, a Earth's radius) are given by

$$h_{eqm} = h_0 + dH(1 - \sin^2(\theta)) \tag{374}$$

$$u_{eqm} = \vec{\nabla}^T \psi_{eqm} = u_0 \sin^2(2\theta) \left(\sin^2(m\theta) - \frac{1}{2} \right) \tag{375}$$

where $\vec{u}$ is purely zonal. A streamfunction can be calculated as

$$\psi_{eqm} = \frac{a u_0}{2}(A + B - C) \tag{376}$$

where

$$A = \frac{\sin[2(m-2)\theta]}{8(m-2)} \tag{377}$$

$$B = \frac{\sin[2(m+2)\theta]}{8(m+2)} \tag{378}$$

$$C = \frac{\sin(2m\theta)}{4m} \tag{379}$$

which gives

$$\zeta_{eqm} = \frac{u_0}{a}(-D + E + F) \tag{380}$$

$$\delta_{eqm} = 0 \tag{381}$$

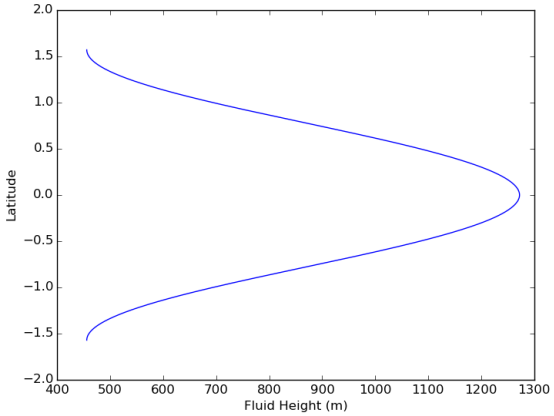

FIGURE 6.80. h_{eqm} forcing function

where

$$D = \tan(\theta)\sin^2(2\theta)[\sin^2(m\theta) - \frac{1}{2}] \tag{382}$$

$$E = 2m\sin^2(2\theta)\sin(m\theta)\cos(m\theta) \tag{383}$$

$$F = 4\cos(2\theta)\sin(2\theta)[\sin^2(m\theta) - \frac{1}{2}] \tag{384}$$

The various constants are $m = 12$, $u_0 = 120$ meters per second, $dH = \frac{8000 \text{ meters}}{g}$, $h_0 = 10^3$ meters $- \frac{2dH}{3}$, $\tau_h = 100$ days and $\tau_u = 100$ days. Plots of the forcing functions are provided in Figures 6.80, 6.81, 6.82 and 6.83. The initial height field is set equal to $10^3 m$. The initial wind field (and therefore vorticity and divergence fields) is set equal to 0. The model is run for 2400 days, with the first 400 days treated as a spin-up time. The underlying forcing is zonally and equatorially symmetric; loss of these symmetries in the statistics is evidence of grid imprinting or other model errors.

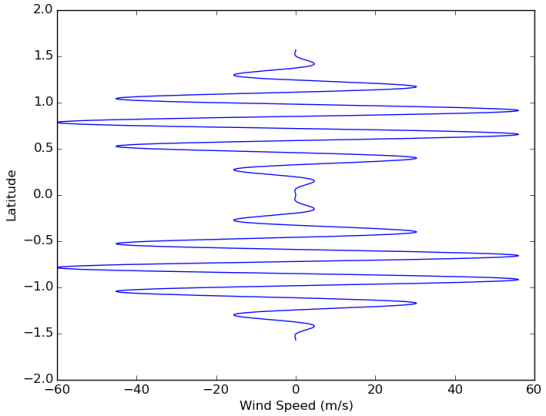

FIGURE 6.81. u_{eqm} forcing function

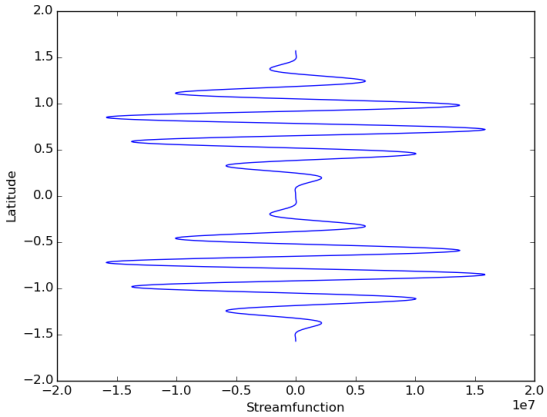

FIGURE 6.82. ψ_{eqm} forcing function

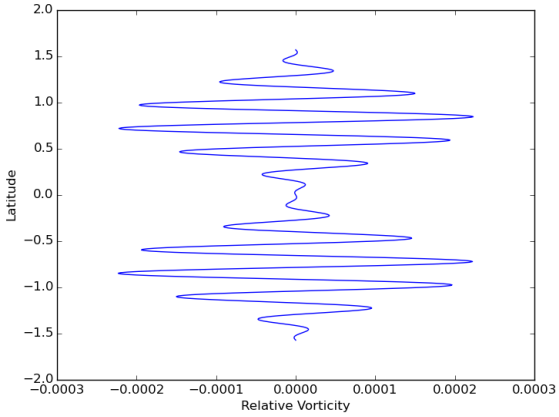

FIGURE 6.83. ζ_{eqm} forcing function

Statistics. To analyze the results, statistics are computed for the last 2000 days of each run; for fluid height h, relative vorticity ζ and divergence δ. The relevant statistics are temporal means $\bar{\delta}^t$, temporal standard deviations δ_{σ_t}, zonal/temporal means6 $\bar{\delta}^{t,z}$ and zonal/temporal standard deviations $\bar{\delta}^z_{\sigma_t}$. Zonal mean statistics are computed by binning area-weighted data based on latitude and taking area-weighted statistics over each bin. Due to the quasi-uniform nature of the grids under consideration, this does have the disadvantage of relative few samples near the poles, and therefore zonal mean statistics from high-latitudes should be treated with caution.

6.7.1. C Grid Results.

Zonal Mean Results. Zonal/temporal means and standard deviations for the cubed sphere grid are provided in Figures 6.84, 6.85, 6.86, 6.87, 6.88 and 6.89; and for the icosahedral grid in Figures 6.90, 6.91, 6.92, 6.93, 6.94 and 6.95.

Looking at the zonal mean statistics for the cubed sphere grid, it is immediately apparent that the total energy conserving variant is producing wildly different results from the potential enstrophy and doubly-conservative variants. However, the potential enstrophy and doubly conservative variants are quite similar, except for the standard deviation of fluid height. Significant differences in this case are seen at all latitudes. These zonal mean statistics can be also compared with results from John Thuburn (personal communication, obtained using a primal-dual mimetic finite element scheme). The primal-dual finite element scheme is very similar to the one presented here, but it is first-order accurate in the Taylor series sense on all grids. The doubly conservative and potential enstrophy conserving variants are very similar to Thuburn's results, indicating that the total energy conserving variant is probably wrong. As might be anticipated, there is significantly more variability in the standard deviations of both relative vorticity and divergence than in the results

from Thuburn. This is not unexpected, since Thuburn uses an upwind advection scheme for both fluid height and potential vorticity. Further examination of the cubed-sphere results is provided below: essentially there is extremely strong grid imprinting seen for all three variants.

On the icosahedral grid, the situation is very different. All three variants show very similar zonal mean statistics. The zonal standard deviation of fluid height shows some differences, especially in the mid-latitudes. Similar results are seen in standard deviation of relative vorticity and divergence. There are also differences in the standard deviation of divergence in the tropics. Since the mid-latitudes are the dynamically active regions for this forcing, these differences are important. Comparing to the results from Thuburn, the zonal means of all variables are quite similar. However, there is again significantly more variability in the standard deviation of relative vorticity and divergence. In addition, the standard deviation of height appears to be missing a peak at around $\pm 30^\circ$ latitude. It does not appear that any particular variants are closer to each other than to the other variants. This is unexpected, since reasoning from incompressible turbulence theory suggests that enstrophy conservation should produce similar results to double conservation. Closer examination of this is certainly warranted, but beyond the scope of this work.

Temporal Statistics. Temporal means and standard deviations for the cubed sphere grid are provided in Figures 6.96, 6.97, 6.98, 6.99, 6.100 and 6.101; and for the icosahedral grid in Figures 6.102, 6.103, 6.104, 6.105, 6.106 and 6.107.

For the total energy conserving variant on the cubed-sphere grid, strong grid imprinting is seen in both means and standard deviations for all variables- especially in the mean divergence. In addition, all three variants show grid imprinting in the standard deviations of relative vorticity and divergence. This is not a surprising result: the "weather" test cases

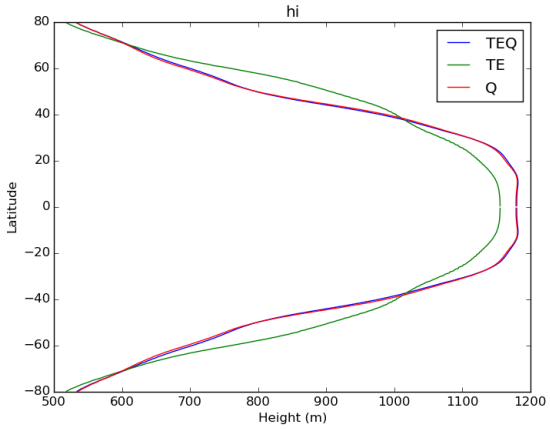

FIGURE 6.84. Zonally averaged mean fluid height for C grid scheme on the cubed-sphere grid, all three variants

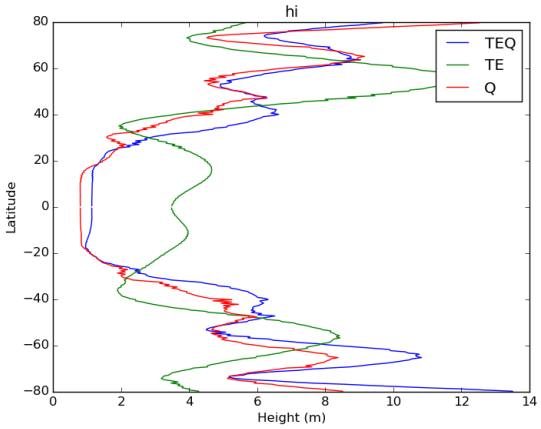

FIGURE 6.85. Zonally averaged standard deviation of fluid height for C grid scheme on the cubed-sphere grid, all three variants

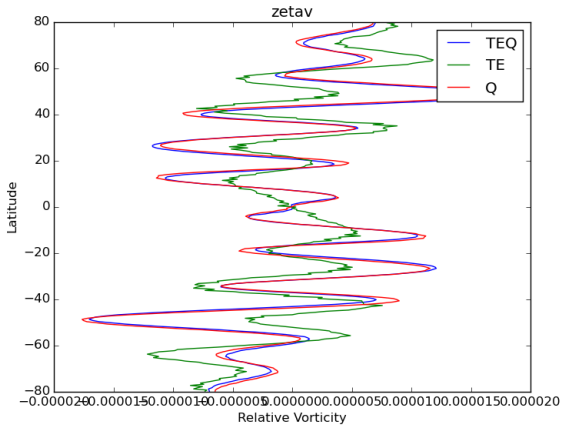

FIGURE 6.86. Zonally averaged mean relative vorticity for C grid scheme on the cubed-sphere grid, all three variants

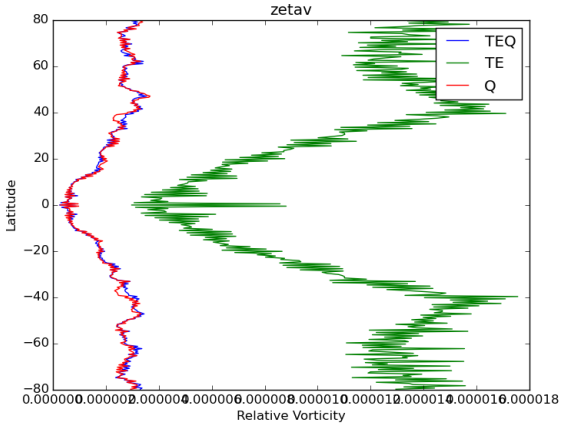

FIGURE 6.87. Zonally averaged standard deviation of relative vorticity for C grid scheme on the cubed-sphere grid, all three variants

(especially the Galewsky test case) revealed issues with the cubed-sphere. However, these results reveal the unsuitability of this scheme on the cubed sphere grid for use in climate simulations. This is not the case for the results from Thuburn, again probably due to the upwind biased advection of height and potential vorticity.

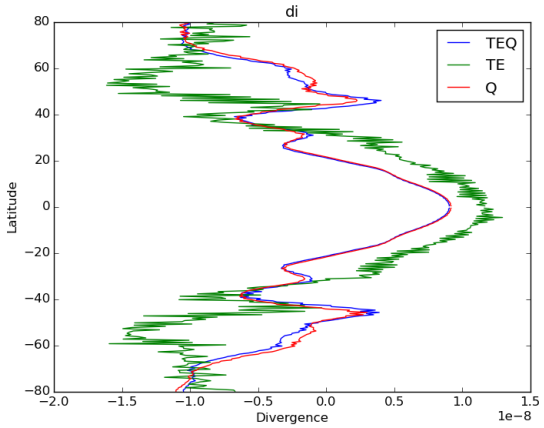

FIGURE 6.88. Zonally averaged mean divergence for C grid scheme on the cubed-sphere grid, all three variants

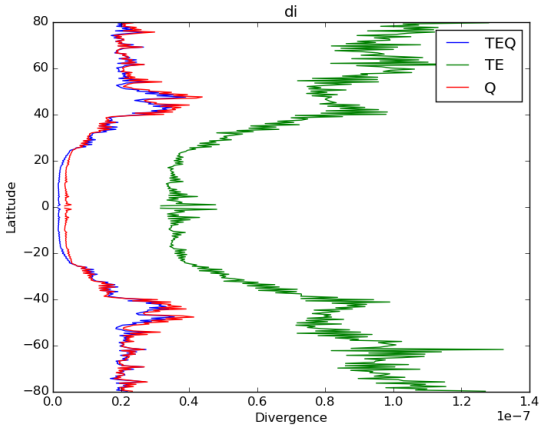

FIGURE 6.89. Zonally averaged standard deviation of divergence for C grid scheme on the cubed-sphere grid, all three variants

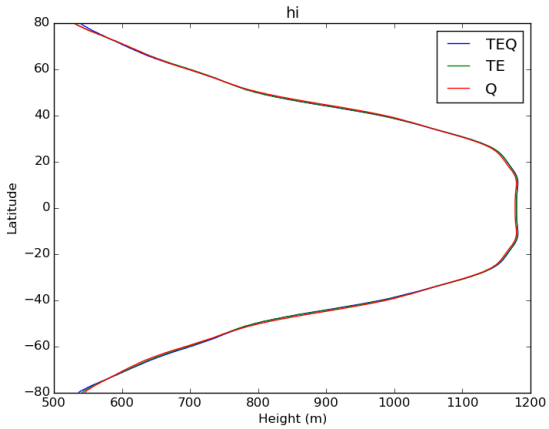

FIGURE 6.90. Zonally averaged mean fluid height for C grid scheme on the icosahedral grid, all three variants

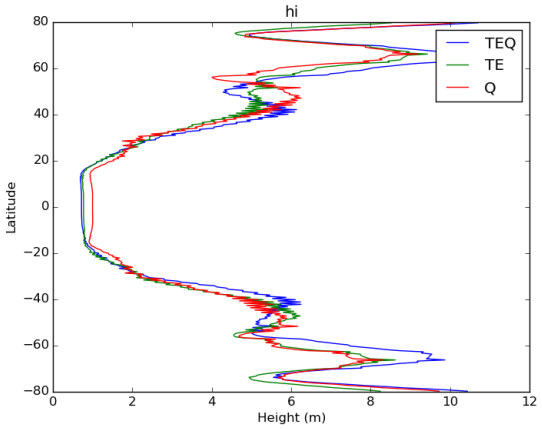

FIGURE 6.91. Zonally averaged standard deviation of fluid height for C grid scheme on the icosahedral grid, all three variants

Results on the icosahedral grid are again quite different from the results on the cubed-sphere grid. All three variants produced very similar mean statistics in fluid height and relative vorticity, and were close to the results from Thuburn. The standard deviation of fluid height was also similar between the variants and to Thuburn. However, the relative

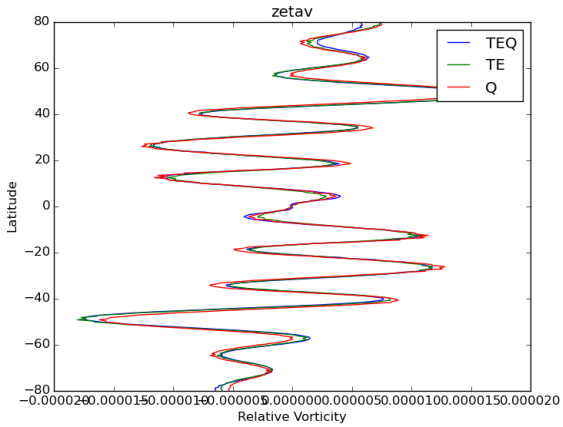

FIGURE 6.92. Zonally averaged mean relative vorticity for C grid scheme on the icosahedral grid, all three variants

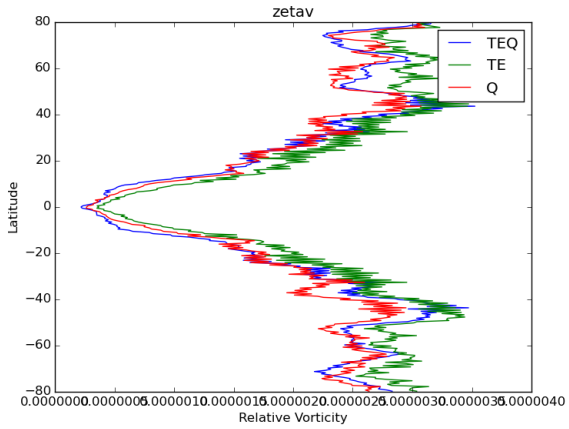

FIGURE 6.93. Zonally averaged standard deviation of relative vorticity for C grid scheme on the icosahedral grid, all three variants

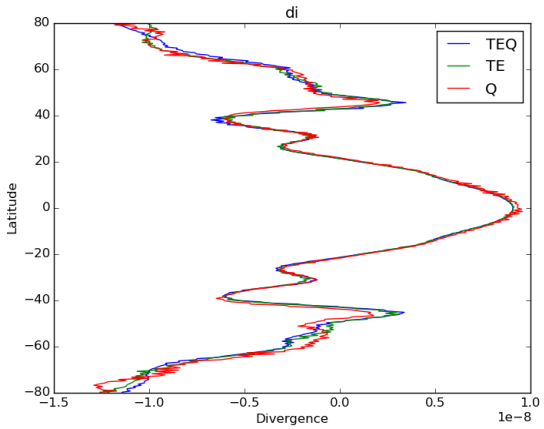

FIGURE 6.94. Zonally averaged mean divergence for C grid scheme on the icosahedral grid, all three variants

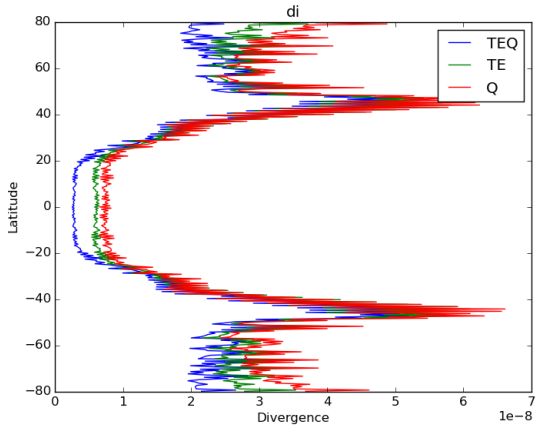

FIGURE 6.95. Zonally averaged standard deviation of divergence for C grid scheme on the icosahedral grid, all three variants

vorticity standard deviation and mean divergence both exhibited significant grid imprinting, although not as severe as that seen on the cubed-sphere grid. This is not the case for the results from Thuburn, again probably due to the upwind biased advection of height and potential vorticity.

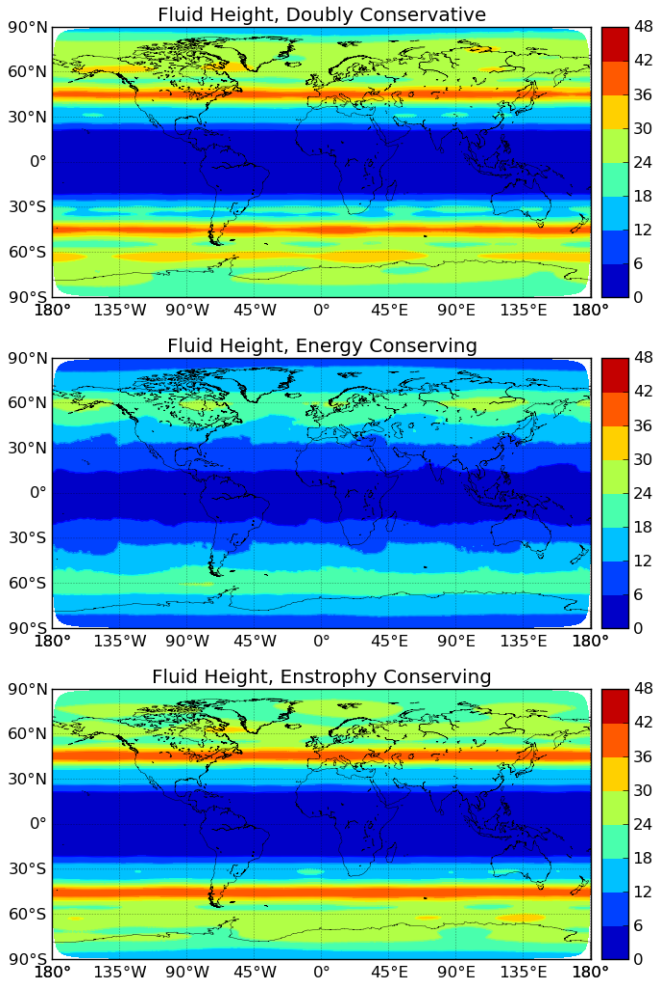

FIGURE 6.96. Standard deviation of fluid height for C grid scheme on cubed-sphere grid. Top is doubly conservative variant, middle is total energy conserving variant and bottom in potential enstrophy conserving variant

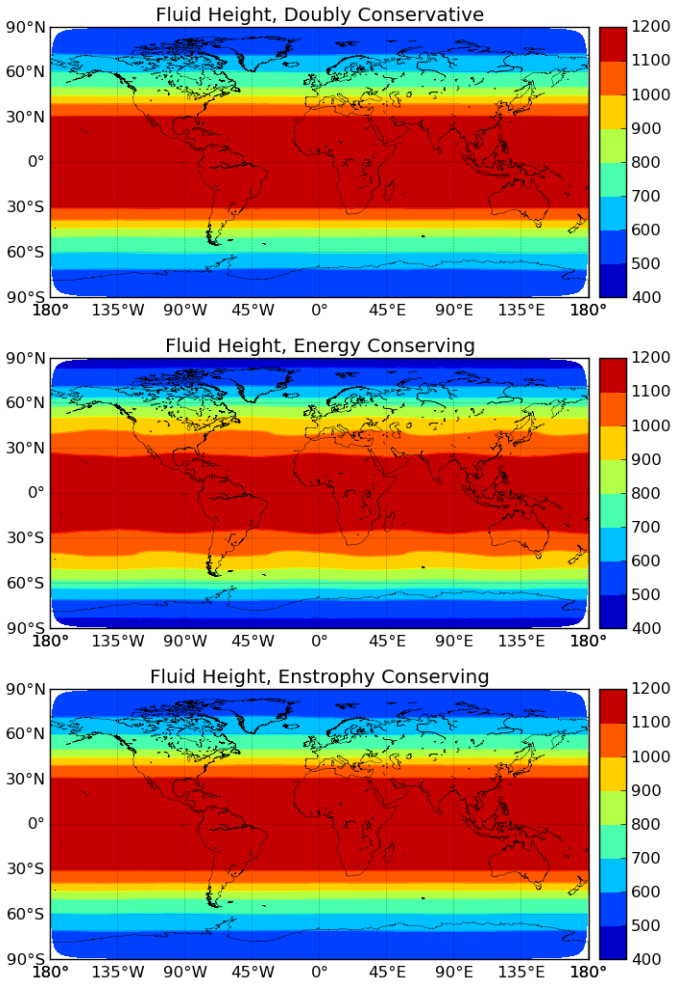

FIGURE 6.97. Mean fluid height for C grid scheme on cubed-sphere grid. Top is doubly conservative variant, middle is total energy conserving variant and bottom in potential enstrophy conserving variant

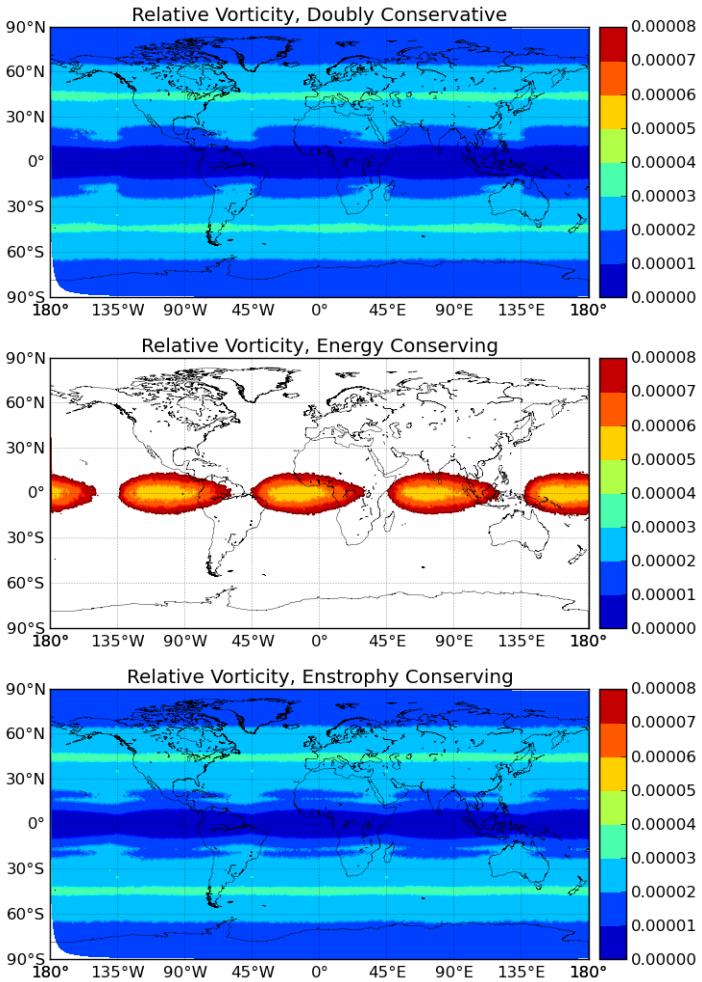

FIGURE 6.98. Standard deviation of relative vorticity for C grid scheme on cubed-sphere grid. Top is doubly conservative variant, middle is total energy conserving variant and bottom in potential enstrophy conserving variant. Note that the total energy conserving variant is producing values that exceed the plot bounds.

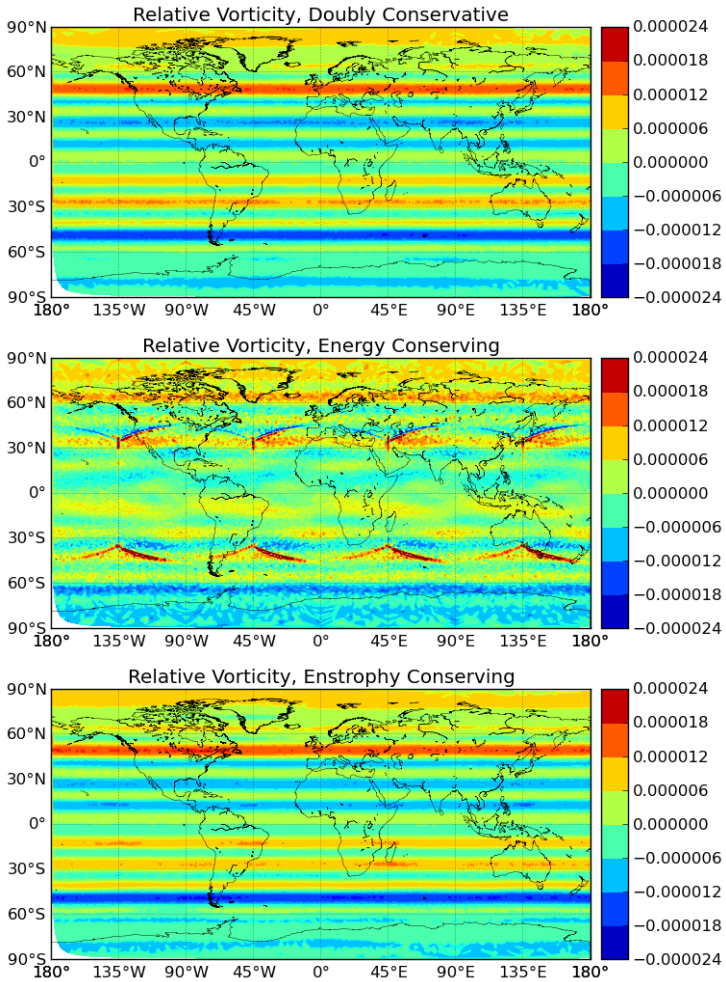

FIGURE 6.99. Mean relative vorticity for C grid scheme on cubed-sphere grid. Top is doubly conservative variant, middle is total energy conserving variant and bottom in potential enstrophy conserving variant

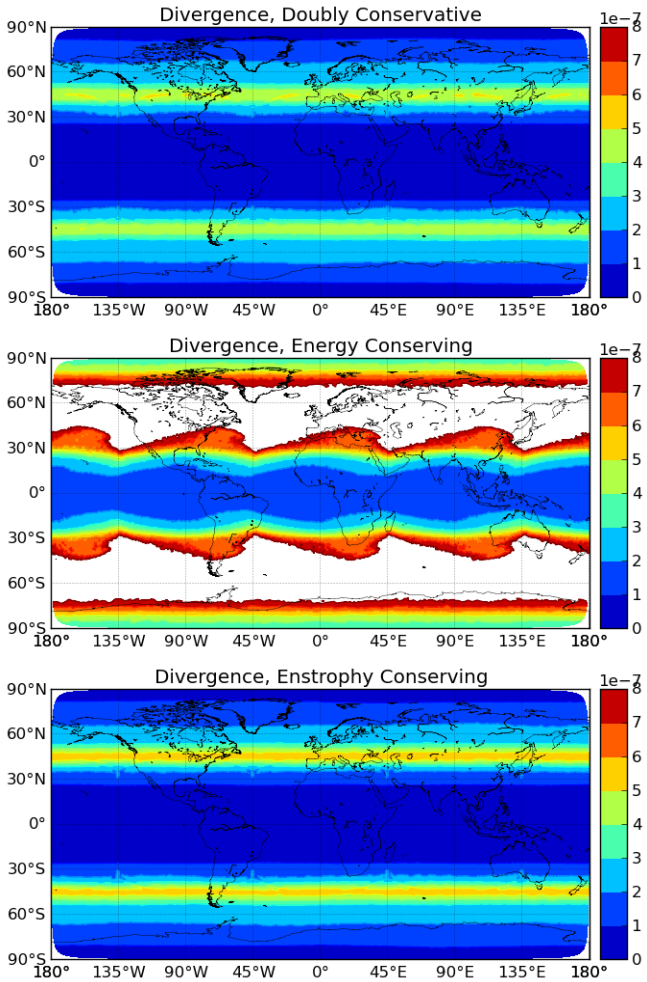

FIGURE 6.100. Standard deviation of divergence for C grid scheme on cubed-sphere grid. Top is doubly conservative variant, middle is total energy conserving variant and bottom in potential enstrophy conserving variant. Note that the total energy conserving variant is producing values that exceed the plot bounds.

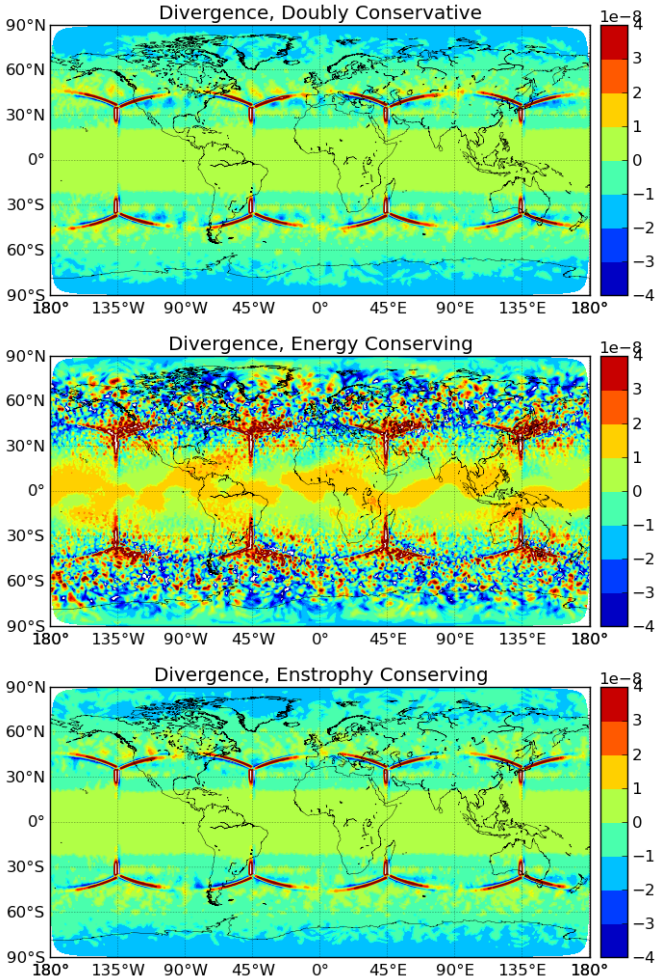

FIGURE 6.101. Mean divergence for C grid scheme on cubed-sphere grid. Top is doubly conservative variant, middle is total energy conserving variant and bottom in potential enstrophy conserving variant

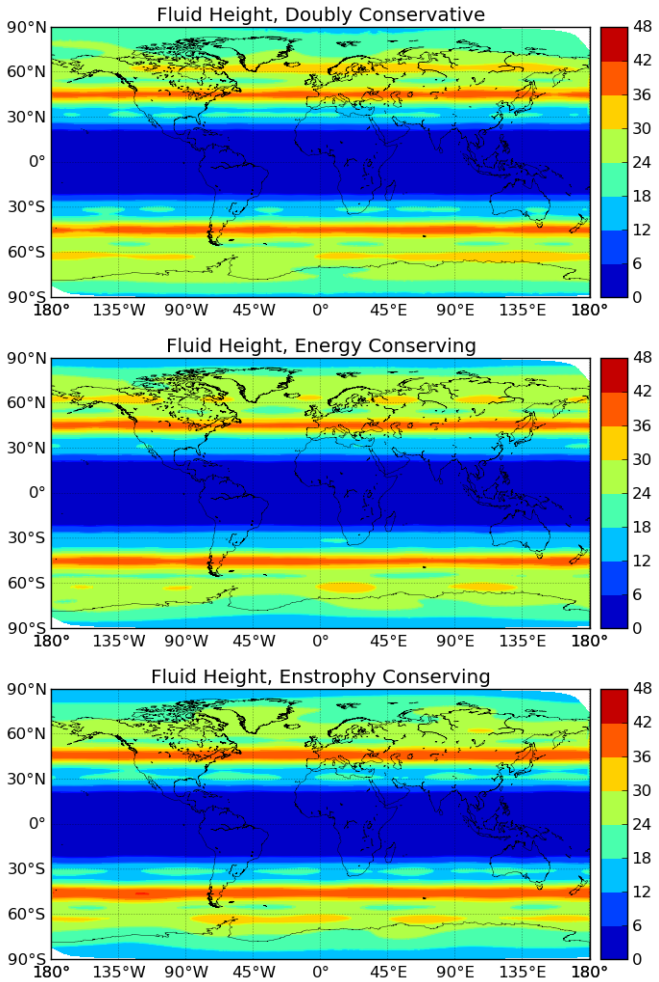

FIGURE 6.102. Standard deviation of fluid height for C grid scheme on icosahedral grid. Top is doubly conservative variant, middle is total energy conserving variant and bottom in potential enstrophy conserving variant

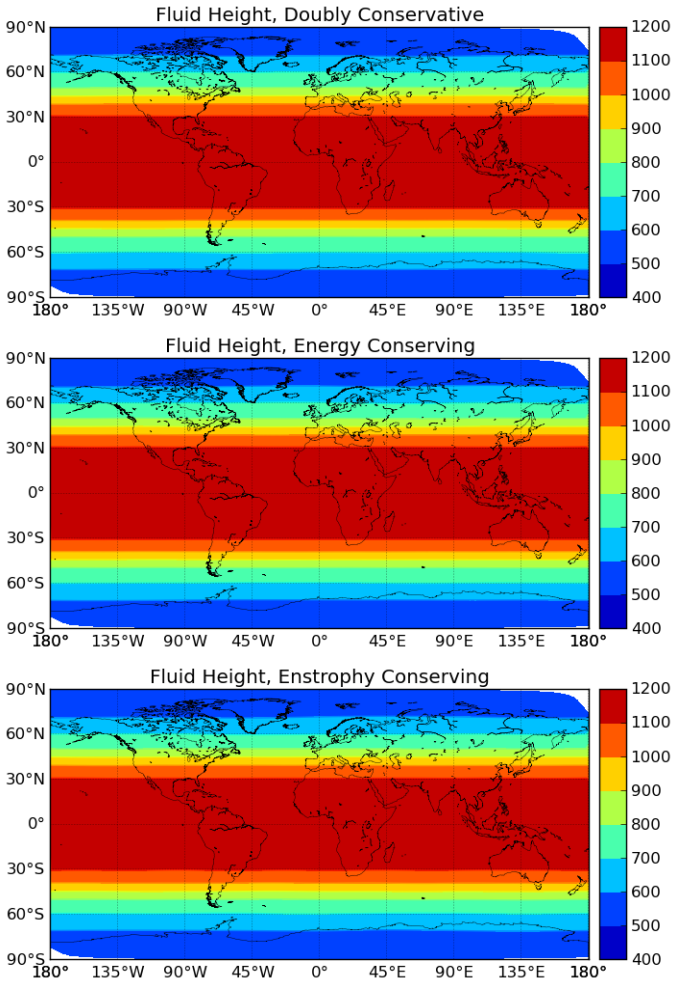

FIGURE 6.103. Mean fluid height for C grid scheme on icosahedral grid. Top is doubly conservative variant, middle is total energy conserving variant and bottom in potential enstrophy conserving variant

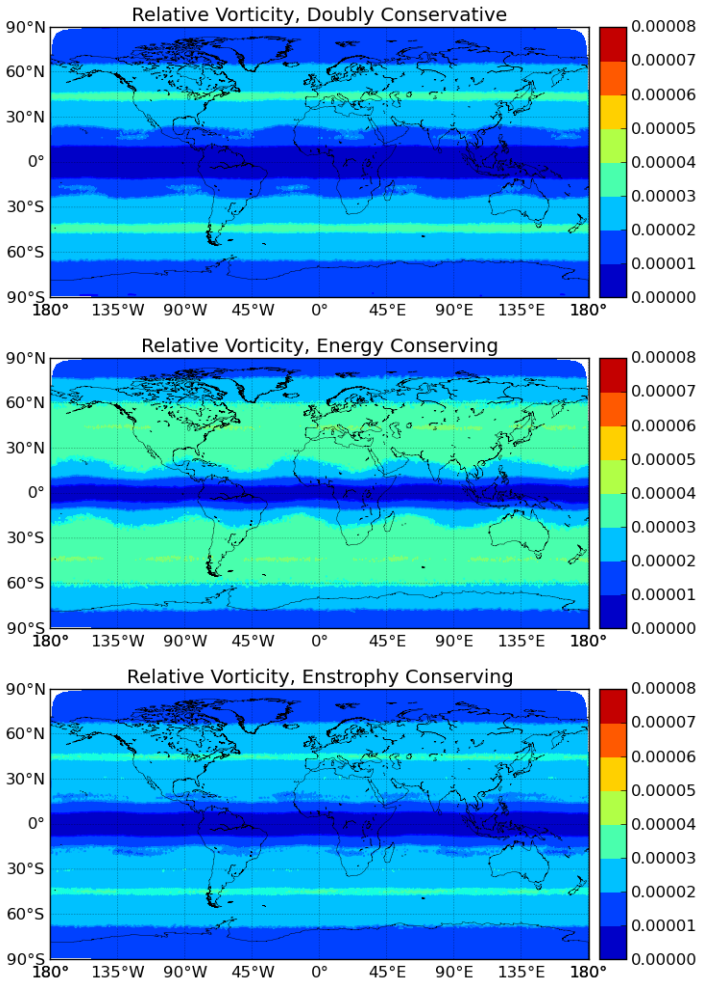

FIGURE 6.104. Standard deviation of relative vorticity for C grid scheme on icosahedral grid. Top is doubly conservative variant, middle is total energy conserving variant and bottom in potential enstrophy conserving variant

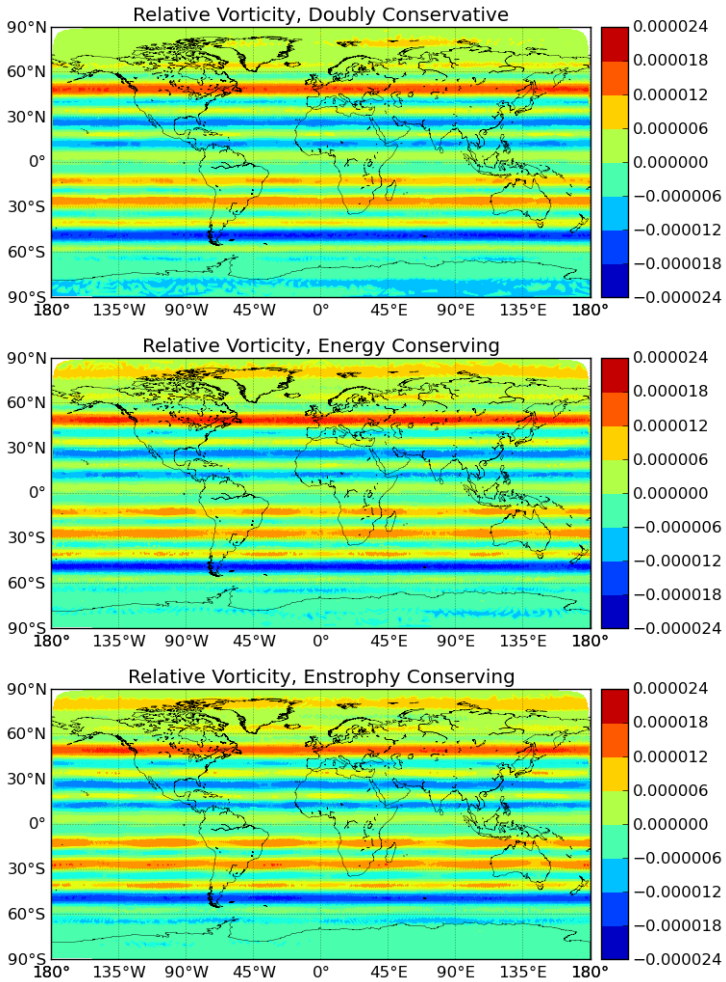

FIGURE 6.105. Mean relative vorticity for C grid scheme on icosahedral grid. Top is doubly conservative variant, middle is total energy conserving variant and bottom in potential enstrophy conserving variant

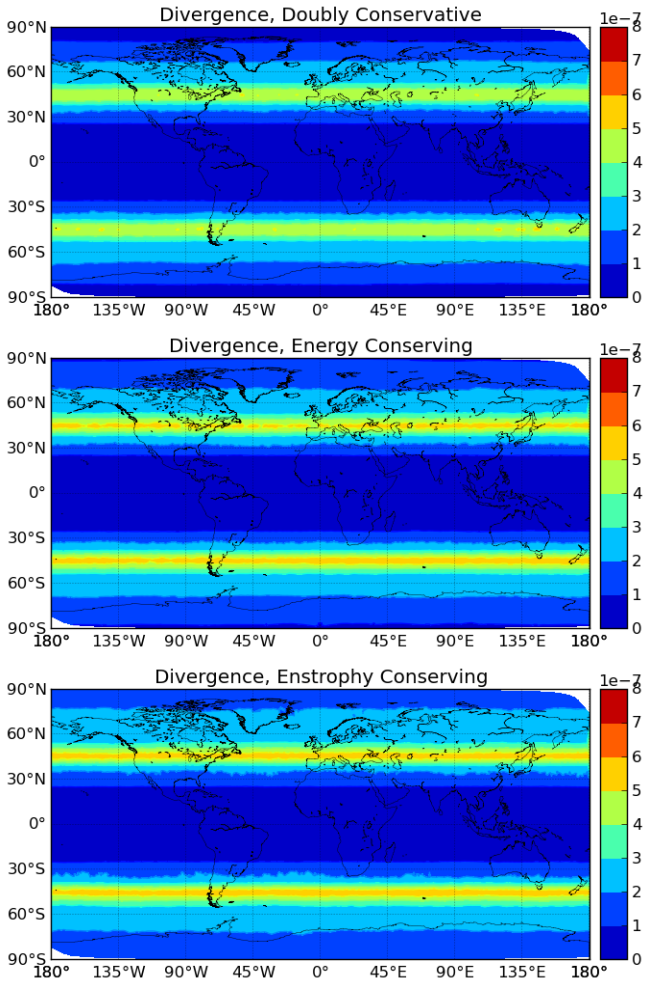

FIGURE 6.106. Standard deviation of divergence for C grid scheme on icosahedral grid. Top is doubly conservative variant, middle is total energy conserving variant and bottom in potential enstrophy conserving variant

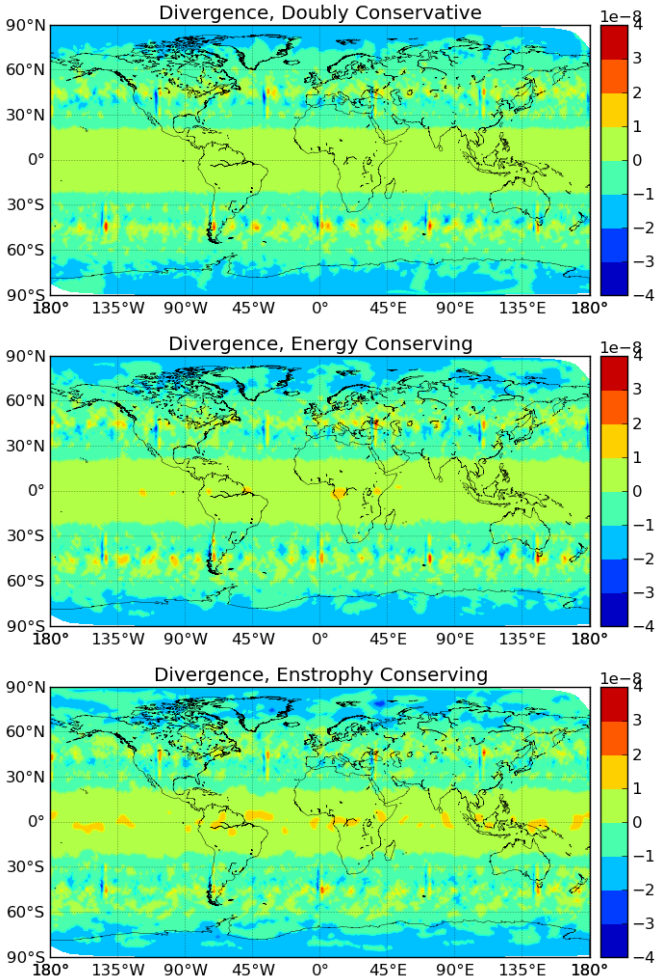

FIGURE 6.107. Mean divergence for C grid scheme on icosahedral grid. Top is doubly conservative variant, middle is total energy conserving variant and bottom in potential enstrophy conserving variant

6.7.2. Z Grid Results.

Zonal Mean Results. Zonal/temporal means and standard deviations for the icosahedral grid are provided in Figures 6.108, 6.109, 6.110, 6.111, 6.112 and 6.113.

The zonally averaged means for fluid height and relative vorticity are quite similar to those found by Thuburn, and those seen for the doubly conservative C grid scheme on icosahedral grids. However, there are significant differences seen in the zonally averaged mean divergence. especially in the mid latitudes. Comparing zonal standard deviations, the fluid height and relative vorticity are quite different, at all latitudes. Interestingly, the zonal standard deviation of divergence between and C and Z grid were quite similar. Compared with Thuburn, the relative vorticty and divergence zonal standard deviations were much noisier.

It was hoped that the doubly conservative C grid scheme on icosahedral grids and Z grid scheme would produce similar results, since they conserve the same quantities and are based on the same grid. Unfortunately, this was not the case.

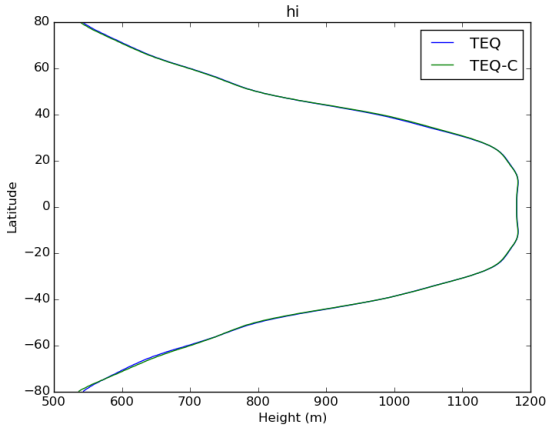

FIGURE 6.108. Zonally averaged mean fluid height for Z grid and C grid (doubly conservative variant) schemes on the icosahedral grid

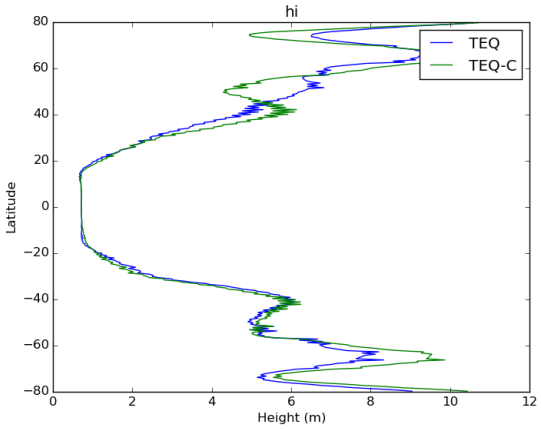

FIGURE 6.109. Zonally averaged standard deviation of fluid height for Z grid and C grid (doubly conservative variant) schemes on the icosahedral grid

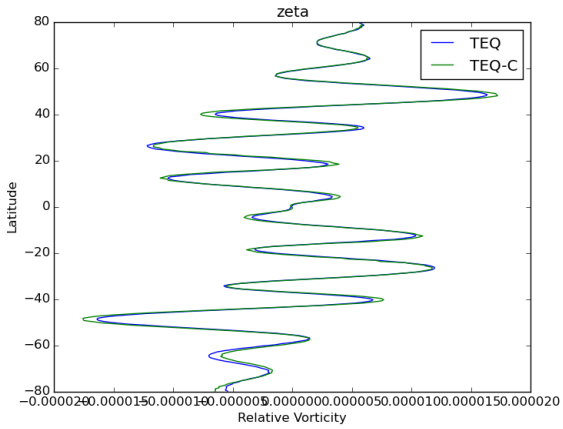

FIGURE 6.110. Zonally averaged mean relative vorticity for Z grid and C grid (doubly conservative variant) schemes on the icosahedral grid

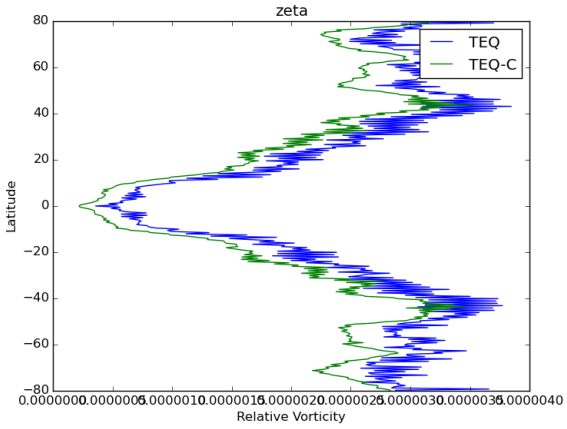

FIGURE 6.111. Zonally averaged standard deviation of relative vorticity for Z grid and C grid (doubly conservative variant) schemes on the icosahedral grid

Temporal Statistics. Temporal means and standard deviations for the icosahedral grid are provided in Figures 6.115 and 6.114.

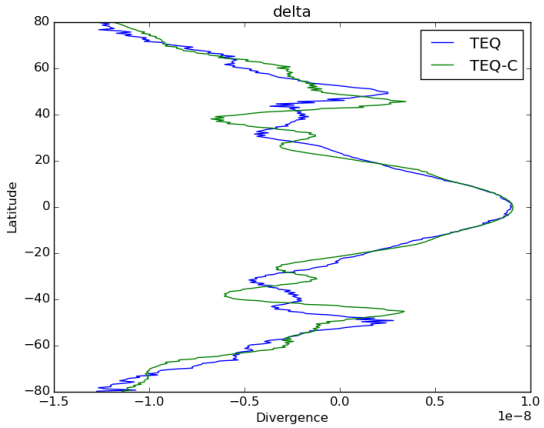

FIGURE 6.112. Zonally averaged mean divergence for Z grid and C grid (doubly conservative variant) schemes on the icosahedral grid

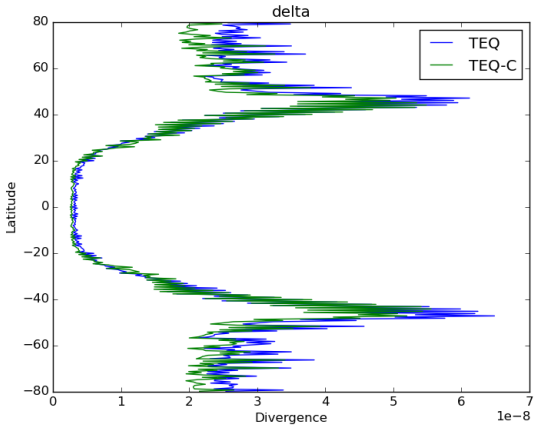

FIGURE 6.113. Zonally averaged standard deviation of divergence for Z grid and C grid (doubly conservative variant) schemes on the icosahedral grid

The spatial distribution of mean fluid height and relative vorticity are quite similar to the C grid doubly conservative scheme on icosahedral grids; and to the results from Thuburn. The same can be said for the standard deviation of divergence and fluid height, with the caveat that the divergence standard deviation is noisier. Unlike the C grid case, the relative vorticity standard deviation does not appear to have significant grid imprinting, and it quite similar to the results in Thuburn, although noisier. The mean divergence does show a little grid imprinting, althogh it is much weaker than that seen on the C grid. It is hypothesized that the grid imprinting on the Z grid scheme is weaker than the C grid scheme because the Jacobian operator is much more consistent than the **W** operator. It seems likely that more serious grid imprinting would be seen on the Z grid at higher resolution, where the inconsistency of the Jacobian approaches that of the **W** operator at lower resolutions.

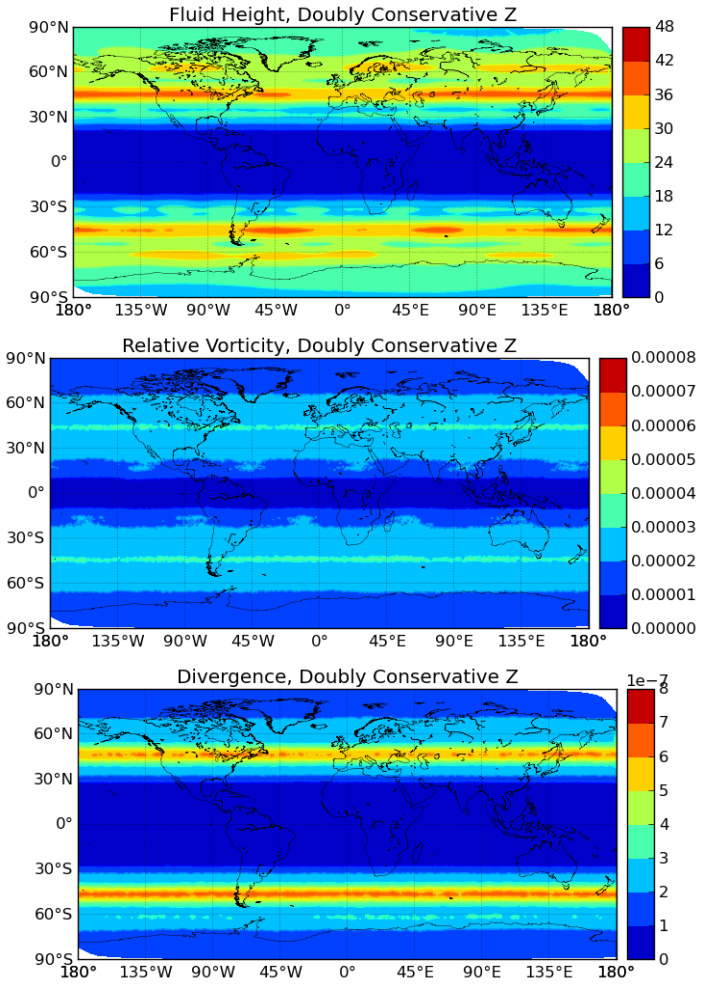

FIGURE 6.114. Standard deviation of fluid height, relative vorticity and divergence for the Z grid scheme on an icosahedral grid.

6.8. CHAPTER SUMMARY

This chapter has evaluated and compared the generalized C and Z grid schemes developed in Chapter 3 and Chapter 4. Essentially all of the material presented is new, with the exception of some of the order of accuracy results that are duplicates of tests done in [154] and [137]. The next Chapter provides a high-level overview of the results from this Chapter and makes suggestions about the utility of various schemes for both weather forecasting and climate prediction.

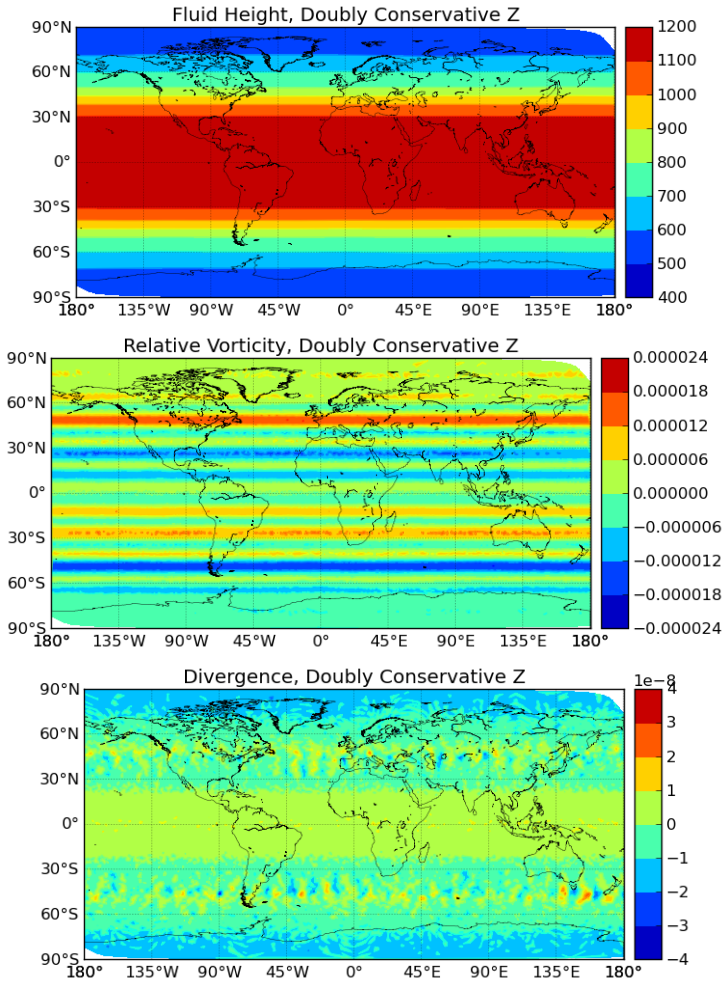

FIGURE 6.115. Mean fluid height, relative vorticity and divergence for the Z grid scheme on an icosahedral grid.

CHAPTER 7

Conclusions

The major thrust of this work was the development of a doubly conservative extension of the 1981 Arakawa and Lamb scheme to arbitrary grids. This was accomplished by following the approach of Salmon 2004 ([115]), in conjunction with the discrete exterior calculus framework of Thuburn, Cotter and Dubos 2012 ([135]). In addition, a doubly conservative Z grid scheme for icosahedral grids free of computational modes was also developed, following Salmon 2007 ([117]). The linear modes and performance of the schemes for various test cases on a variety of grids were then investigated. Broad conclusions are drawn below from these investigations, and some remarks about the suitability of these schemes as the basis for weather and climate models are given.

7.1. Linear Modes Summary

Stationary Modes. For the f-sphere, the stationary modes for all three schemes were found to be linear combinations of the geostrophic modes (with zero divergence). On the full sphere, all of the stationary or quasi-stationary modes were zonally symmetric (again with zero divergence). This was in contrast to the results from Weller ([153]), who found stationary or quasi-stationary modes with zonal structure. It is hypothesized that this difference is due to the more accurate calculation of $\mathbf{A}$ compared to that study. In all cases (f-sphere and full sphere, with and without dissipation), no damaging spurious stationary modes were found. This supports the theoretical analysis, and is what is expected from planar grid results. The addition of dissipation did not alter the mode structures for either the f-sphere or the full sphere case, although the only truly stationary mode in the case

of dissipation was a mode with constant height and zero wind (and therefore zero relative vorticity and divergence).

Propagating Modes. All of the scheme tested had broadly similar wave dispersion properties, with the some differences in the highest wavenumbers. Encouragingly, none of the schemes had any spectral gaps or jumps, and all showed increasing frequency with wavenumber. Both the C and Z grid schemes on icosahedral grids showed the expected flattening of frequency at the highest wavenumbers, while the C grid scheme on the cubed sphere grid had a linear increase in frequency. These high frequency modes were shown to be unphysical and strongly localized around the singular points of the grid. Although this was also the case for the icosahedral grid schemes, it was much less pronounced. These results broadly mimic what is seen in the planar grid case, and also what was found in Weller. There was no evidence of damaging spurious Rossby modes, in particular, the stationary modes of the full sphere were all zonally symmetric. The strength of dissipation (in the form of viscosity) linearly increased with increasing wavenumber for the inertia-gravity modes for both the f-sphere and the full sphere, in accordance with the planar grid results. It was quasi-randomly distributed for the Rossby modes. The reason for this remains unclear, although it is possible that the method used to characterized the Rossby modes is not an accurate reflection of their spatial wavenumber.

7.2. Test Cases Summary

Accuracy. Both the C and the Z grid scheme were found to be inconsistent, even with optimized grids. The **W** operator for the C grid scheme was inconsistent on all grids, as was the Jacobian operator for the Z grid scheme. For the cubed-sphere C grid scheme, even the Laplacian operators were inconsistent. However, on the tweaked icosahedral grid both

the Z grid and C grid schemes were able to obtain approximately first order accuracy in the TC2 test case, despite their inconsistency. Unfortunately, the TC2 test case (solid body rotation) is not particularly challenging- it is quite linear; and probably does not represent the performance of the scheme for realistic situations.

"Weather" Test Cases. Results from TC5 indicate the presence of significant near grid-scale variability for the C grid scheme on icosahedral grids, especially when compared to the C grid scheme on cubed-sphere grids or the Z grid scheme. This variability is believed to be associated with the spurious branch of Rossby waves associated with the icosahedral C grid. However, this additional variability does not appear to impact the ability of the model to resolve the larger scales. The Rossby-Haurwitz test case (TC6) indicated that the icosahedral grid imprinting (a wavenumber 5 forcing) was causing the initial state to break down. This occurs after around 20 days for both the C and Z grid models on icosahedral grids. The cubed-sphere C grid was stable out to 50 days. The Galewsky et. al test case, run without the initial perturbation, indicated the presence of grid imprinting on all grids, associated with a breakdown of the balanced but unstable initial state. In a 3D model, this could cause the spurious release of baroclinic instability. The total energy conserving and doubly conservative C grid schemes on icosahedral grids, and the Z grid scheme showed the least evidence of grid imprinting. When the initial perturbation was added, these three schemes also produced very similar results. The cubed-sphere grid schemes (except for the total energy conserving variant) appears to be converging to the consensus solution, but slower than the icosahedral schemes. All of the schemes required extremely high resolution (G8 and C8) to eliminate the wavenumber 4 (cubed-sphere) or 5 (icosahedral) patterns seen in the inactive regions of the jet. No evidence of issues from the spurious modes on the icosahedral C grid was found. On the optimized icosahedral grids, there were additionally

no issues seen from the inconsistency of the **W** or Jacobian operators. For the cubed-sphere grid, there were instability issues with the total energy conserving variant in the Galewsky test case, probably associated with the inconsistency of the C grid scheme on the cubed sphere grid in general.

Climate Test Cases. Unlike the results from the weather test cases (where the total energy and doubly conservative variants of the C grid scheme on icosahedral grids; and the Z grid scheme both performed well), the "Held-Suarez" climate test case revealed major issues with all of the schemes tested. In particular, all of the C grid schemes exhibited significant grid imprinting in at least the mean divergence. The Z grid scheme also showed this, but it was much weaker than that seen in the C grid schemes. However, as discussed in Chapter 6, this was probably due to the increased accuracy of the Jacobian operator at the resolutions tested compared with the **W** operator. At higher resolutions, it is anticipated that the inconsistency of the Jacobian operator would produce similar grid imprinting issues. Encouragingly, however, no evidence of issues from the spurious modes on the icosahedral C grid was found.

7.3. Selection of a scheme for developing a weather model

Weather forecasting is fundamentally an initial value problem, and conservation aspects are less important. Instead, the ability of a scheme to accurately evolve an initial state; and properly represent processes such as baroclinic instability are paramount. The cubed sphere C grid schemes and the enstrophy conserving C grid scheme on icosahedral grids all suffered from very strong grid imprinting, and associated spurious breakdown of the unstable balanced jet. On the basis of these results from the "weather" test cases (TC2, TC5, TC6 and Galewsky), it appears that the total energy or doubly conservative variants of the C

grid scheme on icosahedral grids; and the Z grid scheme are the only viable possibilities. However, the spurious release of barotropic instability could be an issue with these schemes, even though their grid imprinting was quite weak. It seems likely that higher-order accuracy (at least between 1st and 2nd order) is desirable in order to suppress this.

Although the issues with the scheme discussed above can be circumvented with the addition of dissipation or filters, this is not a desirable approach. The real atmosphere is essentially inviscid at the scales of interest for most NWP, and therefore any dissipation (either explicit or implicit) is really a representation of the interaction between resolved and unresolved scales. There is growing evidence ([138] and [68]) that viscosity, hyperviscosity and other commonly used dissipation schemes are a poor representation of this subgrid interaction. Therefore, it is not unreasonable to say dissipation that is added purely to control bad numerics represents an unphysical parameterization, and it should be avoided wherever possible.

7.4. Selection of a scheme for developing a climate model

Climate simulation is a very different problem from weather forecasting. The basic question becomes: given a set of (possibly time varying) forcings, what are the statistics of possible dynamical states? In such a case, a strong argument can be made for the importance of conservation laws, since they constrain the possible dynamical states that a system can explore. This is very different from weather forecasting, which is trying to determine the evolution of a dynamical system from a given state.

On the basis of the grid imprinting seen for all of the C grid schemes, only the Z grid scheme seems to be a viable possibility for a climate model. However, as discussed above, this lack of grid imprinting is probably only an artifact of the coarse resolution used, where

the Jacobian operator is still fairly accurate. Again, at higher resolutions it is anticipated that the inconsistency of the Jacobian operator will would produce similar grid imprinting issues.

7.5. Future Work

In reality, none of these scheme are truly viable as candidates for next generation dynamical cores being used for either climate or weather. If a choice had to be made, the Z grid scheme might be made viable for climate, and the Z grid and total energy or doubly conservative C grid schemes on icosahedral grids could be made to work for weather. All of these would likely require unphysical amounts of dissipation to control the grid imprinting induced by the inconsistency of the **W** and Jacobian operators.

However, all is not lost. Recent work by John Thuburn and Collin Cotter ([136]) has extended the C grid framework discussed in Chapter 3 to the case of primal-dual mimetic finite elements. It seems very likely that the doubly conservative C grid scheme can also be extended to this framework: it is believed that the same form of operator **Q** can in fact be used. The **W** operator in this framework is now consistent, and the whole scheme is more accurate, which should help alleviate grid imprinting issues. In addition, since the scheme is still single-moment with the same degrees of freedom, the linear modes should be very similar to those seen in the current study.

A finite-element scheme requires the solution of elliptic problems at each time step. This motivates the use of a semi-implicit or fully implicit time stepping scheme, since unlike the current framework the additional cost compared to explicit time stepping is not very large. Also, it would be possible to obtain a fully conservative scheme (rather than just semi-discrete conservative) using implicit time stepping, which might be desirable for climate applications.

The accuracy issues with the Z grid scheme could also be solved. Two routes seem fruitful: the first would be the extension of finite element exterior calculus approach to the vorticity-divergence framework. This would require careful investigation into the resulting linear modes, since anything beyond the lowest-order finite element schemes would have multiple degrees of freedom per geometry entity, which has been know to cause issues in the dispersion relationship. The second would be recent work done by Ross Heikes (personal communication) on improving the accuracy of individual operators while retaining a single moment per grid cell. Again, semi-implicit or fully implicit time stepping should probably be explored in these frameworks.

It also seems likely that the inhomogeneity of the cubed-sphere grid used in this study contributes to the issues seen on that grid. As has been found by other work, it appears that good performance of the low order finite-difference/finite volume type schemes requires careful optimization of the underlying grid. Recent work by Jim Purser ([99], and personal communication) has led to a method for generating much smoother cubed sphere grids. It seems likely that similar performance to that seen on the tweaked icosahedral grid could be obtained on an optimized cubed sphere grid, although grid imprinting issues from the inconsistency of $\mathbf{W}$ would remain. It would also be useful to explore other choices of grid such as Hilary Weller's diamond grid ([154]), which is obtained from a cubed sphere grid by creating new grid cells at each edge from the two primal vertices and two dual vertices that define the edge.

Bibliography

[1] Adcroft, A. J., C. N. Hill, and J. C. Marshall, 1999: A new treatment of the coriolis terms in c-grid models at both high and low resolutions. *Monthly Weather Review*, **127 (8)**, 1928–1936, doi:10.1175/1520-0493(1999)127¡1928:ANTOTC¿2.0.CO;2, URL http://dx.doi.org/10.1175/1520-0493(1999)127<1928:ANTOTC>2.0.CO;2.

[2] Antoniou, I. and G. P. Pronko, 2001: On the Hamiltonian Description of Fluid Mechanics. *arXiv*, 24, URL http://arxiv.org/abs/hep-th/0106119, 0106119.

[3] Arakawa, A. and V. R. Lamb, 1977: Computational design of the basic dynamical processes of the ucla general circulation model. *General Circulation Models of the Atmosphere*, Elsevier, Methods in Computational Physics: Advances in Research and Applications, Vol. 17, 173 – 265, doi:10.1016/B978-0-12-460817-7.50009-4, URL http://www.sciencedirect.com/science/article/pii/B9780124608177500094.

[4] Arakawa, A. and V. R. Lamb, 1981: A Potential Enstrophy and Energy Conserving Scheme for the Shallow Water Equations. *Monthly Weather Review*, **109 (1)**, 18–36, doi:10.1175/1520-0493(1981)109¡0018:APEAEC¿2.0.CO;2.

[5] Arnold, D. N., R. S. Falk, and R. Winther, 2006: Finite element exterior calculus, homological techniques, and applications. *Acta Numerica*, **15**, 1, doi:10.1017/S0962492906210018, URL http://journals.cambridge.org/abstract_S0962492906210018.ewline

[6] Arnold, D. N., R. S. Falk, and R. Winther, 2010: Finite element exterior calculus: from Hodge theory to numerical stability. *Bulletin of the American Mathematical Society*, **47 (2)**, 281–354, doi:10.1090/S0273-0979-10-01278-4, URL http://www.ams.org/bull/2010-47-02/S0273-0979-10-01278-4/.ewline

[7] Atkinson, J. H., J. J. Westerink, and R. A. Luettich, 2004: Two-dimensional dispersion analyses of finite element approximations to the shallow water equations. *International Journal for Numerical Methods in Fluids*, **45 (7)**, 715–749, doi:10.1002/fld.701, URL http://dx.doi.org/10.1002/fld.701.

[8] Audusse, E., R. Klein, and A. Owinoh, 2009: Conservative discretization of coriolis force in a finite volume framework. *Journal of Computational Physics*, **228 (8)**, 2934 – 2950, doi:10.1016/j.jcp.2009.01.004, URL http://www.sciencedirect.com/science/article/pii/S0021999109000102.

[9] Batteen, M. L. and Y.-J. Han, 1981: On the computational noise of finite-difference schemes used in ocean models. *Tellus*, **33 (4)**, 387–396, doi:10.1111/j.2153-3490.1981.tb01761.x, URL http://dx.doi.org/10.1111/j.2153-3490.1981.tb01761.x.

[10] Bauer, W., 2013: Toward goal-oriented R-adaptive models in geophysical fluid dynamics using a generalized discretization approach. Ph.D. thesis, MPI for Meteorology, Hamburg.

[11] Baumgardner, J. R. and P. O. Frederickson, 1985: Icosahedral Discretization of the Two-Sphere. *SIAM Journal on Numerical Analysis*, **22 (6)**, 1107–1115, doi: 10.1137/0722066, URL http://epubs.siam.org/doi/abs/10.1137/0722066.

[12] Beckers, J. M., 2002: Selection of a staggered grid for inertia-gravity waves in shallow water. *International Journal for Numerical Methods in Fluids*, **38 (8)**, 729–746, doi:10.1002/fld.245, URL http://dx.doi.org/10.1002/fld.245.

[13] Bernard, P.-E., E. Deleersnijder, V. Legat, and J.-F. Remacle, 2008: Dispersion analysis of discontinuous galerkin schemes applied to poincare, kelvin and rossby waves. *Journal of Scientific Computing*, **34**, 26–47, doi:10.1007/s10915-007-9156-6, URL http://dx.doi.org/10.1007/s10915-007-9156-6.

[14] Bernard, P.-E., J.-F. Remacle, and V. Legat, 2009: Modal analysis on unstructured meshes of the dispersion properties of the pair. *Ocean Modelling*, **28 (13)**, 2 – 11, doi:10.1016/j.ocemod.2008.03.005, URL http://www.sciencedirect.com/science/article/pii/S1463500308000565, the Sixth International Workshop on Unstructured Mesh Numerical Modelling of Coastal, Shelf and Ocean Flows.

[15] Blair Perot, J. and C. J. Zusi, 2014: Differential forms for scientists and engineers. *Journal of Computational Physics*, **257**, 1373–1393, doi:10.1016/j.jcp.2013.08.007, URL http://www.sciencedirect.com/science/article/pii/S0021999113005354.

[16] Bonaventura, L., A. Iske, and E. Miglio, 2011: Kernel-based vector field reconstruction in computational fluid dynamic models. *International Journal for Numerical Methods in Fluids*, **66 (6)**, 714–729, doi:10.1002/fld.2279, URL http://dx.doi.org/10.1002/fld.2279.

[17] Bonaventura, L. and T. Ringler, 2005: Analysis of Discrete Shallow-Water Models on Geodesic Delaunay Grids with C-Type Staggering. *Monthly Weather Review*, **133 (8)**, 2351–2373, doi:10.1175/MWR2986.1, URL http://dx.doi.org/10.1175/MWR2986.1.

[18] Castro, M., J. Lpez, and C. Pars, 2008: Finite volume simulation of the geostrophic adjustment in a rotating shallow-water system. *SIAM Journal on Scientific Computing*, **31 (1)**, 444–477, doi: 10.1137/070707166, URL http://epubs.siam.org/doi/abs/10.1137/070707166, http://epubs.siam.org/doi/pdf/10.1137/070707166.

[19] Chen, Q., 2015: On staggering techniques and the non-staggered Z-grid scheme. *Numerische Mathematik*, doi:10.1007/s00211-015-0715-8, URL http://link.springer.com/10.1007/s00211-015-0715-8.

[20] Chen, Q., M. Gunzburger, and T. Ringler, 2011: A Scale-Invariant Formulation of the Anticipated Potential Vorticity Method. *Monthly Weather Review*, **139 (8)**, 2614–2629, doi:10.1175/MWR-D-10-05004.1, URL http://journals.ametsoc.org/doi/abs/10.1175/MWR-D-10-05004.1.

[21] Cotter, C. and D. Ham, 2011: Numerical wave propagation for the triangular $p^1_{DG}p^2$ finite element pair. *Journal of Computational Physics*, **230 (8)**, 2806 – 2820, doi:10.1016/j.jcp.2010.12.024, URL http://www.sciencedirect.com/science/article/pii/S0021999110006984.

[22] Cotter, C. and J. Shipton, 2012: Mixed finite elements for numerical weather prediction. *Journal of Computational Physics*, **231 (21)**, 7076–7091, doi:10.1016/j.jcp.2012.05.020, URL http://www.sciencedirect.com/science/article/pii/S0021999112002628.

[23] Cotter, C. and J. Thuburn, 2014: A finite element exterior calculus framework for the rotating shallow-water equations. *Journal of Computational Physics*, **257**, 1506–1526, doi:10.1016/j.jcp.2013.10.008, URL http://www.sciencedirect.com/science/article/pii/S0021999113006761.

[24] Cotter, C. J., D. A. Ham, and C. C. Pain, 2009: A mixed discontinuous/continuous finite element pair for shallow-water ocean modelling. *Ocean Modelling*, **26 (12)**, 86 – 90, doi:10.1016/j.ocemod.2008.09.002, URL http://www.sciencedirect.com/science/article/pii/S1463500308001479.

[25] Cotter, C. J. and A. T. T. McRae, 2014: Compatible finite element methods for numerical weather prediction. *arXiv*, URL http://arxiv.org/abs/1401.0616, 1401.0616.

[26] Danilov, S., 2010: On utility of triangular C-grid type discretization for numerical modeling of large-scale ocean flows. *Ocean Dynamics*, **60 (6)**, 1361–1369, doi:10.1007/s10236-010-0339-6, URL http://link.springer.com/10.1007/s10236-010-0339-6.

[27] Dobricic, S., 2006: An improved calculation of coriolis terms on the c grid. *Monthly Weather Review*, **134 (12)**, 3764–3773, doi:10.1175/MWR3277.1, URL http://dx.doi.org/10.1175/MWR3277.1.

[28] Du, Q., M. Gunzburger, and L. Ju, 2010: Advances in studies and applications of centroidal voronoi tessellations. *Numerical Mathematics: Theory, Methods and Applications*, **3 (2)**, 119–142.

[29] Dubos, T., 2012: Variational derivation of energy-conserving finite-difference schemes for geophysical fluid equations, solution of Partial Differential Equations on the Sphere.

[30] Dubos, T., S. Dubey, M. Tort, R. Mittal, Y. Meurdesoif, and F. Hourdin, 2015: Dynamico, an icosahedral hydrostatic dynamical core designed for consistency and versatility. *Geoscientific Model Development Discussions*, **8 (2)**, 1749–1800, doi:10.5194/gmdd-8-1749-2015, URL http://www.geosci-model-dev-discuss.net/8/1749/2015/.

[31] Dubos, T. and M. Tort, 2014: Equations of Atmospheric Motion in Non-Eulerian Vertical Coordinates: Vector-Invariant Form and Quasi-Hamiltonian Formulation. *Monthly Weather Review*, **142 (10)**, 3860–3880, doi:10.1175/MWR-D-14-00069.1, URL http://journals.ametsoc.org/doi/abs/10.1175/MWR-D-14-00069.1.

[32] Dubos, T. and F. Voitus, 2014: A Semihydrostatic Theory of Gravity-Dominated Compressible Flow. *Journal of the Atmospheric Sciences*, **71 (12)**, 4621–4638, doi:10.1175/JAS-D-14-0080.1, URL http://journals.ametsoc.org/doi/abs/10.1175/JAS-D-14-0080.1.

[33] Dukowicz, J. K., 1995: Mesh effects for Rossby waves. *Journal of Computational Physics*, **119 (1)**, 188 – 194, doi:10.1006/jcph.1995.1126, URL http://www.sciencedirect.com/science/article/pii/S0021999185711266.

[34] Durran, D. R., 1991: The Third-Order Adams-Bashforth Method: An Attractive Alternative to Leapfrog Time Differencing. *Monthly Weather Review*, **119 (3)**, 702–720, doi:10.1175/1520-0493(1991)119¡0702:TTOABM¿2.0.CO;2.

[35] Espelid, T. O. and J. Berntsen, 2007: Coriolis weighting on unstructured staggered grids. *Ocean Modelling*, **16 (12)**, 61 – 75, doi:10.1016/j.ocemod.2006.07.002, URL http://www.sciencedirect.com/science/article/pii/S1463500306000795.

[36] et. al, N., 2002: Geostrophic adjustment on hexagonal grids. *Monthly Weather Review*, **130 (3)**, 668–683, doi:10.1175/1520-0493(2002)130¡0668:GAOHG¿2.0.CO;2, URL http://dx.doi.org/10.1175/1520-0493(2002)130<0668:GAOHG>2.0.CO;2.

[37] Faure, S., M. Petcu, R. Temam, and J. Tribbia, 2011: On the inaccuracies of some finite volume discretizations of the linearized shallow water problem. *International Journal of Numerical Analysis and Modeling*, **8 (3)**, 518–541.

[38] Fjortoft, R., 1953: On the changes in the spectral distribution of kinetic energy for twodimensional, nondivergent flow. *Tellus*, **5 (3)**, 225–230, doi:10.1111/j.2153-3490.1953.tb01051.x, URL http://dx.doi.org/10.1111/j.2153-3490.1953.tb01051.x.

[39] Foreman, M., 1983: An analysis of the wave equation model for finite element tidal computations. *Journal of Computational Physics*, **52 (2)**, 290 – 312, doi:10.1016/0021-9991(83)90032-3, URL http://www.sciencedirect.com/science/article/pii/0021999183900323.

[40] Foreman, M., 1983: An analysis of two-step time discretizations in the solution of the linearized shallow water equations. *Journal of Computational Physics*, **51 (3)**, 454 – 483, doi:10.1016/0021-9991(83)90164-X, URL http://www.sciencedirect.com/science/article/pii/002199918390164X.

[41] Foreman, M., 1984: A two-dimensional dispersion analysis of selected methods for solving the linearized shallow water equations. *Journal of Computational Physics*, **56 (2)**, 287 – 323, doi:10.1016/0021-9991(84)90097-4, URL http://www.sciencedirect.com/science/article/pii/0021999184900974.

[42] Fox-Rabinovitz, M., 1991: Computational dispersion properties of horizontal staggered grids for atmospheric and ocean models. *Monthly Weather Review*, **119**, 1624–1639.

[43] Galewsky, J., R. K. Scott, and L. M. Polvani, 2011: An initial-value problem for testing numerical models of the global shallow-water equations. *Tellus A*, **56 (5)**, doi:10.3402/tellusa.v56i5.14436, URL http://www.tellusa.net/index.php/tellusa/article/view/14436.

[44] Gassmann, A., 2011: Inspection of hexagonal and triangular C-grid discretizations of the shallow water equations. *Journal of Computational Physics*, **230 (7)**, 2706–2721, doi:10.1016/j.jcp.2011.01.014, URL http://www.sciencedirect.com/science/article/pii/S0021999111000325.

[45] Gassmann, A., 2013: A global hexagonal C-grid non-hydrostatic dynamical core (ICON-IAP) designed for energetic consistency. *Quarterly Journal of the Royal Meteorological Society*, **139 (670)**, 152–175, doi:10.1002/qj.1960, URL http://doi.wiley.com/10.1002/qj.1960.

[46] Gassmann, A. and H.-J. Herzog, 2008: Towards a consistent numerical compressible non-hydrostatic model using generalized Hamiltonian tools. *Quarterly Journal of the Royal Meteorological Society*, **134 (635)**, 1597–1613, doi:10.1002/qj.297, URL http://doi.wiley.com/10.1002/qj.297.

[47] Gassmann, A. and H.-J. Herzog, 2014: How is local material entropy production represented in a numerical model? *Quarterly Journal of the Royal Meteorological Society*, n/a–n/a, doi:10.1002/qj.2404, URL http://doi.wiley.com/10.1002/qj.2404.

[48] Gavrilov, M. and I. Toi, 1998: Propagation of the rossby waves on two dimensional rectangular grids. *Meteorology and Atmospheric Physics*, **68**, 119–125, doi:10.1007/BF01030204, URL http://dx.doi.org/10.1007/BF01030204.

[49] Gay-Balmaz, F. and D. D. Holm, 2013: Selective decay by Casimir dissipation in inviscid fluids. *Nonlinearity*, **26 (2)**, 495–524, doi:10.1088/0951-7715/26/2/495, URL http://stacks.iop.org/0951-7715/26/i=2/a=495.

[50] Gilbert, A. D., X. Riedinger, and J. Thuburn, 2014: On the form of the viscous term for two dimensional Navier-Stokes flows. *The Quarterly Journal of Mechanics and Applied Mathematics*, **67 (2)**, 205–228, doi:10.1093/qjmam/hbu004, URL `http://qjmam.oxfordjournals.org/content/67/2/205.short?rss=1`.

[51] Gorski, K. M., E. Hivon, A. J. Banday, B. D. Wandelt, F. K. Hansen, M. Reinecke, and M. Bartelmann, 2005: HEALPix: A Framework for HighResolution Discretization and Fast Analysis of Data Distributed on the Sphere. *The Astrophysical Journal*, **622 (2)**, 759–771, doi:10.1086/427976, URL `http://iopscience.iop.org/0004-637X/622/2/759/fulltext/`.line

[52] Ham, D. A., S. C. Kramer, G. S. Stelling, and J. Pietrzak, 2007: The symmetry and stability of unstructured mesh c-grid shallow water models under the influence of coriolis. *Ocean Modelling*, **16 (12)**, 47 – 60, doi:10.1016/j.ocemod.2006.05.008, URL `http://www.sciencedirect.com/science/article/pii/S1463500306000783`.

[53] Hanert, E., R. A. Walters, D. Y. L. Roux, and J. D. Pietrzak, 2009: A tale of two elements: $p_1^{NC} - p_1$ and rt_0. *Ocean Modelling*, **28 (13)**, 24 – 33, doi:10.1016/j.ocemod.2008.07.002, URL `http://www.sciencedirect.com/science/article/pii/S1463500308000978`, the Sixth International Workshop on Unstructured Mesh Numerical Modelling of Coastal, Shelf and Ocean Flows.

[54] Hatcher, A., 2001: *Algebraic Topology*. Cambridge University Press.

[55] Haynes, P. H. and M. E. McIntyre, 1987: On the Evolution of Vorticity and Potential Vorticity in the Presence of Diabatic Heating and Frictional or Other Forces. *Journal of the Atmospheric Sciences*, **44 (5)**, 828–841, doi:10.1175/1520-0469(1987)044¡0828:OTEOVA¿2.0.CO;2.

[56] Haynes, P. H. and M. E. McIntyre, 1990: On the Conservation and Impermeability Theorems for Potential Vorticity. *Journal of the Atmospheric Sciences*, **47 (16)**, 2021–2031, doi:10.1175/1520-0469(1990)047¡2021:OTCAIT¿2.0.CO;2.

[57] Heikes, R. and D. A. Randall, 1995: Numerical Integration of the Shallow-Water Equations on a Twisted Icosahedral Grid. Part I: Basic Design and Results of Tests. *Monthly Weather Review*, **123 (6)**, 1862–1880, doi:10.1175/1520-0493(1995)123¡1862:NIOTSW¿2.0.CO;2.

[58] Heikes, R. and D. A. Randall, 1995: Numerical Integration of the Shallow-Water Equations on a Twisted Icosahedral Grid. Part II. A Detailed Description of the Grid and an Analysis of Numerical Accuracy. *Monthly Weather Review*, **123 (6)**, 1881–1887, doi:10.1175/1520-0493(1995)123¡1881:NIOTSW¿2.0.CO;2.

[59] Heikes, R. P., D. A. Randall, and C. S. Konor, 2013: Optimized Icosahedral Grids: Performance of Finite-Difference Operators and Multigrid Solver. *Monthly Weather Review*, **141 (12)**, 4450–4469, doi:10.1175/MWR-D-12-00236.1, URL http://journals.ametsoc.org/doi/abs/10.1175/MWR-D-12-00236.1.

[60] Hirani, A. N., 2003: Discrete exterior calculus. Ph.D. thesis, Caltech, URL http://thesis.library.caltech.edu/1885/3/thesis_hirani.pdf.

[61] Hollingsworth, A., P. Kå llberg, V. Renner, and D. M. Burridge, 1983: An internal symmetric computational instability. *Quarterly Journal of the Royal Meteorological Society*, **109 (460)**, 417–428, doi:10.1002/qj.49710946012, URL http://doi.wiley.com/10.1002/qj.49710946012.

[62] Hoskins, B. J., M. E. McIntyre, and A. W. Robertson, 1985: On the use and significance of isentropic potential vorticity maps. *Quarterly Journal of the Royal Meteorological Society*, **111 (470)**, 877–946, doi:10.1002/qj.49711147002.

[63] Hua, B.-L. and F. Thomasset, 2011: A noise-free finite element scheme for the two-layer shallow water equations. *Tellus A*, **36 (2)**, URL http://www.tellusa.net/index.php/tellusa/article/view/11478.

[64] Iga, S.-i. and H. Tomita, 2014: Improved smoothness and homogeneity of icosahedral grids using the spring dynamics method. *Journal of Computational Physics*, **258**, 208–226, doi:10.1016/j.jcp.2013.10.013, URL http://www.sciencedirect.com/science/article/pii/S0021999113006815.

[65] Ii, S. and F. Xiao, 2010: A global shallow water model using high order multimoment constrained finite volume method and icosahedral grid. *Journal of Computational Physics*, **229 (5)**, 1774–1796, doi:10.1016/j.jcp.2009.11.008, URL http://www.sciencedirect.com/science/article/pii/S0021999109006275.

[66] Jacobsen, D. W., M. Gunzburger, T. Ringler, J. Burkardt, and J. Peterson, 2013: Parallel algorithms for planar and spherical Delaunay construction with an application to centroidal Voronoi tessellations. *Geoscientific Model Development*, **6 (4)**, 1353–1365, doi:10.5194/gmd-6-1353-2013, URL http://www.geosci-model-dev.net/6/1353/2013/gmd-6-1353-2013.html.

[67] Jones, E., T. Oliphant, P. Peterson, et al., 2001–: *SciPy: Open source scientific tools for Python*. URL http://www.scipy.org/, [Online; accessed 2015-04-29].

[68] Kent, J., J. Thuburn, and N. Wood, 2012: Assessing implicit large eddy simulation for two-dimensional flow. *Quarterly Journal of the Royal Meteorological Society*, **138 (663)**, 365–376, doi:10.1002/qj.925, URL http://doi.wiley.com/10.1002/qj.925.

[69] Kleptsova, O., J. Pietrzak, and G. Stelling, 2009: On the accurate and stable reconstruction of tangential velocities in c-grid ocean models. *Ocean Modelling*, **28 (13)**, 118 – 126, doi:10.1016/j.ocemod.2008.12.007, URL http://www.sciencedirect.com/science/article/pii/S146350030800190X, the Sixth International Workshop on Unstructured Mesh Numerical Modelling of Coastal, Shelf and Ocean Flows.

[70] Lazić, L., Z. Janjić, and F. Mesinger, 1986: Non-cancellation instability in horizontal advection schemes for momentum equations. *Meteorology and Atmospheric Physics*, **35 (1-2)**, 49–52, doi:10.1007/BF01029522, URL http://link.springer.com/10.1007/BF01029522.

[71] Le Roux, D., 2005: Dispersion relation analysis of the $p_1^{NC} - p_1$ finite-element pair in shallow-water models. *SIAM Journal on Scientific Computing*, **27 (2)**, 394–414, doi:10.1137/030602435, URL http://epubs.siam.org/doi/abs/10.1137/030602435, http://epubs.siam.org/doi/pdf/10.1137/030602435.

[72] Le Roux, D., V. Rostand, and B. Pouliot, 2007: Analysis of numerically induced oscillations in 2d finite-element shallow-water models part i: Inertia-gravity waves. *SIAM Journal on Scientific Computing*, **29 (1)**, 331–360, doi:10.1137/060650106, URL http://epubs.siam.org/doi/abs/10.1137/060650106, http://epubs.siam.org/doi/pdf/10.1137/060650106.

[73] Le Roux, D. Y., 2012: Spurious inertial oscillations in shallow-water models. *Journal of Computational Physics*, **231 (24)**, 7959–7987, doi:10.1016/j.jcp.2012.04.052, URL http://www.sciencedirect.com/science/article/pii/S0021999112002872.

[74] Le Roux, D. Y., E. Hanert, V. Rostand, and B. Pouliot, 2009: Impact of mass lumping on gravity and rossby waves in 2d finite-element shallow-water models. *International Journal for Numerical Methods in Fluids*, **59 (7)**, 767–790, doi:10.1002/fld.1837, URL http://dx.doi.org/10.1002/fld.1837.

[75] LeFloch, P. G., J. M. Mercier, and C. Rohde, 2002: Fully Discrete, Entropy Conservative Schemes of ArbitraryOrder. *SIAM Journal on Numerical Analysis*, **40 (5)**, 1968–1992, doi:10.1137/S003614290240069X, URL http://epubs.siam.org/doi/abs/10.1137/S003614290240069X.line

[76] Liu, Y., B. Wang, and Z. Ji, 2014: Research on Atmospheric Motion in Horizontal Discrete Grids. *Advances in Atmospheric Sciences*, **20 (1)**, 139–148, doi:10.1007/BF03342058, URL http://link.springer.com/10.1007/BF03342058.

[77] LIU, Y.-D., Q.-H. ZHANG, and J. YUAN, 2006: Computational Properties of a New Horizontal Staggered Grid for Rossby Waves. *Chinese Journal of Geophysics*, **49 (3)**, 575–587, doi:10.1002/cjg2.871, URL http://doi.wiley.com/10.1002/cjg2.871.

[78] Lu, L., F. Sun, H. Pan, and W. Wang, 2012: Global Optimization of Centroidal Voronoi Tessellation with Monte Carlo Approach. *IEEE transactions on visualization and computer graphics*, 1880–1890, doi:10.1109/TVCG.2012.28, URL http://www.computer.org/csdl/trans/tg/2012/11/ttg2012111880.html.

[79] Marras, S., M. A. Kopera, and F. X. Giraldo, 2014: Simulation of shallow-water jets with a unified element-based continuous/discontinuous Galerkin model with grid flexibility on the sphere. *Quarterly Journal of the Royal Meteorological Society*, n/a–n/a, doi:10.1002/qj.2474, URL http://doi.wiley.com/10.1002/qj.2474.

[80] Mattiussi, C., 2002: *A Reference Discretization Strategy for the Numerical Solution of Physical Field Problems*, Advances in Imaging and Electron Physics, Vol. 121. Elsevier, doi:10.1016/S1076-5670(02)80027-1.

[81] McGregor, J. L., 2005: Geostrophic adjustment for reversibly staggered grids. *Monthly Weather Review*, **133 (5)**, 1119–1128, doi:10.1175/MWR2908.1, URL http://dx.doi.org/10.1175/MWR2908.1.

[82] McRae, A. T. T. and C. J. Cotter, 2014: Energy- and enstrophy-conserving schemes for the shallow-water equations, based on mimetic finite elements. *Quarterly Journal of the Royal Meteorological Society*, n/a–n/a, doi:10.1002/qj.2291, URL http://doi.wiley.com/10.1002/qj.2291.

[83] Melvin, T., A. Staniforth, and C. Cotter, 2014: A two-dimensional mixed finite-element pair on rectangles. *Quarterly Journal of the Royal Meteorological Society*, **140 (680)**, 930–942, doi:10.1002/qj.2189, URL http://doi.wiley.com/10.1002/qj.2189.

[84] Melvin, T., A. Staniforth, and J. Thuburn, 2012: Dispersion analysis of the spectral element method. *Quarterly Journal of the Royal Meteorological Society*, **138 (668)**, 1934–1947, doi:10.1002/qj.1906, URL http://doi.wiley.com/10.1002/qj.1906.

[85] Mesinger, F., 1981: Horizontal Advection Schemes of a Staggered Grid - An Enstrophy and Energy-Conserving Model. *Monthly Weather Review*, **109 (3)**, 467–478, doi:10.1175/1520-0493(1981)109¡0467:HASOAS¿2.0.CO;2.

[86] Mesinger, F. and A. Arakawa, 1976: Numerical methods used in atmospheric models, volume 1. *Global Atmospheric Research Program World Meteorological Organization, Geneva (Switzerland).*, Vol. 1.

[87] Miura, H. and M. Kimoto, 2005: A Comparison of Grid Quality of Optimized Spherical HexagonalPentagonal Geodesic Grids. *Monthly Weather Review*, **133 (10)**, 2817–2833, doi:10.1175/MWR2991.1, URL http://journals.ametsoc.org/doi/abs/10.1175/MWR2991.1.ne

[88] Mohammadian, A. M. and D. Y. Le Roux, 2008: Fourier analysis of a class of upwind schemes in shallow water systems for gravity and rossby waves. *International Journal for Numerical Methods in Fluids*, **57 (4)**, 389–416, doi:10.1002/fld.1617, URL http://dx.doi.org/10.1002/fld.1617.

[89] Mueller, E. H. and R. Scheichl, 2013: Massively parallel solvers for elliptic PDEs in Numerical Weather- and Climate Prediction. *arXiv*, 24, URL http://arxiv.org/abs/1307.2036, 1307.2036.

[90] Müller, E. H., R. Scheichl, B. Muite, and E. Vainikko, 2014: Petascale elliptic solvers for anisotropic PDEs on GPU clusters. *arXiv*, 17, URL http://arxiv.org/abs/1402.3545, 1402.3545.

[91] Nechaev, D. and M. Yaremchuk, 2004: On the approximation of the coriolis terms in c-grid models. *Monthly Weather Review*, **132 (9)**, 2283–2289, doi:10.1175/1520-0493(2004)132¡2283:OTAOTC¿2.0.CO;2, URL http://dx.doi.org/10.1175/1520-0493(2004)132<2283:OTAOTC>2.0.CO;2.

[92] Nevir, P. and M. Sommer, 2009: Energy-vorticity theory of ideal fluid mechanics. *Journal of the Atmospheric Sciences*, **66 (7)**, 2073–2084, doi:10.1175/2008JAS2897.1, URL http://dx.doi.org/10.1175/2008JAS2897.1.

[93] Paldor, N. and A. Sigalov, 2008: A unified linear wave theory of the shallow water equations on a rotating plane. *IUTAM Symposium on Hamiltonian Dynamics, Vortex Structures, Turbulence*, Springer Netherlands, IUTAM Bookseries, Vol. 6, 403–413, doi:10.1007/978-1-4020-6744-$0_3$6, *URL*

APPENDIX A

Hamiltonian Methods

A brief, non mathematically rigorous overview of infinite-dimensional Hamiltonian mechanics is provided below. The reader is referred to [122], [2], [121], [114] and [113] for more information. This material is purely pedagogical and no claims to originality are made.

A.1. Infinite Dimensional Non-Canonical Hamiltonian Systems

Consider a dynamical system described by a state vector $\vec{x} \in X$, where X is some infinite-dimensional space. Typically, X is a Banach space over some domain. If the dynamics can be represented as

$$\frac{\partial \vec{x}}{\partial t} = \mathbb{J}\frac{\delta \mathcal{H}}{\delta \vec{x}} \tag{385}$$

where $\mathcal{H}$ is some functional of the state vector $\vec{x}$ (called the Hamiltonian, making $\frac{\delta \mathcal{H}}{\delta \vec{x}}$ a functional derivative in the dual space X^*) and $\mathbb{J}$ is a antisymmetric bilinear form that satisfies the Jacobi identity on $X^* \times X^*$, then we say that the system is Hamiltonian. Many dynamical systems of interest in physics (including essentially all adiabatic and inviscid fluid dynamical systems) are Hamiltonian. Note that $\mathbb{J}$ can be a function of the state vector $\vec{x}$, although it must be anti-symmetric and satisfy the Jacobi identity for ANY values of the state vector. This particular representation of the dynamics is called the symplectic form. There are equivalent ways of representing Hamiltonian dynamics, but the symplectic form is useful in fluid mechanics because it works for both canonical and non-canonical Hamiltonian systems. In practice, $\frac{\delta \mathcal{H}}{\delta \vec{x}}$ can be associated uniquely with an element of X and $\mathbb{J}$ with a skew-symmetric differential operator on $X \times X$.

Poisson Brackets. The evolution of a general functional $\mathcal{F}$ is described by

$$\frac{d\mathcal{F}}{dt} = (\frac{\delta\mathcal{F}}{\delta\vec{x}}, \mathbb{J}\frac{\delta\mathcal{H}}{\delta\vec{x}}) = -(\frac{\delta\mathcal{H}}{\delta\vec{x}}, \mathbb{J}\frac{\delta\mathcal{F}}{\delta\vec{x}}) = \{\mathcal{F}, \mathcal{H}\} = -\{\mathcal{H}, \mathcal{F}\} \tag{386}$$

where we have used the skew-symmetry of $\mathbb{J}$, $(,)$ is the inner product associated with the function space that $\mathcal{F}$ is defined on and

$$\{\mathcal{A}, \mathcal{B}\} = (\frac{\delta\mathcal{A}}{\delta\vec{x}}, \mathbb{J}\frac{\delta\mathcal{B}}{\delta\vec{x}}) \tag{387}$$

is the Poisson bracket.

Properties of $\mathbb{J}$/Poisson Brackets. As mentioned above, $\mathbb{J}$ satisfies two key properties: skew-symmetry and the Jacobi identity. Skew symmetry simply means that

$$\{\mathcal{A}, \mathcal{B}\} = -\{\mathcal{B}, \mathcal{A}\} \tag{388}$$

for any two functionals $\mathcal{A}$ and $\mathcal{B}$. The Jacobi identity is

$$\{\mathcal{A}, \{\mathcal{B}, \mathcal{C}\}\} + \{\mathcal{C}, \{\mathcal{A}, \mathcal{B}\}\} + \{\mathcal{B}, \{\mathcal{C}, \mathcal{A}\}\} = 0 \tag{389}$$

for any three functionals $\mathcal{A}$, $\mathcal{B}$ and $\mathcal{C}$. For non-canonical Hamiltonian systems, $\mathbb{J}$ is singular and therefore there also exist functionals (termed Casimirs) that satisfy

$$\{\mathcal{C}, \mathcal{G}\} = 0 \quad \forall\mathcal{G} \tag{390}$$

where $\mathcal{G}$ is some arbitrary functional. By the chain rule for functional derivatives, this reduces to

$$\{\mathcal{C}, x_i\} = 0 \quad \forall x_i \tag{391}$$

In practice, when discretizing Hamiltonian systems, it is usually possible only to preserve the skew-symmetric aspect of $\mathbb{J}$ along with a few of the Casimirs. Fortunately, this is typically good enough.

A.2. Linearized Hamiltonian Dynamics

Consider a state of a Hamiltonian system $\vec{x} = \vec{x}_0$ where

$$\frac{\partial \vec{x}_0}{\partial t} = \mathbb{J}\frac{\delta \mathcal{H}}{\delta \vec{x}}|_{\vec{x}=\vec{x}_0} = 0 \tag{392}$$

ie it is stationary. It is always possible (since $\mathbb{J}\frac{\delta \mathcal{C}}{\delta \vec{x}} = 0$) to find a Casimir $\mathcal{C}_0$ such that

$$\frac{\delta \mathcal{H}}{\delta \vec{x}}|_{\vec{x}=\vec{x}_0} = -\frac{\delta \mathcal{C}_0}{\delta \vec{x}}|_{\vec{x}=\vec{x}_0} \tag{393}$$

Now form the quantity

$$\mathcal{A} = \mathcal{H} + \mathcal{C}_0 - \mathcal{H}|_{\vec{x}=\vec{x}_0} - \mathcal{C}_0|_{\vec{x}=\vec{x}_0} \tag{394}$$

This is called the psuedoenergy (or wave-activity) associated with the steady state $\vec{x}_0$. Note that it is an exact invariant of the system. For small disturbances from $\vec{x}$, it is quadratic in the disturbance amplitude. Since the Hamiltonian is arbitrary to a Casimir or constant, we

have

$$\frac{\partial \vec{x}}{\partial t} = \mathbf{J}\frac{\delta \mathcal{A}}{\delta \vec{x}} \tag{395}$$

This represents a fundamental gauge invariance in non-canonical Hamiltonian dynamics- the exact same dynamics are obtained for an infinite class of Hamiltonians. If $\mathbb{J}$ and $\mathcal{A}$ are expanded for small amplitude disturbances, the first-order approximation to this equation is

$$\frac{\partial \vec{x}}{\partial t} = \mathbb{J}_{linear}\frac{\delta \mathcal{H}_{linear}}{\delta \vec{x}} \tag{396}$$

where

$$\mathbb{J}_{linear} = \mathbb{J}|_{\vec{x}=\vec{x}_0} \tag{397}$$

and

$$\mathcal{H}_{linear} = \mathcal{A} \qquad \text{with small amplitude approximation} \tag{398}$$

This is (by definition) the linearized dynamics about $\vec{x}_0$.

A.3. Conserved Quantities

We now seek the invariants of the dynamical system; that is, the functionals $\mathcal{F}$ such that

$$\frac{d\mathcal{F}}{dt} = 0 \tag{399}$$

There are three types of such invariants: the Hamiltonian, Casimirs and Symmetry Invariants. By definition, the time evolution of $\mathcal{F}$ is given as

$$\frac{d\mathcal{F}}{dt} = \{\mathcal{F}, \mathcal{H}\} \tag{400}$$

A.3.1. Hamiltonian.

Consider the case where $\mathcal{F} = \mathcal{H}$. Then we have

$$\frac{d\mathcal{H}}{dt} = \{\mathcal{H}, \mathcal{H}\} = -\{\mathcal{H}, \mathcal{H}\} = 0 \tag{401}$$

where the second to last equality has been obtained using the skew-symmetry of the Poisson bracket and the final equality comes from the definition of the inner product along with the Poisson bracket. Note that this required two things: a skew-symmetric Poisson bracket and a positive-definite inner product. When discretizing a Hamiltonian system, the same two properties are required for conservation of the Hamiltonian.

A.3.2. Casimirs.

Now consider the case where $\mathcal{F} = \mathcal{C}$. Then we have

$$\frac{d\mathcal{C}}{dt} = \{\mathcal{C}, \mathcal{H}\} = 0 \tag{402}$$

by the definition of a Casimir ($\{\mathcal{C}, \mathcal{A}\} = 0$ for any functional $\mathcal{A}$).

A.3.3. Symmetry Invariants.

Let the state vector $\vec{x}$ be a function of some set of independent coordinates $\vec{y}$. Typically these are spatial and temporal coordinates, although their particular interpretation does not

matter. Consider a translation of one of the these coordinates:

$$y_k = y_k + \epsilon \tag{403}$$

If $\mathcal{H}$ (and $\mathbb{J}$) are invariant under this translation, such that

$$\mathcal{H}(\vec{x}(y_0, y_1, \dots, y_k, \dots)) = \mathcal{H}(\vec{x}(y_0, y_1, \dots, y_k + \epsilon, \dots)) \tag{404}$$

and

$$\mathbb{J}(\vec{x}(y_0, y_1, \dots, y_k, \dots)) = \mathbb{J}(\vec{x}(y_0, y_1, \dots, y_k + \epsilon, \dots)) \tag{405}$$

; and there exists some functional $\mathcal{M}$ that satisfies

$$\mathbb{J}\frac{\delta \mathcal{M}}{\delta \vec{x}} = -\frac{\partial \vec{x}}{\partial y^k} \tag{406}$$

then $\mathcal{M}$ is invariant in time. This is Noether's theorem- it relates symmetries to conserved quantities and is a fundamental tool of mathematical physics and Hamiltonian methods. In fact, if we let $\mathcal{M} = \mathcal{H}$ and $y_k = t$, it is easy to see that the invariance of the Hamiltonian arises due to a temporal symmetry.

A.3.4. Boundary Conditions.

Notice that nothing here has been said about boundary conditions, especially in the important area of conserved quantities and boundary conditions. For example, it is quite possible to have a physical system where energy (or mass, or momentum) are exchanged across some boundary. Obviously, energy will no longer be an invariant of the system anyway. However, the net flow of energy across the boundary will precisely balance the change in the

total energy of the system. This thesis does not consider systems with boundaries (all of the domains under consideration are closed). It is possible to incorporate boundary conditions into the Hamiltonian formulation given above, but for simplicity this point is ignored.

APPENDIX B

Horizontal Grids and Discretization Methods

A brief overview of discretization methods and meshes is provided below. This material is purely pedagogical and no claims to originality are made. The focus in this chapter is on Eulerian methods using a single mesh or primal-dual mesh pair.

B.1. Design of a Numerical Method

Consider a set of dependent variables $\vec{x} = (x_0, x_1, \dots)$ (called field functions) and independent variables $\vec{y} = (y_0, y_1, \dots)$. Typically the independent variables are spatial and/or temporal coordinates that describe a particular domain; and the dependent variables might be scalars such as pressure or vectors such as velocity. The evolution of the dependent variables is described by a set of coupled partial differential equations. This form is general enough to encompass most physical systems of interest. Fundamentally, the process of designing a numerical method for solving this system involves three connected steps:

(1) Choice of a discrete mesh in space and time to represent the domain: Usually the spatial mesh and the temporal mesh are determined independently, but coupled meshes are possible. Certain methods might even use multiple meshes (for example, a spectral transform method) or primal-dual mesh pairs.

(2) Choice of the representation of field functions on the mesh: This involves determining how many degrees of freedom for each field function are associated with each mesh element. Another name for this is grid staggering.

(3) Choice of how the various DOFs are combined to approximate the set of PDEs: Coupling can be local (confined to a small subset of other DOFs) or non-local (all DOFs are coupled). There are many possibilities here.

It is easy to see how different choices made here give rise to finite-difference, finite-volume, spectral transform, finite-element and other methods. It is also easy to see that the possible space of choices has not been well explored. **This work concerns itself only with the spatial mesh and associated grid staggering for single moment schemes and two spatial dimensions (each grid element has at most a single DOF for each field function associated with it); where the coupling between DOFs is local.** In addition, this appendix focuses primarily on items 1 and 2, while the thesis itself focuses on item 3. Additional information about mesh choice and field function representation using ideas from Discrete Exterior Calculus is found in Appendix C.

B.2. Horizontal Mesh Overview

When considering the rotating shallow water equations in the context of building an atmospheric dynamical core, there are two domains that need to be discretized: the doubly periodic plane (topologically isomorphic to $\mathbb{T}^2$) and the two-sphere $\mathbb{S}^2$. We are interested in quasi-uniform meshes without internal or external boundaries, although many of the same considerations apply to multiresolution meshes or meshes with boundaries.

B.2.1. Primal Mesh.

An excellent overview of quasi-uniform spherical grids and design criterion for their use in solving the rotating shallow water equations is given by [127]. Fundamentally, a horizontal mesh can be thought of as a set of mesh elements (faces, edges and vertices) that

are connected in a topologically consistent manner. They serve to divide the original physical domain in a set of connected subdomains on which the field functions are represented. In our case, a mesh starts with a set of primal vertices (dimensionality 0) that are connected by edges (dimensionality 1), which are geodesics of the underlying domain (straight lines for the plane, great circle arcs for the sphere). This creates a set of contiguous (spherical or planar) polygons (dimensionality 2), which are the mesh faces.

B.2.2. Dual Mesh.

In addition to these primal mesh elements, it is useful to consider a dual mesh. It is a well-known fact from algebraic topology that a consistent dual mesh always exists (for the case of a contiguous primal mesh) for a given primal mesh. In fact, the elements of the dual mesh have a one to one correspondence with the elements of the primal mesh; with the their dimensionality equal to n-k (n is the underlying dimension of the space, k is the dimensionality of the corresponding primal mesh element). For example, primal vertices can be associated in a unique 1-1 relationship with dual faces. This is a deep result from algebraic topology, and is the discrete analogue of the isomorphism between ordinary and twisted differential forms. See [54] for more details. There are many ways to construct a dual mesh; the most common are the Voronoi (or circumcentric) dual and the barycentric dual. They all amount to a choice of where to place the dual vertices that are associated with each primal face. Typically, this will be somewhere within the associated primal face. However, strongly distorted meshes will have some dual vertices that lie outside of their associated primal face. Such meshes can cause numerical difficulties. The general type of grid that we are interested in is shown in Figure B.1.

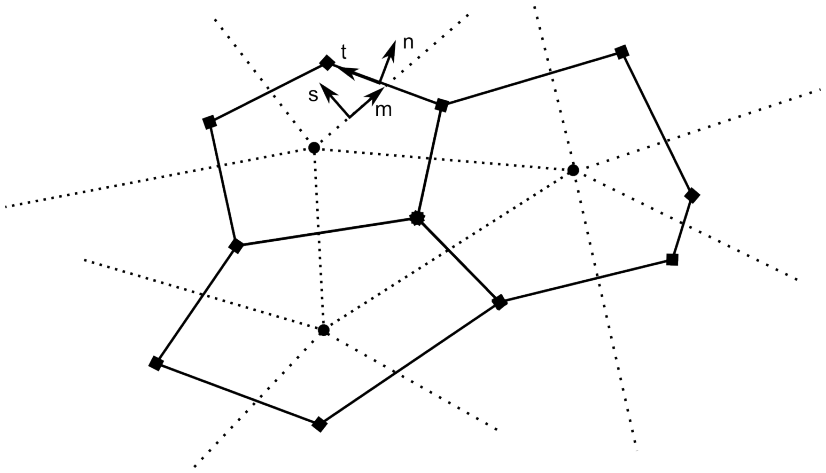

FIGURE B.1. A general non-orthogonal polygonal grid with an associated dual grid. If m and n are parallel for every edge, then the grid is orthogonal.

B.2.3. GRID GEOMETRY.

In addition to the topology of the grid, there are many geometric quantities associated with it of interest. Primarily, we are interested in:

(1) edge lengths le (primal edges) and de (dual edges)

(2) primal face areas A_i

(3) dual face areas A_v

(4) edge areas A_e

(5) overlapping dual and primal face areas A_{iv}

(6) overlapping edge primal face areas A_{ie}

These quantities are depicted pictorially in Figure B.2.

B.2.4. PITTEWAY GRIDS.

A Pitteway triangulation has the property each primal-dual edge pair intersects (see Figure B.3). It is a special case of the more general Delauney triangulation. This is a useful property for computing various geometric areas, and ensures that the grid is "well-behaved"

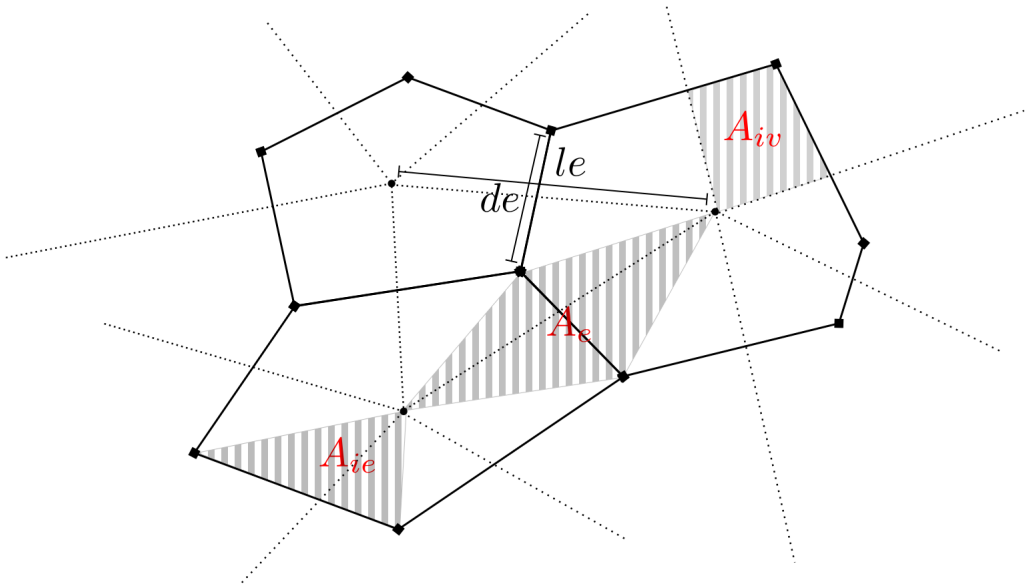

FIGURE B.2. Grid geometry

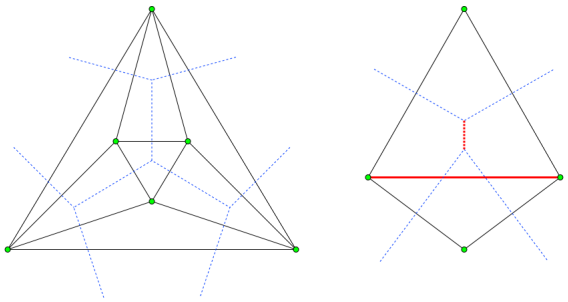

FIGURE B.3. On the left is a Pitteway triangulation, on the right is a non-Pitteway triangulation. This figure is from http://upload.wikimedia.org/wikipedia/commons/e/ee/Pitteway.svg, obtained under a Creative Commons license

in some sense. As discussed more below, quasi-uniform grids will almost always avoid these grid pathologies. Multiresolution grids, however, might not.

B.2.5. NEIGHBORS.

In addition to mesh geometry, there is also mesh topology to consider: in particular, the interconnection between neighboring grid elements. For example CV(v) denotes cells adjacent to a given vertex. The relevant stencils are given in Table 1.1. All of these stencils are self-explanatory, with the exception of ECP(e). ECP(e) is $\{EC(i1) \cup EC(i2)\}$, where $i1$

and $i2$ are $CE(e)$: it is the union of edges for the two cells on either side of an edge. More details about these stencils can be found in [135].

TABLE B.1. Mesh element neighbor stencils

Stencil	From	To
CV(v)	cells	vertices
EC(v)	edges	vertices
VC(i)	vertices	cells
EC(i)	edges	cells
CE(e)	cells	edges
VE(e)	vertices	edges
ECP(e)	edges	edges

B.2.6. Desirable Mesh Properties.

There are many desirable properties that a horizontal mesh can posses. When considering a quasi-uniform mesh, the following are key:

(1) Isotropic: Different directions in the mesh should look the same. Another way to say this is that the mesh is invariant under rotation (or since meshes are discrete, invariant under some subgroup of rotation).

(2) Local Uniformity: Adjacent grid cells are similar in size and shape.

(3) Global Uniformity: Global variation in grid cell size and shape is small.

(4) Orthogonality/Skewness: The primal and dual edges are orthogonal to each other. The degreee of non-orthogonality is termed skewness.

(5) Centroidality: The location of dual vertices is close to the centroid of the associated primal face.

(6) Cell types: The primal faces are composed of one type of polygon; and the dual faces are composed of another (possible the same) type of polygon.

(7) Cell shape: The primal and dual faces are both quadrilateral, which ensures that DOFs for a staggered grid method are balanced.

(8) Absence of Mesh Pathologies- The mesh should be free of pathologies. Dual vertices should lie in their associated primal cells. Dual and primal edges should intersect. Quasi-uniform grids almost always satisfy this. Multiresolution grids might not.

Clearly, these requirements can often come into conflict. More example, the uniform planar hexagonal grid is more isotropic than the uniform planar square grid, but it is no longer quadrilateral. Some of these requirements are topological (cell type and shape) and others are geometrical (uniformity, skewness, etc.). There are unavoidable topological constraints on polygonal meshes on the sphere (discussed below). Typically some weighted combination of the geometric requirements are optimized for actual applications.

Ideally a discretization scheme will work on arbitrary, non-orthogonal polygonal meshes. This gives the most flexibility in mesh optimization and construction for various applications; and to optimize computational performance. Obviously, better performance in a quantitative sense can be obtained for optimized meshes for a given method. However, the fundamental characteristics of the method (such as mimetic or conservation properties) should be independent of the mesh. The generalized C grid discretization presented above keeps its desirable properties on arbitrary, non-orthogonal polygonal meshes. The only exception to this are the linear mode properties of the C grid discretization, which has avoidable DOF ratio issues for non-quadrilateral grids. The generalized Z grid discretization works on for orthogonal polygonal grids, however as discussed this does not seems to be a major stumbling block.

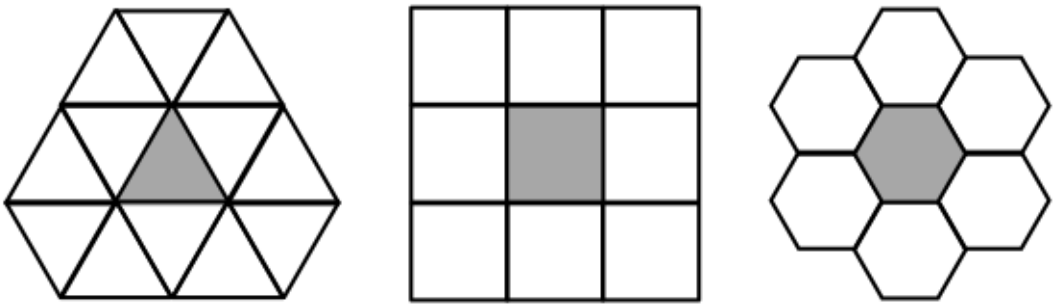

FIGURE B.4. Triangular, square and hexagonal uniform planar grids

B.3. Specific Meshes

As a matter of necessity, this will focus only on a subset of meshes on the plane and sphere. They are described below.

B.3.1. Planar Meshes.

Regular tiling of the plane with a single polygon type is possible only using hexagons, square or triangles (see Figure B.4). These meshes (using the circumcentric dual) are orthogonal, centroidal, completely uniform and have no mesh pathologies. The hexagonal mesh is the most isotropic, followed by the square mesh and then the triangular mesh (which suffers from an anisotropy in that there are "up" and "down" triangles). Note that the triangular and hexagonal meshes are dual to each other, while the square mesh is dual to itself.

It is also possible to build orthogonal, non-uniform meshes using Voronoi tesselations which will give either hexagonal (with some pentagonal and heptagonal cells; using the Voronoi tesselation) or triangular cells (using the Delauney dual). These meshes are orthogonal, and can be optimized to be centroidal using the Centroidal Voronoi Tesselation. They are useful primarily when multiresolution meshes are desired.

B.3.2. Spherical Meshes.

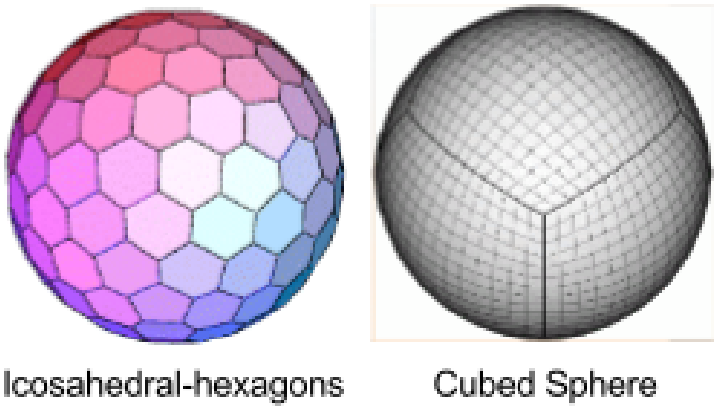

FIGURE B.5. Icosahedral-hexagonal and (gnomic) cubed sphere grids

We consider only the case of a single, non-overlapping primal grid created by projection of a Platonic solid onto the sphere, followed by subdivision of its faces. More details can be found in [127] and [98]. Some examples of these grids are shown in Figure B.5.

Topology of the Sphere. Unlike the plane, it is impossible to tile the sphere with polygons such that both the primal and the dual grid have a single type of cell. Fortunately, these singular points are limited in number and isolated. These unavoidable singularities arise from topological nature of the sphere (in particular, its Euler characteristic of 2).

B.3.3. ICOSAHEDRAL GRID.

Icosahedral grids are based on the subdivision and projection of the icosahedron onto the sphere (equivalently, one can start from dodecahedron- the dual of the icosahedron). One obtains a grid made entirely of triangles in this manner, while the dual grid is made of hexagons and 12 pentagons corresponding to the original vertices of the icosahedron. From linear mode and isotropy considerations, typically the hexagonal-pentagonal grid is used as the primal grid; while the triangular grid is used as the dual. There are 12 point singularities located at the pentagons, and weak singularities along the lines connection pentagons.

Geodesic grids can be centroidal, depending on how exactly the dual grid is defined (see SCVT methods, discussed in Chapter 7). They are also orthogonal, and the quasi-uniform construction described here does not posses any grid pathologies. More discussion of various construction and optimization methods for geodesic grids is provided in Chapter 7.

B.3.4. Cubed-Sphere.

The cubed sphere grid is based on the subdivision and projection of the cube onto the sphere. The primal grid is composed of square elements, while the dual grid is made of squares and 8 triangles (corresponding to the original vertices of the cube). There are 8 point singularities located at the triangles (called panel corners), and weak singularities along the lines connecting triangles (called panel edges). Cubed sphere grids do not posses any grid pathologies. Depending on the projection method, the grid can orthogonal (conformal projection) or non-orthogonal (gnomic projection). Since there is strong grid cell clustering at the singular points using the conformal project, typically the gnomic projection is used. More discussion of various construction and optimization methods for cubed sphere grids is provided in Chapter 7.

B.3.5. Mesh Optimization Methods.

Once the topology of a mesh has been established, there remains a great deal of optimization of the geometry properties that is possible. Extant examples of optimizations methods in current use include SCVT/CVT, Spring Dynamics and Tweaked Grids. There are many other possible methods, usually optimizing some combination of local and global uniformity, centroidality and skewness. Again, the space of possible optimizations is greatly enlarged if the discretization method supports very general grids.

B.3.6. Other Grids.

In addition to the cube and the icosahedron/dodecahedron, it is also possible start from the octagon ([101]) to generate a quasi-uniform spherical grid. There have also been various quadrilateral "kite" grids based on either the cubed sphere or the geodesic grid. There are also other attempts to create quasi-uniform spherical grids not based on polyhedral projection. Such attempts include the electrostatic grid and the Fibonnaci grid. Two unexplored areas of possible quasi-uniform spherical grids for atmospheric dynamical cores are those used in astronomy to map and analyse the Cosmic Microwave Background Radiation; and those used in other branches of earth science (such as [51]). At least one of those (HEALPIX) shows promise.

B.4. Field Function Representation

Once a mesh has been obtained, there are many different ways to represent the field functions on it: point vales, edge or face integrated values, polynomial basis function, etc. As stated before, this thesis deals with methods that associate one degree of freedom per mesh element for each field function; and each field function is associated with only one type of mesh element. This is consistent with finite-difference or finite-volume methods. In addition, these degrees of freedom are coupled in a local manner: only DOFs within some limited neighbourhood are coupled.

B.4.1. Grid Staggering.

When a system of equations encompasses several variables, there are choices to be made in how to place these variables on the horizontal mesh. This is referred to as grid staggering. For the shallow water equations, there are either two or three variables depending on the

formulation chosen- height and velocity (a vector quantity) for the vector invariant formulation OR height, vorticity and divergence for the vorticity-divergence formulation. Various possible staggerings for these variables are described in REFS and reproduced in Figure B.6. The A grid collocates all variables at the same point (usually considered the center of a grid cell). The B grid places the mass variable at the center of a cell and the wind vector at cell vertices. The C grid places the mass variable at the center of a cell and the normal component of the velocity at cell walls (for certain schemes on non-orthogonal grids the velocity component at the walls is not necessarily the normal component, but it is similar in spirit to a C-grid). The D grid places the mass variable at the center of a cell and the tangential component of velocity at cell walls (again for certain schemes on non-orthogonal grids the velocity component at the walls is not necessarily the tangential component, but it is similar in spirit to a D-grid). The Z grid places the mass variable, vorticity and divergence all at the center of a cell. The ZC grid places the height and divergence at cell centers and vorticity at cell vertices. These grid staggering definitions are general enough to apply to arbitrary polygonal meshes, including all the spherical meshes currently in use. Note that the A, B, C and D grids apply for the vector invariant or flux form formulations, while the Z grid and ZC grid apply for the vorticity-divergence formulation.

From considerations in DEC and Hamiltonian Mechanics, it is advisable to use either the C grid staggering, the Z grid staggering or the ZC grid staggering. This thesis focuses on Z and C grid staggerings. The ZC grid, although theoretically interesting, suffers from the same DOF balancing issues as the C grid but has a similar computational cost to the Z grid staggering. Therefore, it offers little practical advantage over the C or Z grid staggerings.

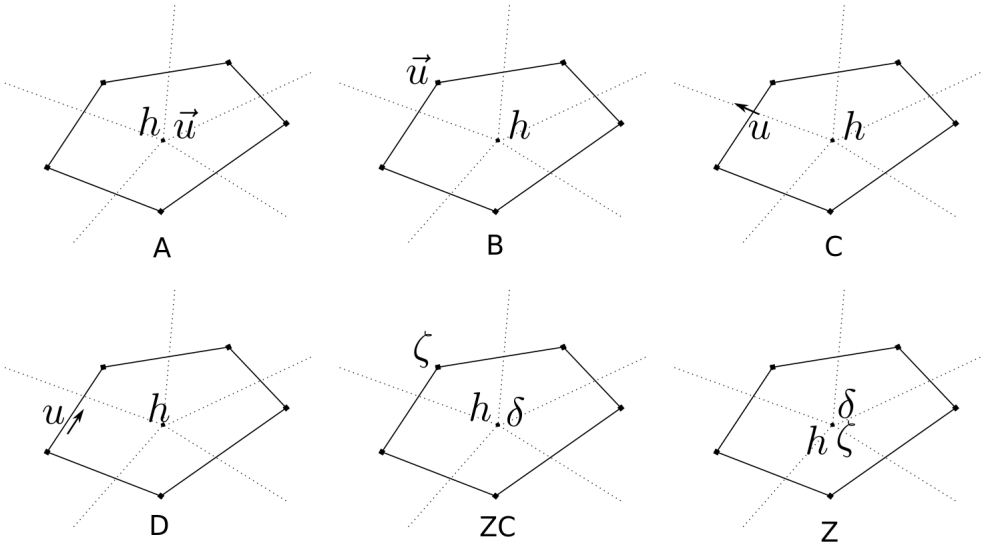

FIGURE B.6. Various choices of grid staggering for the shallow water equations

APPENDIX C

Discrete Exterior Calculus

A brief review of discrete exterior calculus on 2D manifolds is given below. More information is available in [15], [97], [145], [144], [80], [143] and [60]. Whenever necessary, mathematical rigor has been sacrificed for ease of exposition. This material is purely pedagogical and no claims to originality are made.

C.1. Discrete Exterior Calculus in 2D

The primary operators of interest are the exterior derivative d and the Hodge star operator $*$. Other operators such as the Lie derivative $\mathcal{L}_{\vec{u}}$, interior product $i_{\vec{u}}$, sharp $\sharp$ and flat $\flat$ can also be derived, but a consistent theory of these remains an active area of research.

C.1.1. General Setup.

Start by considering a two dimensional primal-dual polygonal mesh such that the dual mesh vertices lie within the associated primal mesh cells. This mesh does not necessarily have to be orthgonal; and it can use the circumcentric (Voronoi) dual, the barycentric dual or some other dual. Such a mesh is sufficiently general to encompass various planar grids (squares, triangles, hexagons) along with many quasi-uniform spherical grids (geodesic hexagonal-pentagonal, geodesic triangular, cubed sphere). There are six types of mesh elements: primal cells, primal edges, primal vertices, dual cells, dual edges and dual vertices. In addition, there is a 1-1 correspondence (isomorphism) between primal cells - dual vertices, primal edges - dual edges and primal vertices - dual cells. This is precisely analogous to the isomorphism between ordinary and twisted forms induced by the Hodge star operator (indeed, such a primal-dual cell complex can be and is used as the basis for defining a discrete Hodge star).

Following from exterior calculus considerations for a 2D manifold, there are six types of objects that we want to represent: ordinary 0,1 and 2-forms; and twisted 0,1 and 2-forms. Each type of object can be uniquely associated with a geometric entity. Conveniently (actually, this is a deep property from algebraic topology), we have also have six types of geometric entities. Ordinary forms will be associated with the primal grid, and twisted forms will associated with the dual grid. 0-forms are associated with points, 1-forms are associated with edges and 2-forms are associated with cells. There is an isomorphism between geometric entities on the primal grid, and geometric entities on the dual grid (this is duality, and is another deep result from algebraic topology). This isomorphism will be represented using the DEC approach by defining a set of discrete Hodge stars. There is one degree of freedom per object associated with each geometric entity (ie this a single moment scheme).

C.1.1.1. *Incidence Matrices.*

Incidence matrices describe the topological relationships between geometric elements on the same (primal or dual) grid. Since we are working in two dimensions, there are four: D_1,D_2,$\bar{D}_1$,$\bar{D}_2$; where for example D_1 maps from primal 0-form to primal 1-form, and D_2 maps from dual 1-forms to dual 2-forms. They are a discrete analogue of the differential operator d, and therefore represent discrete divergence, gradient and curl. Continuous properties such as $\vec{\nabla}^T \cdot \vec{\nabla} = 0$ are automatically enforced by construction (ex $D_2 D_1 = 0$). These operators are defined purely topologically using the cell complex structure from algebraic topology. Specifically, they are defined as:

$$D_2 = \sum_{e \in EC(i)} n_{e,i} \tag{407}$$

$$\bar{D}_1 = \sum_{i \in CE(e)} -n_{e,i} \tag{408}$$

$$\bar{D}_2 = \sum_{e \in EV(v)} t_{e,v} \tag{409}$$

$$D_1 = \sum_{v \in VE(e)} t_{e,v} \tag{410}$$

The following properties hold:

$$D_2 D_1 = 0 \tag{411}$$

$$\bar{D}_2 \bar{D}_1 = 0 \tag{412}$$

$$D_2 = -\bar{D}_1{}^T \tag{413}$$

$$\bar{D}_2 = D_1^T \tag{414}$$

C.1.1.2. *Hodge Star Operators.*

The discrete Hodge Star operators map between variables defined on the primal grid and variables defined on the dual grid (in fact, they DEFINE the dual grid). There are two types of discrete Hodge stars that are typically used: circumcentric (or Voronoi) and barycentric. In this work, we will use exclusively circumcentric Hodge stars (which are diagonal) with the

exception of the dual 1-form circulations to primal 1-form fluxes Hodge star **H** for cubed-sphere grids. Note that a discrete Hodge star induces a discrete inner product. Of couse, this process could be reversed: an inner product could be used to define a Hodge star. This leads to mixed finite-element methods and is the basis of the finite-element exterior calculus (FEEC) approach (see [5] and [6] for an excellent, albeit technical, introduction to FEEC).

Specifically, the circumcentric Hodge star operators are defined as

$$\mathbf{I} = \frac{1}{A_i} \tag{415}$$

$$\mathbf{J} = \frac{1}{A_v} \tag{416}$$

$$\mathbf{H} = \frac{le}{de} \tag{417}$$

where the geometric quantities are defined using either planar OR spherical operators, where appropriate.

The incidence matrices combined with the Hodge star operators form what is known as a discrete DeRham cohomology, which is depicted pictorially in Figure C.1. Note however, that paths do not commute (unlike in the continuous case).

C.1.1.3. *Inner Products.*

As discussed above, the three discrete hodge star operators (**I**,**J** and **H**) each induce inner products. There are nine inner products that arise, and they are defined as:

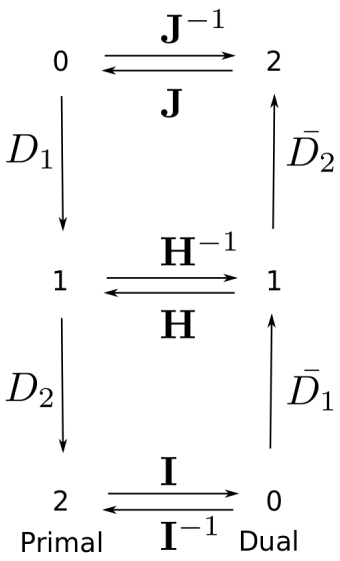

FIGURE C.1. The discrete DeRham cohomology induced by the incidence matrices and Hodge stars

(418) $(A_i, B_i)_{\mathbf{I}} = (A_i)^T \mathbf{I} B_i = (B_i)^T \mathbf{I} A_i$ where A_i and B_i are primal 2-forms

(419) $(A_i, B_i)_{\mathbf{I^{-1}}} = (A_i)^T \mathbf{I}^{-1} B_i = (B_i)^T \mathbf{I}^{-1} A_i$ where A_i and B_i are dual 0-forms

(420) $(A_i, B_i)_{\mathbf{I}} = (A_i)^T B_i = (B_i)^T A_i$ where A_i is a primal 2-form and B_i is a dual 0-form

(421) $(A_i, B_i)_{\mathbf{J}} = (A_i)^T \mathbf{J} B_i = (B_i)^T \mathbf{J} A_i$ where A_i and B_i are dual 2-forms

(422) $(A_i, B_i)_{\mathbf{J^{-1}}} = (A_i)^T \mathbf{J}^{-1} B_i = (B_i)^T \mathbf{J}^{-1} A_i$ where A_i and B_i are primal 0-forms

(423) $(A_i, B_i)_{\mathbf{J}} = (A_i)^T B_i = (B_i)^T A_i$ where A_i is a dual 2-form and B_i is a primal 0-form

(424) $(A_i, B_i)_{\mathbf{H}} = (A_i)^T \mathbf{H} B_i = (B_i)^T \mathbf{H} A_i$ where A_i and B_i are dual 1-forms

(425) $(A_i, B_i)_{\mathbf{H^{-1}}} = (A_i)^T \mathbf{H}^{-1} B_i = (B_i)^T \mathbf{H}^{-1} A_i$ where A_i and B_i are primal 1-forms

(426) $(A_i, B_i)_{\mathbf{H}} = (A_i)^T B_i = (B_i)^T A_i$ where A_i is a primal 1-form and B_i is a dual 1-form

In order for these inner products to exist and have the correct properties, it is required that **I**,**J** and **H** are symmetric and positive definite (which, among other things, ensures that they are invertible).

C.1.1.4. *Laplacian Operators.*

Since there are six types of discrete objects, there are six different Laplacian operators. They are

(427) $\vec{\nabla}^2 a_i = D_2 \mathbf{H} \bar{D}_1 \mathbf{I} a_i$ where $a_i$is a primal 2-form

(428) $\vec{\nabla}^2 a_i = \mathbf{I} D_2 \mathbf{H} \bar{D}_1 a_i$ where $a_i$is a dual 0-form

(429) $\vec{\nabla}^2 a_v = -\bar{D}_2 \mathbf{H}^{-1} D_1 \mathbf{J} a_v$ where $a_v$is a dual 2-form

(430) $$\vec{\nabla}^2 a_v = -\mathbf{J}\bar{D}_2\mathbf{H}^{-1}D_1 a_v \text{ where } a_v\text{is a primal 0-form}$$

(431) $$\vec{\nabla}^2 a_e = \mathbf{H}\bar{D}_1\mathbf{I}D_2 a_e - D_1\mathbf{J}\bar{D}_2\mathbf{H}^{-1}a_e \text{ where } a_e\text{is a primal 1-form}$$

(432) $$\vec{\nabla}^2 a_e = \bar{D}_1\mathbf{I}D_2\mathbf{H}a_e - \mathbf{H}^{-1}D_1\mathbf{J}\bar{D}_2 a_e \text{ where } a_e\text{is a dual 1-form}$$

APPENDIX D

Dispersion Relations and Allowed Wavenumbers for Planar Grids

D.1. Dispersion Relations for Planar Grids

Analytic expressions for the dispersion relations for the C and Z grid schemes on perfect square and perfect hexagonal planar grids are presented below. These results are not new, they can be found in [100] and [132].

In all cases, $C = \frac{\lambda}{d}$ where d is the grid spacing, $kd + ld$ are the non-dimensional wavenumbers and $\lambda = \frac{\sqrt{gH}}{f}$.

D.1.1. Perfect Planar Square Grids.

SZ. On a uniform square grid, the Z grid scheme dispersion relationship is:

$$\frac{\sigma^2}{f^2} = 1 + 4C^2(\sin^2(\frac{kd}{2}) + \sin^2(\frac{ld}{2})) \tag{433}$$

SC. On a uniform square grid, the C grid scheme dispersion relationship is:

$$\frac{\sigma^2}{f^2} = \frac{1}{4}(1 + \cos(ld) + cos(kd) + \cos(kd)\cos(ld)) + 4C^2(\sin^2(\frac{kd}{2}) + \sin^2(\frac{ld}{2})) \tag{434}$$

D.1.2. Perfect Planar Hexagonal Grids.

It is useful to define two auxiliary quantities on hexagonal grids:

$$a = \frac{kd}{4} \tag{435}$$

$$b = \frac{\sqrt{3}}{4} ld \tag{436}$$

HZ. On a uniform hexagonal grid, the Z grid scheme dispersion relationship is:

$$\frac{\sigma^2}{f^2} = 1 + R \tag{437}$$

where

$$R = \frac{8}{3} C^2 \left[\sin^2(2a) + sin^2(-a + b) + sin^2(-a - b) \right] \tag{438}$$

and

HC. On a uniform hexagonal grid, the C grid scheme dispersion relationship is:

$$\frac{\sigma^2}{f^2} = \frac{A}{3} + \frac{8}{3} C^2 B \tag{439}$$

where

$$A = a_1^2 + a_2^2 + a_3^2 \tag{440}$$

$$B = s_1^2 + s_2^2 + s_3^2 \tag{441}$$

$$a_1 = \frac{2c_2c_3 + c_1}{3} \tag{442}$$

$$a_2 = \frac{2c_3c_1 + c_2}{3} \tag{443}$$

$$a_3 = \frac{2c_1c_2 + c_3}{3} \tag{444}$$

$$c_1 = \cos(2a) \tag{445}$$

$$c_2 = \cos(-a + b) \tag{446}$$

$$c_3 = \cos(-a - b) \tag{447}$$

$$s_1 = \sin(2a) \tag{448}$$

$$s_2 = \sin(-a + b) \tag{449}$$

$$s_3 = \sin(-a - b) \tag{450}$$

D.2. Allowed Wavenumbers for Planar Grids

On a discrete grid, only certain wavenumbers will be supported. These wavenumbers will be determined by the type of grid element and the number of grid cells. The actual grid spacing does not play a role (when viewed from the non-dimensional perspective). In particular, there will be a minimal wavenumber corresponding the longest wavelength that can be resolved and a maximumal wavenumber corresponding to the shortest wavelength that be resolved (typically twice the grid spacing). In addition to a discrete and finite

wavenumber space, there will also be aliasing associated with a grid. Waves with a higher wavenumber than those supported by the grid will be aliased into waves that are supported on the grid. Specific examples of discrete wavenumber spaces and aliasing are given below.

D.2.1. Perfect Planar Square.

The perfect planar square mesh is a doubly periodic mesh composed of regular rectangles (squares) of identical size. Assume such a mesh of size nx by ny grid cells. Such a mesh will support discrete wavenumbers of the form:

$$kd = \frac{2\pi x_n}{nx};\ ld = \frac{2\pi y_n}{ny} \tag{451}$$

where $x_n = -nx + 1, \ldots, nx$ and $y_n = -ny + 1, \ldots, ny$. This set of wavenumbers is then truncated to lie in the first Brioullin zone given by

$$S = [(\pi, \pi), (-\pi, \pi), (-\pi, -\pi), (\pi, -\pi)] \tag{452}$$

This gives maximal wavenumbers of $x_n = \frac{nx}{2}$ for nx even and $x_n = \frac{nx-1}{2}$ for nx odd (with similar results for y_n). The minimal wavenumber is given by $x_n = 1$ (discounting the $x_n = 0$ mode, which is simply constant in space).

D.2.2. Perfect Planar Hexagonal.

The perfect planar hexagonal mesh is a doubly periodic mesh composed of regular hexagons of identical size. Assume such a mesh of size nx by ny grid cells. Such a mesh will support discrete wavenumbers of the form:

$$kd = \frac{2\pi x_n}{nx};\ ld = \frac{2\pi y_n}{\sqrt{3}ny} - \frac{2\pi x_n}{\sqrt{3}nx} \tag{453}$$

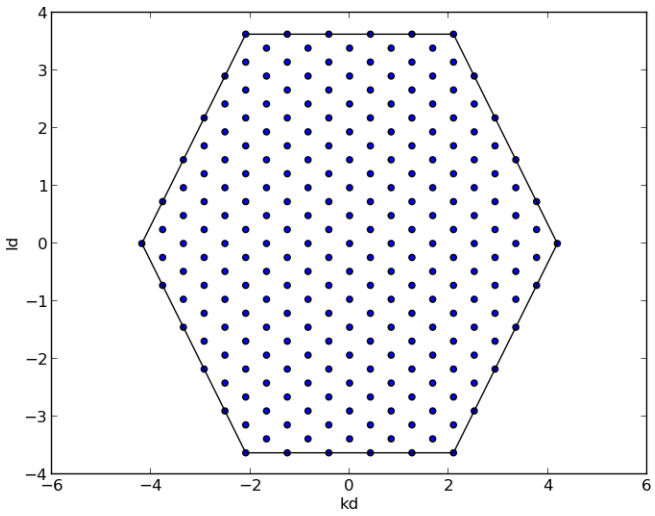

FIGURE D.1. Allowed wavenumbers on the hexagonal grid

where $x_n = -nx + 1, \ldots, nx$ and $y_n = -2nx - ny + 1, \ldots, 2nx + ny$. A plot of the allowed wavenumbers is shown in Figure D.1.

This set of wavenumbers is then truncated to lie in the first Brioullin zone given by

(454)

$$H = \left[(-4\pi/3, 0), (-2\pi/3, 2\pi/\sqrt{3})), (2\pi/3, 2\pi/\sqrt{3})), (4\pi/3, 0), (2\pi/3, -2\pi/\sqrt{3}), (-2\pi/3, -2\pi/\sqrt{3})\right]$$

The maximal wavenumber occurs at the corners of the hexagonal Brioullin zone. For example, for the corner $(-4\pi/3, 0)$, the associated maximal wavenumber is $x_n = \frac{2nx}{3}$ and $y_n = \frac{2ny}{3}$. The minimal wavenumbers are again, $x_n = 1$ and $y_n = 1$.